FUNCTIONALLY GRADED FIBER-REINFORCED CEMENTITIOUS COMPOSITES – MANUFACTURING AND EXTRACTION OF COHESIVE FRACTURE PROPERTIES USING FINITE ELEMENTS AND DIGITAL IMAGE CORRELATION

BY

BIN SHEN

B.S., Zhejiang University, 1999
M.Phil., Hong Kong University of Science and Technology, 2003

DISSERTATION

Submitted in partial fulfillment of the requirements
for the degree of Doctor of Philosophy in Civil Engineering
in the Graduate College of the
University of Illinois at Urbana-Champaign, 2009

Urbana, Illinois

Doctoral Committee

Professor Glaucio H. Paulino, Chair, Director of Research
Professor Surendra P. Shah, Northwestern University
Professor Leslie J. Struble
Professor David A. Lange
Assistant Professor Ilinca Stanciulescu

ABSTRACT

FUNCTIONALLY GRADED FIBER-REINFORCED CEMENTITIOUS COMPOSITES – MANUFACTURING AND EXTRACTION OF COHESIVE FRACTURE PROPERTIES USING FINITE ELEMENTS AND DIGITAL IMAGE CORRELATION

Bin Shen

Department of Civil and Environmental Engineering
University of Illinois at Urbana Champaign

Glaucio. H. Paulino, Adviser

A novel four-layer functionally graded fiber-reinforced cementitious composite (FGFRCC) as a beam component has been fabricated using extrusion and pressing techniques. The FGFRCC features a linear gradation of fiber volume fraction through the beam depth. The bending test shows the enhanced bending strength of the FGFRCC without delamination at layer interface. Microstructure investigation verifies the fiber gradation and the smooth transition between homogeneous layers. The remaining part of the study is the development of a hybrid technique for the extraction of mode I cohesive zone model (CZM). First, a full-field digital image correlation (DIC) technique has been adopted to compute the two-dimensional displacement fields. Such displacement fields are used as the input to the finite element (FE) formulation of an inverse problem for computing the CZM. The CZM is parameterized using flexible splines without assumption of the model shape. The Nelder-Mead optimization method is used to solve the ill-posed nonlinear inverse problem. Barrier and regularization terms are incorporated in the objective function for the inverse problem to assist optimization. Numerical tests show the robustness of the technique and the tolerance to experimental noise. The techniques are then applied to plastics and homogeneous FRCCs to demonstrate its broader application.

To my parents

ACKNOWLEDGEMENT

I take this opportunity to express my profound gratitude to my advisor, Professor Glaucio H. Paulino. It is through his warm encouragement, constant support and guidance, and invaluable suggestions and feedback that this work can finally be accomplished. His dedications to research, rich knowledge, high standard and great enthusiasm have been the source of motivation during my study.

I express my deep appreciation to Professor Leslie J. Struble for her kind support and advice at different stages of my study. Appreciation extends to Professor David A. Lange and Professor Surendra P. Shah, who kindly served in my dissertation committee and provided insightful suggestions and feedbacks. Special thanks are given to Professor Ilinca Stanciulescu, who shared her expertise with me and kindly helped me with detailed research problems. Working with her is really a pleasant experience.

I would also like to thank my officemates: Matthew Carl Walters, Alok Sutradhar, Seong-Hyeok Song, Huiming Yin, Zhengyu Zhang, Kyoungsoo Park, Tam Hong Nguyen, Arun L. Gain and Cameron Talischi. Their company makes my study here at the Newmark Civil Engineering Laboratory enjoyable. I also thank Mija Hubler and Mathew Fadden for their help in the research project and for their contribution to this work. Special thanks are due to Eshan Dave, who has been an invaluable friend for me, for helping me immensely in my life here at Champaign and for bringing me a lot of fun. Special thanks are also given to Dr. Grzegorz Banas for his very kind consideration and constant technical support -- without him this work would be impossible.

I finally would like to show my deepest gratefulness to my family. They witnessed my happiness and my struggle through the years. It was them who have always shown their confidence on me. I thank them for bearing my absence for the many years while I was pursuing my Ph.D. in the United States.

TABLE OF CONTENTS

LIST OF TABLES

LIST OF FIGURES

CHAPTER 1 – INTRODUCTION

Cementitious materials, including cement paste, mortar, concrete, etc. are the fundamental construction materials that our modern infrastructure is built upon. The three primary reasons that make cement-based materials the most popular engineering materials are: excellent resistance to water, ease of forming a variety of shapes and sizes, and being inexpensive and most readily available on the job [1]. Primarily applied as a structural building material, the most important requirement of cement-based materials is the mechanical property. Although cementitious materials are rigid and strong in compression, they are usually regarded as brittle materials when they are used as structural materials. Over the years, the researchers and engineers have been constantly trying to improve the tensile strength and ductility of cementitious materials. The most effective solution to date is the incorporation of fibers. Such fiber-cement matrix system is known as the fiber reinforced cementitious composites (FRCC). Strong in tension, the fibers act as crack bridging agents for the brittle matrix, thus preserving the structural integrity of the material system. On the other hand, the rigid matrix provides anchorage for the fibers so that the strength of fibers can be utilized. Such synergistic effect shows great potential in the application to new and challenging construction applications.

A new functionally graded FRCC (FGFRCC) has been explored in the current research. It is realized that the cohesive properties shall be more accurately obtained through new experimental techniques for the purpose of accurate fracture simulation of FGFRCC. In the remaining of this introductory chapter, some background material is provided first. Then the need of a new type of FRCC, which makes efficient use of fibers, therefore reducing cost, is elaborated upon. Afterwards, the functionally-graded materials (FGM) concept is explained and related to the current research. A review of CZM follows and then available techniques for measuring or computing the CZM are presented. Lastly, after all the literature review, the research objectives and thesis organization are introduced.

1.1 BACKGROUND

In the past few decades, great improvement has been achieved in FRCC. Ductile fiber reinforced cementitious composite (DFRCC), which exhibits multiple cracking and deflection hardening in bending, and high performance fiber reinforced cementitious composite (HPFRCC), which exhibits multiple cracking and tensile strain hardening, can now be routinely and reliably produced and some have also been commercialized [2]. Figure 1.1 shows the mechanical response of brittle cement-based matrix, conventional FRCC, DFRCC and HPFRCC. Figure 1.2 shows the relation between these cement-based materials, especially for FRCC, based on the mechanical properties. Such performance improvement relies on materials selection, mix design and processing solutions that ensures a homogeneous dispersion of fibers in the FRCC. The enhancement in homogeneity reduces the size and number of potentially weak regions, thus improves the overall performance.

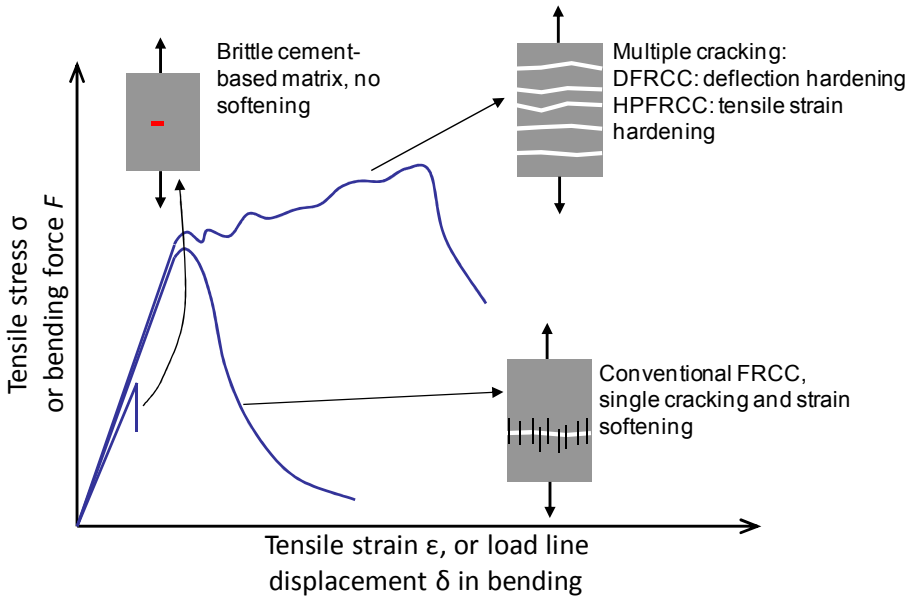

Figure 1.1: Relation between brittle cement-based matrix, conventional FRCC, DFRCC and HPFRCC (only schematic tensile coupon is shown)

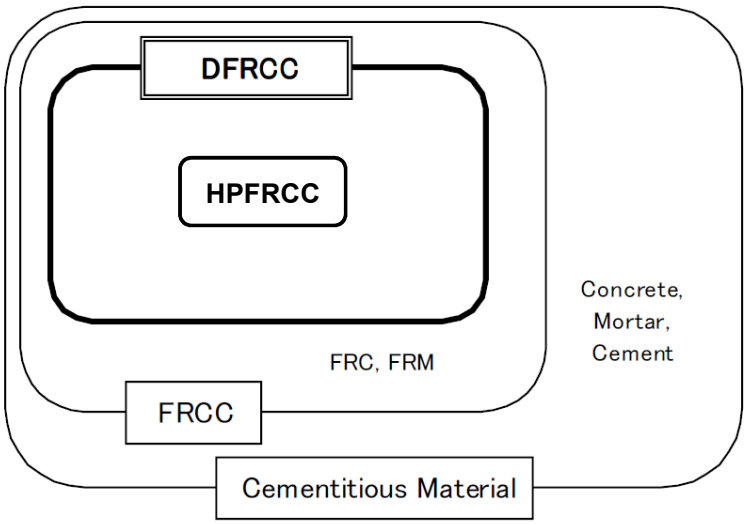

Figure 1.2: Classification of cementitious material based on mechanical performance

When the desired mechanical properties are achieved with improved technique based on a new scientific theory, the next step is to apply the materials to engineering applications. A very important factor is associated with the cost, due to the high fraction of the overall material cost taken by the fibers. Great effort has been taken to reduce the volume fraction of fibers in FRCC while maintaining the desired performance. Such material optimization is at material microstructure level. Another potential optimal use of fibers lies between material microstructure level and structural component level, where the concept and idea of functionally graded materials are utilized. The basic idea is to distribute materials microstructure to achieve the optimized performance for a particular application. At such level, material mechanical property design becomes more complicated, requiring, first, the accurate measurement of constitutive properties for the different microstructures. For FRCC, the measurement of fracture properties, especially the constitutive description, e.g., the cohesive fracture properties, is usually challenging. The state-of-the-art experimental and numerical techniques have exhibited great potential in the measurement of complex material properties that used to be extremely difficult and sometimes even impossible.

1.2 FIBER-REINFORCED CEMENTITIOUS-COMPOSITES

Various kinds of FRCC have been developed, and applied in construction in the past few decades. A few proceedings and books provide comprehensive information about FRCC [2-7]. Many kinds of micro-fibers have been commercially developed and are now being used in FRCC. A properly designed FRCC offers enhanced mechanical behavior, higher strength and higher toughness [6].

As already mentioned, high cost is one important issue associated with the practical use of FRCC [8]. Thus, there is a need for new technology to make more effective and efficient use of costly fibers. Conventionally, the FRCC is homogeneous in a bulk scale, i.e., the fiber volume fraction is uniform, apart from the potential unintended variations caused by the production processes (settlement, segregation, etc). For certain FRCC components, a significant fraction of the fibers is not utilized to its full potential. One typical example is the case of FRCC beams or panels under bending. In ordinary service situations without considering substantial cracking, near half of the volume of the beam is under compression, where the fibers usually do not contribute much to strength, and the compressive strength of the cementitious matrix itself is normally sufficient to carry the load. In the tensile region, as stress varies from zero at neutral axis to maximum tensile stress through beam depth, fibers near neutral axis carry smaller portion of the tensile loading than those fibers that are away from the neutral axis. In this sense, many of the fibers are not used efficiently. In such a case, an efficient use of the fibers is achieved if fibers are distributed according to the amount of load to be carried and if they are placed where they are needed the most. One solution for more efficient use of the fibers is to build sandwich panels from thin fiber reinforced faces and a lightweight core (pp 143-151, [7]). This is also similar to the case of repairing damaged beams or strengthening in-service beams, where carbon fiber sheets are usually bonded to the bottom of the beam. While this procedure can be effective, significantly different properties between the fiber sheets and the host concrete may cause potential delamination problems. This deficiency can be addressed by utilizing the concept of FGM [9] - i.e., by distributing a fixed amount of fibers according to the proportion of the load to carry; the graded composite may provide better performance than the homogeneous composite. Recently, preliminary investigations of a new functionally-graded fiber-reinforced cement composite

were presented at the Multiscale and Functionally Graded Materials (M&FGM2006) conference and the reader is referred to the proceedings of the event [10-13].

1.3 FUNCTIONALLY GRADED MATERIALS

Conventionally, composites are homogeneous mixtures of two or more material components. Therefore, they feature uniform bulk properties, which are the compromise between the desired properties of the compositional materials. In contrast, FGMs are a new generation of composite, which are engineered to vary spatially the microstructures through a compositional gradient from one material component to the other [14]. The compositional gradient can be obtained through nonuniform distribution of one phase, usually the reinforcement materials, with different volume fractions, sizes, or shapes. In an FGM, the roles of the materials as either reinforcement or matrix can interchange, and the transition of such role change is in a continuous and smooth manner. As significant fractions of an FGM can be the pure form of each compositional material, the desired properties from each of the component can be maximized without compromise. A binary materials system contains pure form of each material, but without the smooth material transition. Such system, although may be structurally efficient, has unavoidable interface problems due to sharp change of materials and properties.

Figure 1.3 shows schematically the material distribution and property profile for continuously graded FGMs, piecewise graded FGMs, binary material system and homogeneous composites. In all cases, the material components and volume fraction are the same. In both FGMs and in the binary system, pure form of each material on each side provides the entire property of that material. However, significant property mismatch concentrates at the interface of the binary system. While the piecewise graded FGMs alleviate the mismatch by distributing it to several interfaces, and it approximates the property profile of the continuously graded FGM.

The original form of FGM was developed in Japan in 1984 during the aerospace project, motivated by the need of an improved thermal barrier coating (TBC). The requirement for the TBC is to withstand a temperature of above 2000 K and a temperature gradient of 1000K across the coating thickness of less than 10 mm.

Traditional TBCs are a binary system consisting of one layer of metallic and one layer of ceramic. The ceramic layer provides thermal insulation, while the metallic layer bonds the ceramic layer to the substrate and at the same time provides protection to the However, the significant mismatch of thermomechanical properties between the ceramic and metal makes the TBC susceptible to interface cracking, delamination or debonding [15-18]. The concept of FGMs [19] is then proposed to alleviate these problems. The volume fractions of the ceramic phase decrease continuously from the thermo-resisting side to the metallic bonding side generating a gradual transition of the thermomechanical properties. Advantages of both materials are maintained, while the residual and thermal stresses are reduced.

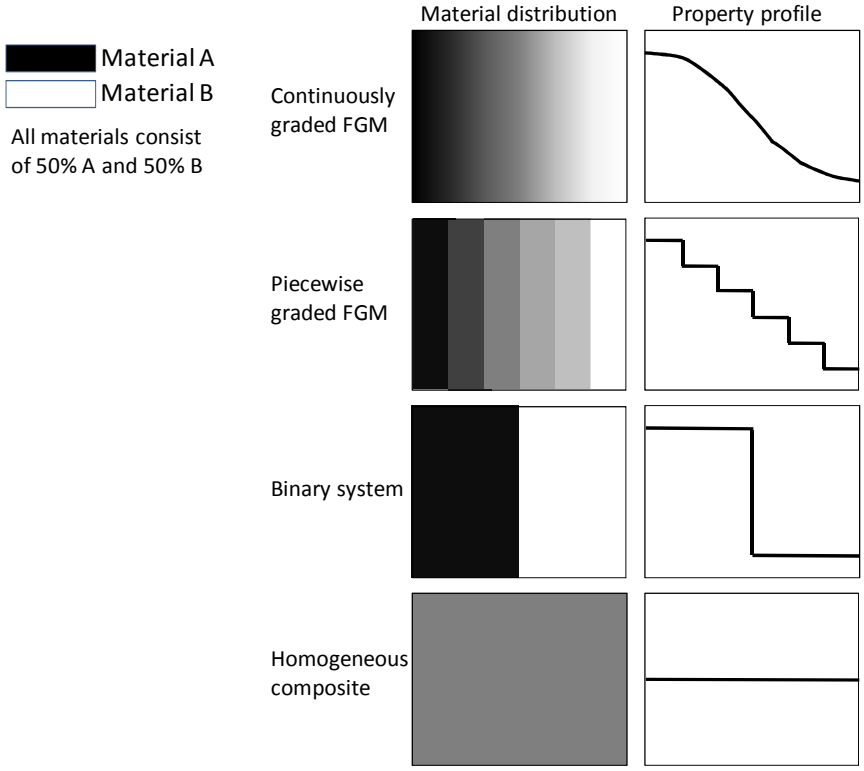

Figure 1.3: Schematic illustrations of material distribution and property profile for continuously graded FGM, piecewise graded FGM, binary material system and homogeneous composite

The FGM concept subsequently attracts a great many research interests, and its applications in different areas have been investigated [9]. One popular application involves the blast or ballistic protection for critical structure or armors for military applications [20,21]. In microelectronics, metal-semiconductor FGM have been applied in actuators and transducers [22]. High-performance cutting tools can be made of FGM [23]. Wide application can be also found in energy conversion, where heat exchangers, combustion systems and fusion reactors, solar energy generators can use FGM components [24]. In biomedical area, graded bone and dental implants have shown better performance than monolithic implants [25]. Filters with porosity gradient show improved efficiency over those with uniform porosity [26]. Other applications include optical materials with refractive indices, piezoelectric and thermoelectric devices, vehicle and spaceflight structures [9,14]. New applications will be continuously discovered with the advancement of materials science and technology.

It is extremely hard to manufacture FGMs with truly continuous gradient. No commercially viable process has yet been developed to make continuously graded FGMs. However, for practical applications, multilayer FGMs with properties varying in a piecewise fashion approximates the performance of ideal FGMs, and they can be reliably manufactured through a variety of techniques. A few techniques are listed here: powder metallurgical processing [27], laser melt injection (LMI) [28], thermal spraying [29,30] and chemical vapor deposition (CVD) [31,32]. A new laboratory method to produce a model polymer FGMs have been explored extensively recently [33,34].

1.4 COHESIVE ZONE MODELS (CZM)

Quasi-brittle materials such as plastics, concrete, asphalt, or adhesives, usually show nonlinear load - deformation behavior and a gradual decrease of load capacity (softening behavior) after peak load. The relatively ductile behavior of quasi-brittle materials is due to the development of a fracture process zone (size of which may be comparable to the size of the specimen) in front of the macroscopic cracks. For example, Figure 1.4 illustrates a fracture process zone formed due to fiber bridging and micro-cracking.

Linear elastic fracture mechanics (LEFM) is inadequate to take account of the nonlinear characteristic of such fracture process zone.

A popular fracture mechanics model that accounts for the process zone behavior is the cohesive zone model (CZM) [35,36], which has also been referred to as fictitious crack model [37]. In the finite element context, the elastic deformation is represented by the bulk elements, while the cohesive fracture behavior is described by cohesive surface elements. Both "intrinsic" models [38,39] and "extrinsic" models [40-42] have been developed. Moreover, the CZM concept has also been implemented in conjunction with extended and generalized finite element method (X-FEM and GFEM) [43,44]. The method has been successfully applied to various types of materials including polymers [45,46], concrete [47], functionally graded materials [48] and asphalt [49,50]. Here, the CZM concept is explored with emphasis on the application to quasi-brittle material systems.

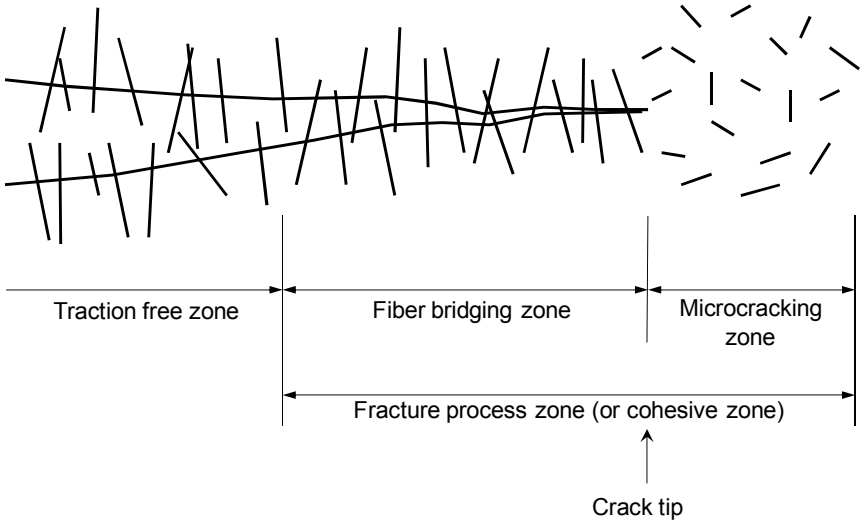

Figure 1.4: Illustration of the fracture process zone in a typical fiber reinforced composite

A popular fracture mechanics model that accounts for the process zone behavior is the cohesive zone model (CZM) [35,36], which has also been referred to as fictitious crack model [37]. In the finite element context, the elastic deformation is represented by the bulk elements, while the cohesive fracture behavior is described by cohesive surface

elements. Both “intrinsic” models [38,39] and “extrinsic” models [40-42] have been developed. Moreover, the CZM concept has also been implemented in conjunction with extended and generalized finite element method (X-FEM and GFEM) [43,44]. The method has been successfully applied to various types of materials including polymers [45,46], concrete [47], functionally graded materials [48] and asphalt [49,50]. Here, the CZM concept is explored with emphasis on the application to quasi-brittle material systems.

Commonly used in the simulation of mode I and/or combined fracture modes, the CZM describes a material level constitutive relation for the idealized damage process zone, which applies only to the fracture surface, while the undamaged bulk material remains elastic. For mode I fracture, the CZM assumes a unique relation between normal traction and crack opening displacement (COD) (Figure 1.5), while for pure mode II, the relation is between shear traction and sliding displacement. In Figure 1.5, Δ_n denotes COD, σ denotes the cohesive traction/stress, Δ_{nc} and σ_c are the critical values of Δ_n and σ, respectively, and $\sigma(\Delta_n)$ describes the traction-separation relation. The CZM may be obtained through experiments, either directly or indirectly.

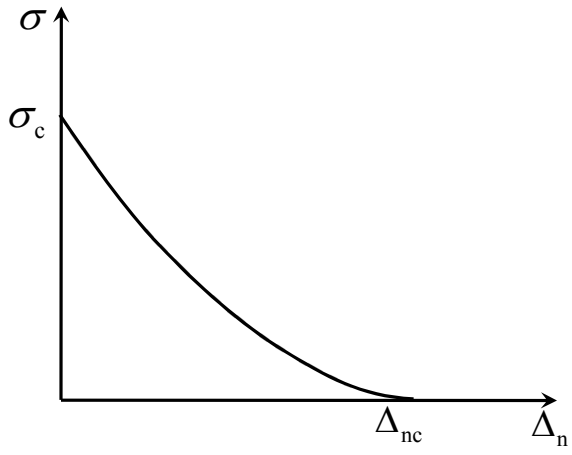

Figure 1.5: Extrinsic crack surface traction-separation model (mode I)

Physically, fracture/damage process is a time-dependent process due to the viscoelasticity of material behavior and/or the rate process of the breakage of bonds [51]. For rate-toughening brittle materials, the effect of phenomenological rate-dependent CZMs has been numerically investigated by means of the finite element method [52]. Although rate effect on the fracture process is present in real materials, for a wide of range materials under normal condition, the rate effect is negligible and the rate-independent CZM has been shown to provide reasonable prediction.

1.5 EXPERIMENTAL DETERMINATION OF CZMS

Many approaches have been proposed to obtain the traction-separation relation $\sigma(\Delta_n)$. Experimentally, the direct tension test may be considered as the fundamental method to determine $\sigma(\Delta_n)$ [53,54]. However, this approach is very difficult [53,55], which led researchers to seek indirect methods. One common way relies on assuming a simple shape of $\sigma(\Delta_n)$ with a few model parameters. Independent investigations by Song *et al.* [50] and Volokh [56] demonstrate that the assumed CZM shape can significantly affect the results of fracture analysis. Moreover, Shah *et al*. [55] reviewed various shapes of $\sigma(\Delta_n)$ that have been proposed, which include linear, bilinear, trilinear, exponential and power functions, and concluded that the local fracture behavior is sensitive to the selection of the shape $\sigma(\Delta_n)$. These models include a few parameters that are computed either directly from experimental measurements or indirectly by inverse analysis. Van Mier [57] summarized the common procedure of inverse analysis: model parameters are adjusted at each iteration by comparing the difference between the computational and experimental outcomes of global response. This method is not computationally efficient since a complete simulation must be carried out at each iteration.

Recently, Elices *et al.* [58] summarized the main streams of the indirect methods used to determine $\sigma(\Delta_n)$. These indirect methods have common characteristics: they all use the global response of the experimental results, load (P) and displacement (δ) or

crack mouth opening displacement (CMOD), from popular notched beams or compact specimens, as the basis of the inverse parametric fitting analysis. This is simply because the global responses are usually the only obtainable outcomes of the experiments. Therefore, the limitations are manifested: these methods are semi-empirical in that the CZMs are assumed, *a priori*, and they cannot be validated confidently at the local level. However, the obtained CZM from these methods still yields satisfactory predictive capability in finite element (FE) simulation of fracture [47,59,60].

1.6 RESEARCH OBJECTIVES

There are two objectives in current study. The first objective is to fabricate a novel FGFRCC using combined extrusion and pressing technique. Specifically, this task includes the processing of a novel four-layer FGFRCC, the microstructure examination to verify the fiber gradation, and the understanding of the basic mechanical behavior.

The second objective will then be on the inverse computation of mode I cohesive fracture properties, specifically the mode I CZM, using a hybrid DIC-FEM method. The rate effect of the fracture process is not investigated in the current scope of study. This second objective includes several tasks:

(1) To make use of a recent DIC with an advanced algorithm; such advanced algorithm provides smoother kinematic field than traditional DIC algorithm [61].

(2) To implement the DIC-FEM inverse procedure for the extraction of mode I cohesive properties; and to verify and evaluate the procedure through numerical examples.

(3) To validate the proposed inverse procedure using homogeneous plastic materials; the plastics must clearly show quasi-brittle fracture behavior and at the same time yield accurate experimental measurement.

(4) To extract the CZM of FRCC and to evaluate the accuracy of the computed CZM by direct fracture simulation.

An integrated approach, which combines material processing, microstructure characterization, mechanical testing and numerical simulation, is adopted to achieve the

objectives. Figure 1.6 illustrates the approach and gives an idea of how different aspects of the study are closely related to each other. The underlying philosophy is to form a research loop, which progresses in a spiral way, such that material science (for manufacturing), engineering mechanics (for characterization and analysis) and computational mechanics (for simulation) can be synergistically integrated for the advancement of technology, both in theory and in practice.

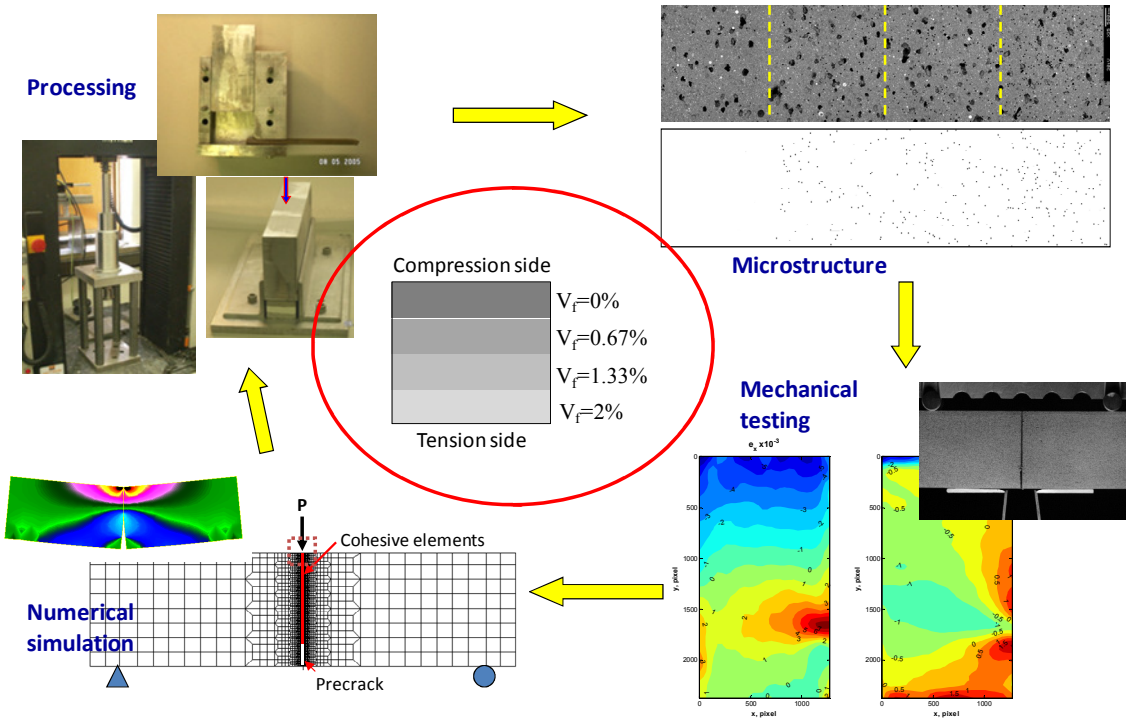

Figure 1.6: Integrated approach adopted in current study

1.7 ORGANIZATION OF THE DISSERTATION

The dissertation consists of seven chapters including this introductory chapter. Chapter 2 presents the processing method for the fabrication of a four-layer FGFRCC. The material selection, the extrusion and pressing techniques, and the mix proportions are described in detail. The fiber gradation is shown through scanning electron microscopy and digital image processing. The bending behavior of FGFRCC and FRCCs are compared quantitatively. In Chapter 3, first, two DIC algorithms, the subset method and

full-field method, are reviewed. Then the accuracies of these two DIC methods are compared by using numerically transformed speckle pattern image. The transformation that features total non-homogeneity is also presented. Chapter 4 presents the theory of the hybrid FEM-DIC inverse procedure. Residual-based and displacement-based approaches are presented separately along with representative numerical examples. The shape representation and parameterization of the CZM are illustrated. The numerical examples for the residual-based method focus on parametric study, while those for the displacement-based method focus on evaluation of error tolerance. Chapter 5 demonstrates the FEM-DIC procedure through two plastics, one ductile adhesive with PMMA as substrate, and one homogeneous composite, Garolite. Use of DIC to measure directly the Young's modulus and Poisson's ratio is also highlighted. Chapter 6 first presents the fracture testing results of FRCCs and FGFRCCs. The displacement fields measured by the full-field DIC for the homogeneous FRCCs are presented. The computed CZMs through the inverse procedure are analyzed. Comparison between the experimental response and the direct simulation using measured CZMs is then presented. Finally, Chapter 7 gives a summary of the major contributions of the present investigation and a series of future extension based on current work.

CHAPTER 2 - PROCESSING, MICROSTRUCTURE, AND PROPERTIES OF FGFRCC

The focus of the present work is on the processing procedure of a novel FGFRCC, its microstructural verification and preliminary mechanical testing. A ram extruder was fabricated to manufacture thin FRCC layers with different fiber volume fractions. Then, extruded beams with increasing fiber volume fraction were stacked and pressed in a mold to integrate them into an FGFRCC. The stacking procedure is chosen because it is a straightforward way to generate functional gradation before subsequent processing is taken to integrate the stacked layers to form FGMs [62,63]. The critical issue of the fabrication process, the matching of paste plasticity properties between different layers, will be discussed later. For comparison, beams with a single global fiber volume fraction were also stacked and pressed. The cross-section of the FGFRCC was observed in a scanning electron microscope (SEM) using backscattered electron image (BEI). Through image processing of the SEM image, fibers were segmented from the matrix and voids to be examined. Three point bending tests were carried out to observe the bending behavior for both graded and homogeneous specimens. Interface conditions were examined in the fractured specimens. The bending response was compared between graded and homogeneous beams.

2.1 INTRODUCTION

In general, dense cementitious matrix and strong fiber-matrix bond are desired for a FRCC so that not only high toughness, but also high strength can be achieved. This is also desired for the fabricated FGFRCC. Extrusion has been an effective way to produce FRCC [64-68]. Essentially, extrusion involves forcing a plastic material through a small die (Figure 2.1). When this technique is applied to the manufacturing of cementitious materials, very low water to cement ratio can be utilized [64], which contributes to the high strength of the matrix. A major advantage of using extrusion for FRCC is that the high shearing action developed during the forming process forces the short fibers to be aligned in the extrusion direction (Figure 2.1). Such fiber alignment improves the

mechanical performance of FRCC in the extrusion direction [65,66], which is beneficial for components that may carry tensile load only in one direction. Fiber alignment by extrusion has been studied quantitatively [67,68]. A recent study has shown that compared with casting, can further enhance fiber-matrix interfacial bonding [69]. However, improvement in bonding may not be beneficial for the toughness of a FRCC [67,69,70], as demonstrated by studies in which interfacial bonding was tailored by either modifying fiber surface chemistry [70] or by modifying binder composition [69].

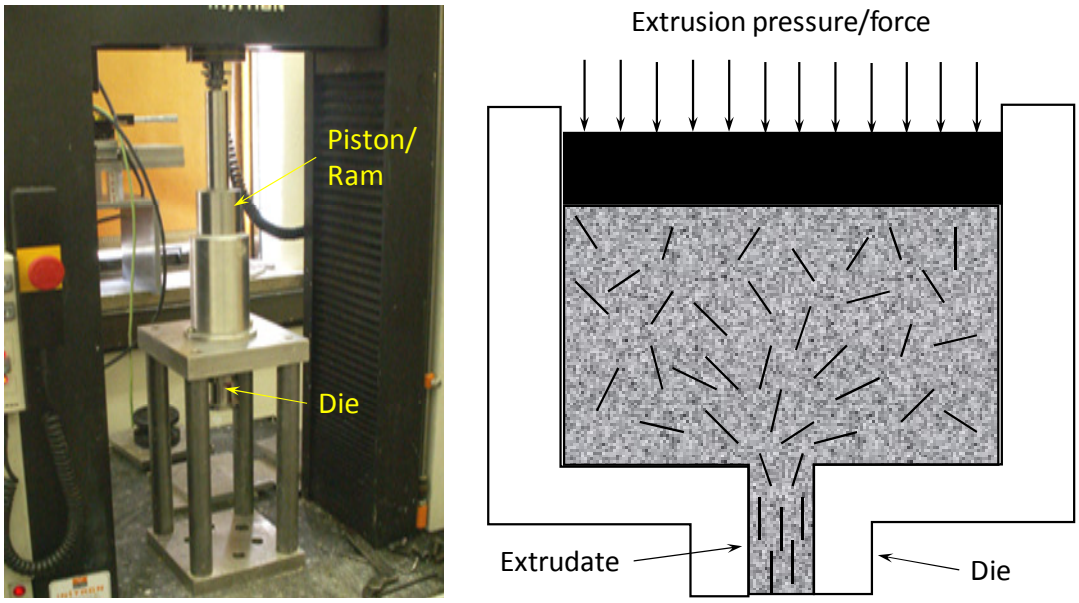

Figure 2.1: Left: a laboratory scale ram extruder; Right: schematic illustration of the principle of an extruder, and the alignment of fibers

2.2 MATERIALS

The main components of the FGFRCC were Type I ordinary portland cement, fly Polyvinylalcohol (PVA) fiber, superplasticizer, rheological modifier and water. Except for the portland cement, the materials were selected to facilitate the fabrication technique, a combination of extrusion and pressing.

Fly ash is a widely used pozzolanic material in making concrete or various kinds of cement-based materials. FRCC with high content fly ash made by extrusion has been

studied [71]. The main reason for adding fly ash in the mix was to improve the plastic properties of the fresh paste so that it is more extrudable, and to reduce the strength of the bond between paste and fiber. The spherical morphology of fly ash particles is particularly beneficial to workability [72]. In addition, when substantial amount of fly ash replaces cement, the overall heat of hydration and rate of heat generation reduces, which prolongs the plastic properties required for pressing. The fly ash used in this study is Class F type.

The PVA fibers used in this study are from Kuraray Co. Ltd, Japan[1]. Its type is with an available cut length of 6 mm and a diameter of 27 μm. The properties of PVA fibers are shown in Table 2.1. We used PVA fibers because their special hydrophilic surface chemistry and the fibers produce a workable mixture. PVA fibers have been successfully used in the manufacturing of FRCC [69]. The surface chemistry of PVA fibers is hydrophilic so that a strong chemical bond can be developed with the hardened cementitious matrix [73]. The PVA fibers are soft so that they will not clog the die entrance, and pliant so that they will not be broken during extrusion.

Table 2.1: Properties of PVA fiber (Provided by Kuraray Co. Ltd)

Cut length (mm)	Diameter (μm)	Density (g/cm3)	Tensile strength (MPa)	Elongation (%)	Tensile modulus (GPa)
6	27	1.3	1600	6	37

Superplasticizer was added to reduce the ratio of water to cementitious materials, and to enhance the fluidity of the fresh paste. The superplasticizer used in this study is Grace ADVA® 100 Superplasticizer. It is an aqueous solution and has a solid content of 35% by mass.

Rheological modifier was added to improve cohesion in the fresh paste to make it dough-like and to prevent separation of water during extrusion, in order for the FRCC extrudate to retain its shape under its own weight. The rheological modifier used in this

[1] http://www.kuraray.co.jp/en/business/fibers.html

study was METHOCEL F4M, a hydroxypropyl methylcellulose (HPMC) manufactured by the Dow Chemical Company, U.S.A. Its liquid solution shows shear thinning properties that facilitates the paste flow in the extruder during extrusion [74]. The use of cellulose has been popular in formulating cementitious mixtures for enhancing extrudability, whether or not they contain fibers.

2.3 EXPERIMENTS

2.3.1 Mix Proportions

For the FGFRCC, linear gradation of fiber volume fraction is considered. The fiber volume fractions for the four layers were selected as 0%, 0.67%, 1.33% and 2%, respectively. Therefore, the total fiber volume fraction of the FGFRCC is 1%. The basic mix proportions of different layers are shown in Table 2.2. The specific four mix proportions for FGFRCC were chosen based on many trial mixes and extrusions. The primary goal was to minimize the paste plasticity difference between layers so that pressing would produce uniform FGFRCC beam components. The selection of mix proportions for FGFRCC fabrication is discussed in a later section.

Table 2.2: Mix proportions of FGFRCC layers

Cement (wt.)	Fly ash Class F (wt.)	Water (wt.)	Fiber (vol.)	Superplasticizer* (wt.)	HPMC/water (wt.)
0.7	0.3	0.23	0%	0.002	0.04
			0.67%		
			1.33%		
			2%		

* Effective weight of superplasticizer (Grace Advance Flow)

2.3.2 Mixing Procedure

A rotary planetary-type mortar mixer was used for mixing. The dry ingredients were first mixed for at least one minute. Water was then added slowly, after which mixing was continued for 5 to 10 minutes to reach a dough-like state with no obvious fiber bundles. The mixing time needed to reach this state was found to depend on the dosage of HPMC,

the fiber volume fraction and the water to binder ratio. Usually a dosage of HPMC was selected such that all formulations could be mixed to a dough-like state in 5-10 minutes irrespective of fiber fraction.

2.3.3 Extrusion

The fabricated extruder is shown schematically in Figure 2.2. The extruder was designed to be assembled and disassembled quickly so that each extrusion could be finished promptly. The ram speed was fixed at 20 mm/min for an extrudate speed of 255 mm/min.

The extrudate was cut to the desired length (a cut length of 120 mm was used in this study) for subsequent pressing. Immediately after each extruded layer was cut, it was covered with a wet cloth to prevent drying, which would cause hardening of the extrudate surface and make subsequent pressing difficult.

2.3.4 Stacking and Pressing

After all four layers were extruded, they were stacked as shown in Figure 2.3, with the fiber volume fraction increased from 0% at the top to 2% at the bottom. The total thickness before pressing was 16 mm. The same procedure was used to make homogeneous FRCC with uniform fiber volume fraction by stacking four layers with the same fiber volume fraction to make one homogeneous FRCC beam. Five fiber volume factions were selected: 0%, 0.67%, 1%, 1.33%, and 2%. To reduce friction, the stacked layers were put in a rigid steel mold lined with smooth plastic sheet (Figure 2.4).

The length of the stacked layers was three-fourths the length of the mold, which is 160 mm, so that pressing caused the FGFRCC to extend in length and correspondingly reduce in thickness. Through this deformation process, the stacked layers bonded to each other and formed a continuous beam. A strong inter-layer bond developed later through cement hydration, which is essential to obtain integral FGMs. Greater thickness reduction made it more likely that layers would be wavy. We found that 25% thickness reduction applied was sufficient to produce interlayer bonding strong enough to avoid delamination while producing layers of uniform thickness.

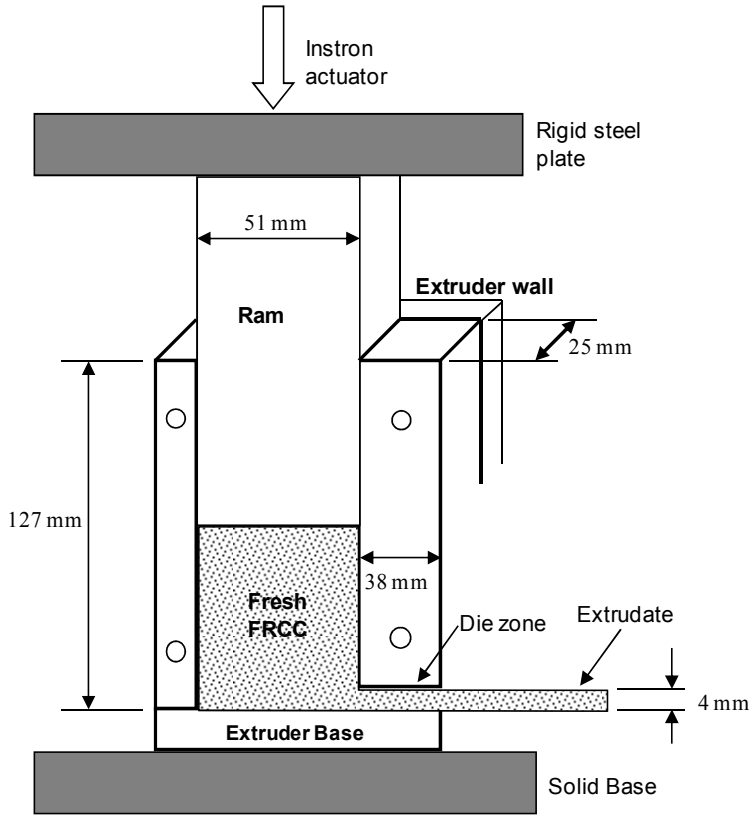

Figure 2.2: Schematic illustration of a cross-section of the actual extruder developed in the present research

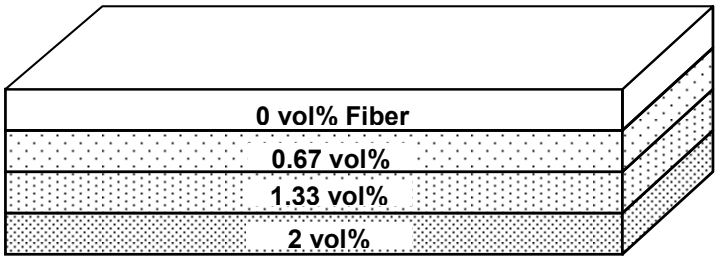

Figure 2.3: Stacked extruded layers with varying fiber volume fraction

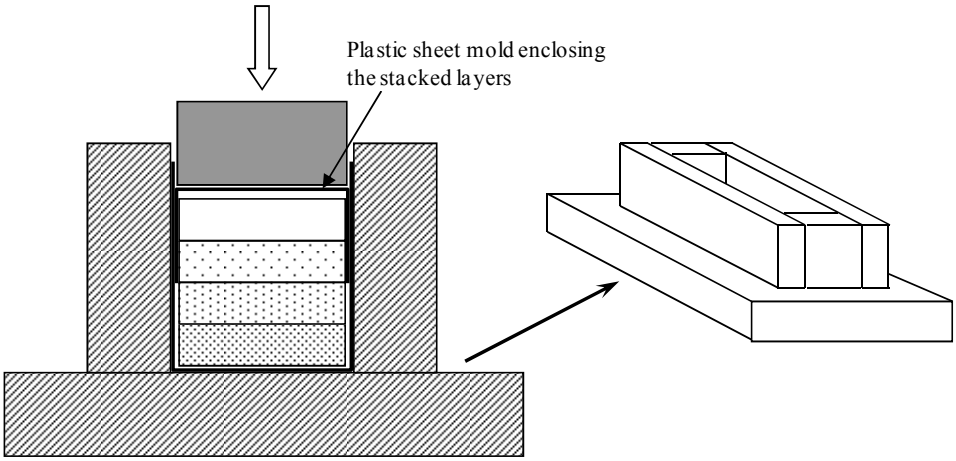

Figure 2.4: Mold for pressing the stacked layers to produce FGFRCC

Pressing was carried out on an Instron 4500 electro-mechanical testing machine using displacement control. Displacement rate of 5 mm/min was used, and pressing of the FGFRCC was finished in about one minute. The pressing force increased sharply when the pressed layers filled the volume of the mold. Pressing was stopped when the force caused an average pressure of about 1.80 MPa.

After each pressing operation, the FGFRCC with its plastic sheet was removed for curing. The plastic sheet mold served to prevent drying and gave support to the soft FGFRCC.

2.3.5 Curing

After extrusion and pressing, all extrudates with plastic mold were covered by a plastic sheet for one day. Then the plastic molds were removed and the specimens were fast cured at 90^{o}C in a water bath for another two days. After this high temperature curing, the specimens were kept at ordinary laboratory conditions for 48 hours. Before flexural testing, the specimens were oven dried at 105 ^{o}C for one day and kept at laboratory condition for another 24 hours. The timing of the flexural testing was 7 days after the specimens were fabricated. The curing scheme is the same as that used by Shah and colleagues [68,69]. It was adopted here to reduce the time to subsequent testing.

2.3.6 Scanning Electron Microscopy Observation

Cross-sectional surfaces of FGFRCC were directly cut and polished to observe the fiber distribution and the interface between layers. The surfaces were examined using SEM backscattered electrons (SEM/BEI). In order to cover an observation field containing all layers, several consecutive images were taken in the gradation direction. The images were then combined into a panorama and analyzed using an image processing software, ImageJ[2], to show fiber gradation.

2.3.7 Flexural Testing

Three-point bending tests were carried out using an Instron testing machine to characterize the deflection behavior of the homogeneous and graded specimens. The FGFRCC and homogeneous FRCC beams have a nominal dimension of: width 25 mm, depth 12 mm and length 160 mm. The span was set to 120 mm so that no further cutting was needed. Displacement was controlled at a cross-head speed of 0.3 mm/min.

2.4 MECHANICAL PROPERTIES

2.4.1 FRCC Properties

The computed equivalent elastic flexural stress is plotted versus stroke displacement in Figure 2.5. The first cracking stress, f_{fc}, the maximum flexural stress, $f_{\max}$, the corresponding displacement, $d_{\max}$, and the work of fracture measured from this figure are summarized in Table 2.3. The first cracking stress, f_{fc}, is defined as the stress at the end of the stress-displacement linearity, sometimes called bend-over-point (BOP). The estimated work of fracture is defined here as the area under the flexural stress versus displacement curve. Each value is an average test result of 3 specimens. All FRCCs show deflection hardening response [75]. The effect of fiber volume ratio on strength and the work of fracture are self-evident from Figure 2.5, both increased with fiber volume ratio.

[2] http://rsb.info.nih.gov/ij/

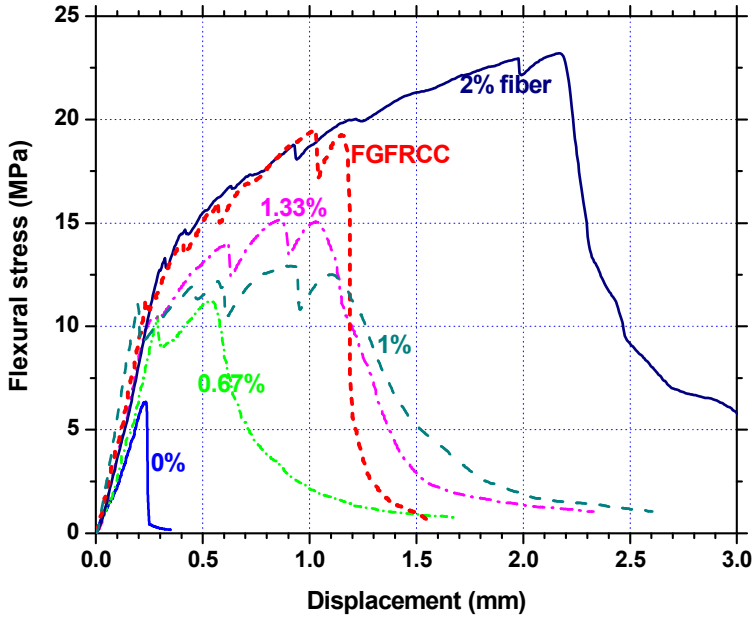

Figure 2.5: Flexural response of homogenous beams with varying fiber volume fractions, and of FGFRCC with 1% overall net fiber volume fraction

Table 2.3: Summary of bending tests of homogeneous FRCC and FGFRCC

	0%	0.67%	1%	1.33%	2%	FGFRCC
f_{fc} (MPa)	5.72	11.46	10.56	9.870	12.12	11.14
$f_{\max}$ (MPa)	5.72	11.83	12.73	14.65	22.94	18.45
$d_{\max}$ (mm)	0.18	0.545	1.01	0.97	2.06	1.19
Work of fracture (MPa-mm)	0.573	5.719	16.64	15.71	46.15	17.45

As shown in Figure 2.6, with addition of fibers, the FRCC and FGFRCC beams have a f_{fc}, or BOP, about two times of the f_{fc} of the beam without fibers. Moreover, it is observed that all FRCCs and FGFRCC have a similar value of f_{fc}, which is about 10-12 MPa. The stress for FRCC with 2% fiber increased much more after the BOP, compared to FRCCs with smaller fiber volume fraction.

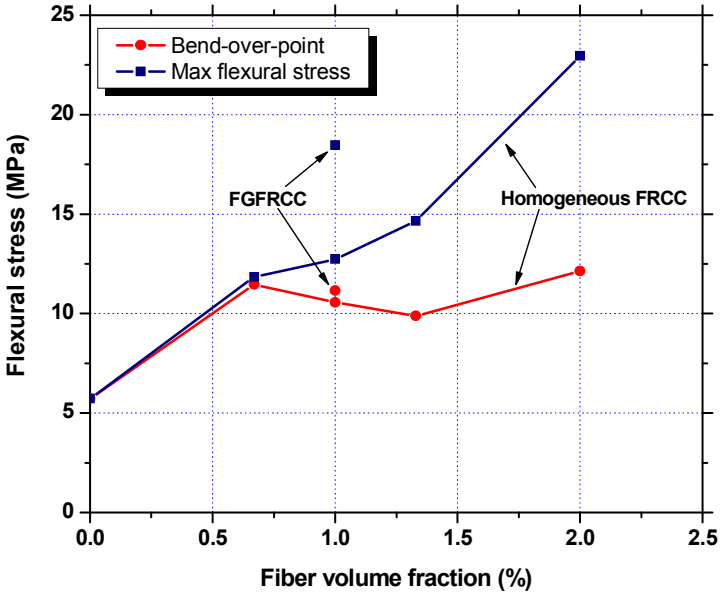

Figure 2.6: First cracking stress and maximum flexural stress of homogeneous FRCC and FGFRCC

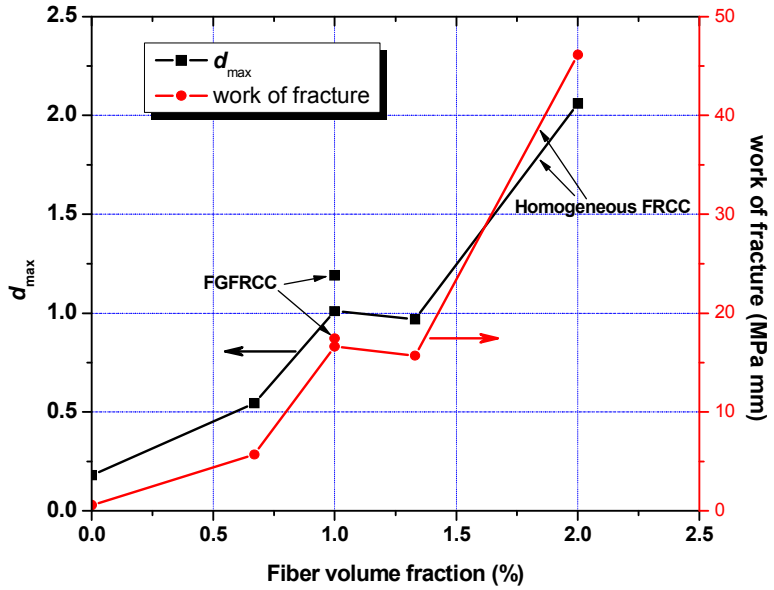

Figure 2.7: Comparison between homogeneous FRCC and FGFRCC

2.4.2 FGFRCC Properties

Figure 2.5 through Figure 2.7 also show the flexural response of the FGFRCC. Compared to homogeneous FRCC, after the BOP, the increase of flexural stress with displacement most closely resembles that of 2% FRCC, up to the mid-point of the hardening part of the 2% FRCC. This can be expected because the response of the FGFRCC is predominantly controlled by its bottom layer, which contained 2% fibers. However, the descending part of the curve dropped more sharply in the FGFRCC because of the relatively low fracture toughness of the upper layers. The softening curves observed in the homogeneous FRCC were not observed for the FGFRCC. This demonstrates that failure of the middle two layers was no later than the bottom layer.

The fact that FGFRCC demonstrates deflection hardening behavior can be appreciated by comparing it to a recent investigation by Shin *et al*. [76]. In their experiments, they tested the flexural behavior of a binary system of plain concrete and ductile fiber reinforced cementitious composite (DFRCC) with the DFRCC on the tension side. Their results show that the relative lack of toughness of the plain concrete above the DFRCC layer leads to the abrupt loss of beam strength when the DFRCC layer fails, which is similar to what is seen of the FGFRCC in Figure 2.5. However, their material system does not show hardening behavior beyond BOP. Moreover, the brittle failure of the plain concrete is prior to the failure of the DFRCC layer. This contrast, apparently, indicates that the FGM solution is able to address such drawbacks typically seen in the binary systems.

The strength and work of fracture were greater for the homogeneous 2% FRCC than for the FGFRCC. This is ascribed to the fact that the former has four 2% FRCC "layers" while the latter has only one 2% FRCC layer at the bottom. However, the FGFRCC has an overall fiber volume fraction of 1%. Compared with homogeneous FRCC, FGFRCC with 1% total fiber volume fraction has higher strength than and comparable work of fracture values as those of 1.33% FRCC. The $f_{\max}$ of FGFRCC is about 50% and 30% higher than that of 1% and 1.33% FRCC, respectively. With 25% less fiber, the FGFRCC beam was able to sustain higher loads than the 1.33% FRCC beam before failure. A

simple gradation allows the fibers to be used more efficiently. This result demonstrates that the idea of FGM for efficient use of fiber in FRCC is promising.

2.4.3 Reverse Bending of FGFRCC

For the fabricated FGFRCC, the usual loading condition is that the 2% fiber layer is under tension. Tests were also performed to investigate the reverse situation when the 2% fiber layer is under compression. Figure 2.8 shows a typical result. For comparison, the results of the normally loaded FGFRCC and the 1% homogeneous FRCC are also shown. As expected, the reversely loaded FGFRCC had a much lower first cracking stress. Only one crack is indicated by the single sharp drop in stress after the BOP. Its post-cracking maximum flexural stress is even lower than the first cracking stress, though for the second peak, the neutral axis moved up so that some of the fibers began to carry tensile load. In the normally loaded FGFRCC, the reduction of flexural stiffness is not as drastic due to the bridging effect from the fibers. Though it had low load carrying capacity, the reversely loaded specimen showed a long softening tail. The plateau of the tail developed as a result of bending of the ductile upper layers that have more fibers than the lower layers.

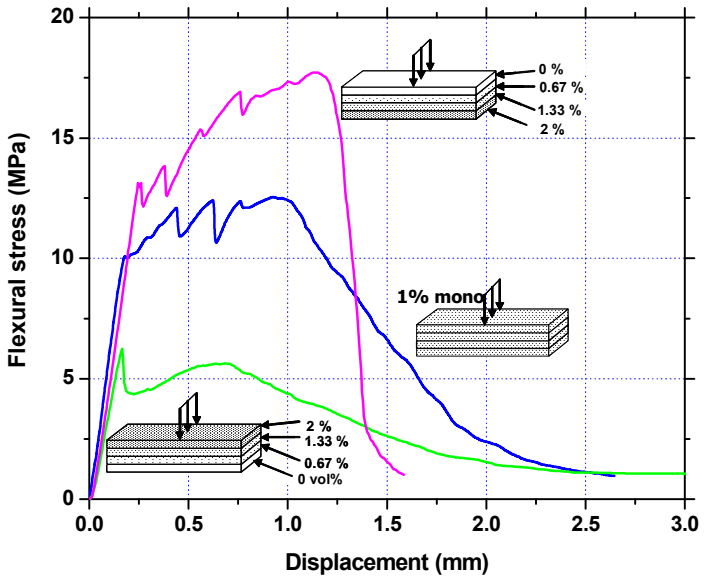

Figure 2.8: Flexural response of FGFRCC with normal and reverse loading, and of homogeneous FRCC, all with the same net fiber volume fraction (1%)

2.5 MICROSTRUCTURE

Figure 2.9 shows a fracture surface of a hardened FRCC. The fracture surface is normal to the extrusion direction. The image clearly shows the high degree of fiber alignment along extrusion direction. Figure 2.10(a) shows the SEM/BEI image of the polished cross-section of the FGFRCC normal to the extrusion direction. From top to bottom is the direction of increasing fiber volume fraction. The small black circles are fibers, while the big, irregular gray and black patches are air voids. The continuous and more homogeneous gray area is the cementitious matrix. Figure 2.10(b) is the segmented binary image of Figure 2.10(a) using image analysis software, showing fibers only. The layer with 0% fiber volume fraction is not analyzed by ImageJ. The criteria for the segmentation are based on pre-defined thresholds of intensity, area size and circularity. Some air voids may be indistinguishable by the criteria. However, it is expected only a negligible number of air voids are counted as fibers. The image clearly shows an increase of the number of fibers from the top to the bottom. The fibers appear to be distributed randomly within each layer. Close-up views show that the cross-sections of fibers are quite circular, demonstrating parallel alignment of fibers along the extrusion direction; otherwise, inclined fibers would show an elliptical cross-sectional shape [67,68]. The random distribution and parallel alignment demonstrates the effectiveness of the mixing and extrusion procedure. In Figure 2.10(a), no distinctive boundaries can be found between layers, showing seamless material transition from one layer to the other.

Many randomly distributed and disconnected air voids are observed, mostly in the range of 100 - 250 μm. Similar voids were also reported by Shao et al. [77] who attributed them to the use of HPMC but concluded that extruded FRCC still has higher strength than FRCC fabricated by casting.

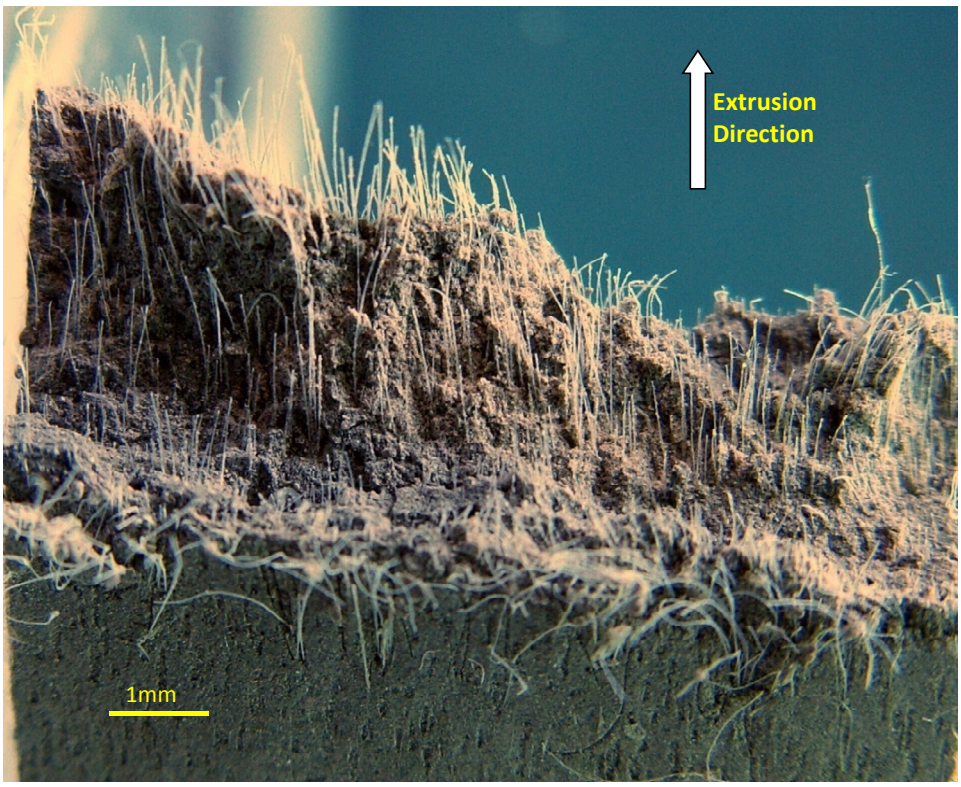

Figure 2.9: Close-up optical image showing the fiber alignment in a broken specimen. Photo obtained with a Konika Minolta Dimage Z3 digital camera

2.6 REMARKS ON PROCESSING

The scheme used to obtain mix proportions that produce good extrudate and make pressing of FGFRCC successful is outlined in Figure 2.11. We started formulating the mix proportion for the FRCC with the highest fiber volume fraction, since the presence of more fibers makes the FRCC more difficult to extrude successfully. The next step consisting of the adjustment of other layers was relatively easy. In this way, the range of mix proportions that produced satisfactory extrudates was found through trial and error.

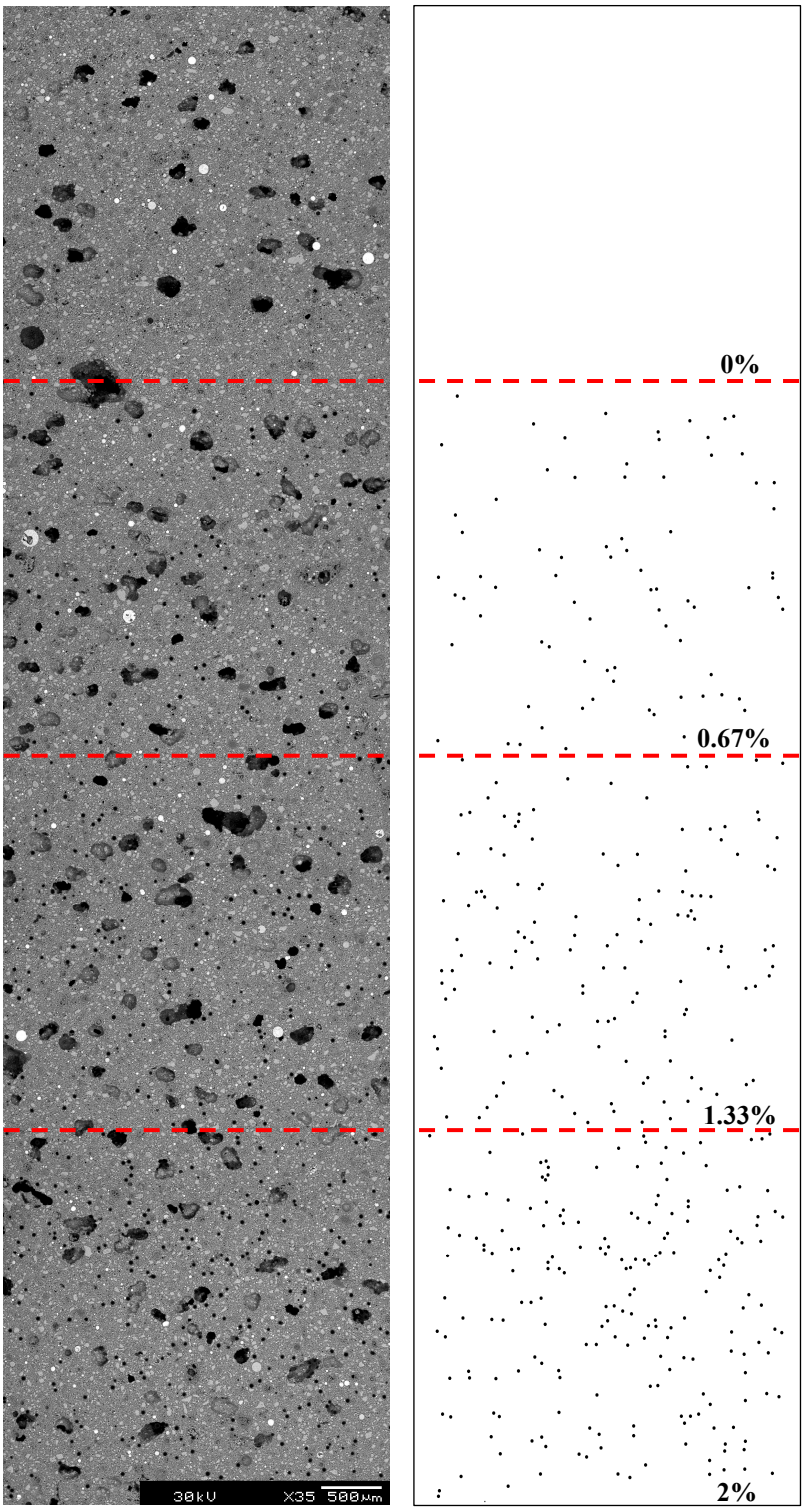

(a) (b)

Figure 2.10: FGFRCC cross-section, (a) SEM/BEI image and (b) corresponding binary image showing fiber distribution

Matching the paste plasticity between layers during pressing is the key for FGFRCC fabrication. Here the term “plasticity” is not used in a strict sense, but rather refers to the deformability of fresh FRCC layers under compression. As a result, when the plasticity was different, wavy interfaces resulted. One example is shown in Figure 2.12, in which different amounts of white cement were added in three different layers for a clear visible view of the layers. The wavy interfaces between layers were due to the use of different cements, which produced different plasticity between layers. Mixes with higher fiber amounts were stiffer. The presence of fibers made the bulk fresh paste more cohesive than paste without fiber. When more fibers were added, it became more difficult to tear apart the fresh FRCC, which shows that the bulk cohesiveness increased. However, there were some tolerances for the rheological difference between layers for pressing. One simple and effective way to control this aspect was through monitoring the total extrusion force during extrusion for each layer. Currently this is also the only parameter we could measure with accuracy. The extrusion forces for the four different layers should be similar, otherwise apparent difference of the stiffness between layers and nonuniform deformation of the layers can be observed. In the four layers we used to successfully fabricate the FGFRCC, we found the extrusion forces for the four layers were between 1,300 N to 1,500 N without necessarily adjusting the water to binder ratio.

The FRCC layer with lower fiber volume fraction was extruded first. Before pressing, the first extruded layer had been extruded for more than half an hour. During this period, the agglomeration of particles and increasing action of HMPC changed the paste plasticity property, making it stiffer. This effect was utilized to help match the plasticity of later extruded layers, which were stiffer. In other words, the waiting time after extrusion of different layers was used to compensate for plasticity differences between layers. This is why the four FRCC mix proportions with different fiber volume fractions can have the same water to binder ratio, yet still produce the similar plasticity for pressing.

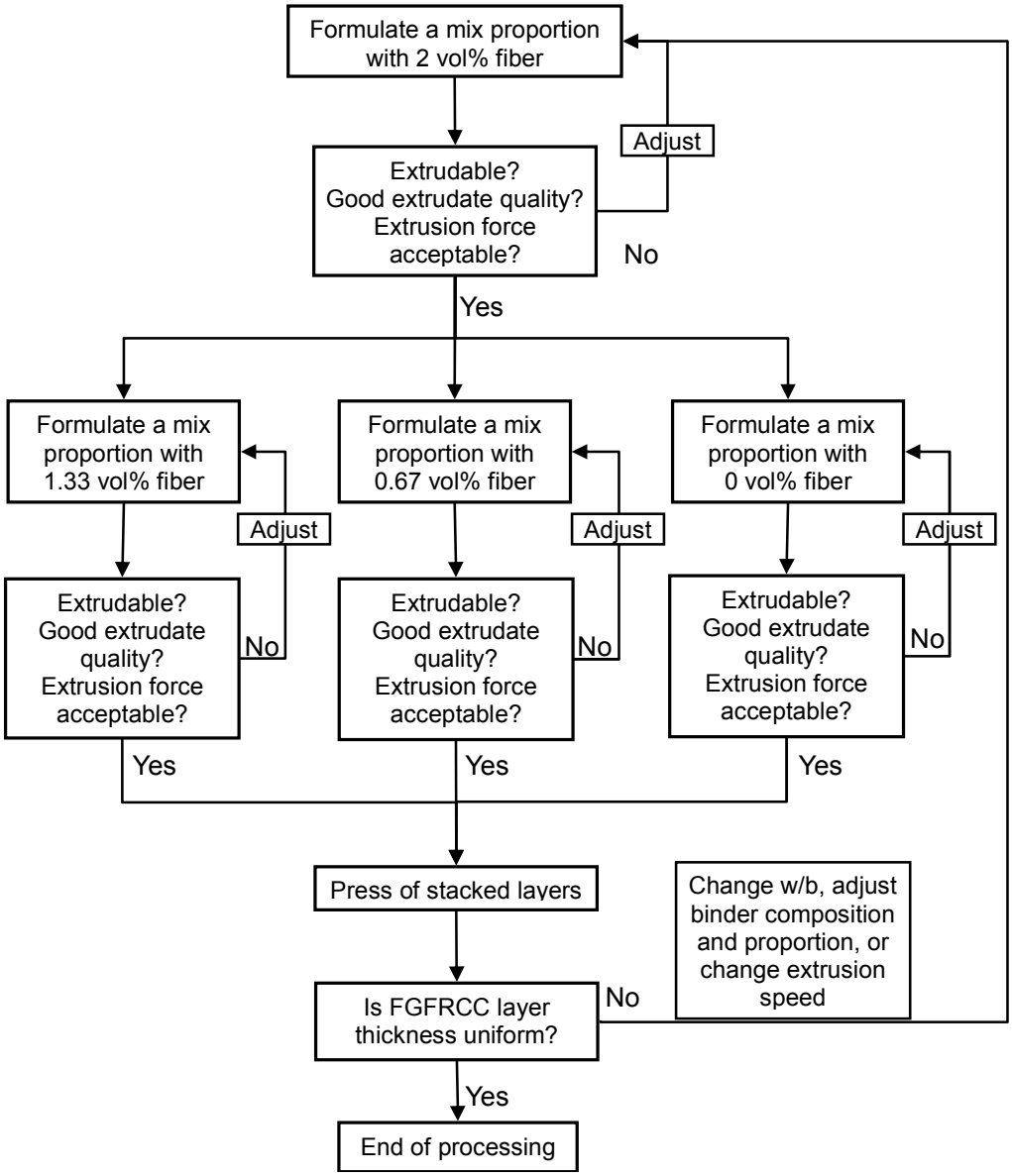

Figure 2.11: Sequence of mix proportion adjustment

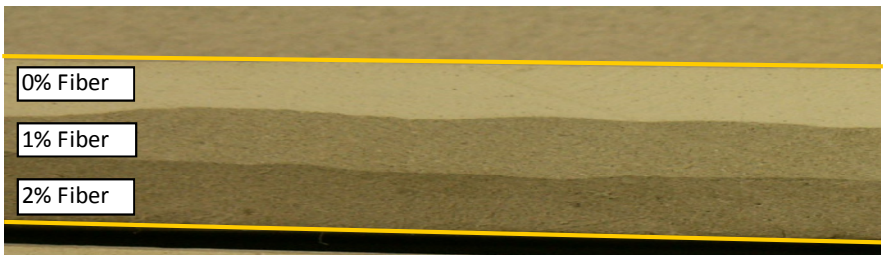

Figure 2.12: Wavy layers and uneven thickness resulting from inadequate control of plasticity

CHAPTER 3 - DIGITAL IMAGE CORRELATION

Digital image correlation (DIC) is a non-contact optical technique that is capable of measuring full-field two-dimensional or three-dimensional surface deformations [78-82]. Over the years, with the rapid advancement of computer vision technology, and with the availability of cheaper and more powerful digital image acquisition devices, DIC has gained increasing popularity among researchers in different fields. The rich information from DIC shows great potential in solving inverse identification problems [83,84], and in experimental fracture analysis [33,85-89].

In this chapter, the DIC techniques employed in this work are described in detail. This includes both the subset and full-field DIC algorithms, the latter one being the algorithm of choice in the present research. The presentation of the DIC algorithms is followed by an assessment of the full-field DIC.

3.1 INTRODUCTION

Choi *et al.* [87] used DIC to measure the deformation data of concrete under fracture. Their measurement obtained accuracy within the micron range. Sokhwan and Shah [88] studied the fracture of quasi-brittle cement paste using DIC under compression. Corr *et* [89] used DIC to examine the bond between carbon fiber reinforced polymers (CFRP) and concrete substrates and measured the softening and fracture behavior at interfacial transition zone of plain concrete. These investigations have demonstrated that DIC is an effective tool for the study of fracture behavior of cementitious materials.

A recent comprehensive review [90] indicates that DIC in fact is a subset of the research area of image registration. Essentially, DIC compares two digital images, one the target image (image of specimen in a reference state) and the other the source image (image of specimen after deformation). The DIC algorithm searches for the one-to-one correspondence of the points (pixels) in both images by matching all the pixel intensities in an area with a unique image pattern. Such correspondence can be displacements only, or a combination of displacements and their gradients. The single most popular type of

image used in DIC is gray-scale image with random speckles. The gray-scale image can be 8-bit, 12-bit, 16-bit or 32-bit depending on the image acquisition device. The size of random speckles is usually very fine, on the scale of 1-100 microns. It can be black speckles in a white background or vice versa. Figure 3.1 shows a typical speckle pattern where the speckles are black. Usually the speckle pattern is generated by spraying either black or white paint using a refined airbrush.

The general set-up of the DIC technique is illustrated in Figure 3.2. The non-contact DIC set-up is independent of the set-up of the experiment investigated, which does not need to be a mechanical testing. The primary components of the set-up are light source, a digital camera with either CCD (charge-coupled device**)** or CMOS (Complementary metal–oxide–semiconductor) sensor and a computer that stores the images. The lens of the digital camera is critical in that its quality determines the sharpness of the image taken. The lens must not have the barrel distortion normally associated with high optical magnification. The resolving power of the DIC system depends on the resolution of the CCD or CMOS sensor and the magnification factor. The magnification factor is the ratio of the physical size of the sensor to the size of the specimen area taken. For example, when a 2 mm by 3 mm sensor takes an image of an area of 1mm by 1.5 mm, the magnification factor is two.

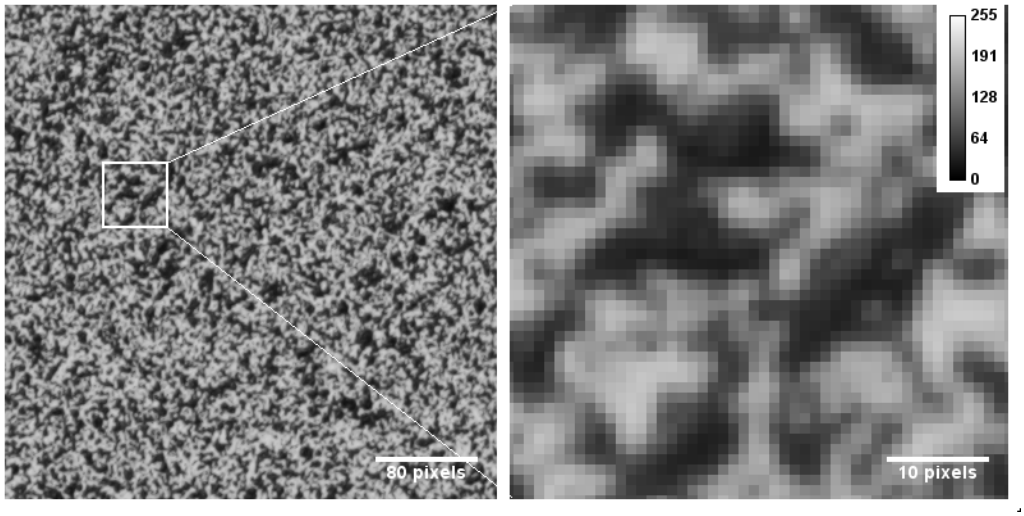

Figure 3.1: A typical speckle pattern used in DIC

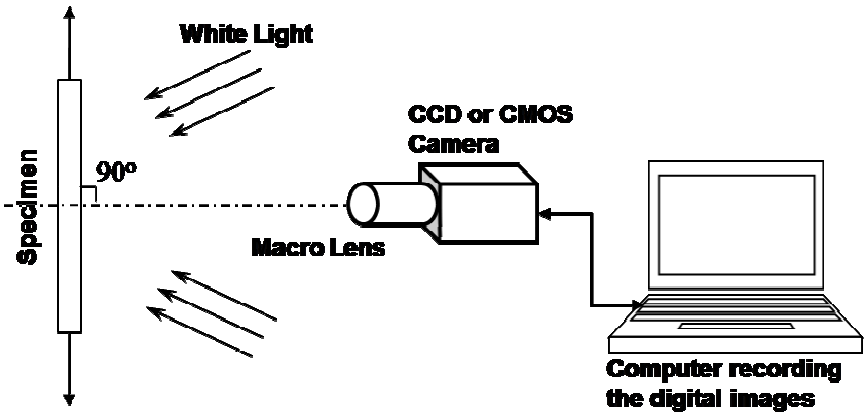

Figure 3.2: Typical arrangement of a 2D deformation measurement with DIC

3.2 SUBSET DIC ALGORITHM

In the subset DIC algorithm, a grid of points (nodes) is first selected on the reference image. A subset is the set of pixels with a pre-selected node as its center (Figure 3.3). Usually the subset is a square consisting $(2m+1) \times (2m+1)$ pixels, where m is an integer. The moving subset is to be correlated from the reference image to the deformed image by a mapping function

$$\begin{aligned} \tilde{x} &= x + u(x, y) \\ \tilde{y} &= y + v(x, y) \end{aligned} \tag{3.1}$$

where (x, y) and $(\tilde{x}, \tilde{y})$ are the same point before and after deformation, and u and v are displacement components defined by a set of mapping parameters. With the prerequisite that the displacement field within the subset is continuous and smooth, the displacement field is usually approximated by Taylor's expansion from zero-order (rigid-body motion) up to second-order (arbitrary deformation).

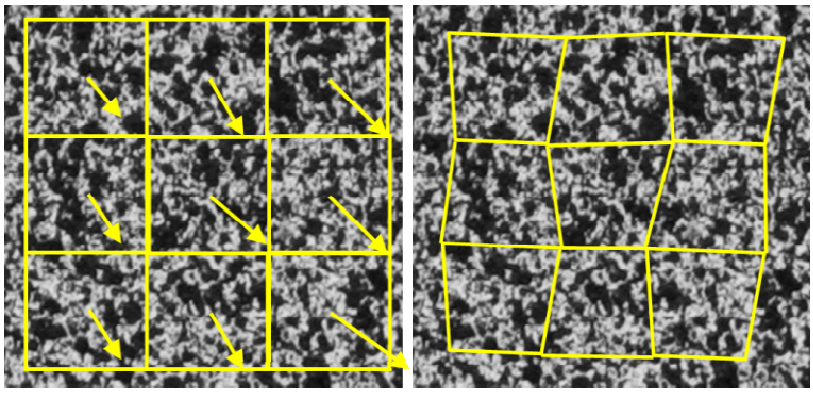

Figure 3.3: Subset DIC algorithm where each image subset is correlated independently

With the prerequisite that the displacement field within the subset is continuous and smooth, the displacement field can be approximated by different order Taylor expansions. Correlation that only searches for rigid body translation, which is actually a zero-order Taylor expansion of the displacement function, is commonly seen in image processing software, e.g., Matlab, ImageJ and ImagePro. Although correlation for rigid body translation can obtain sub-pixel displacement, first or second-order Taylor series may be employed to achieve greater accuracy. The zero-order mapping functions are

$$\begin{aligned} \tilde{x} &= x_0 + u_0 \\ \tilde{y} &= y_0 + v_0 \ , \end{aligned} \tag{3.2}$$

where (x_0, y_0) is the node location, u_0 and v_0 are the components of rigid body translation. The first-order mapping functions are

$$\begin{aligned} \tilde{x} &= x_0 + u_0 + u_x \Delta x + u_y \Delta y \\ \tilde{y} &= y_0 + v_0 + v_x \Delta x + v_y \Delta y \ , \end{aligned} \tag{3.3}$$

where u_x, u_y, v_x and v_y are the first-order displacement gradients, and

$$\begin{aligned} \Delta x &= x - x_0 \\ \Delta y &= y - y_0 \ . \end{aligned}$$

Accordingly, the second-order mapping functions are

$$\tilde{x} = x_0 + u_0 + u_x\Delta x + u_y\Delta y + \frac{1}{2}u_{xx}\Delta x^2 + \frac{1}{2}u_{yy}\Delta y^2 + u_{xy}\Delta x\Delta y$$
$$\tilde{y} = y_0 + v_0 + v_x\Delta x + v_y\Delta y + \frac{1}{2}v_{xx}\Delta x^2 + \frac{1}{2}v_{yy}\Delta y^2 + v_{xy}\Delta x\Delta y \ , \tag{3.4}$$

where u_{xx}, u_{yy}, u_{xy}, v_{xx}, v_{yy} and v_{xy} are the second-order displacement gradients. From Equations (3.2)-(3.4), the number of mapping parameters for zero-, first- and second-order approximations are 2, 6 and 12 respectively. In general, the increased number of parameters results in higher accuracy of the correlated displacement.

We use $I_r(x,y)$ and $I_d(x,y)$ to denote the intensity of the reference and the source images, respectively. One assumption in DIC is that the relative light intensity of the specimen surface either does not change or changes uniformly during deformation. Under this assumption, if the mapping functions are correct, then

$$I_d(\tilde{x},\tilde{y}) = I_d\left(x+u(x,y), y+v(x,y)\right) = I_r(x,y). \tag{3.5}$$

Both $I_r(x,y)$ and $I_d(x,y)$ are discrete digital intensity arrays representing the continuously specimen surface image. Figure 3.4 demonstrates the discrete intensity arrays, which show abrupt changes of intensity between adjacent pixels. If $(\tilde{x},\tilde{y})$ is at a pixel location, which is rarely the case, its intensity can be directly read from image $I_d(x,y)$. However, if $(\tilde{x},\tilde{y})$ is at a sub-pixel location (Figure 3.5), its intensity value in the deformed image has to be interpolated from adjacent pixels. Bilinear interpolation and bicubic interpolation are two popular interpolation schemes.

3.2.1 Bilinear Interpolation

Bilinear interpolation uses the intensity values of the nearest four pixels:

$$I_d(\tilde{x},\tilde{y}) = \alpha_{00} + \alpha_{10}h + \alpha_{01}t + \alpha_{11}ht \ , \tag{3.6}$$

where

$$h = (x' - i),\ t = (y' - j),$$
$$\alpha_{00} = I_d(i, j),\ \alpha_{10} = I_d(i+1, j) - I_d(i, j),$$
$$\alpha_{01} = I_d(i, j+1) - I_d(i, j),$$
$$\alpha_{11} = I_d(i+1, j+1) + I_d(i, j) - I_d(i+1, j) - I_d(i, j+1),$$

and h and t (Figure 3.5) are the relative distances to pixel (i, j). As can be seen, bilinear interpolation has the advantage of ease of implementation and low computational cost. However, for greater accuracy, higher order bicubic interpolation is used.

76	80	77	71	64	89	111	99	88	86
72	54	41	29	36	58	109	148	140	124
56	42	28	30	40	67	114	158	167	144
73	52	40	41	57	80	106	145	155	153
156	110	82	85	89	87	92	107	122	135
172	148	135	129	125	123	109	104	105	120
153	152	152	157	171	151	134	135	143	144
138	146	153	164	163	158	152	156	163	166
141	151	162	162	161	157	155	162	173	153

Figure 3.4: Illustration of the discrete nature of a digital image (8-bit), the number in each pixel cell indicates the intensity of that pixel

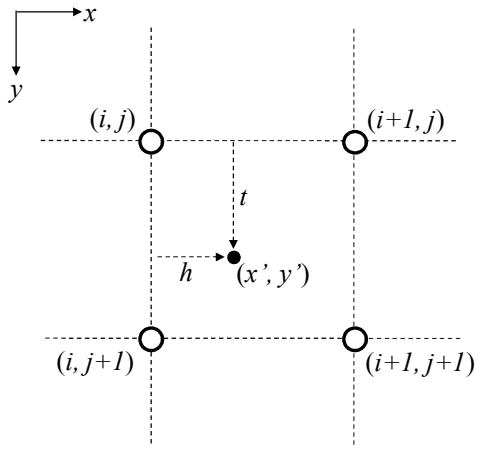

Figure 3.5: Computational cell for bilinear and bicubic interpolation

3.2.2 Bicubic Interpolation

The expression for bicubic interpolation is:

$$I_d\left(\tilde{x},\tilde{y}\right)=\sum_{m=0}^{3}\sum_{n=0}^{3}\alpha_{mn}h^m t^n \ , \tag{3.7}$$

where α_{mn} are the fitting coefficients determined from I, I_x, I_y and I_{xy} at the four nearest pixel locations. The I_x, I_y and I_{xy} are the x-direction, y-direction and cross gradients of the intensity. The computation of I_x, I_y and I_{xy} is not well documented in published papers about DIC. Thus we describe a complete procedure for determining I_x, I_y and I_{xy}, as well as for computing α_{mn} in Appendix A.

A modified version of Equation (3.7) is

$$I_d\left(\tilde{x},\tilde{y}\right)=\sum_{m=0}^{3}\sum_{n=0}^{3}\alpha_{mn}h^m t^n+\chi \ , \tag{3.8}$$

where χ is an additional parameter taking into account differences of the intensity of reference and deformed images due to two different exposures [91].

The mapping parameters for a subset are determined through minimizing a correlation coefficient, of which there are two popular forms:

$$C=\frac{\sum_{R_p\in\Omega_p}\left\{I_r\left(R_p\right)-I_d\left(R_p,\boldsymbol{\lambda}\right)\right\}^2}{\sum_{R_p\in\Omega_p}I_r{}^2\left(R_p\right)} \tag{3.9}$$

and

$$C=1-\frac{\sum_{R_p\in\Omega_p}I_r\left(R_p\right)I_d\left(R_p,\boldsymbol{\lambda}\right)}{\left[\sum_{R_p\in\Omega_p}I_r{}^2\left(R_p\right)\sum_{R_p\in\Omega_p}I_d{}^2\left(R_p,\boldsymbol{\lambda}\right)\right]^{1/2}} \ , \tag{3.10}$$

where R_p represents any single pixel point in subset domain Ω_P in the reference image that centers node "P", and $\boldsymbol{\lambda}$ represents the vector of the mapping parameters. In both Equations (3.9) and (3.10), the summation shall be carried out for all points in Ω_P. In ideal situation, the best computed mapping parameters would yield the correlation coefficient C → 0.

Minimization of equations (3.9) or (3.10) is a nonlinear optimization problem where different optimization solvers can be applied, among which the Newton-Raphson method is usually used. In the following, the Newton-Raphson procedure for the case of minimizing correlation coefficient defined by Equation (3.9) using second-order mapping functions and using bicubic interpolation is given.

Minimizing C means that ∇C converges to zero, or

$$\nabla C = \frac{-2}{\sum_{R_p \in \Omega_p} I_r^{\,2}\left(R_p\right)} \left\{ \sum_{R_p \in \Omega_p} \left[I_r\left(R_p\right) - I_d\left(R_p, \boldsymbol{\lambda}\right) \right] \frac{\partial I_d\left(R_p, \boldsymbol{\lambda}\right)}{\partial \lambda_i} \right\}_{i=1,\ldots,13} = \mathbf{0}\,, \quad (3.11)$$

where $\boldsymbol{\lambda} = \left\{ u_0, u_x, u_y, u_{xx}, u_{yy}, u_{xy}, v_0, v_y, v_{xx}, v_{yy}, v_{xy}, \chi \right\}$. Applying the standard Newton-Raphson procedure, Equation (3.11) becomes an iteration loop

$$\nabla\nabla C\left(\boldsymbol{\lambda}_0\right)\left(\boldsymbol{\lambda} - \boldsymbol{\lambda}_0\right) = -\nabla C\left(\boldsymbol{\lambda}_0\right), \quad (3.12)$$

where $\boldsymbol{\lambda}_0$ is an initial guess of the solution and $\boldsymbol{\lambda}$ is the next approximate solution of Equation (3.11); $\nabla\nabla C$ is the Hessian matrix of C. Equation (3.12) iterates until either $\boldsymbol{\lambda}$, or ∇C converges. The Hessian matrix $\nabla\nabla C$ can be derived as

$$\nabla\nabla C = \left(\frac{\partial^2 C}{\partial \lambda_i \partial \lambda_j} \right)_{\substack{i=1,\ldots,13 \\ j=1,\ldots,13}}$$

$$= \frac{-2}{\sum_{R_p \in \Omega_p} {I_r}^2 \left(R_p \right)} \left\{ \sum_{R_p \in \Omega_p} \left[I_r \left(R_p \right) - I_d \left(R_p, \boldsymbol{\lambda} \right) \right] \frac{\partial {I_d}^2 \left(R_p, \boldsymbol{\lambda} \right)}{\partial \lambda_i \partial \lambda_j} \right.$$

$$\left. - \sum_{R_p \in \Omega_p} \frac{\partial I_d \left(R_p, \boldsymbol{\lambda} \right)}{\partial \lambda_i} \frac{\partial I_d \left(R_p, \boldsymbol{\lambda} \right)}{\partial \lambda_j} \right\}_{\substack{i=1,\ldots,13 \\ j=1,\ldots,13}} . \tag{3.13}$$

When $\boldsymbol{\lambda}$ is close to the final solution, $I_r \left(R_p \right) \approx I_d \left(R_p, \boldsymbol{\lambda} \right)$. Therefore, Equation (3.13) can be approximated as

$$\nabla\nabla C = \frac{2}{\sum_{R_p \in \Omega_p} {I_r}^2 \left(R_p \right)} \sum_{R_p \in \Omega_p} \frac{\partial I_d \left(R_p, \boldsymbol{\lambda} \right)}{\partial \lambda_i} \frac{\partial I_d \left(R_p, \boldsymbol{\lambda} \right)}{\partial \lambda_j} . \tag{3.14}$$

The derivatives of $I_d \left(R_p, \boldsymbol{\lambda} \right)$ with respect to λ_i can be evaluated using the chain rule, i.e.,

$$\frac{\partial I_d \left(R_p, \boldsymbol{\lambda} \right)}{\partial \lambda_i} = \frac{\partial I_d \left(\tilde{x}, \tilde{y}, \boldsymbol{\lambda} \right)}{\partial \tilde{x}} \frac{\partial \tilde{x} \left(R_p \right)}{\partial \lambda_i} + \frac{\partial I_d \left(\tilde{x}, \tilde{y}, \boldsymbol{\lambda} \right)}{\partial \tilde{y}} \frac{\partial \tilde{y} \left(R_p \right)}{\partial \lambda_i} + \frac{\partial I_d \left(\tilde{x}, \tilde{y}, \boldsymbol{\lambda} \right)}{\partial \lambda_i} . \tag{3.15}$$

where $\partial I_d \left(\tilde{x}, \tilde{y}, \boldsymbol{\lambda} \right) / \partial \tilde{x}$ and $\partial I_d \left(\tilde{x}, \tilde{y}, \boldsymbol{\lambda} \right) / \partial \tilde{y}$ are the gradients of the bicubic spline interpolated intensity of the deformed image. With Equation (3.8), we have

$$\begin{aligned} \frac{\partial I_d \left(\tilde{x}, \tilde{y}, \boldsymbol{\lambda} \right)}{\partial \tilde{x}} = {} & \alpha_{10} + \alpha_{11} t + \alpha_{12} t^2 + \alpha_{13} t^3 \\ & + 2\alpha_{20} h + 2\alpha_{21} ht + 2\alpha_{22} ht^2 + 2\alpha_{23} ht^3 \\ & + 3\alpha_{30} h^2 + 3\alpha_{31} h^2 t + 3\alpha_{32} h^2 t^2 + 3\alpha_{33} h^2 t^3 \end{aligned} \tag{3.16}$$

and

$$\begin{aligned} \frac{\partial I_d \left(\tilde{x}, \tilde{y}, \boldsymbol{\lambda} \right)}{\partial \tilde{y}} = {} & \alpha_{01} + \alpha_{11} h + \alpha_{21} h^2 + \alpha_{31} h^3 \\ & + 2\alpha_{02} t + 2\alpha_{12} ht + 2\alpha_{22} h^2 t + 2\alpha_{32} h^3 t \\ & + 3\alpha_{03} t^2 + 3\alpha_{13} ht^2 + 3\alpha_{23} h^2 t^2 + 3\alpha_{33} h^3 t^2 . \end{aligned} \tag{3.17}$$

Since $\partial\tilde{x}\left(R_p\right)/\partial\lambda_i$ and $\partial\tilde{y}\left(R_p\right)/\partial\lambda_i$ can be easily derived from Equation (3.4), together with Equation (3.16) and (3.17), explicit forms for Equation (3.15) are as follows:

$$
\begin{aligned}
&\frac{\partial I_d}{\partial u_0}=\frac{\partial I_d}{\partial \tilde{x}} && \frac{\partial I_d}{\partial v_0}=\frac{\partial I_d}{\partial \tilde{y}}\\
&\frac{\partial I_d}{\partial u_x}=\frac{\partial I_d}{\partial \tilde{x}}\Delta x && \frac{\partial I_d}{\partial v_x}=\frac{\partial I_d}{\partial \tilde{y}}\Delta x\\
&\frac{\partial I_d}{\partial u_y}=\frac{\partial I_d}{\partial \tilde{x}}\Delta y && \frac{\partial I_d}{\partial v_y}=\frac{\partial I_d}{\partial \tilde{y}}\Delta y\\
&\frac{\partial I_d}{\partial u_{xx}}=\frac{1}{2}\frac{\partial I_d}{\partial \tilde{x}}\Delta x^2 && \frac{\partial I_d}{\partial v_{xx}}=\frac{1}{2}\frac{\partial I_d}{\partial \tilde{y}}\Delta x^2\\
&\frac{\partial I_d}{\partial u_{yy}}=\frac{1}{2}\frac{\partial I_d}{\partial \tilde{x}}\Delta y^2 && \frac{\partial I_d}{\partial v_{yy}}=\frac{1}{2}\frac{\partial I_d}{\partial \tilde{y}}\Delta y^2\\
&\frac{\partial I_d}{\partial u_{xy}}=\frac{1}{2}\frac{\partial I_d}{\partial \tilde{x}}\Delta x\Delta y && \frac{\partial I_d}{\partial v_{xy}}=\frac{1}{2}\frac{\partial I_d}{\partial \tilde{y}}\Delta x\Delta y\\
&\frac{\partial I_d}{\partial \chi}=1 &&
\end{aligned}
\qquad (3.18)
$$

where $I_d = I_d\left(\tilde{x},\tilde{y},\boldsymbol{\lambda}\right)$.

Lu and Cary reported that the subset algorithm can obtain a displacement field with accuracy within ±0.005 pixels and the displacement gradients within ±0.0002 [92]. In their tests, they used 8-bit gray scale images with the subset size 41 × 41pixels and they tested both first and second order deformations.

3.3 FULL-FIELD DIC ALGORITHM

Although the subset DIC algorithm is able to obtain a high degree of accuracy in the measurement of the displacement field and/or the strain field, there are errors associated with the lack of consideration of the displacement compatibility between adjacent
As can be seen from the subset DIC procedure, each subset has its own converged deformation field, which is independent of the deformation fields of surrounding subsets. Such discrete fields degrade the accuracy in that the subset DIC measured displacement field is not very smooth over the whole correlated domain. The gradient of the

displacement field computed using subset DIC is very noisy. To improve the accuracy from subset DIC, the discrete displacements at the centers of all subsets can be smoothed. Taking derivatives of the smoothed displacement field, better estimation of the gradient field can be obtained. However, such remedy negates the effort of directly obtaining the gradient during the subset DIC process. Another disadvantage of the subset DIC algorithm is that the algorithm is very sensitive to the quality of the speckle pattern [93]. Also the selection of the optimal size of the subset more or less depends on trial and error for a particular speckle pattern [94].

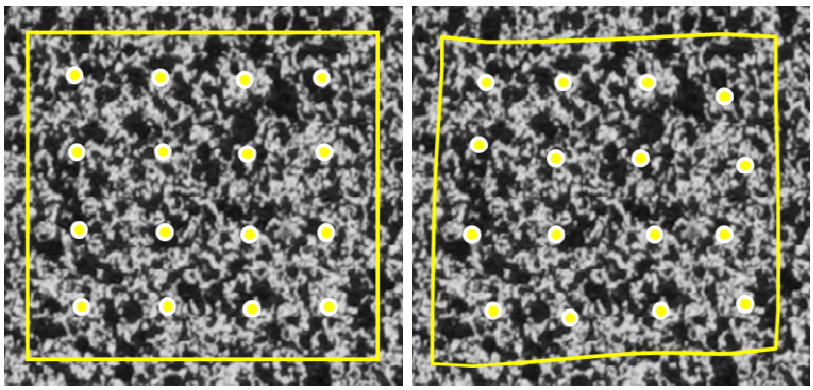

Figure 3.6: Full-field DIC algorithm where the whole image is correlated

Contrary to the subset DIC algorithm, the entire images are correlated in the full-field DIC algorithm (Figure 3.6). Similar to Equation (3.9), the full-field DIC algorithm seeks to minimize the dissimilarity between the reference image and the correlated deformed image

$$C_{\text{img}} = \frac{1}{\#\Omega_{\text{img}}} \sum_{R_p \in \Omega_{\text{img}}} \left\{ I_r\left(R_p\right) - I_d\left(R_p, \boldsymbol{\lambda}\right) \right\}^2 , \tag{3.19}$$

where C_{img} is the objective correlation function, Ω_{img} is the domain of the region of interest (ROI) on the image, and $\#\Omega_{\text{img}}$ is the total number of pixels in Ω_{img}. Here $\boldsymbol{\lambda}$ is the only set of parameters that determines the deformation field for the whole ROI.

As the ROI on the image may have inhomogeneous deformation field, e.g., near a crack tip, the approximation of the deformation field using a truncated Taylor series is apparently inadequate. For the case of continuous elastic deformation, a smooth parametric function must be employed to be able to represent the inhomogeneous field. B-spline (basis spline) surface representation appears to be very attractive in that it is smooth (C^2 continuous), flexible and requires a relatively small number of unknown parameters. Figure 3.7 shows a single bicubic B-spline surface described by

$$f(x,y)=\beta^3(x)\cdot\beta^3(y), \tag{3.20}$$

where $\beta^3(x)$ is the B-spline of degree 3 with the expression

$$\beta^3(x)=\begin{cases}\dfrac{2}{3}-\dfrac{1}{2}|x|^2\left(2-|x|\right), & 0\le|x|<1\\ \dfrac{1}{6}\left(2-|x|\right)^3, & 1\le|x|<2\\ 0 & 2\le|x|.\end{cases} \tag{3.21}$$

Similar expressions can be developed for $\beta^3(y)$.

A uniform grid is first applied to the ROI on the specimen surface image (Figure 3.6). The spacing between the grid points can be arbitrary and need not be the same in x- and y-directions. The smaller the spacing between grid points, the more detail of the displacement field can be represented. Each grid point is associated with a bicubic B-spline surface with a certain height. The complete representation of the displacement field is a linear combination of all the bicubic B-splines expressed by

$$\mathbf{u}(\mathbf{x})=\begin{cases}u(x,y)\\ v(x,y)\end{cases}=\sum_{i=0}^{m}\sum_{j=0}^{n}\begin{pmatrix}c_{x,i,j}\\ c_{y,i,j}\end{pmatrix}\beta^3\left(x/h_x-i\right)\beta^3\left(y/h_y-j\right), \tag{3.22}$$

where m and n are the number of grid points in x- and y-directions, h_x and h_y are the grid spacing, and $c_{x,i,j}$ and $c_{y,i,j}$ are the coefficients associated with the two bicubic B-

spline surfaces at grid point (i, j) for displacement u and v respectively. Equation (3.19) can be rewritten as

$$C_{\text{img}} = \frac{1}{\#\Omega_{\text{img}}} \sum_{\mathbf{x}\in\Omega_{\text{img}}} \left\{ I_r\left(\mathbf{x}\right) - I_d\left(\mathbf{x}+\mathbf{u}\left(\mathbf{x}\right)\right)\right\}^2, \tag{3.23}$$

where the optimal unknowns $c_{x,i,j}$ and $c_{y,i,j}$ yield the best estimate of $\mathbf{u}\left(\mathbf{x}\right)$, therefore the minimum C_{img}.

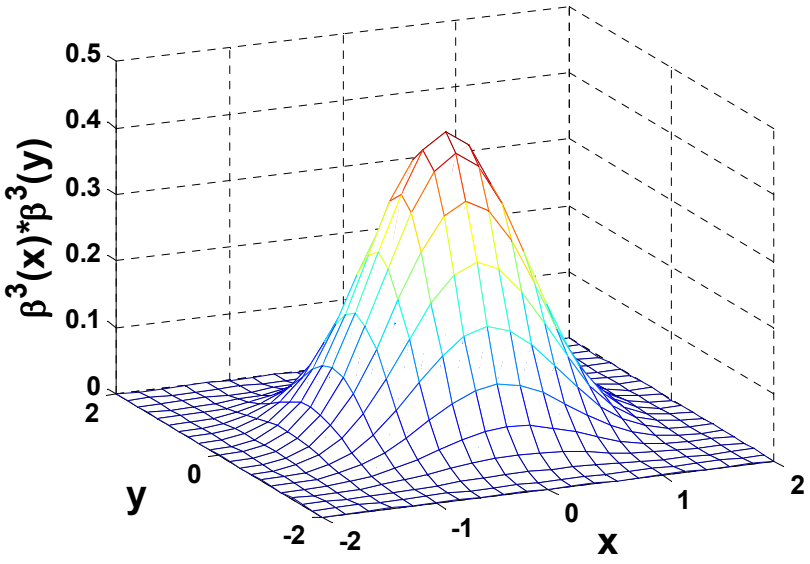

Figure 3.7: Bicubic B-spline basis function

In Equation (3.23), the deformation parameters to be correlated only includes displacement, while for the subset DIC algorithm, the deformation parameters may include derivatives of the displacement. However, the B-spline form of $\mathbf{u}\left(\mathbf{x}\right)$ (Equation (3.22)) allows one to compute a smooth and continuous gradient field efficiently. The smoothness of the computed gradient field is not to the same level of the displacement field. This is due to the fact that the gradient of $\mathbf{u}\left(\mathbf{x}\right)$ is more sensitive than $\mathbf{u}\left(\mathbf{x}\right)$ itself

to the change of the unknown parameters $c_{x,i,j}$ and $c_{y,i,j}$. This issue can be resolved by minimizing an additional regularization term [95]

$$G_{\text{img}} = \frac{1}{\#\Omega_{\text{img}}}\left(\sum_{\mathbf{x}\in\Omega_{\text{img}}} \left\| D^2 u(\mathbf{x}) \right\|^2 + \sum_{\mathbf{x}\in\Omega_{\text{img}}} \left\| D^2 v(\mathbf{x}) \right\|^2 \right), \tag{3.24}$$

where $D^2 = \left(\frac{\partial^2}{\partial x^2}, 2\frac{\partial^2}{\partial x \partial y}, \frac{\partial^2}{\partial y^2} \right)$ is the second-order total differential operator, and $\|\cdot\|$ is the Euclidean norm. Combining Equations (3.19) and (3.24) and assigning different weights to the two terms, the new objective function to be minimized becomes

$$\Psi = w_c C_{\text{img}} + w_g G_{\text{img}}, \tag{3.25}$$

where w_c and w_g are the scalar-valued weights.

The Newton-Raphson procedure to minimize the correlation coefficient C can be used to minimize Ψ. Cheng *et al.* [61] and Sorzano *et al.* [95] have proposed using the Levenberg-Marquardt optimization method as the solver to improve the computational efficiency.

3.4 ASSESSMENT OF THE FULL-FIELD DIC

In this section, the performance of the full-field DIC is evaluated by comparing it to the subset DIC with the second order mapping function. Assessment of the accuracy of DIC needs at least one pair of images with known displacement transformation between them. Usually, numerically transformed images are used [61,84,92] or transformation can be made by experimental means [96]. In the latter case, the transformations are usually limited to be uniform one degree-of-freedom deformation, e.g. translation, uniaxial stretching or compression, or rigid body rotation. In the former case, much more complicated transformations can be applied, e.g., the transformation can be a combination of translation, stretching and rotation. In this study, a more complicated numerical transformation is used to generate the deformed image from a reference image, which is a real speckle image. It is anticipated that such transformation simulates the

more general cases of inhomogeneous deformation. Equation (3.26) shows the displacement functions, horizontal and vertical, for the image transformation:

$$\begin{aligned} u(x,y) &= \left[\sin\left((x-x_0)\pi/W\right)+\cos\left(3(x-x_0)\pi/W\right)\right]\left[\cos\left((y-y_0)\pi/H\right)+\sin\left(3(y-y_0)\pi/H\right)\right] \\ v(x,y) &= \left[\cos\left((x-x_0)\pi/W\right)+\sin\left(3(x-x_0)\pi/W\right)\right]\left[\sin\left((y-y_0)\pi/H\right)+\cos\left(3(y-y_0)\pi/H\right)\right], \end{aligned} \quad (3.26)$$

where (x_0, y_0) are the coordinate of the origin of the reference image, W and H are the width and height of the reference image in pixels. The image transformation involves evaluation of subpixel intensity from the reference image, which is done through cubic interpolation (Appendix A). The image used for the assessment of the in-house DIC is shown in Figure 3.8, which also shows the deformed image. The vector plot of the displacement field by equation (3.26) is shown in Figure 3.9, which clearly illustrates the heterogeneous deformation imposed by transformation.

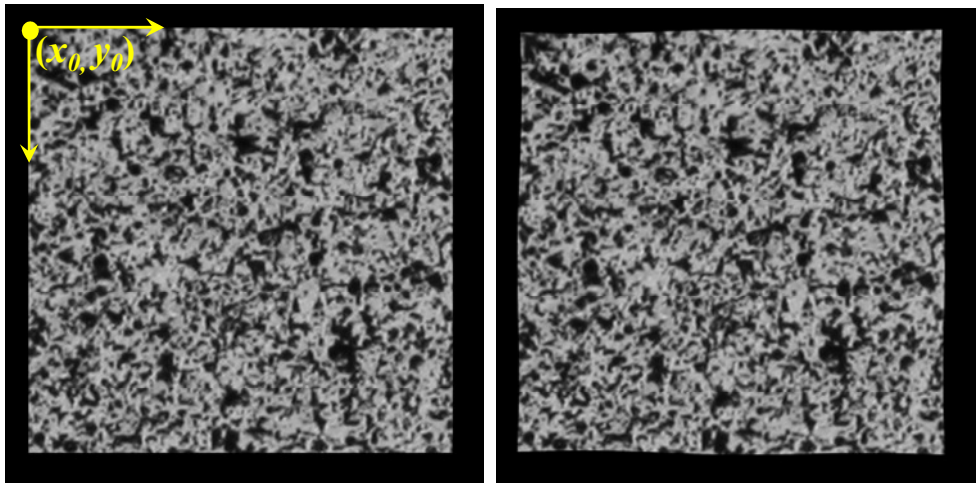

Figure 3.8: Left: reference image 300 x 300 pixels, black background; Right: deformed image using the transformation functions

The gradient of the displacement field, i.e., the strain of the deformation, for horizontal and vertical direction, can be easily derived from equation (3.26) and is not provided here. Only the components of the gradient of the horizontal displacement, u_x and u_y, are shown in Figure 3.10 and Figure 3.11, respectively.

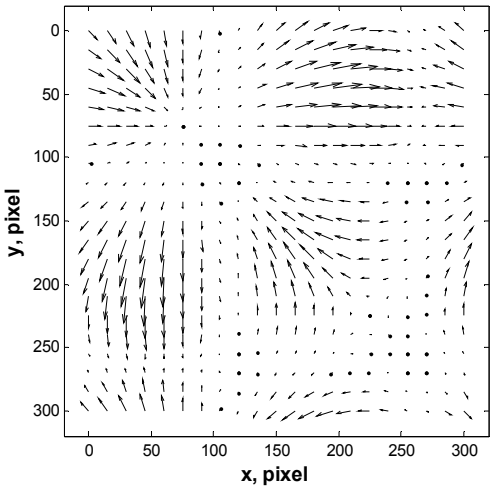

Figure 3.9: Vector plot of displacement field by the transformation

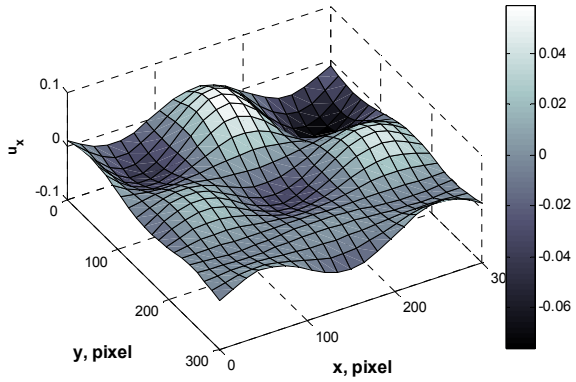

Figure 3.10: Surface plot of the field u_x

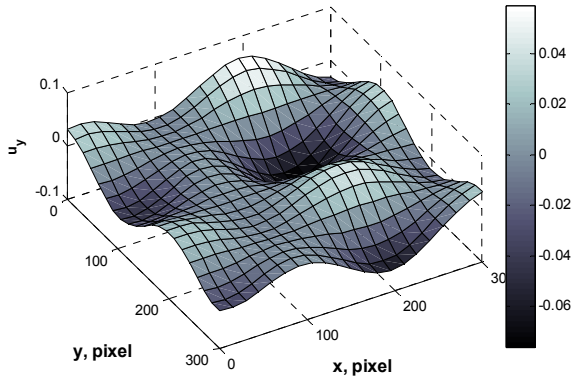

Figure 3.11: Surface plot of the field u_y

3.4.1 Displacement Field

A uniform grid of 21x21 points over the entire reference image is used for the evaluation. The measured displacements by subset DIC (subset size: 31×31 pixels) and full-field DIC are compared with the displacements calculated from equation (3.26). The displacement errors, i.e., difference between DIC measurement and the analytical values, at the grid points for u and v are plotted in Figure 3.12 and Figure 3.13, respectively. Larger errors can be seen from both DIC measurements near the image boundary, but the errors of the subset DIC are more significant. While away from the image boundary, both DIC's seems to have consistent small errors.

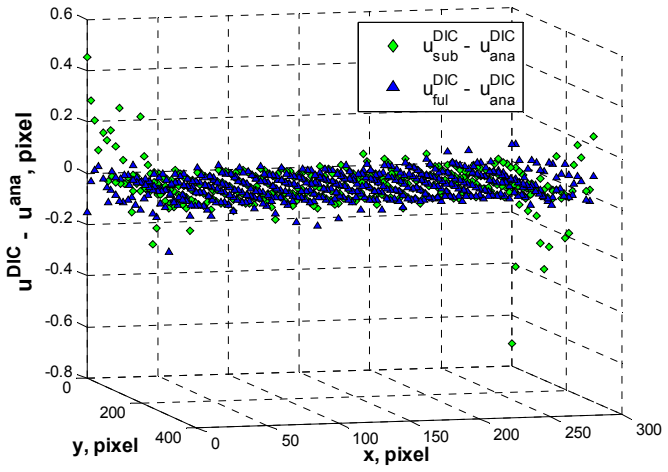

Figure 3.12: Errors of displacement component, u, for subset DIC and full-field DIC

The errors of displacement are plotted against the displacement in Figure 3.14, in which u^{DIC}_{ana} and v^{DIC}_{ana} denote the analytical displacement components computed from the transformation function, u^{DIC}_{sub} and v^{DIC}_{sub} denote the displacement measured by subset DIC, and u^{DIC}_{ful} and v^{DIC}_{ful} denote the displacement measured by full-field DIC. As the figure shows, in average, the full-field DIC yields better measurement than the subset DIC. Notice that the error level does not depend on the displacement value. This is contrary to

what was observed in simple transformation: the mean errors are small when the displacement is close to a whole pixel number [84].

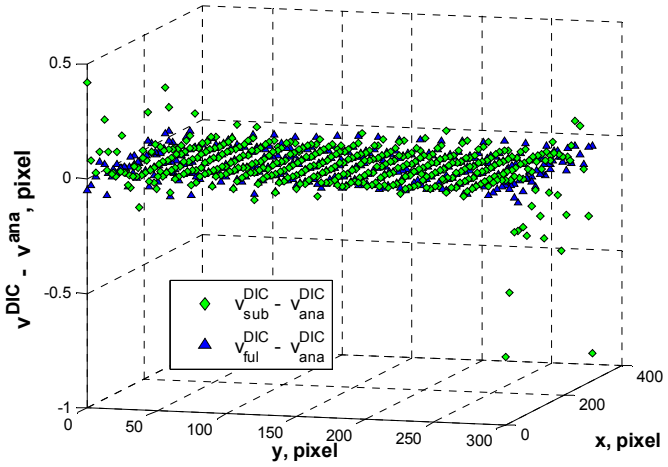

Figure 3.13: Errors of displacement component, v, for subset DIC and full-field DIC

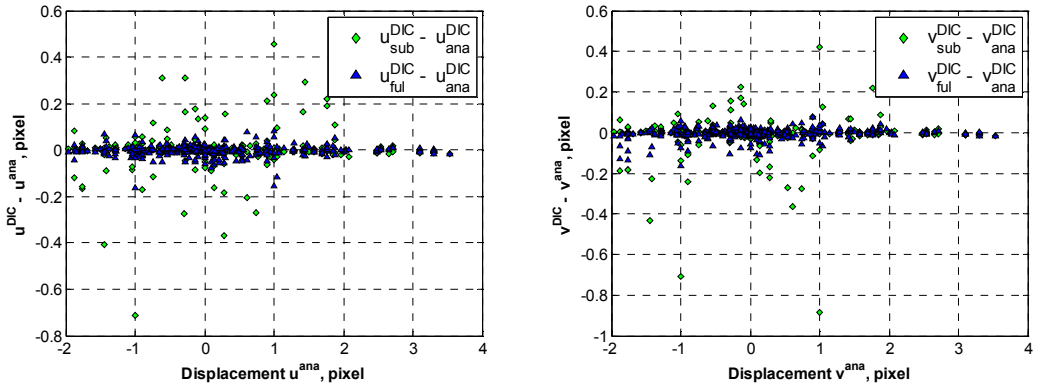

Figure 3.14: Displacement error versus displacement for subset and full-field DIC's, left: errors for u, right: errors for v

Figure 3.15 clearly shows that those problematic points having higher errors by both the subset and the full-field DIC measurements are located at the image boundary. Away from the boundary, both DICs seems to have similar level of accuracy. The reason that the subset DIC is prone to errors near the boundary can be explained by the fact that only a partial subset for the boundary grid points can be used for the correlation, while for the

full-field DIC there is no such issue. The imperfect interpolation near the image boundary for the transformation may be the reason that relatively larger errors at the boundary also occur for full-field DIC.

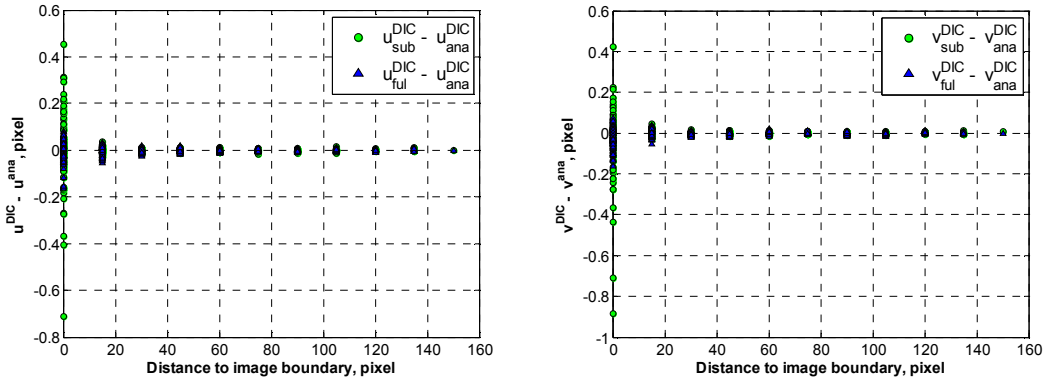

Figure 3.15: Displacement errors plotted against distance from grid point to image boundary, left: errors for u, right: errors for v

The accuracy of the boundary displacement measurement may be important for certain problems, e.g., the fracture problems investigated in current study. In this sense, the full-field DIC seems to be superior to the subset DIC.

3.4.2 Strain Field

Figure 3.16 shows the errors of normal strains, $u_x^{DIC} - u_x^{ana}$ and $v_y^{DIC} - v_y^{ana}$, plotted against the distance from grid point to boundary for the subset and full-field DICs. Notice the same scale used for both plots for easy comparison. Again, for both DICs, larger errors are seen for the measurement at boundary grid points, but the full-field DIC yields better measurement. The full-field DIC is also more accurate at grid points inside the image.

The errors of shear strains, $u_y^{DIC} - u_y^{ana}$ and $v_x^{DIC} - v_x^{ana}$ are shown in Figure 3.17. Similar measurement errors are seen for both DIC's. However, for grid points inside the image, the full-field DIC yields much better results. Comparing Figure 3.16 to Figure

3.17, the subset DIC gives better measurement in normal strain than in shear strain, while the full-field DIC gives accurate measurement for both normal and shear strains.

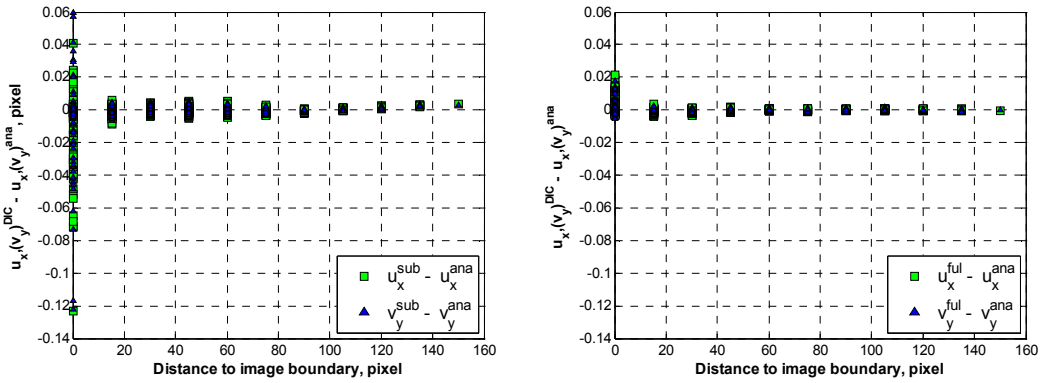

Figure 3.16: Normal strain errors plotted against distance from grid point to image boundary, left: for subset DIC, right: for full-field DIC

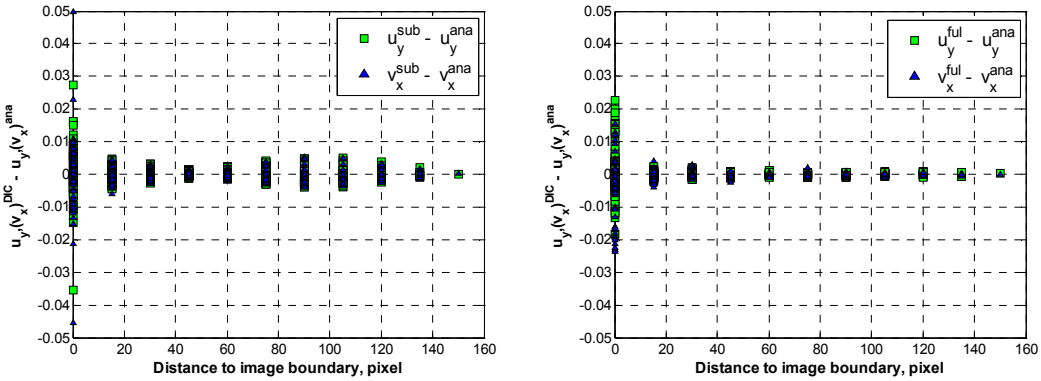

Figure 3.17: Shear strain errors plotted against distance from grid point to image boundary, left: for subset DIC, right: for full-field DIC

The gradient of the strain, or the second-order displacement gradient, can also be extracted from full-field DIC results. Since second-order displacement gradient is rarely used, only errors of u_{xx} and u_{xy} are shown here in Figure 3.18. Again, full-field DIC gives better results at boundary grid points for u_{xx}. However, for u_{xy}, both methods show comparable level of accuracies.

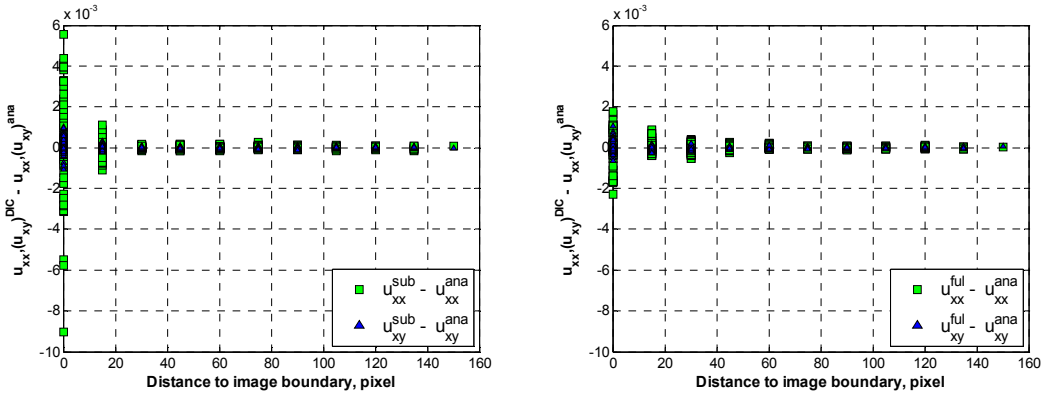

Figure 3.18: Errors of second-order displacement gradient plotted against distance from grid point to image boundary, left: for subset DIC, right: for full-field DIC

3.4.3 Statistics of the DIC Measurement

Table 3.1 shows the statistics for all the available kinematic fields measured by both the subset and the full-field DICs, for a population of 21×21 points. Careful inspection of the statistics of the mean absolute error and standard deviation of the errors proves that the full-field DIC has better performance than the subset DIC. In general, for displacement and strain, the mean error of the full-field DIC is about half of or less than the mean error of the subset DIC. At this point, the second-order displacement gradient seems to be of little interest

3.5 REMARKS

Contrary to the many DIC accuracy evaluations reported in the literature, which primarily use deformed images by simple transformations, here a fully heterogeneous transformation is applied. The average error of displacement measured by the subset DIC for such heterogeneous field is about 5 times higher than the error generally claimed in the literature using simpler fields (e.g. rigid body motions, uniform stretching or compression). The measurement error of the full-field DIC is about half of the error by the subset DIC, which is different from what is reported in some articles claiming that the full-field DIC has one order higher accuracy over the subset DIC. Again, the reason for that relates to the use of simpler fields in the literature. The point here is that one should

not take for granted that the high DIC precision claimed in other studies can be also obtained for specific complicated deformations/configurations. Each material and each DIC setup have their own particular features.

Besides improved average accuracy, the major advantage of full-field DIC over subfield DIC, as has been demonstrated in this chapter, is that the errors measured by full-field DIC near the image boundary are much smaller. As will be presented in later chapters, the inverse fracture problem requires accurate measurement of the displacement field on the crack vicinity.

Table 3.1: Mean displacement error and the standard deviation of the displacement error, α denotes a particular kinematic term, e.g. u, v, ..., etc.

	Mean error: $\mu_{\alpha^{DIC}-\alpha^{ana}}$		Mean absolute error: $\mu_{\lvert\alpha^{DIC}-\alpha^{ana}\rvert}$		Standard deviation of the error: $\sigma_{\alpha^{DIC}-\alpha^{ana}}$	
DIC type	Subset	Full-field	Subset	Full-field	Subset	Full-field
u	-0.00023	-0.00182	0.0243	0.0127	0.0699	0.0219
v	-0.00703	-0.00352	0.0244	0.0142	0.0774	0.0251
u_x	-0.002277	0.000699	0.00474	0.00146	0.01227	0.00319
u_y	0.000130	0.000191	0.00217	0.00137	0.00382	0.00332
v_x	0.000089	-0.000587	0.00236	0.00174	0.00477	0.00422
v_y	-0.001419	0.000506	0.00465	0.00124	0.01294	0.00264
u_{xx}	0.000045	-0.000010	0.000351	0.000195	0.000981	0.000395
u_{xy}	0.000024	0.000004	0.000093	0.000071	0.000179	0.000132
u_{yy}	-0.000032	-0.000080	0.000136	0.000180	0.000283	0.000467
v_{xx}	-0.000008	-0.000114	0.000141	0.000222	0.000357	0.000452
v_{xy}	0.000016	0.000006	0.000109	0.000066	0.000222	0.000117
v_{yy}	-0.000142	-0.000040	0.000343	0.000166	0.000980	0.000408

CHAPTER 4 - INVERSE COMPUTATION OF COHESIVE FRACTURE PROPERTIES

The investigation of the proposed scheme is conducted through a 2D FE model of single edge-notched beam (SENB) specimen. The SENB specimen is commonly used in experiments for the measurements of mode I fracture behavior and properties. In this study, only one crack along the symmetry line of the specimen is considered. The CZM is implemented along this line. In the direct problem, a known CZM is assumed. An intrinsic CZM implementation is then carried out to solve the nonlinear fracture process, results of which include global load (P) versus CMOD and the displacement field at each loading step. The inverse problem uses the displacement field corresponding to certain post-peak load levels in the P versus CMOD curve, where the full cohesive zone is formed. In the inverse problem, the CZM is the unknown while the displacement data, recorded at every node, from the direct problem is treated as synthetic experimental data. Synthetic errors of different levels are added to the displacement data before it is used in the inverse analysis. The inverse problem is formulated as an unconstrained optimization problem in which a flexible CZM shape representation defined by a set of unconstrained parameters is to be obtained. Both residual and displacement based optimization approaches are presented and discussed.

4.1 INTRODUCTION

Fundamentally, stress can only be measured indirectly, while displacement or strain is traditionally measured at limited number of discrete points. Recent developments in experimental stress analysis techniques, such as photoelasticity, laser interferometry and digital image correlation (DIC), enable measurements of whole deformation field [78]. The rich experimental data has attracted the attention of researchers who work on inverse identification problems [83]. Among these techniques, DIC shows great potential in experimental fracture analysis [33,85,86].

Recent hardware and software development of DIC technique enable researchers to obtain sub-micron measurement of 2D whole displacement field on a flat specimen surface. Such accurate measurement of the displacement field allows one to take numerical derivatives to obtain the strain field, though it may introduce errors in the process of differentiating discrete experimental data. The stress is then obtained using the known elastic properties. In such a way, stress near the crack surface can be obtained to approximate the cohesive stress. By statistically correlating the crack opening displacement (COD), which is a part of the DIC measured displacement field, with the cohesive stress, one can obtain the cohesive zone model from the local level [86]. This scheme correlates cohesive stress with COD in a discrete fashion without considering the possible influence from adjacent materials, which may degrade the accuracy. In addition, for stiff, brittle materials, the failure stress of the material is normally very low and thus, the associated strain level in the bulk material is also low, which leads to high error/noise to signal ratio. This can lead to extreme difficulty in obtaining accurately derived strain.

Motivated by the access to the full displacement field obtainable from DIC and by the power of FE simulations of fracture phenomena, the idea of combining DIC with the FEM is explained in this investigation. The key idea is to utilize the full displacement field in an FEM frame. Avoiding the computation of the stress from the derived strain field (a potentially significant source of errors) is the major advantage of using FEM. The proposed scheme is described in the next section.

4.2 DIRECT PROBLEM

In a general fracture mechanics problem, the geometry of the solids, the constitutive parameters for the bulk materials and its cohesive properties, and a set of well-posed boundary conditions are known or given. The solution of the problem consists of the displacement, strain and stress fields. Such fracture problems are referred to as *direct* problems. The FEM formulation of these direct problems, based upon the principle of virtual work, can be expressed as [39]:

$$\int_{\Omega} \boldsymbol{\sigma} : \delta \mathbf{E} d\Omega - \int_{\Gamma_{ext}} \mathbf{T}_{ext} \cdot \delta \mathbf{u} d\Gamma_{ext} - \int_{\Gamma_{coh}} \mathbf{T}_{coh} \cdot \delta \Delta \mathbf{u} d\Gamma_{coh} = 0, \qquad (4.1)$$

where Ω represents the specimen domain, Γ_{ext} represents the boundary on which the surface traction $\mathbf{T}_{ext}$ is applied, Γ_{coh} represents the cohesive surface where the cohesive traction $\mathbf{T}_{coh}$ and the crack opening displacement $\Delta\mathbf{u}$ are present, $\boldsymbol{\sigma}$ is the Cauchy stress tensor, $\mathbf{E}$ is the Green strain tensor, and $\mathbf{u}$ is the displacement vector. Applying the Galerkin discretization procedure that uses FEM shape functions leads to the set of standard FEM system of equations

$$\mathbf{K}\left(\mathbf{u};\boldsymbol{\lambda}\right)\mathbf{u} = \mathbf{F}^{ext} \,, \tag{4.2}$$

where $\mathbf{K}$ is the stiffness matrix which is a function of the given constitutive parameters $\boldsymbol{\lambda}$ and the displacement $\mathbf{u}$, and $\mathbf{F}^{ext}$ is the generalized external force vector. Note that the dependence of $\mathbf{K}$ on $\mathbf{u}$ implies a nonlinear response, as this is the usual case in nonlinear fracture mechanics problems.

In an FEM context, the CZM can be implemented through a special intrinsic cohesive element [38,59], or be treated as a special nonlinear surface traction that acts on the cohesive surfaces. For the fracture problems presented in this thesis, a plain-stress single-edge notched beam (SENB) specimen is used. The specimen is idealized by a 2D FEM model discretized using Q4 element. The latter approach of implementing CZM is found to be convenient and is therefore adopted. Figure 4.1 shows one bulk Q4 element aligned to the cohesive surface on the SENB specimen, where σ denotes the mode I cohesive stress.

For this Q4 element

$$\mathbf{K}_{\mathrm{b}}^{e}\mathbf{u}^{e} = \mathbf{r} \,, \tag{4.3}$$

where $\mathbf{K}_{\mathrm{b}}^{e}$ is the bulk element stiffness matrix, $\mathbf{u}^{e}$ is the element nodal displacement, and $\mathbf{r}$ is the element nodal force. When the cohesive stress is the only stress contributing to $\mathbf{r}$, we have

$$\mathbf{r} = \int_0^l \sigma\left(\Delta_{\mathrm{n}}\left(s\right)\right) t\mathbf{N}_{\mathrm{s}} ds = \int_0^l k_{\mathrm{c}}\left(\Delta_{\mathrm{n}}\left(s\right)\right)\Delta_{\mathrm{n}}\left(s\right) t\mathbf{N}_{\mathrm{s}} ds = -\mathbf{K}_{\mathrm{c}}^{e}\mathbf{u}_{x} \,, \tag{4.4}$$

where s is the local natural coordinate shown in Figure 4.1, l is the size of the Q4 element, t is beam thickness, $k_c = \sigma/\Delta_n$, $\mathbf{N}_s = \{(l-s)/l,\ s/l\}^T$ is the shape function in natural coordinate system, and $\Delta_n(s) = -2u(s) = -2\mathbf{u}_x^T\mathbf{N}_s$. The vector $\mathbf{u}_x = \{u_{1x},\ u_{2x}\}^T$ denotes the nodal displacement in the *x* direction, and $\mathbf{K}_c^e = 2\int_0^l k_c(-2u(s))\mathbf{N}_s\mathbf{N}_s^T t ds$ denotes the cohesive element stiffness matrix. As $l = y_2^{(e)} - y_1^{(e)}$, $s = l(\eta+1)/2$, $\mathbf{K}_c^e$ can be simplified:

$$\mathbf{K}_c^e = \int_{-1}^{1} k_c(-2\mathbf{u}_x^T\mathbf{N})\mathbf{N}\mathbf{N}^T t d\eta, \tag{4.5}$$

where $\mathbf{N} = \{(1-\eta)/2,\ \ (1+\eta)/2\}^T$ is the shape function in the isoparametric coordinate system.

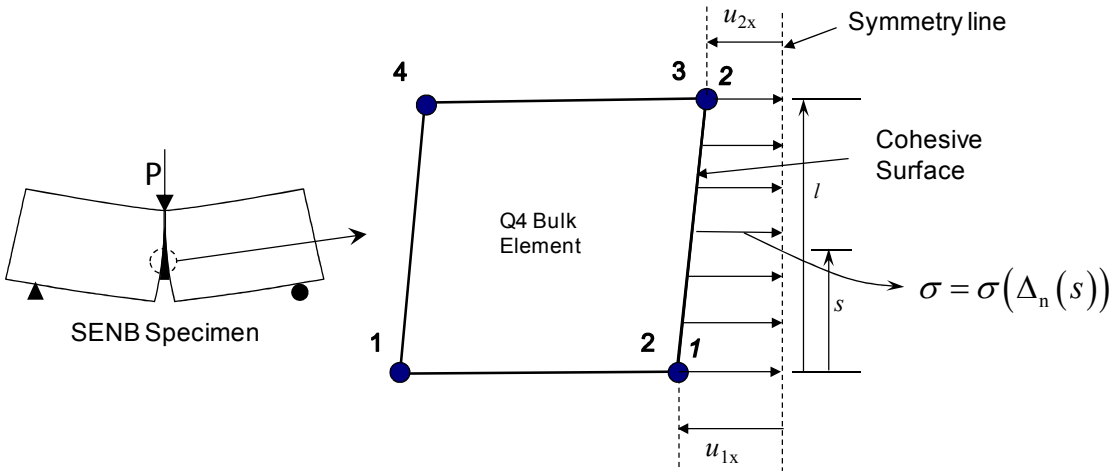

Figure 4.1: A bulk Q4 element along the cohesive surface

Equations (4.3) and (4.4) give the contributions of each element to the cohesive and bulk stiffness, and the global system of equations becomes

$$(\mathbf{K}_b + \mathbf{K}_c(\mathbf{u}))\mathbf{u} = \mathbf{F}^{ext}, \tag{4.6}$$

where $\mathbf{K}_b$ is the global stiffness matrix of the bulk material, $\mathbf{K}_c$ is the global cohesive stiffness matrix, $\mathbf{u}$ is the global displacement vector, and $\mathbf{F}^{ext}$ is the generalized global external force vector. With the realistic assumption that no damage occurs on the bulk materials during a fracture process, $\mathbf{K}_b$ remains essentially a constant matrix. One can see that equation (4.6) is a particular case of the equation (4.2).

The sequence of iterations for the displacement field $\mathbf{u}$ at a specified load can be obtained through

$$\left(\mathbf{K}_b + \mathbf{K}_c\left(\mathbf{u}^{(n),m}\right)\right)\mathbf{u}^{(n),m+1} = \mathbf{F}^{ext}, \tag{4.7}$$

where n is the n^{th} loading step and m is the m^{th} iteration for the current loading step. The loading in the FE analysis is displacement controlled and is defined by the generalized external force vector $\mathbf{F}^{ext}$. For the cases when the loading response shows a snap-back behavior in the post-peak load versus load-line displacement curve, a more advanced arc-length solution scheme is applied. Details of the algorithm of the nonlinear arc-length procedure can found in references [97,98].

4.3 INVERSE PROBLEM

The current problem belongs to the particular type of inverse problem that involves constitutive parameter identification through a set of given or measured kinematic measurements [83]. In this study, a full-field displacement data is the basis for the inverse problem. The parameters defining the cohesive traction-separation relation, denoted exclusively as $\boldsymbol{\lambda}$ hereafter, are the constitutive parameters to be identified. The basic equation (4.2) remains identical except in that $\mathbf{u}$ is now assumed to be known while $\boldsymbol{\lambda}$ becomes the unknown to be solved. Numerically, one can see that the inverse problem is in fact an overdetermined system with respect to $\boldsymbol{\lambda}$, as the number of constitutive parameters is always less than the total number of equations. To estimate the constitutive parameters in an average sense, an optimization approach is usually adopted which consists of minimizing a least-square functional with respect to residual, displacement, or

strain fields [84]. In this study, the residual-based (section 4.3.2) and displacement-based (section 4.3.3) optimization approaches are compared.

The description of a CZM requires a well-defined traction-separation relation. The shape of the curve of this traction-separation relation is, in general, unknown, and must be identified in the inverse problem. The identification of a constitutive curve rather than of a set of independent scalar constitutive parameters commonly seen in typical inverse problems is the unique characteristic of current inverse problem. The effective parameterization of a CZM shape becomes one of the key elements in a successful inverse analysis. It is therefore natural to introduce the proposed shape representation, i.e., parameterization, of the CZM before presenting the optimization formulations for the inverse problem.

4.3.1 Shape Representation of CZMs

It is desired to extract the CZM without making any assumption about its shape because in practice, only limited or no knowledge of the cohesive property of new materials or material systems are available.

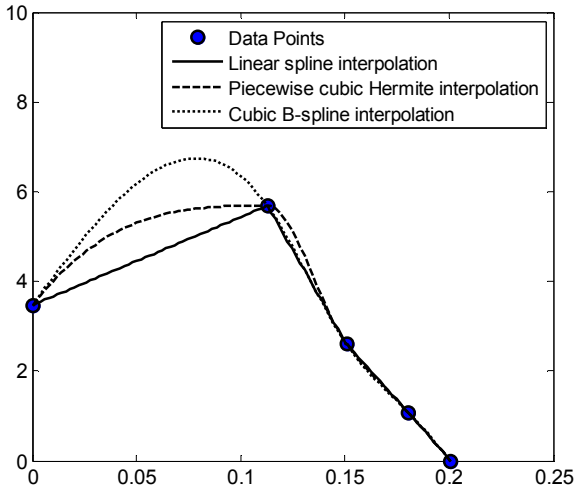

Figure 4.2: Illustration of various interpolation schemes

Splines are selected to describe the CZM, i.e., the relation traction-separation. The reasons to use splines are the flexibility to construct arbitrary curves, and the mathematical conciseness and simplicity. Three common spline interpolations are used: linear spline (LS) interpolation, piecewise cubic Hermite (PCH) interpolation and cubic B-spline (CBS) interpolation. Detailed information on these interpolation options can be found in references [99,100]. A brief description of the CBS interpolation with the explicit expression of the 4th order (cubic) B-spline non-uniformly spaced knots is provided in Appendix B. These three types of splines provide different levels of smoothness, as illustrated in Figure 4.2, thus they offer choices on the type of description, e.g., polylinear or smooth.

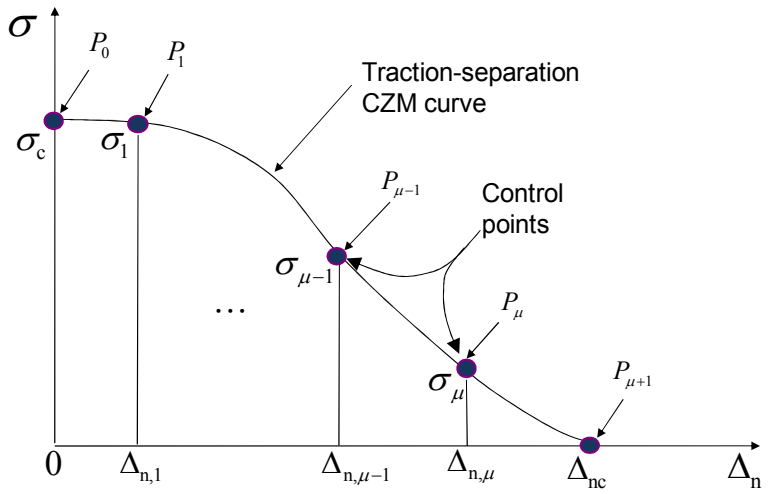

Figure 4.3: Parameterization for splines

The use of splines allows for a shape representation based on an arbitrary number of control points. Let us define the coordinates of the $\mu+2$ control points according to Figure 4.3, i.e.,

$$\begin{cases} \boldsymbol{\Delta}_{\mathrm{n}} = \left\{0,\ \Delta_{\mathrm{n},1},\ \cdots,\ \Delta_{\mathrm{n},\mu},\ \Delta_{\mathrm{nc}}\right\} \\ \boldsymbol{\sigma} = \left\{\sigma_{\mathrm{c}},\ \sigma_{1},\ \cdots,\ \sigma_{\mu},\ 0\right\} \end{cases}, \tag{4.8}$$

which leads to the unknown physical CZM parameters as

$$\boldsymbol{\lambda} = \left\{ \sigma_c,\ \Delta_{\mathrm{nc}},\ \sigma_1,\ \Delta_{\mathrm{n},1},\ \cdots,\ \sigma_\mu,\ \Delta_{\mathrm{n},\mu} \right\} . \tag{4.9}$$

4.3.2 Residual-based Optimization Approach

Denote by $\bar{\mathbf{u}}$ the displacement vector representing the whole displacement field already available, either from the direct problem, or from experimental measurement. Equation (4.6) can be rewritten to reflect the inverse problem

$$\left(\mathbf{K}_{\mathrm{b}} + \mathbf{K}_{\mathrm{c}} \left(\boldsymbol{\lambda} \right) \right) \bar{\mathbf{u}} = \mathbf{F}^{\mathrm{ext}} . \tag{4.10}$$

The $\boldsymbol{\Delta}_{\mathrm{n}} = \left\{ 0,\ \Delta_{\mathrm{n},1},\ \cdots,\ \Delta_{\mathrm{n},\mu},\ \Delta_{\mathrm{nc}} \right\}$ for the control points in (4.8) is a subset of the continuous COD , which in turn is also a subset of $\bar{\mathbf{u}}$. Therefore, $\boldsymbol{\lambda}$ in the inverse problem is a function of $\bar{\mathbf{u}}$, and equation (4.10) can be rewritten as

$$\left(\mathbf{K}_{\mathrm{b}} + \mathbf{K}_{\mathrm{c}} \left(\boldsymbol{\lambda} \left(\bar{\mathbf{u}} \right) \right) \right) \bar{\mathbf{u}} = \mathbf{F}^{\mathrm{ext}} . \tag{4.11}$$

$\mathbf{K}_{\mathrm{c}}$ can only be evaluated when values of $\boldsymbol{\lambda}$ are known or given. Gauss quadrature is used to evaluate $\mathbf{K}_{\mathrm{c}}$ since an explicit expression of $\mathbf{K}_{\mathrm{c}}$ as function of $\boldsymbol{\lambda}$ is not available. Subsequently, nonlinear solvers must be used to obtain the estimate of $\boldsymbol{\lambda}$ so that, as one may immediately recognize, the average difference between LHS and RHS of equation (4.11), i.e., the residual of equation (4.11)

$$\mathbf{R} \left(\boldsymbol{\lambda} \right) = \left(\mathbf{K}_{\mathrm{b}} + \mathbf{K}_{\mathrm{c}} \left(\boldsymbol{\lambda} \left(\bar{\mathbf{u}} \right) \right) \right) \bar{\mathbf{u}} - \mathbf{F}^{\mathrm{ext}} , \tag{4.12}$$

can be minimized. In an optimization format, the inverse problem can be expressed as

$$\min_{\boldsymbol{\lambda}}\ \Phi_R \left(\boldsymbol{\lambda} \right) = \left\| \mathbf{R} \left(\boldsymbol{\lambda} \right)^{\mathrm{T}} \cdot \mathbf{w}_R \right\|_2 , \text{ subject to } c_i \left(\boldsymbol{\lambda} \right) \geq 0,\ i = 1 \ldots L , \tag{4.13}$$

where M is the number of input parameters, $\Phi_R : \mathbb{R}^{\mathrm{M}} \rightarrow \mathbb{R}$ is the non constrained objective function, $\mathbf{w}_R$ is the vector of weighting factors, $c_i \left(\boldsymbol{\lambda} \right)$ are the constraint functions, L is the number of constraint functions, and $\left\| \cdot \right\|_2$ is the Euclidean norm of a vector.

4.3.3 Displacement-based Optimization Approach

Equation (4.13) defines the straightforward formulation for the inverse problem. However, $\mathbf{K}_\mathrm{b}$ as an operator being applied to $\bar{\mathbf{u}}$ filters out the rigid-body-motion part of $\bar{\mathbf{u}}$, and $\mathbf{K}_\mathrm{b}$ significantly magnifies the errors existing in $\bar{\mathbf{u}}$ since $\mathbf{K}_\mathrm{b}\bar{\mathbf{u}}$ implicitly compute the gradients of $\bar{\mathbf{u}}$. To avoid any possible degradation of $\bar{\mathbf{u}}$, it may be more desirable to directly match the difference between $\bar{\mathbf{u}}$ and a computed displacement field, $\mathbf{u}^*$, which is based on an assumed $\boldsymbol{\lambda}$. To compute $\mathbf{u}^*$, first rearrange equation (4.10) as

$$\mathbf{K}_\mathrm{b}\bar{\mathbf{u}} = \hat{\mathbf{F}}^{\mathrm{ext}}\left(\bar{\mathbf{u}};\boldsymbol{\lambda}\right), \tag{4.14}$$

where

$$\hat{\mathbf{F}}^{\mathrm{ext}}\left(\bar{\mathbf{u}};\boldsymbol{\lambda}\right) = \mathbf{F}^{\mathrm{ext}} - \mathbf{K}_\mathrm{c}\left(\boldsymbol{\lambda}\left(\bar{\mathbf{u}}\right)\right)\bar{\mathbf{u}}. \tag{4.15}$$

Now the cohesive stress is included as boundary stress and is accounted for in the new global external force vector $\hat{\mathbf{F}}^{\mathrm{ext}}\left(\bar{\mathbf{u}};\boldsymbol{\lambda}\right)$. From equation (4.14), $\mathbf{u}^*$ can be computed by

$$\mathbf{u}^*\left(\boldsymbol{\lambda}\right) = \mathbf{K}_\mathrm{b}^{-1}\hat{\mathbf{F}}^{\mathrm{ext}}\left(\bar{\mathbf{u}};\boldsymbol{\lambda}\right). \tag{4.16}$$

Nest the optimization formulation of the inverse problem based on minimizing displacement difference is written as

$$\min_{\boldsymbol{\lambda}\in\mathbb{R}^\mathrm{M}} \Phi_u\left(\boldsymbol{\lambda}\right) = \left\| \left(\mathbf{u}^*\left(\boldsymbol{\lambda}\right) - \bar{\mathbf{u}}\right)^\mathrm{T} \cdot \mathbf{w}_u \right\|_2, \text{ subject to } c_i\left(\boldsymbol{\lambda}\right) \geq 0,\ i = 1 \ldots L, \tag{4.17}$$

where $\Phi_u\left(\boldsymbol{\lambda}\right)$ is the objective function, and $\mathbf{w}_u$ is the vector of weighting factors.

The external force vector $\hat{\mathbf{F}}^{\mathrm{ext}}$ can be computed in the following manner. First from $\bar{\mathbf{u}}$, the crack opening displacement vector $\boldsymbol{\Delta}_\mathrm{n}$ for all nodes at crack surface can be extracted directly. With an estimated $\boldsymbol{\lambda}$, the CZM function $\sigma = \sigma\left(\Delta_\mathrm{n};\boldsymbol{\lambda}\right)$ is defined. The first part of Equation (4.4) is used to compute the equivalent element nodal force vector of the cohesive stress. By assembling all the element nodal force vectors, $\hat{\mathbf{F}}^{\mathrm{ext}}$ can be

obtained. Equation (4.14) can be computed efficiently by first factorizing the constant matrix $\mathbf{K}_b$.

4.3.4 The Nelder-Mead Solver

The Nelder-Mead (N-M) optimization method [101-103], an unconstrained and derivative-free optimization method, is utilized to solve equations (4.13) and (4.17). An initial guess of the CZM parameters, $\boldsymbol{\lambda}$, is provided to the N-M solver, which carries out the procedure described below. The stop criterion of the N-M algorithm can be set by comparing the best simplex vertex (explained in the next paragraph) or the value of $\Phi(\boldsymbol{\lambda})$ between adjacent iterations, or be set by when value of $\Phi(\boldsymbol{\lambda})$ is sufficiently small.

For an objective function $\Phi(\boldsymbol{\lambda}): \mathbb{R}^M \to \mathbb{R}$ to be minimized, a simplex of $M+1$ vertices is first formed. A simplex in $\mathbb{R}^1$ is a line segment, in $\mathbb{R}^2$ is a triangle, in $\mathbb{R}^3$ is a tetrahedron, and so on. Let $\boldsymbol{\lambda}_0 = \boldsymbol{\lambda}^{(0)}$ be the initial guess/point, which is also a vertex of the simplex to be formed. The other vertices can be selected by making $\boldsymbol{\lambda}_i - \boldsymbol{\lambda}_0$ parallel to the i^{th} M-dimensional unit vector $\{0,...,1,0...\}^T$, in which "1" appears as the value of the i^{th} component. The length of the vector $\|\boldsymbol{\lambda}_i - \boldsymbol{\lambda}_0\|_2$ can be a typical length scale in i^{th} dimension. This way, $\boldsymbol{\lambda}_1 - \boldsymbol{\lambda}_0$, $\boldsymbol{\lambda}_1 - \boldsymbol{\lambda}_0$, …, $\boldsymbol{\lambda}_M - \boldsymbol{\lambda}_0$ are mutually normal to each other, i.e., points $\boldsymbol{\lambda}_0$, $\boldsymbol{\lambda}_1$, …, $\boldsymbol{\lambda}_M$ are not co-planar in the $\mathbb{R}^M$ Euclidian space.

At any stage, the N-M method aims to remove the vertex with the largest function value and to replace it with a new vertex with a smaller function value. This procedure guarantees that the average objective function value at each step is non-increasing.

Figure 4.4 demonstrates the algorithm of N-M method for one step. Vertices $\boldsymbol{\lambda}_1$, ..., $\boldsymbol{\lambda}_4$ are ordered such that $\Phi(\boldsymbol{\lambda}_1) < \Phi(\boldsymbol{\lambda}_2) < \cdots < \Phi(\boldsymbol{\lambda}_4)$. We say point $\boldsymbol{\lambda}_i$ is better than point $\boldsymbol{\lambda}_j$ if $\Phi(\boldsymbol{\lambda}_i) < \Phi(\boldsymbol{\lambda}_j)$. The centroid of the best 3 points is $\bar{\boldsymbol{\lambda}}(0) = (\boldsymbol{\lambda}_1 + \boldsymbol{\lambda}_2 + \boldsymbol{\lambda}_3)/3$. Any point along the line joining points $\boldsymbol{\lambda}_4$ and $\bar{\boldsymbol{\lambda}}(0)$ can be defined by $\bar{\boldsymbol{\lambda}}(s) = \bar{\boldsymbol{\lambda}}(0) + s(\boldsymbol{\lambda}_4 - \bar{\boldsymbol{\lambda}}(0))$. One commonly used scheme is to replace $\boldsymbol{\lambda}_4$ with one of

the four points along the line: expansion point $\bar{\lambda}(-2)$, reflection point $\bar{\lambda}(-1)$, outside contraction point $\bar{\lambda}(-1/2)$, or inside contraction point $\bar{\lambda}(1/2)$. The details of which point to replace could be found in reference [103]. If all those four points are still worse than λ_4, shrinking of points λ_2 to λ_4 towards the best point λ_1 is performed. Either the replacement of the worst point or the shrinking finishes one step in the N-M method.

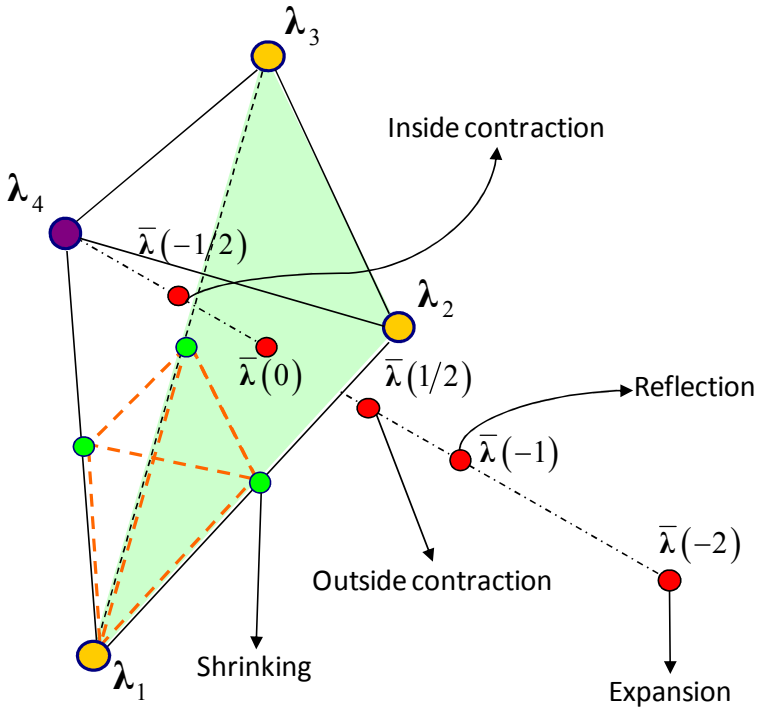

Figure 4.4: Schematic demonstration of the N-M method (three unknowns).

The N-M method is chosen because: (1) it is a derivative-free optimization method, it eliminates the derivation and computation of the gradient or the Hessian of the objective function; (2) inclusion of various constraint functions, if needed, as part of the objective function is easy; (3) it is more robust than common Newton-like solvers. One must note that the N-M method is not as computationally efficient as other optimization methods. However, the computational cost of optimization algorithms is beyond the scope of this work.

4.3.5 Parametric Mapping for Residual-based Formulation

The CZM parameters $\boldsymbol{\lambda}$ defined previously have physical bounds. For example, the critical COD, Δ_{nc}, can be neither negative nor larger than the specimen size. However, in its standard form, the N-M method does not accept any direct constraint imposed on the input parameters. During the N-M iteration, if one or a few parameters become negative, unphysical solutions for the CZM are obtained with compressive cohesive stress. The erroneous CZM either may lead to difficulty in computing the objective functions or may lead to convergence to another local minimum causing the failure of the solution process. A novel parametric mapping is proposed so that the standard procedure of N-M method can be used, which is applied to residual-based formulation. A trigonometric function is selected which effectively maps the physically bounded $\boldsymbol{\lambda}$ to the unbounded parameters $\boldsymbol{\lambda}^*$ appropriate for use as variables in the N-M method.

The mapping function

$$\lambda_i = \left(\frac{\tan^{-1}\left(\lambda_i^*\right)}{\pi} + \frac{1}{2} \right)\left(\overline{\lambda}_i - \underline{\lambda}_i\right) + \underline{\lambda}_i \ , \ \ \lambda_i^* \in \left(-\text{inf},\ \text{inf}\right) \rightarrow \lambda_i \in \left(\overline{\lambda}_i,\ \underline{\lambda}_i\right), \quad (4.18)$$

where $\left(\overline{\lambda}_i,\ \underline{\lambda}_i\right)$ is the physical bound for parameter λ_i, ensures that CZM parameters λ_i are always physical. However, the independence of the parameters still enables the points to move freely within their own bounds, which can also produce an erroneous CZM. Figure 4.5 illustrates two erroneous cases:

- the k_c at point P_i is smaller than the k_c at point P_{i+1},
- $\Delta_n\left(P_{i+2}\right) < \Delta_n\left(P_{i+1}\right)$ causing snap-back which is unphysical for CZM.

Such erroneous CZM curve can be regularized through further refinement of the mapping by considering the inter-constraint between the control points from the physical meaning of CZM. By looking at k_c defined in Figure 4.5, it is assumed that for a legitimate CZM, k_c must be monotonically decreasing as Δ_n increases. In addition, to

avoid snap-back, the condition $0 < \Delta_{n1} < \cdots < \Delta_{nl} < \Delta_{nc}$ must be satisfied for each optimization iteration. The following mapping scheme (Figure 4.6) is therefore proposed.

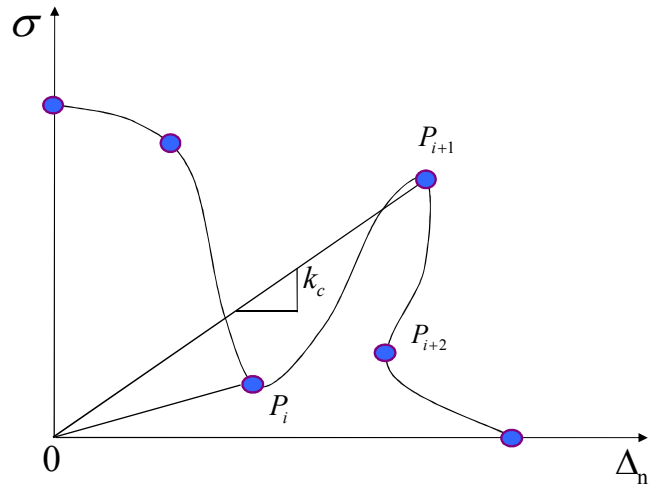

Figure 4.5: Erroneous CZM description due to independence of the control points: increasing k_c and snapback

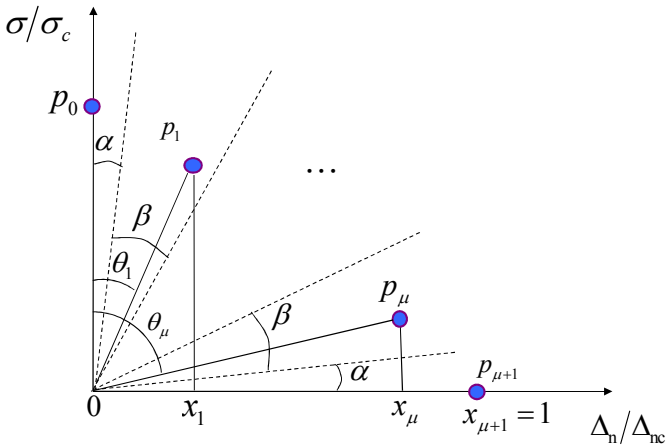

Figure 4.6: Mapping scheme that considers relative relation between control points

In Figure 4.6, the first quadrant of σ/σ_c axis versus Δ_n/Δ_{nc} axis is divided into $\mu+2$ domains by $\mu+1$ half-lines starting at the origin. Each control point is constrained

within two adjacent half-lines, except control points p_0 and $p_{\mu+1}$, which can only move along σ/σ_c and $\Delta_{\mathrm{n}}/\Delta_{\mathrm{nc}}$ axes, respectively. Therefore, the angle θ_i satisfies

$$\alpha+(i-1)\beta<\theta_i<\alpha+i\beta. \tag{4.19}$$

This constraint basically ensures the monotone decrease of k_c, with the possible exception of the extreme case of the CBS interpolation, which will be discussed later (Section 4.4.2.2). In the numerical examples given in section 4.4, $\alpha=\pi/32$ and $\beta=(\pi/2-\pi/32)/\mu$ are used.

The condition that $\Delta_{\mathrm{n},i}$ is non-decreasing is equivalent to $0<x_1<\cdots<x_\mu<1$ (Figure 4.6), i.e., x_i is a fraction of x_{i+1} for all i. Defining a set of $\boldsymbol{\lambda}^*$ indirectly by

$$\begin{cases}\Delta_{\mathrm{nc}}=\Delta_{\mathrm{nc}}^{(0)}\cdot e^{\tan^{-1}\left(\lambda_1^*\right)/h_1}\\ \sigma_{\mathrm{c}}=\sigma_{\mathrm{c}}^{(0)}\cdot e^{\tan^{-1}\left(\lambda_2^*\right)/h_2}\\ \theta_i=\left[\tan^{-1}\left(\lambda_{2i+1}^*\right)/\pi+0.5\right]\beta+\left[\alpha+(i-1)\beta\right],\ i=1,\cdots,\mu\ ,\\ x_i=\left\{\left[\tan^{-1}\left(\lambda_{2i}^*\right)/\pi+0.5\right](\overline{x}-\underline{x})+\underline{x}\right\}x_{i+1},\ i=1,\cdots,\mu\\ x_{\mu+1}=1\end{cases} \tag{4.20}$$

where $\lambda_j^*\in(-\infty,\ \infty)$, $j=1,\cdots,2\mu+2$, $\Delta_{\mathrm{nc}}^{(0)}$ and $\sigma_{\mathrm{c}}^{(0)}$ are initial guesses of Δ_{nc} and σ_{c}, respectively, h_1 and h_2 are parameters controlling the ratio of $\sigma_{\mathrm{c}}/\sigma_{\mathrm{c}}^{(0)}$ and $\Delta_{\mathrm{nc}}/\Delta_{\mathrm{nc}}^{(0)}$, respectively, $\overline{x}$ and $\underline{x}$ are the upper and lower bounds for x_i/x_{i+1}. In the examples, values of $h_1=h_2=\pi/8$, $\underline{x}=0.4$ and $\overline{x}=0.99$ are used. For these parameters, the bounds are $e^{-4}\Delta_{\mathrm{nc}}^{(0)}<\Delta_{\mathrm{nc}}<e^4\Delta_{\mathrm{nc}}^{(0)}$, $e^{-4}\sigma_{\mathrm{c}}^{(0)}<\sigma_{\mathrm{c}}<e^4\sigma_{\mathrm{c}}^{(0)}$ and $0.4x_{i+1}<x_i<0.99x_{i+1}$, $i=1,...,\mu$ Equation (4.19) is also satisfied. The coordinates of the control points can be computed as

$$\begin{cases}\mathbf{X}=\left\{0,\ x_1,\ \cdots,\ x_\mu,\ 1\right\}\Delta_{\mathrm{nc}}^{(0)}\\ \mathbf{Y}=\left\{1,\ x_1\cot\theta_1,\ \cdots,\ x_\mu\cot\theta_\mu,\ 0\right\}\sigma_{\mathrm{c}}^{(0)}\ .\end{cases}$$

To compute $\boldsymbol{\lambda}^{*(0)}$, an initial guess of $\boldsymbol{\lambda}^{(0)}$ is first made so that $\mathbf{X}$ and $\mathbf{Y}$ can be computed and then Equation (4.20) is solved for $\boldsymbol{\lambda}^{*}$

$$\begin{cases} \lambda_1^* = \tan\left[h_1 \ln\left(\Delta_{\mathrm{nc}} / \Delta_{\mathrm{nc}}^{(0)} \right) \right] \\ \lambda_2^* = \tan\left[h_2 \ln\left(\sigma_{\mathrm{c}} / \sigma_{\mathrm{c}}^{(0)} \right) \right], \\ \lambda_{2i+1}^* = \tan\left\{ \left[\dfrac{\theta_i - \left(\alpha + (i-1)\beta \right)}{\beta} - 0.5 \right] \pi \right\}, \; i = 1, \; \cdots \; , \mu \; , \\ \lambda_{2i+2}^* = \tan\left\{ \left[\dfrac{\left(x_i / x_{i+1} - \underline{x} \right)}{\left(\overline{x} - \underline{x} \right)} - 0.5 \right] \pi \right\}, \; i = 1, \; \cdots \; , \mu \end{cases} \tag{4.21}$$

which can be used to compute $\boldsymbol{\lambda}^{*(0)}$.

Pseudo-code: N-M solver (with parametric mapping):

- Set $\varepsilon = \varepsilon_0 > \varepsilon_T$, where ε is the error, and ε_T is the convergence measure
- $\boldsymbol{\lambda}^{(0)} \Rightarrow \mathbf{X}^{(0)}, \mathbf{Y}^{(0)}$, $\boldsymbol{\lambda}^{(0)} \in \left(\underline{\boldsymbol{\lambda}}, \overline{\boldsymbol{\lambda}} \right)$
- Apply Equation (14): $\mathbf{X}^{(0)}, \mathbf{Y}^{(0)} \Rightarrow \boldsymbol{\lambda}^{*(0)}$
- **while** $\varepsilon > \varepsilon_T$, **do**
- Apply Equation (13): $\boldsymbol{\lambda}^{*} \Rightarrow \boldsymbol{\lambda}$
- Use $\boldsymbol{\lambda}$ to construct CZM using LS, PCH or CBS interpolation
- Compute $\Phi\left(\boldsymbol{\lambda}^{*} \right)$ at simplex vertices
- Compute new $\boldsymbol{\lambda}^{*}$ (standard N-M algorithm)
- $\varepsilon \leftarrow \left\{ \left\| \boldsymbol{\lambda}^{*(n)} - \boldsymbol{\lambda}^{*(n-1)} \right\|_2 / \left\| \boldsymbol{\lambda}^{*(n-1)} \right\|_2, \; \left\| \Phi\left(\boldsymbol{\lambda}^{*(n)} \right) - \Phi\left(\boldsymbol{\lambda}^{*(n-1)} \right) \right\|_2 / \left\| \Phi\left(\boldsymbol{\lambda}^{*(n-1)} \right) \right\|_2, \; \Phi\left(\boldsymbol{\lambda}^{*(n)} \right) \right\}$
- **end while**
- Apply Equation (13): $\boldsymbol{\lambda}^{*} \Rightarrow \boldsymbol{\lambda}$, and construct the converged CZM

Finally, the pseudo-code illustrates the use of the mapping scheme in the N-M solver.

4.3.6 Barrier Functions and Regularization for Displacement-based Formulation

The particular shape regularization introduced in section 4.3.5 is implemented through parametric mapping, which avoids the explicit use of any constraint function or additional regularization terms in the objective function. However, the disadvantage of such implementation of the regularization is that it imposes too strong a (regularization)

condition on the parameter space such that the CZM shape at each iteration is strictly conforming to the desired condition. Moreover, such shape regularization through mapping is non-adaptive that it may totally fail in situations where the traditional regularization methods may succeed. While it may be effective for ideal input data, as will be illustrated in section 4.4, it may be too sensitive to perturbed data, i.e., noisy data, resulting in the instability of the method. The high sensitivity of the parametric mapping to noisy data will restrict its general application. The displacement-based formulation is more robust than the residual-based formulation [104]. Therefore, the widely used barrier functions and regularization techniques, which directly modify the objective function, are applied to the displacement-based formulation.

4.3.6.1 Barrier functions

The computation of the force vector $\hat{\mathbf{F}}^{\text{ext}}$ relies on a valid $\sigma\left(\Delta_{\text{n}};\boldsymbol{\lambda}\right)$ curve. The base-line requirements are $\sigma_i > 0$ and $0 < \Delta_{\text{n},1} < \Delta_{\text{n},1} < \ldots < \Delta_{\text{n},\mu+1}$ for the control points as mentioned in section 4.3.5. The former condition requires the cohesive stress to be a tensile (positive) stress. The latter condition is to avoid invalid snapback.

There is no direct mechanism in the N-M method to handle constraints. The parametric mapping is one technique to address the issue. Traditionally, barrier functions can be added to enable one to solve a constrained optimization problem using an unconstraint optimization method [105]. However, the commonly used barrier functions, while providing the option of applying a penalty as it approaches the infeasible domain, cannot prevent the N-M method from selecting a point in the infeasible domain. The barrier function must be extended to the complete infeasible domain. The non-increasing nature and the particular point-selection procedure of the N-M approach provide a possible implementation. To ensure the computed $\boldsymbol{\lambda}$ at each N-M iteration satisfies the condition $\sigma_i > 0$, consider the barrier function in the form

$$\beta_1\left(\boldsymbol{\lambda}\right) = \sum_i 10^{N_b\left(\theta_b - \sigma_i\right)/\theta_b} \quad , \tag{4.22}$$

where $0 < \theta_b << 1$, and $N_b >> 1$. Apparently, $\beta_1(\boldsymbol{\lambda})$ is negligible when $\sigma_i > \theta_b$ but becomes a sharply increasing barrier when $\sigma_i < \theta_b$. To satisfy the condition $0 < \Delta_{\mathrm{n},1} < \Delta_{\mathrm{n},1} < \ldots < \Delta_{\mathrm{n},\mu+1}$, the barrier function in a similar form to Equation (4.22) can be used

$$\beta_2(\boldsymbol{\lambda}) = \sum_i 10^{N_b\{[\xi_i - (1-\theta_b)]/\theta_b\}} \quad , \tag{4.23}$$

where

$$\xi_i = \left| \frac{\Delta_{\mathrm{n},i} - (\Delta_{\mathrm{n},i-1} + \Delta_{\mathrm{n},i+1})/2}{(\Delta_{\mathrm{n},i+1} - \Delta_{\mathrm{n},i-1})/2} \right| \tag{4.24}$$

is the normalized horizontal distance of point i from the midpoint of the adjacent two points $i-1$ and $i+1$. When $\xi_i < 1$, condition $\Delta_{\mathrm{n},i\text{-}1} < \Delta_{\mathrm{n},i} < \Delta_{\mathrm{n},i+1}$ is satisfied. Again, $\beta_2(\boldsymbol{\lambda})$ is negligible when $0 \le \xi_i < 1 - \theta_b$ but becomes a barrier when $\xi_i > 1 - \theta_b$. Incorporating barrier functions (4.22) and (4.23), the objective function is finally augmented to be

$$\Phi_u(\boldsymbol{\lambda}) = \left\| \left(\mathbf{u}^*(\boldsymbol{\lambda}) - \bar{\mathbf{u}} \right)^{\mathrm{T}} \right\|_2 + w_{\beta_1}\beta_1(\boldsymbol{\lambda}) + w_{\beta_2}\beta_2(\boldsymbol{\lambda}) \ , \tag{4.25}$$

where w_{β_1} and $w_{\beta 2}$ are the weighting factors. Now the constraints are embedded in the objective function. Notice that during any N-M iteration, infeasible points may still be evaluated. This is allowed by evaluating only the barrier functions in the objective function for the infeasible points, which will yield a very large objective function value. The parameters θ_b, N_b, w_{β_1} and $w_{\beta 2}$ are set so that the following condition is guaranteed

$$\Phi(\boldsymbol{\lambda}^{\text{infeasible}}) > \Phi(\boldsymbol{\lambda}^{\text{feasible}}).$$

If the initial guess of $\boldsymbol{\lambda}$ is feasible, the non-increasing nature of N-M method will always discard the infeasible points if encountered but select feasible points only.

The advantage of using barrier functions (4.22) and (4.23) lies in that they are continuous but they do not alter the feasible domain, as their values are very small in comparison to the original objective function in the feasible domain. Furthermore, due to the discrete nature of the N-M method for computation of the objective function value, penalty can be applied to the objective function by directly adding a relatively large number to the objective function for an infeasible point. The effect of using penalty technique is somehow equivalent to using the barrier function, but the difference is that when penalty value is directly added, the objective function loses continuity at the boundary between infeasible and feasible domains.

4.3.6.2 Shape regularization for CZM curve

It is well-known that most inverse problems are ill-posed, and therefore the uniqueness and stability of the solutions are not guaranteed [106]. The complexity of the parameter space is directly related to the number of control points used. Intuitively, the higher the dimension of the parameter space, the higher the possibility that more local minimum may be generated. The current inverse problem is further aggravated by the use of the spline constructed from control points. While the spline has the total flexibility in constructing any possible shape, the negative side of such flexibility is that the independent, freely moving control points may generate CZM curve without physical meanings. The possible situations that may hinder or fail the optimization are the formation of cluster, spike or tail points (Figure 4.7(a)). In either of these situations, one or more control points are trapped and become ineffective for the CZM shape construction. Numerical tests have shown the cluster and tail points are more frequently formed during the optimization process and many times the curve is locked to an apparently incorrect CZM representation.

If a polynomial functional is used to define CZM, such issue may not exist but the generality is also lost [107]. To overcome the ill-posedness due to such parameterization, regularization must be applied. Regularization involves introducing prior or additional information in order to solve an ill-posed problem effectively or efficiently. We notice the iterative nature of the nonlinear inverse problem. Therefore, simple algorithms with pre-defined criteria can be implemented to monitor the control points of the CZM curve

computed before each restarting of the N-M solver and detect if any of the adverse situation appears. The number of iterations is commonly selected from 50 to 150, which is based on the number of control points used. Usually more iterations are needed for more unknowns. The cluster points can be redistributed uniformly along the currently computed CZM curve, while the spike or tail points can be removed and additional control points can be added to other locations in the curve (see Figure 4.7(b)). After the control points are adjusted, the optimization is then restarted with a set of better-estimated and well-conditioned initial guess. Sometimes there is a jump in the objective function, which is associated to the restart operation. Numerical examples shown in reference [108] have demonstrated the efficient performance of such "*ad hoc*" regularization for various cases. The major advantage of this approach is that it does not need explicit regularization terms, therefore there is no difficult issue as how to choose the appropriate regularization weights. However, as current hybrid inverse technique may be extended to solve other inverse problems in fracture, the "ad hoc" method may not be applicable and the more general regularization methods, such as the most widely used Tikhonov regularization method, may have to be used. The investigation of the regularization effects is the immediate topic extending current study. The Tikhonov regularization is presented briefly here.

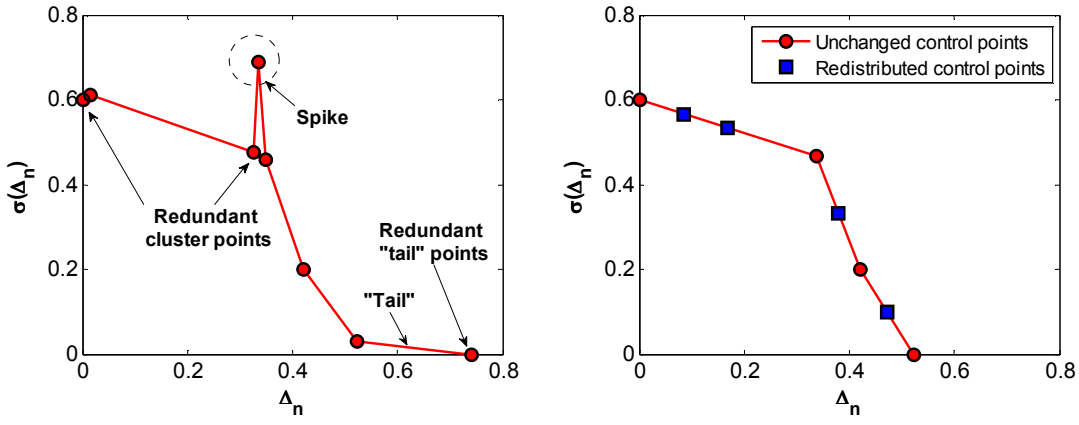

Figure 4.7: (a) Schematic illustrations of the cluster, spike and "tail" points possibly formed during the iterative optimization; (b) After the ill-positioned control points are redistributed

The Tikhonov regularization method in its general form is expressed as [109-112]

$$\Phi_u(\boldsymbol{\lambda}) = \left\| \left(\mathbf{u}^*(\boldsymbol{\lambda}) - \overline{\mathbf{u}} \right)^{\mathrm{T}} \right\|_2^2 + \gamma^2 \left\| \left(\sum_i \mathbf{L}^{(i)} \right) \boldsymbol{\lambda} \right\|_2^2, \tag{4.26}$$

where γ is the positive Tikhonov parameter, and $\mathbf{L}^{(i)}$ is a matrix represents the ith order derivative operator. Notice the square of the residual norm is used. The zero-order term tends to minimize the norm of the solution, the first-order term tends to reduce the fluctuation of the data and thus smooth the solution, higher-order terms impose further smoothing on the parameter space. Physically, a CZM curve shall be a smooth curve, which leads to the selection of the first and the second Tikhonov terms. However, the form shall be adapted as the CZM has two different physical quantities, the cohesive traction and the COD. Written explicitly, the first order smoothing term is

$$\psi_1(\boldsymbol{\lambda}) = \sum_i \left[\frac{\sigma_{i+1} - \sigma_i}{\Delta_{\mathrm{n},i+1} - \Delta_{\mathrm{n},i}} \right]^2, \; i = 1 \ldots \mu + 1, \tag{4.27}$$

and the second order term is

$$\psi_2(\boldsymbol{\lambda}) = \sum_i \left[\frac{\sigma_{i+2} - \sigma_{i+1}}{\Delta_{\mathrm{n},i+2} - \Delta_{\mathrm{n},i+1}} - \frac{\sigma_{i+1} - \sigma_i}{\Delta_{\mathrm{n},i+1} - \Delta_{\mathrm{n},i}} \right]^2, \; i = 1 \ldots \mu. \tag{4.28}$$

One additional term is included to penalize the forming of clustering points

$$\psi_3(\boldsymbol{\lambda}) = \sum_i \left[\frac{l_i}{\min(l_i)} \right]^2, \; i = 1 \ldots \mu + 1 \tag{4.29}$$

where l_i is the length between points $\left(\Delta_{\mathrm{n},i}, \sigma_i\right)$ and $\left(\Delta_{\mathrm{n},i+1}, \sigma_{i+1}\right)$. The complete form of the objective function becomes

$$\Phi(\boldsymbol{\lambda}) = \left\| \left(\mathbf{u}^*(\boldsymbol{\lambda}) - \overline{\mathbf{u}} \right)^{\mathrm{T}} \right\|_2^2 + \beta_1(\boldsymbol{\lambda}) + \beta_2(\boldsymbol{\lambda}) + \sum_{i=1}^{3} w_i \psi_i(\boldsymbol{\lambda}) \tag{4.30}$$

where w_i is the weighting factor for the regularization term.

The amount of regularization depends on the values of w_i [105,111]. The optimal value of w_i is usually determined by certain *ad hoc* methods in practical problems. One of the widely used approaches is the so-called *L*-curve method [111,113]: the computed $\left\| \left(\mathbf{u}^* - \bar{\mathbf{u}} \right)^{\mathrm{T}} \right\|_2^2$ can be plotted against $\psi_i(\boldsymbol{\lambda})$ as a curve parameterized by different values of w_i, which usually shows a characteristic *L*-shaped curve. The optimal value of w_i is then chosen at the corner of the *L*-curve. Since there are three regularization parameters to be optimized, significant numerical evaluation needs to be carried out before employing the routine application. Preliminary tests have shown the effectiveness of the regularization terms adopted. However, alternatively, a shortcut approach for the CZM curve regularization is adopted for the current investigation in order to verify the practical usefulness of the current hybrid inverse scheme.

4.4 NUMERICAL EXAMPLES: RESIDUAL-BASED OPTIMIZATION APPROACH

Figure 4.8 shows the geometry of the SENB specimen used in the numerical examples presented in this section. As synthetic data is used for the inverse problem, special attention is paid to the potential *inverse crime* [114], which has also been addressed by previous researchers [115-118]. Different discretization (meshes) for the direct and the inverse problems are used (Figure 4.9 and Figure 4.10). In addition, different solution methods are used for the forward problem (quasi-explicit solution scheme) and the inverse problem (optimization method). These two precautions conform to the suggestions provided in the book by Colton and Kress [114] and thus avoid the inverse crime.

4.4.1 Direct Problem

In the following examples, we consider the case of a linear elastic and isotropic material for the bulk with modulus of elasticity $E = 30$ GPa and Poisson's ratio $\nu = 0.3$. Figure 4.11 shows the specific power law CZM and hardening CZM used in the direct problem. For the power-law CZM, regular mesh (Figure 4.9) is used in the direct problem while irregular (i.e., unstructured) mesh (Figure 4.10) is used in the inverse problem. For

the hardening CZM, the irregular mesh is used in the direct problem while the regular mesh is used in the inverse problem.

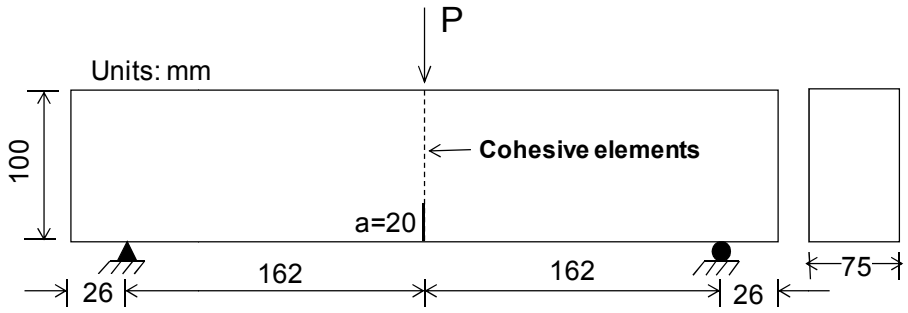

Figure 4.8: Geometry of the SENB and the test set-up

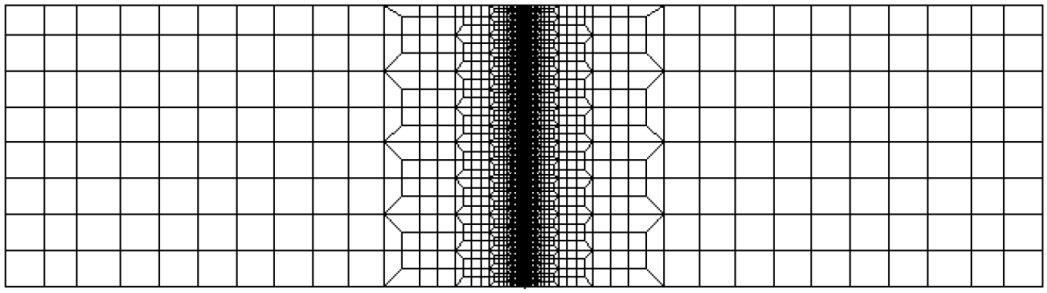

(a)

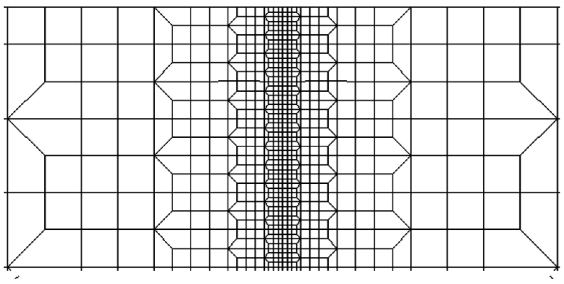

(b)

Figure 4.9: (a) FEM mesh (regular) for the entire geometry; (b) Close-up view of the mesh detail in the central region - CZM is implemented along the centerline

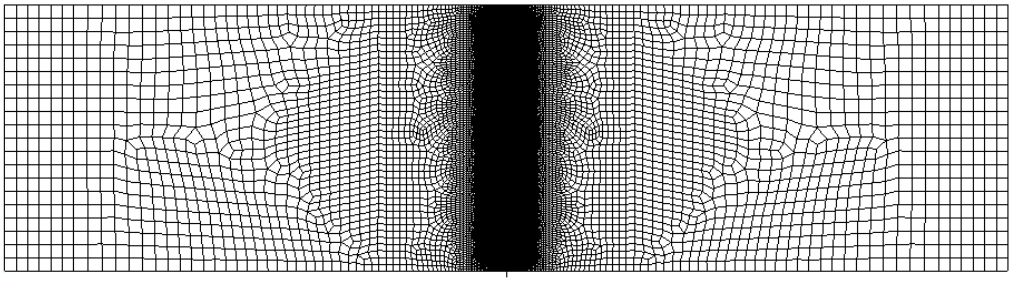

(a)

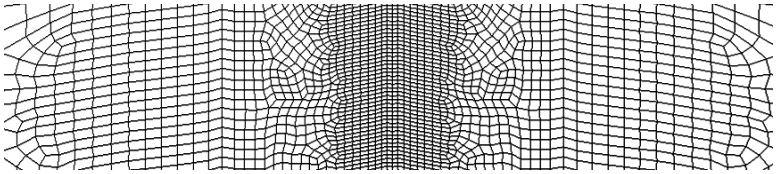

(b)

Figure 4.10: (a) FEM mesh (irregular) for the entire geometry; (b) Close-up view of the mesh detail in the central region - CZM is implemented along the center line

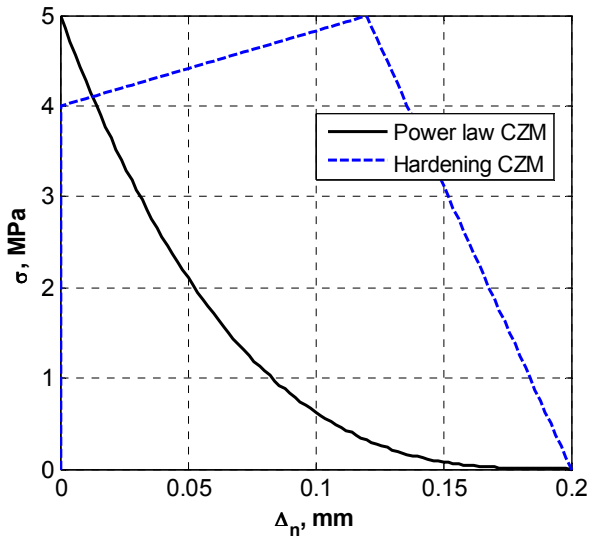

Figure 4.11: Power law and hardening CZMs used in the direct problem

The loading is displacement controlled. The maximum load-line displacement is 1.2 mm downwards, and 200 equally spaced loading steps are used. At maximum displacement, the crack tip propagates close to the top surface. The global responses, P versus CMOD, are shown in Figure 4.12. The areas under the P versus CMOD curves

divided by the area of crack surface can be used to estimate the fracture energy G_f, i.e. the area under the σ versus Δ_n curve. A value comparable to the maximum measured CMOD can also be used as an estimate of Δ_{nc}. If linear softening CZM (same as the power-law CZM with $\gamma = 1$) is used, then the critical stress is given by

$$\sigma_c = \frac{2G_f}{\Delta_{nc}}.$$

An initial guess of CZM is thereby obtained.

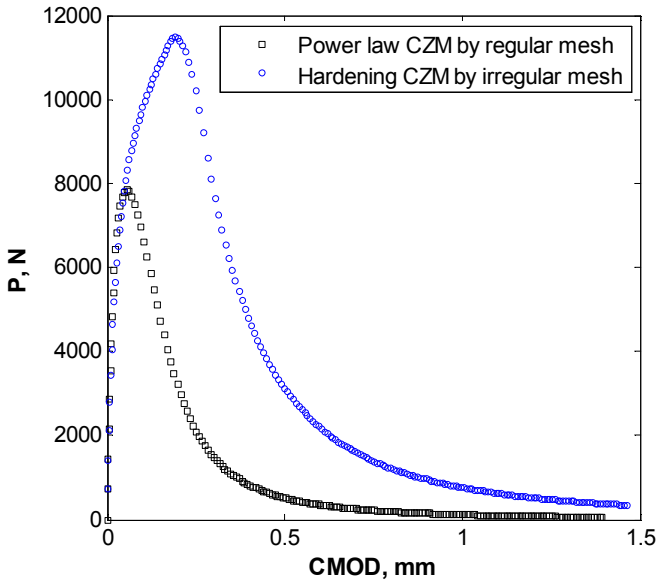

Figure 4.12: P versus CMOD curves for power law and hardening CZMs

4.4.2 Results of Inverse Problems

The N-M optimizations for the inverse problem are carried out to recover both the power-law and the hardening CZMs. For both cases, three initial guesses are investigated: one above, one below and one intersecting the target CZM (Figure 4.13). The one that intersects the correct CZM is estimated by the procedure described in Section 4.4.1 assuming $\Delta_{nc} = \text{CMOD}_{max}/2$. For each of these six cases, five interpolations are used:

LS interpolation with 3, 4 and 5 control points, PCH interpolation with 5 control points, and CBS interpolation with 5 control points. The initial guesses along with the computed CZMs for each case are presented in Figure 4.14 to Figure 4.19.

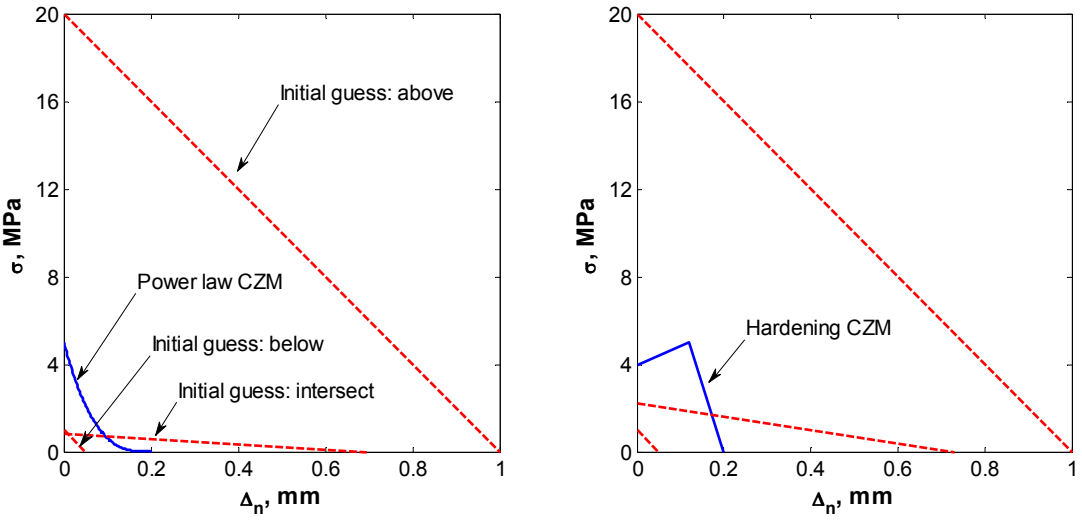

Figure 4.13: Three different initial guesses used in inverse computing both the power law and the hardening CZMs

In most cases, the computed CZM converges to the target CZM. The exceptions appeared when PCH or CBS are used with initial guesses intersecting the target hardening CZM (see Figure 4.19 (c3) and (c4)). Even though the computed CZM displays "tails" that are not present in the target CZM for the cases, the remaining parts of the curves still capture the correct hardening CZM shape quite accurately.

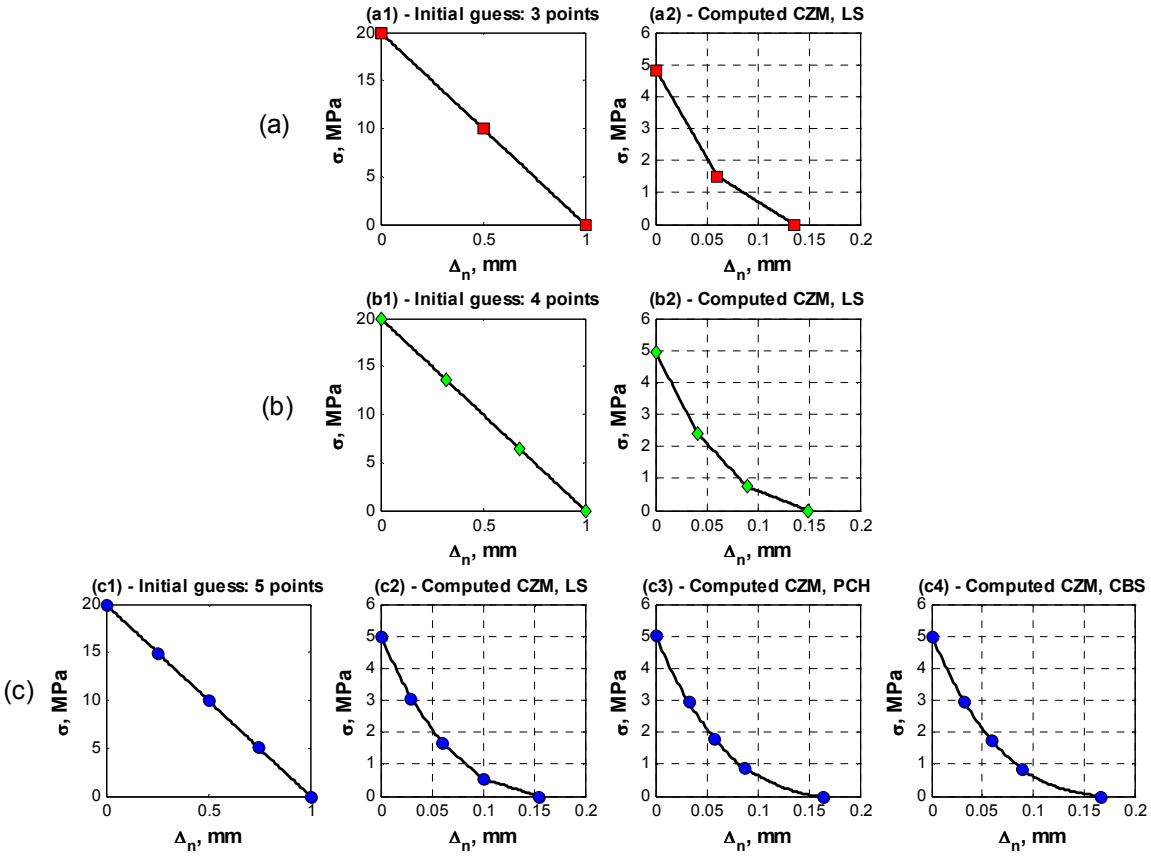

Figure 4.14: Computed power -law CZM with initial guess above the correct CZM: (a) three control points using LS interpolation; (b) 4 control points using LS interpolation; (c) 5 control points using LS, PCH and CBS interpolations

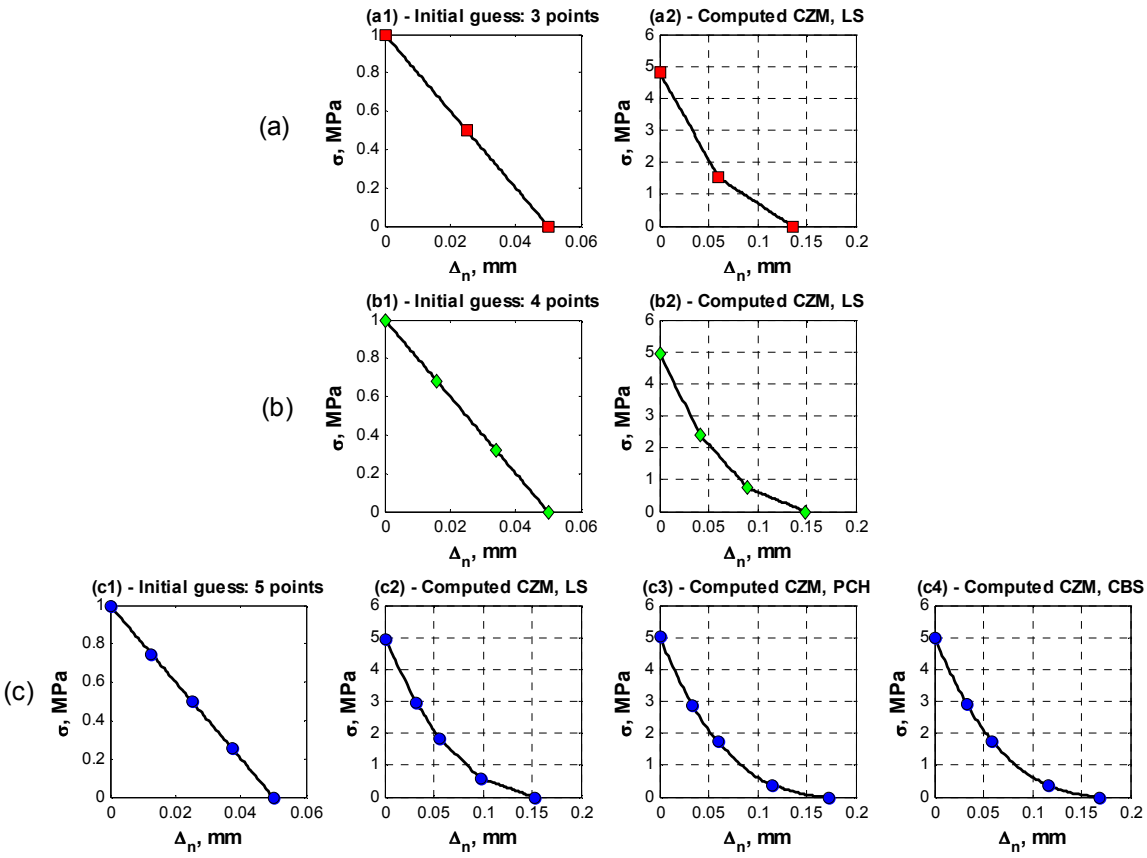

Figure 4.15: Computed power-law CZM with initial guess below the correct CZM: (a) three control points using LS interpolation; (b) 4 control points using LS interpolation; (c) 5 control points using LS, PCH and CBS interpolations

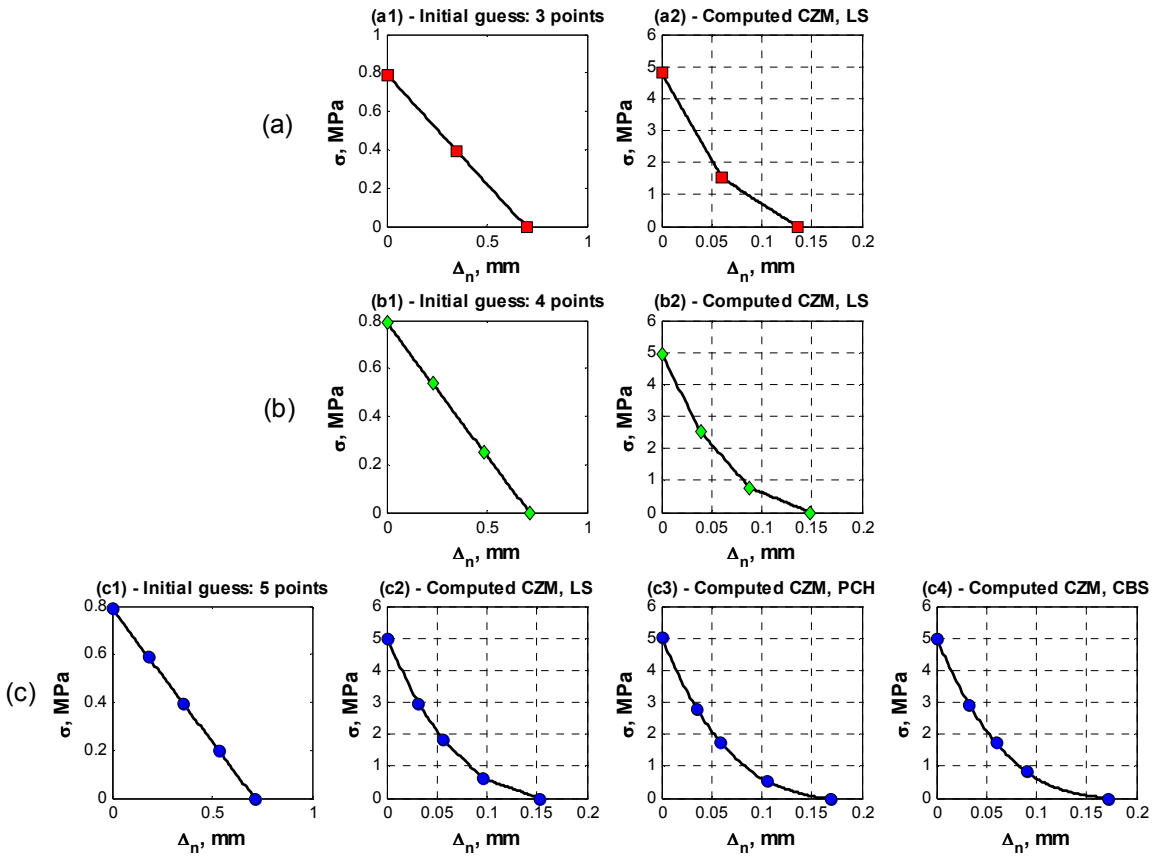

Figure 4.16: Computed power-law CZM with initial guess intersects the correct CZM: (a) three control points using LS interpolation; (b) 4 control points using LS interpolation; (c) 5 control points using LS, PCH and CBS interpolations

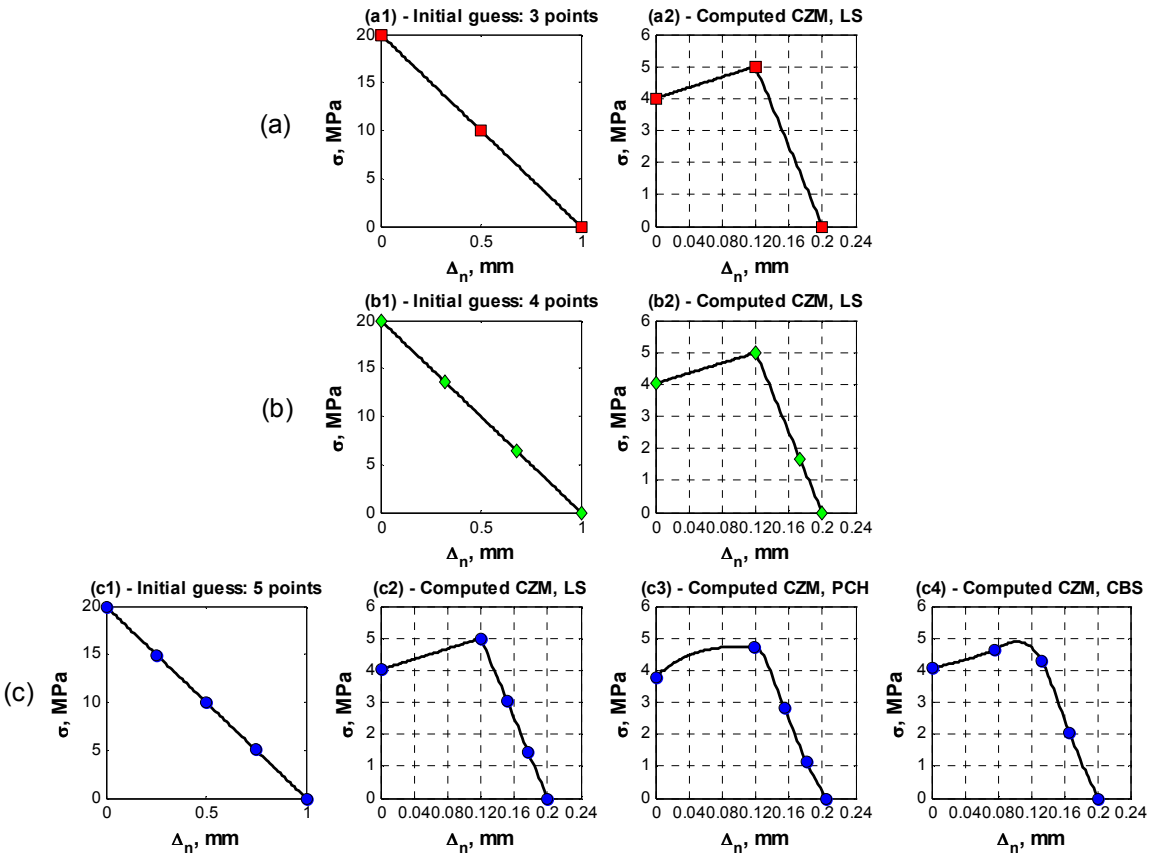

Figure 4.17: Computed hardening CZM with initial guess above the correct CZM: (a) three control points using LS interpolation; (b) 4 control points using LS interpolation; (c) 5 control points using LS, PCH and CBS interpolations

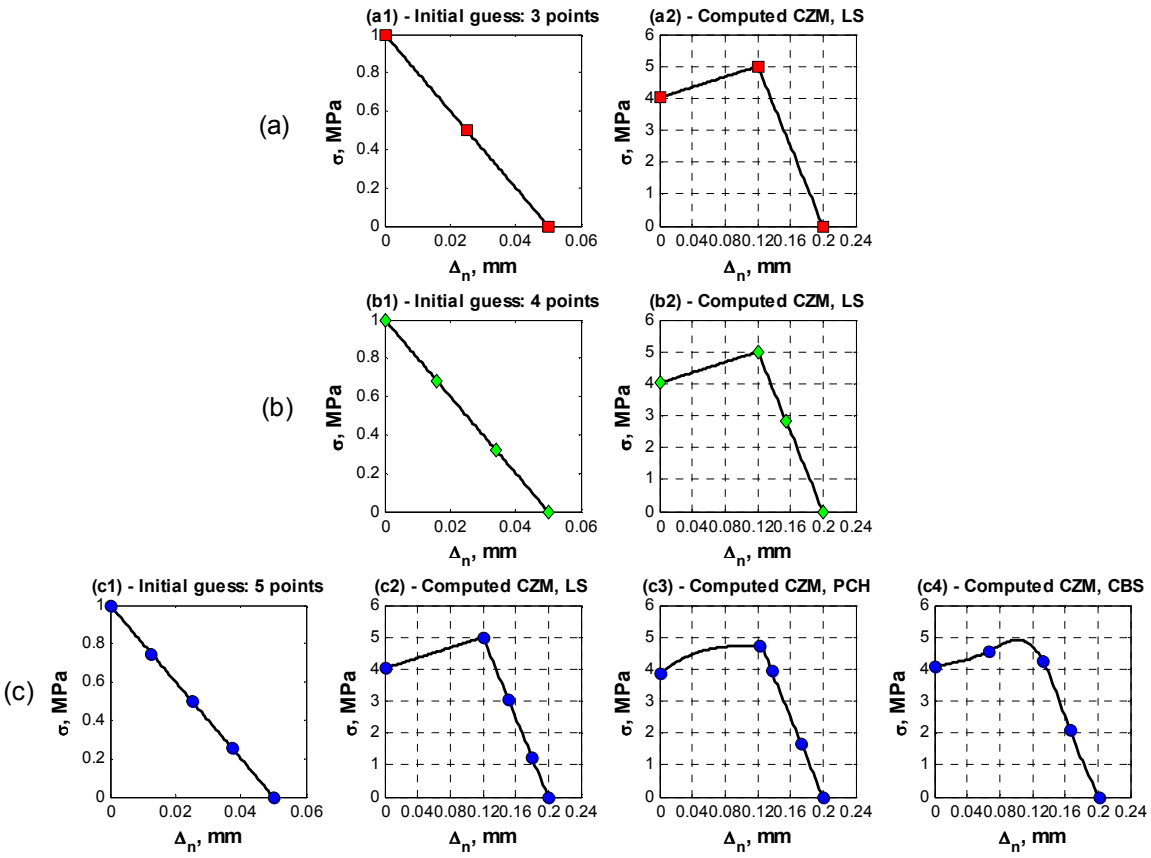

Figure 4.18: Computed hardening CZM with initial guess below the correct CZM: (a) three control points using LS interpolation; (b) 4 control points using LS interpolation; (c) 5 control points using LS, PCH and CBS interpolations

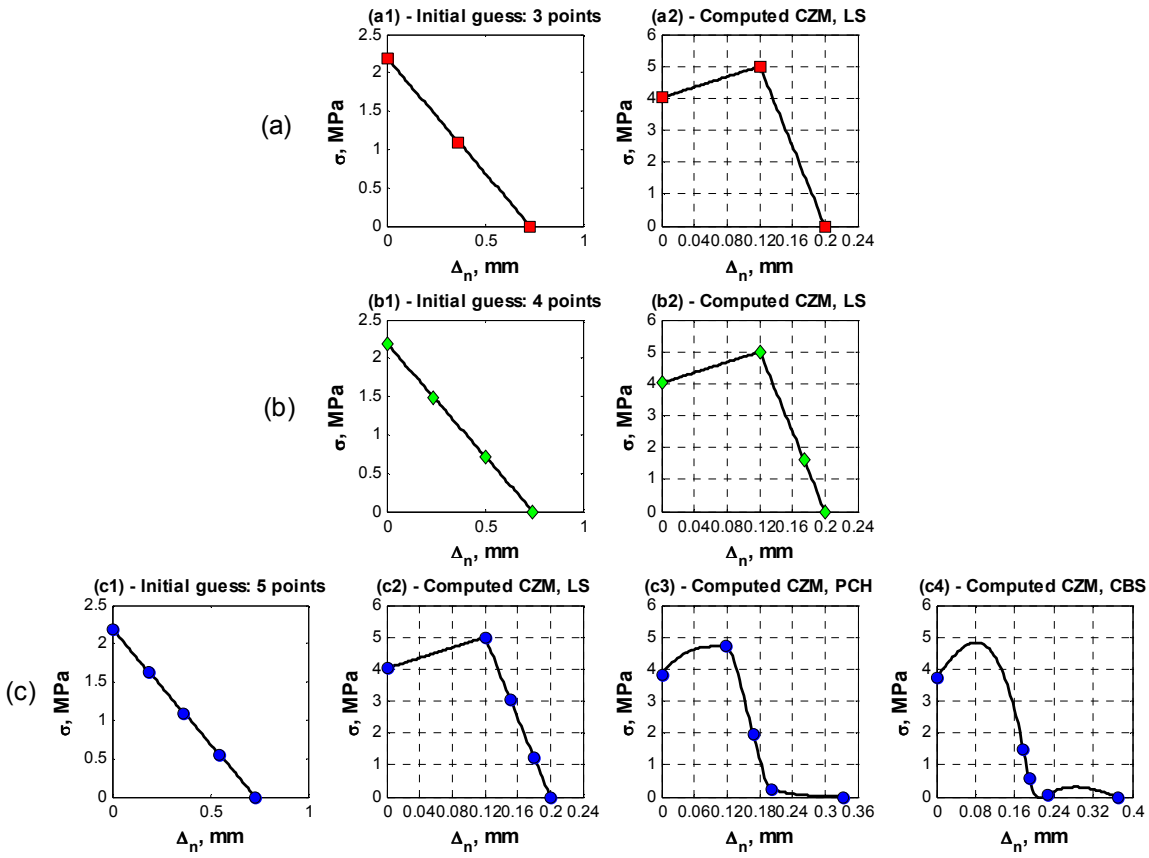

Figure 4.19: Computed hardening CZM with initial guess intersects the correct CZM: (a) three control points using LS interpolation; (b) 4 control points using LS interpolation; (c) 5 control points using LS, PCH and CBS interpolations

4.4.2.1 Effect of the number of control points

When using the LS interpolation, the calculated power-law CZM is most accurate if more control points are used (see plots (a2), (b2) and (c2) in Figure 4.14 - Figure 4.16). Also from these plots, the locations of the control points from different initial guesses are identical. Since the 3-point LS interpolation could recover exactly the shape of the hardening CZM, adding more points does not have additional benefit, as can be seen in plots (a2), (b2) and (c2) in Figure 4.17 through Figure 4.19. Comparing the computed CZM using the LS interpolation with 4 or 5 control points (see plots (b2) or (c2) in Figure 4.17 through Figure 4.19), one can see that the locations of additional points are

not exactly the same. In fact, as long as the additional points are on the exact curves, the solution is the same, leading to numerous solutions but the same interpolated CZM shape.

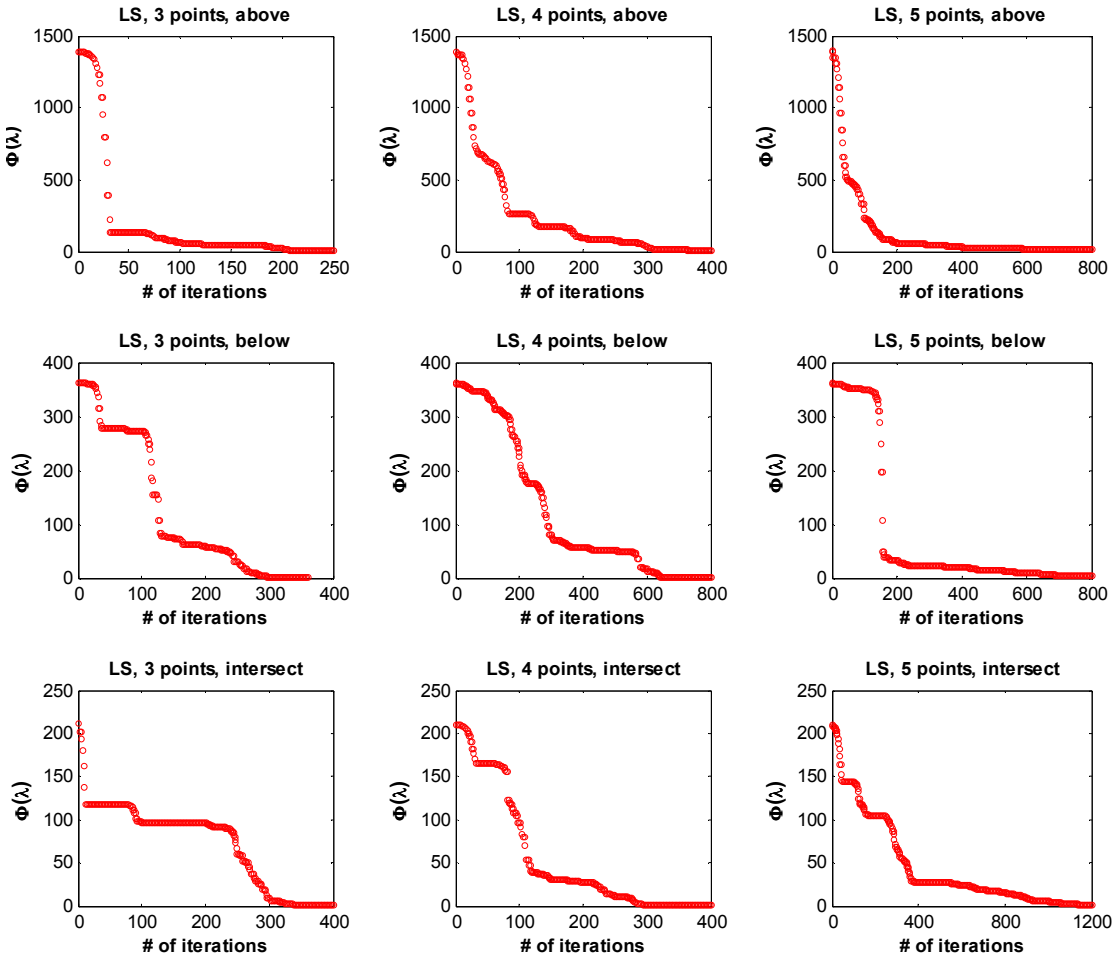

Figure 4.20: Evolution of objective function values for computing hardening CZM using linear spline interpolation but various number of control points and initial guesses

Figure 4.20 shows the evolution of the objective function value for different number of control points and initial guesses when the LS interpolation is used. The general trend is that more N-M iterations are needed to obtain the optimal result when more interpolation points are used. However, from the plots no particular evolution pattern can be concluded.

Figure 4.21 to Figure 4.23 shows a sequence of snapshots for the evolution of CZM using LS interpolation with 3, 4 and 5 control points. It can be seen that the mapping scheme constrains the relative location of control points effectively, which is especially apparent in the snapshots at point “2”, “3” and “4” of plot (b). Here we can see that the trend of snap-back of the curve is effectively suppressed.

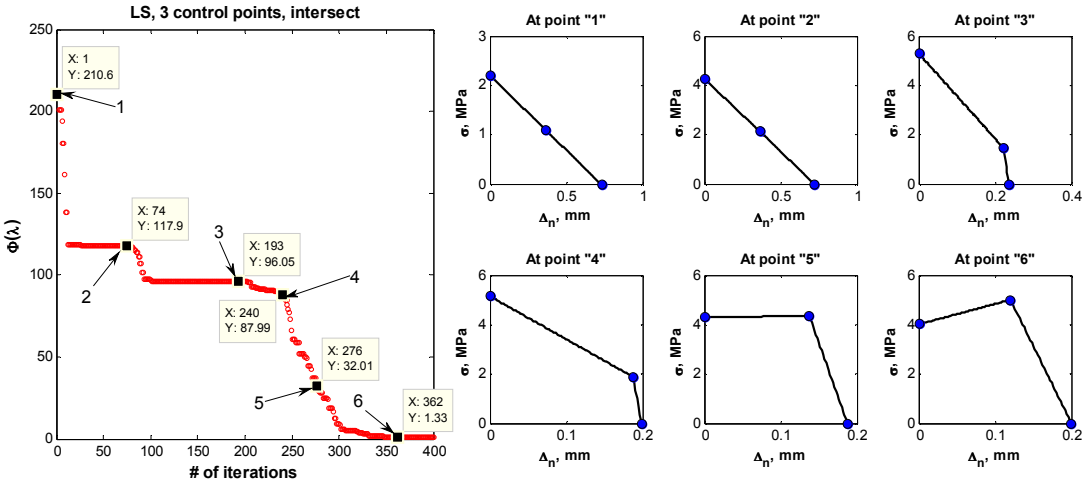

Figure 4.21: Evolution of computed CZM for computing hardening CZM using LS interpolations with 3 control points

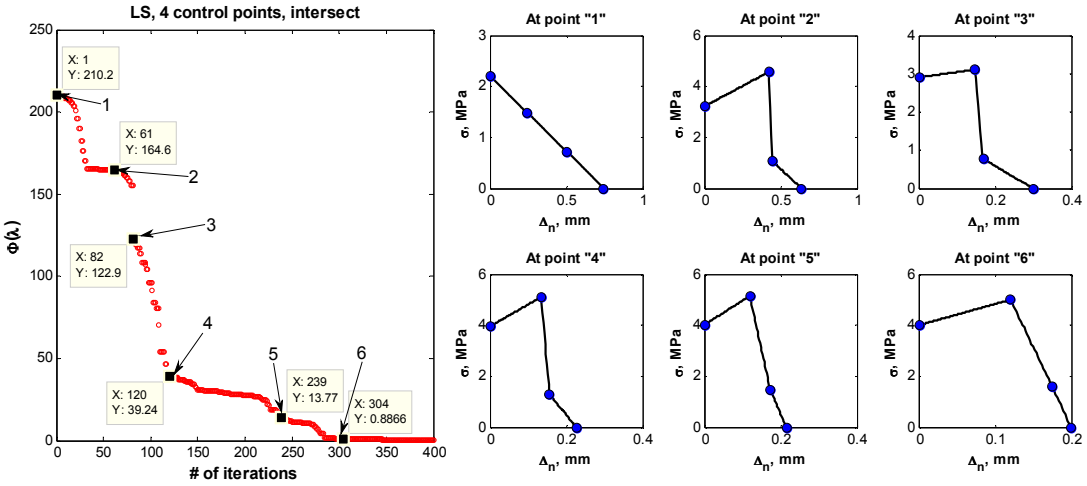

Figure 4.22: Evolution of computed CZM for computing hardening CZM using LS interpolations with 4 control points

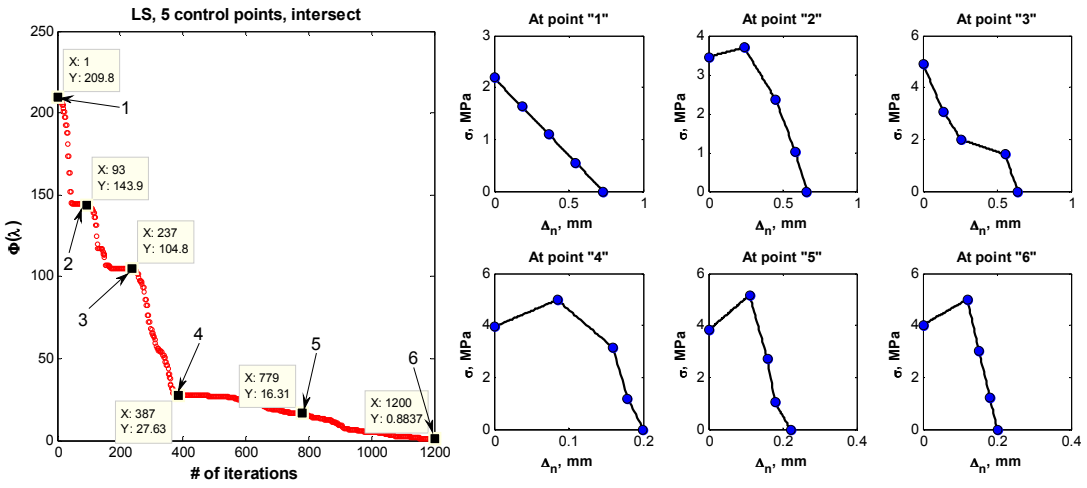

Figure 4.23: Evolution of computed CZM for computing hardening CZM using LS interpolations with 5 control points

4.4.2.2 Effect of different interpolations and initial guesses

Plots group (c) in Figure 4.14 through Figure 4.19 demonstrate that the quality of the result is influenced by the choice of the interpolation. For simple shape like the power-law CZM, all three interpolations work well, while for the hardening CZM, which has a sharp turning at the kink point, smooth CBS interpolation cannot capture the exact COD at peak load. In this case, the less smooth PCH interpolation yields better results compared to LS and CBS results.

Figure 4.24 shows the evolution of objective function values for different interpolations and initial guesses. From the plots, it seems that when initial guesses are either above or below the actual solution, the optimization proceeds more quickly with only one major drop in objective function value. This might be due to the fact that it is easier for points to expand and shrink together to maintain the proper shape. When the initial guess intersects the correct CZM, the optimization takes a few more major drops in objective function value. The computed CZMs by both PCH and CBS interpolations also display a "tail" (Figure 4.19 (c3) and (c4)). Due to errors introduced by the "tail", the values of $\Phi(\boldsymbol{\lambda})$ are 11.4 and 35.7 for PCH and CBS interpolations, respectively (see Figure 4.27 (b) and (c)), which are higher than all other cases for which $\Phi(\boldsymbol{\lambda}) \approx 1$ (see

Figure 4.23 (a)-(c) and Figure 4.27 (a)). This indicates that the residual may have a local minimum in the domain obtained by the current mapping and constraining scheme. Fortunately, the algorithm will not be trapped in this local minimum for most of the Furthermore, the major part of these two computed erroneous CZMs still capture the correct CZM except the "tailing". As all these cases all converge to the same CZM with a small objective function value, $\Phi(\boldsymbol{\lambda})$, it is confident that within the parameter space investigated, there is probably one global minimum of $\Phi(\boldsymbol{\lambda})$. However, before a mathematical proof can be provided, this statement is only a phenomenological conclusion.

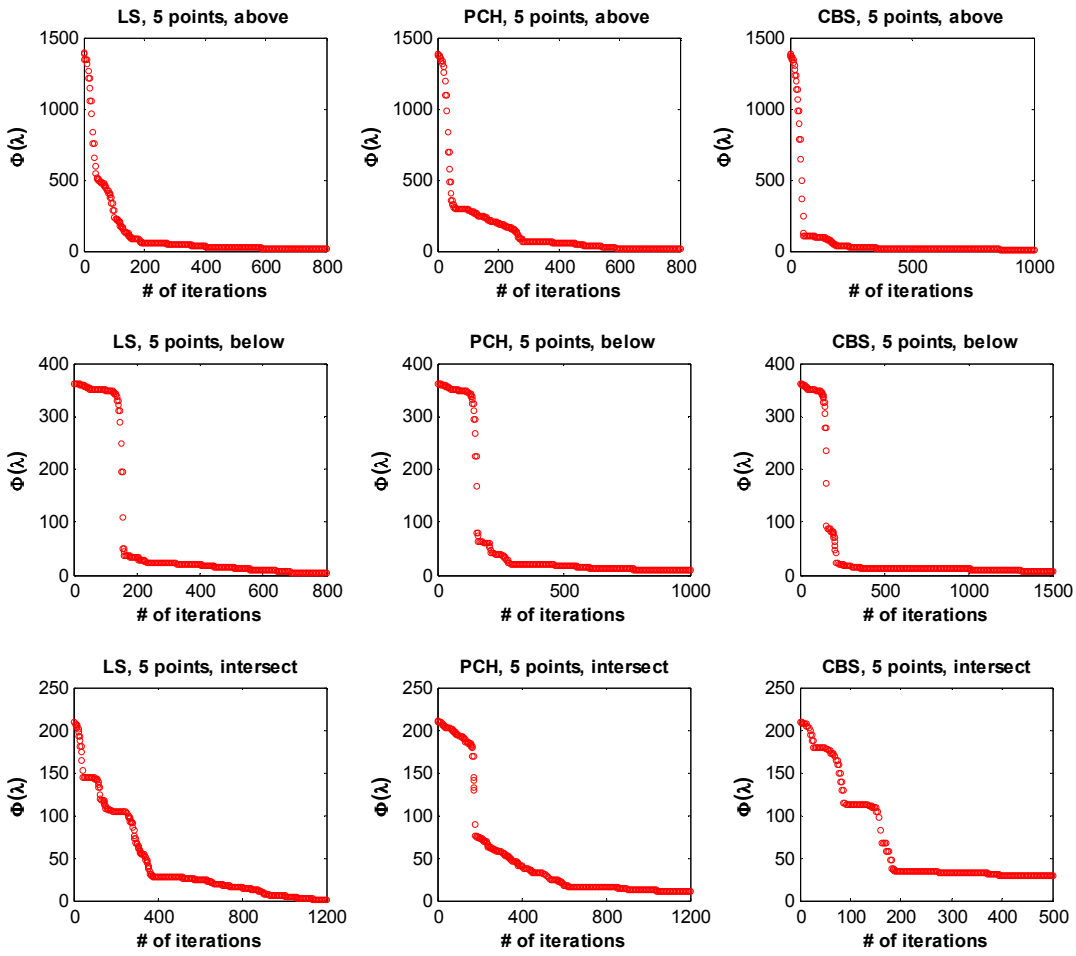

Figure 4.24: Evolution of objective function values for computing hardening CZM with 5 control points but various interpolations and initial guesses

Figure 4.25 to Figure 4.27 shows snapshots for the CZM evolution for the intersecting initial guess using LS, PCH and CBS interpolations. In the case of the less smooth PCH interpolation no erroneous shape appear during optimization, while the smooth CBS interpolation yields an unphysical CZM near the end of the optimization process.

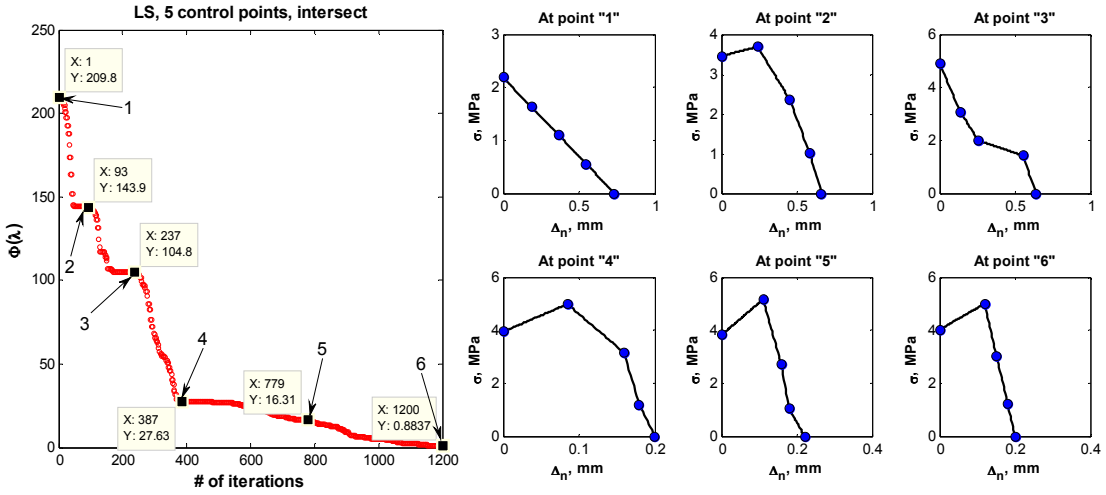

Figure 4.25: Evolution of computed CZM for computing hardening CZM using LS interpolation

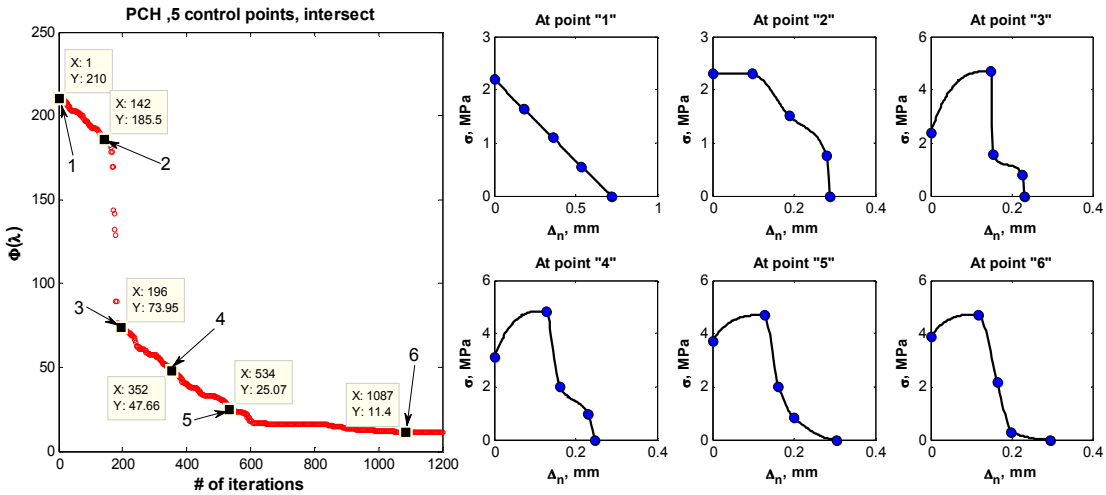

Figure 4.26: Evolution of computed CZM for computing hardening CZM using PCH interpolation

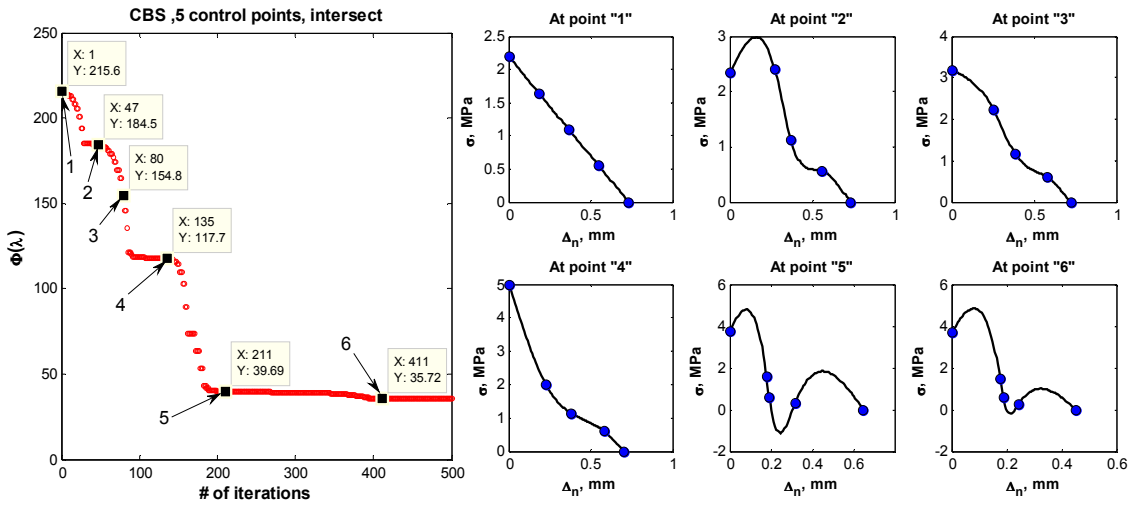

Figure 4.27: Evolution of computed CZM for computing hardening CZM using CBS interpolation

4.4.2.3 Systematic way of obtaining CZM in practice

Based on observations from numerical examples, a strategy is proposed for the inverse analysis for real problems. First, the fracture energy can be estimated from the measured P~CMOD curve. An initial guess using LS interpolation with 3 control points can be the initial step to quickly obtain the rough shape of the CZM. Several initial guesses (analogous to the three initial guesses used in the examples) can be tested to verify if they all converge to the same shape and to identify which initial guess is easier to converge to the target CZM. Sticking to the best possible initial guess location, one can gradually increase the number of control points until finding the sufficient number of control points for representing the shape of the target CZM. Finally, PCH or CBS interpolation can be used to obtain fine tuned smooth, maybe more accurate, CZM curve.

4.5 NUMERICAL EXAMPLES: DISPLACEMENT-BASED OPTIMIZATION APPROACH

4.5.1 FEM Model

Figure 4.28 shows the geometry of the SENB specimen for the numerical examples using displacement-based optimization. Again, the problem considered currently is in a

2D plane-stress condition. The bulk material is kept isotropic and linear elastic. Since the relative accuracy of the DIC measurement also depends on the stiffness of the bulk material, three modulus of elasticity are considered for current examples: E = 10 GPa, 30 GPa and 100 GPa. The Poisson's ratio is fixed as 0.2.

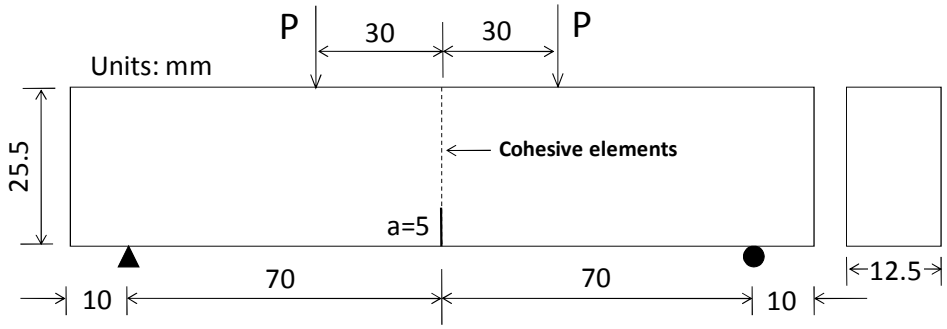

Figure 4.28: Geometry of the SENB and the test set-up

The subsequent analysis uses a two-dimensional (2D) FE model. Fine meshes are used to simulate the level of detail for the displacement field that could be obtained by the DIC technique. Figure 4.29 shows the mesh used for both the direct and inverse problems, where Q4 elements are utilized for the bulk material and the cohesive zone model is implemented for mode I fracture only. The size of the element (bulk material) along the crack surface is 0.0425 mm, which is fine enough to yield accurate crack propagation simulation.

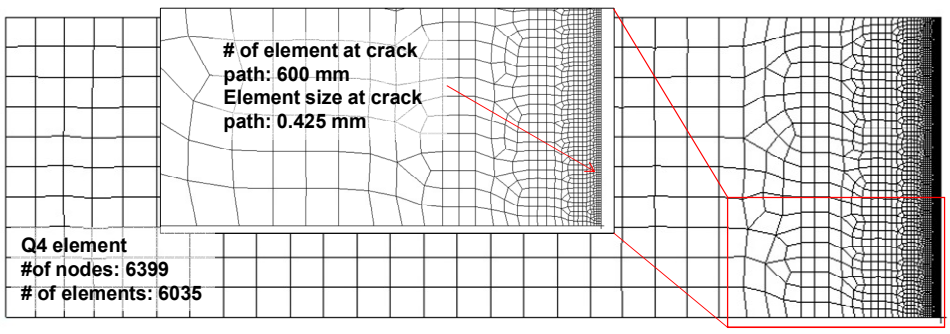

Figure 4.29: FEM mesh for the half of the geometry (due to symmetry)

4.5.2 Idealized CZMs

Idealized CZMs describing three representative behaviors are used (Figure 4.30): one with a linear softening behavior, one with a hardening then followed by a linear softening behavior and one with a power-law softening behavior. The linear CZM is appropriate for the high explosives [86], the power-law CZM is effective to simulate the fracture process of quasi-brittle concrete [119], while the hardening CZM may be used for some strong fiber reinforced composites [54,120].

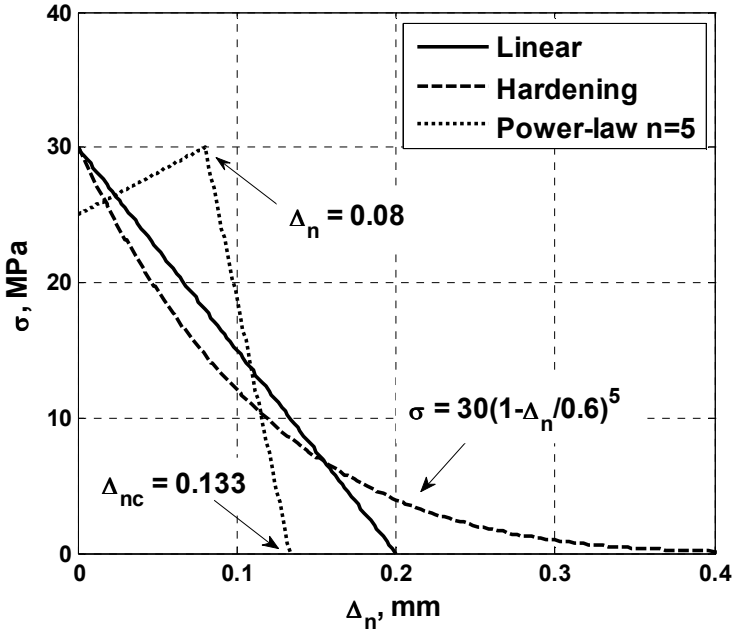

Figure 4.30: The mode I CZMs used in this study

4.5.3 Direct Problem

Five cases are simulated (Table 4.1), combinations of a particular modulus of elasticity of the bulk material and a CZM (Figure 4.30). Cases I, II and III compare the effect of different CZM shapes. Cases I, IV and V compare the effect of the bulk material stiffness.

Table 4.1: Five direct problem cases, combinations of CZM and modulus of elasticity

	Case I	Case II	Case III	Case IV	Case V
CZM	Linear	Hardening	Power-law	Linear	Linear
E of bulk material, GPa	30	30	30	10	100

4.5.3.1 Global responses

In the simulation, the loading is displacement controlled. The global responses, *P* versus CMOD and *P* versus load-line displacement δ, for cases I, II and III are shown in Figure 4.31 and Figure 4.32, respectively. One can see that the CZM shape affect the global response apparently around the peak load, while for the rest of the softening curves the curves are similar. An important implication is that numerical simulation that matches the initial and softening parts of the experimental global response curve does not prove that the right shape of CZM is obtained.

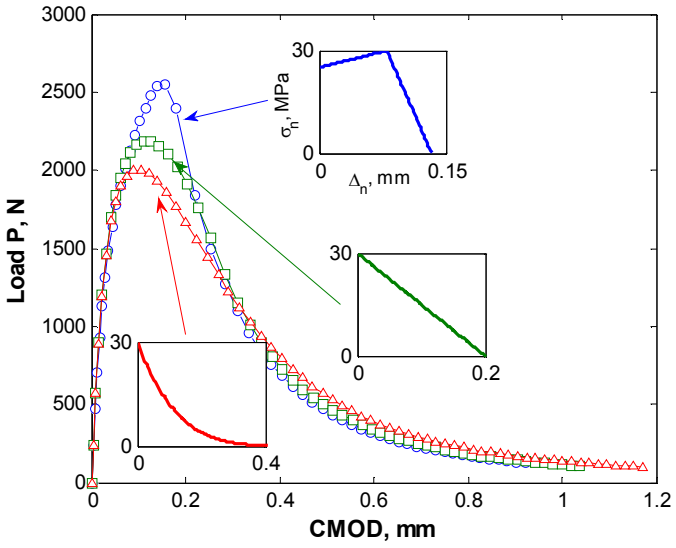

Figure 4.31: Load, P, versus CMOD curve for different (linear, power-law and hardening) CZMs, but the same bulk elastic modulus E = 30 GPa

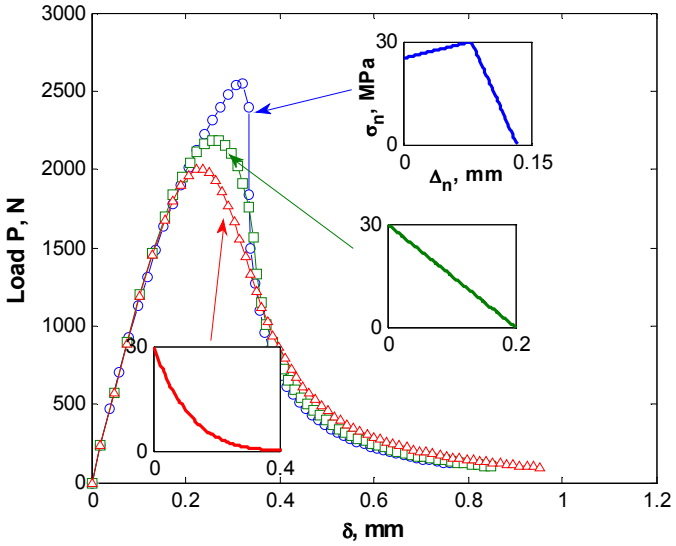

Figure 4.32: Load, P, versus load-line displacement, δ, curve for different (linear, power-law and hardening) CZMs, but the same bulk elastic modulus E = 30 GPa

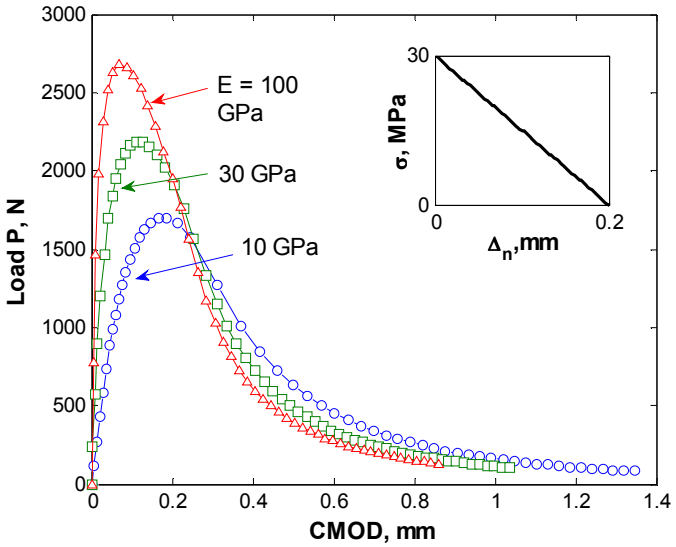

Figure 4.33: Load, P, versus CMOD curve for different bulk elastic moduli (E = 10, 30 and 100 GPa), but the same linear CZM

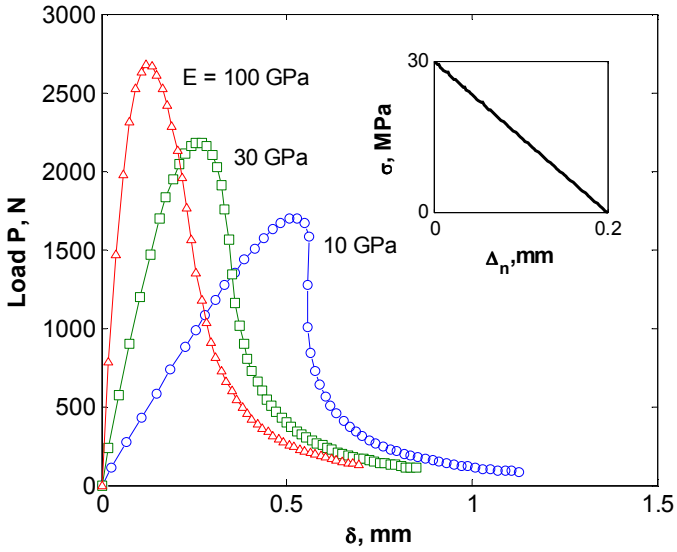

Figure 4.34: Load, P, versus load-line displacement, δ, curve for different bulk elastic moduli (E = 10, 30 and 100 GPa), but the same linear CZM

The areas under the P versus δ curves divided by the area of crack surface are used to estimate the fracture energy G_f, i.e., the area under the σ versus Δ_n curve. A value comparable to the measured CMOD (0.95 CMOD in our case) is used as an estimate of Δ_{nc}. The target CZM to be computed is first assumed to have linear softening curve, the critical stress is then given by

$$\sigma_c = \frac{2G_f}{\Delta_{nc}}.$$

An initial guess of CZM, equivalently the unknown set of parameters $\boldsymbol{\lambda}$, is thereby obtained.

4.5.3.2 Formation of cohesive zone

The load level where the complete cohesive zone forms is important for the inverse problem. The DIC image should be taken at a load level that provides complete information of the cohesive zone for the inverse analysis. It has been demonstrated by Kyoungsoo *et al.* [121] that the complete cohesive zone may not form at peak load level but rather at a post-peak load level. In their study, a bilinear softening CZM is used for

the mode I fracture of concrete. To estimate the critical load levels where the complete cohesive zone forms for the examples in this study, the cohesive stress distribution can be plotted along the crack path and direct inspection can provide the estimation. In the following, qualitative estimations for the threshold load levels are made for Case I and Case II, which refer to the linear CZM and the hardening CZM, respectively, as shown in Table 4.1.

Figure 4.35 illustrates the formation of cohesive zone for Case I. In the figure, the cohesive stress profiles are plotted along the crack at pre-peak load, peak load, and post-peak load levels. The crack is located from x = 5.5 mm to x = 25.5 mm. Figure 4.36 illustrates the formation of cohesive zone for Case II. When the COD at initial crack tip reaches the crack separation, Δ_{nc}, the corresponding traction at initial crack tip drops to zero. At this moment, a complete cohesive zone first forms behind the initial crack tip. From both figures, it can be seen only at load level "C" does the complete cohesive zone forms. For linear CZM, this point corresponds to 70% of the post-peak load level, while for hardening CZM, the threshold is at about 80% of the post-peak load level. Therefore, displacement data at a post-peak load level shall be used in the inverse analysis.

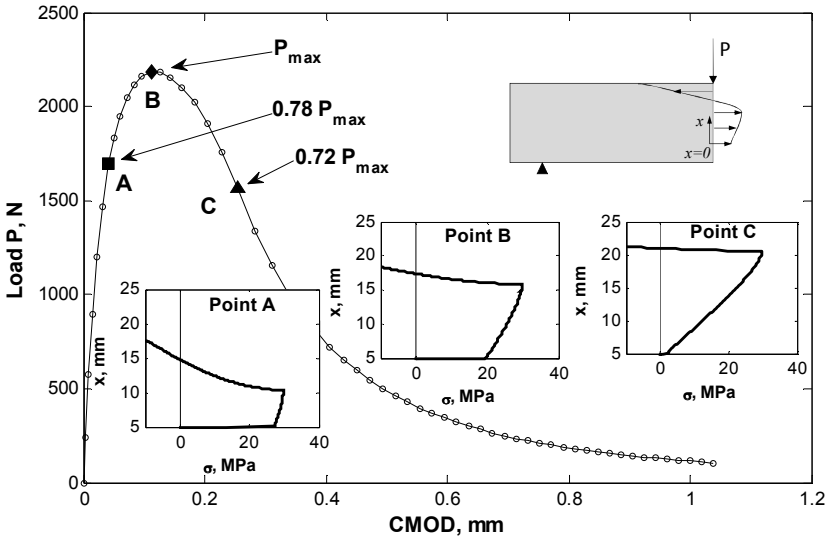

Figure 4.35: Illustration of the formation of cohesive zone for Case I (linear CZM of Table 4.1) at different points: at pre-peak load level "A", at peak load level "B", and at post-peak load level "C"

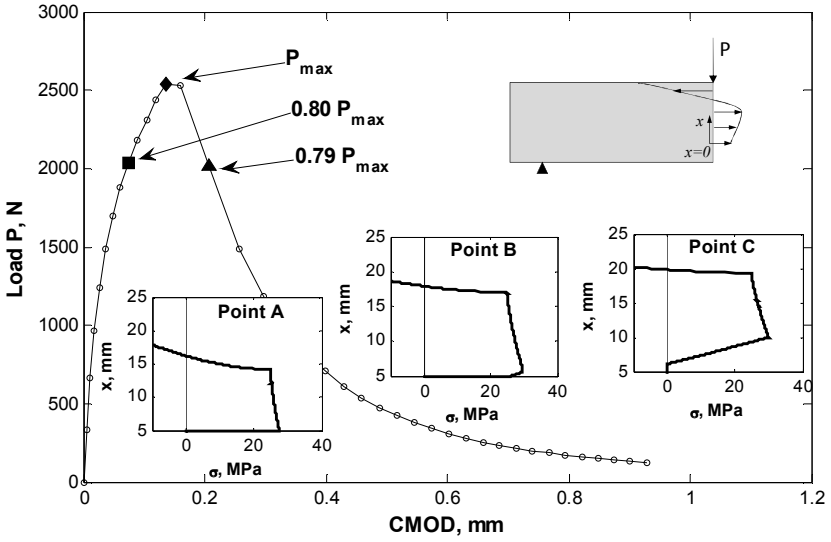

Figure 4.36: Illustration of the formation of cohesive zone for Case II (hardening CZM of Table 4.1) at different points: at pre-peak load level "A", at peak load level "B", and at post-peak load level "C"

4.5.4 Errors for the Displacement Field

Obtaining CZM properties requires high precision measurement for at least the complete profile of crack opening displacement, which can be part of the whole displacement field obtained by, e.g., DIC technique. However, noisy data is the real outcome of any experimental measurement. Therefore, we need to take into account the possible measurement errors in the inverse procedure to compute CZM. The nature of the errors, e.g., random or systematic, and the magnitude of the errors can be estimated from their sources. For the current study, it is assumed that the displacement field is measured by DIC technique and the primary sources of errors are from the digital image resolution and the DIC algorithm. Actually, DIC is an optical technique and its resolving power depends both on the correlation algorithm and the image acquisition device. Usually the quality of a digital image can be guaranteed with modern CCD (charge-coupled device) or CMOS (complementary metal–oxide–semiconductor) cameras. High CCD or CMOS sensor resolution, together with high magnification lenses, are able to achieve a resolution in the scale of $10^0 - 10^2$ microns/pixel. This is the base-line resolution, or maximum error, if displacement is directly obtained from the image. Resolution of DIC

software is measured as a fraction of pixels. It has been reported [92] that DIC can obtain a sub-pixel precision of 0.005 pixel or even higher [61]. The combined resolving power of high image resolution and high precision DIC algorithm can reach 10^{-2}-10^{0} microns/pixel. The most popular DIC algorithm is based on subset cross correlation; the displacements measured at all points are independent of each other. The errors can be assumed to be randomly and normally distributed.

For the current inverse procedure, we introduce errors by only considering the DIC resolution since the displacement error from digital image itself never exceeds one pixel. Assume a moderate image resolution of 1000 pixels along the specimen height, which corresponds to 0.0254 mm/pixel. We then introduce three levels of errors by specifying different maximum error magnitude (Table 4.2).

Table 4.2: Different levels of errors added to the synthetic displacement field

Image resolution, mm/pixel		DIC resolution, pixel		Maximum absolute error, mm	Estimated standard deviation or errors, mm	Comments on the errors
0.0255	×	No error	=	0	0	ideal
0.0255	×	0.005	=	1.28×10^{-4}	$7.2 – 7.4 \times 10^{-5}$	accurate
0.0255	×	0.05	=	1.28×10^{-3}	$7.2 – 7.4 \times 10^{-4}$	moderate
0.0255	×	0.2	=	5.1×10^{-3}	$2.9 – 3.0 \times 10^{-3}$	coarse

In Table 4.2, the case with no errors serves as the control case. The standard deviation of the introduced errors is estimated based on a population of 5,000 random data. The errors added are all between the interval of negative and positive maximum error. The mean value of the errors is zero. The comments on the errors are our subjective judgment based on reported accuracy of DIC. The moderate error level is reasonable and can be easily achieved for well-control experiments.

4.5.5 Results of Inverse Analysis

The specified errors in Table 4.2 are added to the displacement field taken at 60% of the peak load for all five cases listed in Table 4.1. The weights in Equation (4.25), w_{β_1} and w_{β_2}, are taken as unit for all the examples. Due to the random nature of the errors,

each case with a specified level of noise has been repeated two more times to see the variance. In all cases, four control points are used to construct the CZM.

there are six unknown parameters to determine in the optimization procedure. Four control points are sufficient for “imaginable” CZM shape. The initial guess of the CZM is estimated from the method described in section 4.4.1. Linear spline interpolation is used for the CZM.

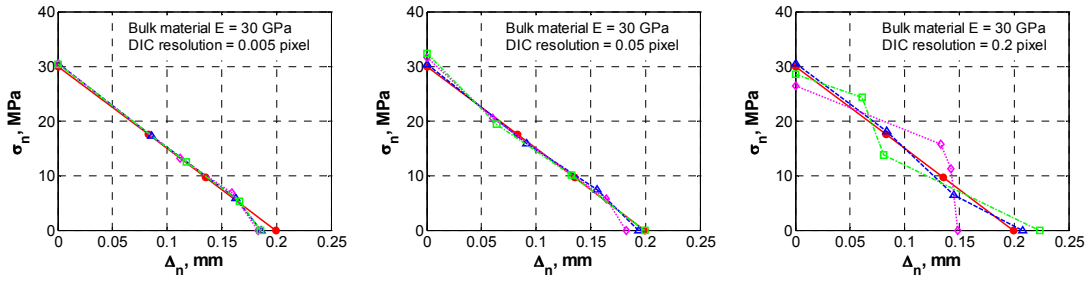

Figure 4.37: Computed CZMs for the Case I with different error levels applied. Each case is repeated three times. The solid circle with solid line is the computed CZM for the ideal case (without errors)

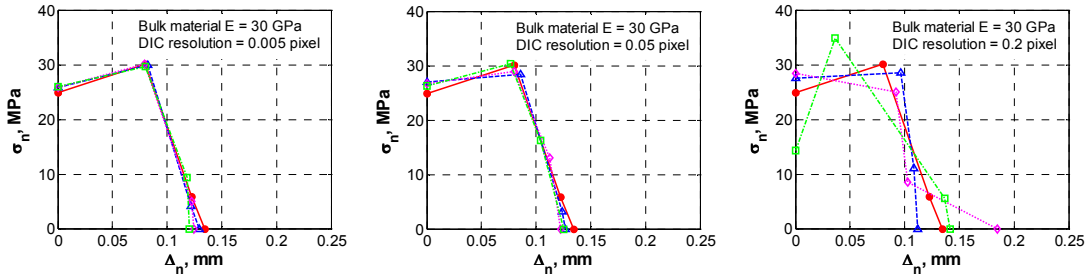

Figure 4.38: Computed CZMs for the Case II with different error levels applied. Each case is repeated three times. The solid circle with solid line is the computed CZM for the ideal case (without errors)

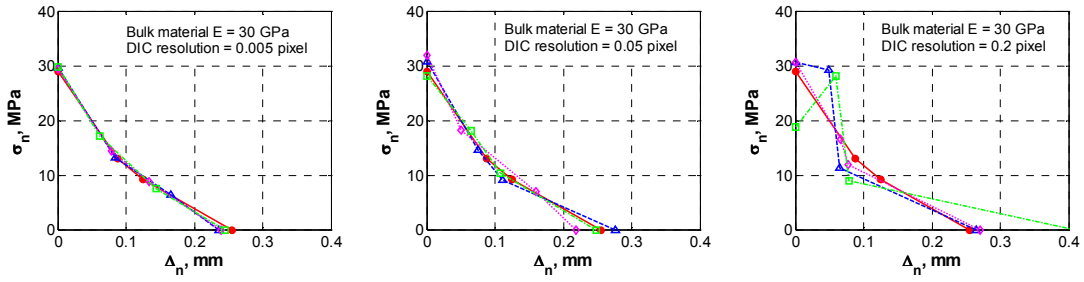

Figure 4.39: Computed CZMs for the Case III with different error levels applied. Each case is repeated three times. The solid circle with solid line is the computed CZM for the ideal case (without errors)

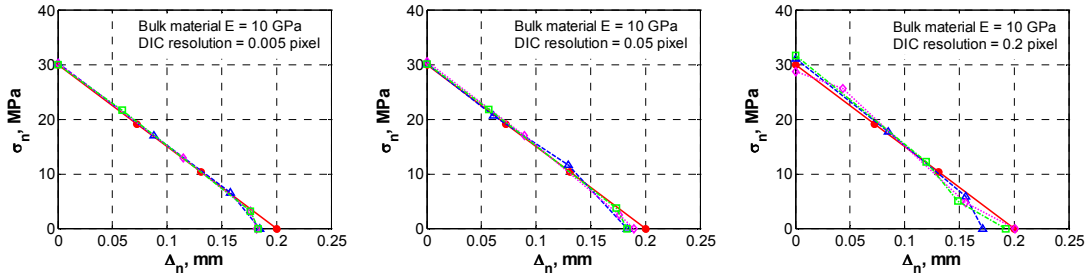

Figure 4.40: Computed CZMs for the Case IV with different error levels applied. Each case is repeated three times. The solid circle with solid line is the computed CZM for the ideal case (without errors)

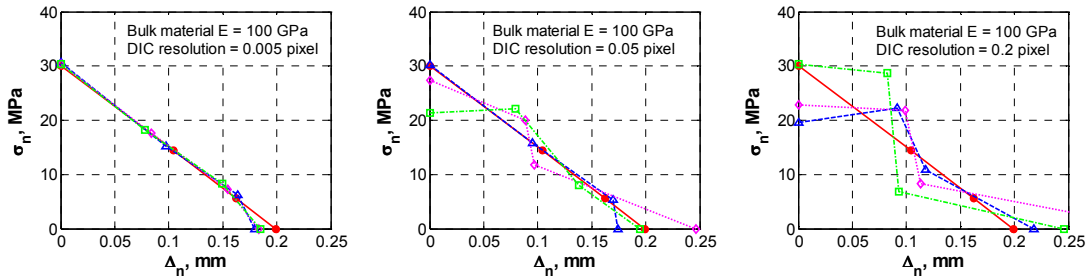

Figure 4.41: Computed CZMs for the Case V with different error levels applied. Each case is repeated three times. The solid circle with solid line is the computed CZM for the ideal case (without errors)

Figure 4.37 to Figure 4.41 show the computed CZMs for all cases (Table 4.1) with different error levels applied. The effects of the bulk material stiffness, the different CZMs and the different error levels are compared. The computed CZM for the case without error is identified in all sub figures as the solid line with solid circular markers.

For the case of bulk material E = 30 GPa, the computed CZMs of all three types (linear, hardening and power-law) are satisfactory up to an error level = 0.05 pixel. At error level = 0.2 pixel, the computed CZMs are significantly off the exact solution. When the bulk material is E = 10 GPa, the computed CZMs are acceptable up to 0.2 pixel error level. In fact, the relative error level with respect to the absolute displacement measurement for the case of E = 10 GPa with error level = 0.2 pixel is similar to that obtained the case of E = 30 GPa with error level = 0.05 pixel. For a bulk material E = 100 GPa, apparently, the relative error is about 3.3 times of that for E = 30 GPa for the same absolute error. Therefore, the bulk material with E = 100 GPa is much less tolerable to errors, as can be seen for the significant deviation of computed CZMs from the exact one when error level = 0.05 pixel.

Table 4.3 shows the initial and final values of objective functions and the number of iterations. For those cases with errors, the data are the averages of three repetitions. The table shows that as the error level increases, both the initial and the final values of objective function increase. The final objective function value does not indicate whether the computed CZM converges to the correct solution or not. For example, for the case of a bulk material with E = 10 GPa at error level = 0.2 pixel, the average final objective function value is 297.3, which is the largest among all cases, yet it still yield the correct CZM. While for the case of bulk material E = 100 GPa at error level = 0.05 pixel, the average final objective function value is 55.6, which is moderate among all cases, but the computed CZMs are not close to the correct solution.

Table 4.3: Initial and final values of objective function and number of iterations for all cases. The data for all cases with errors are the averages of three repetitions.

Bulk material elastic modulus	Target CZM	Peak error level (DIC resolution)	$\Phi\left(\boldsymbol{\lambda}^{(0)}\right)$	$\Phi\left(\boldsymbol{\lambda}^{(n)}\right)$	# of iterations
30 GPa	Linear	0	1562.0	1.0	408
		0.005	1647.4	34.5	307
		0.05	1656.6	55.2	342
		0.2	1732.8	149.0	250
30 GPa	Hardening	0	1139.4	1.6	826
		0.005	1245.3	42.1	590
		0.05	1288.2	70.1	435
		0.2	1331.2	147.3	390
30 GPa	Power-law	0	2413.9	5.5	522
		0.005	2535.1	31.1	349
		0.05	2546.6	47.1	293
		0.2	2601.8	154.0	242
10 GPa	Linear	0	2340.8	0.8	261
		0.005	2425.1	82.7	365
		0.05	2461.5	99.5	364
		0.2	2685.4	297.3	240
100 GPa	Linear	0	926.4	0.7	422
		0.005	988.9	19.8	346
		0.05	1054.1	55.6	283
		0.2	1009.2	170.3	214

Note: $\boldsymbol{\lambda}^{(0)}$ is initial guess and $\boldsymbol{\lambda}^{(n)}$ is the converged result. The convergent criteria is set as $\left(\Phi\left(\boldsymbol{\lambda}^{(n-100)}\right)-\Phi\left(\boldsymbol{\lambda}^{(n)}\right)\right)\Big/\Phi\left(\boldsymbol{\lambda}^{(n-100)}\right) < 0.01$.

4.5.5.1 Displacement data at different load levels

At high error levels, each individual inverse analysis converges to an inaccurate CZM. Using a few data sets of the same case enhances the estimation of the computed CZM. For example, one would naturally choose to estimate the CZM using all three repetitions for cases of bulk material E = 30 GPa at error level = 0.2 pixel or bulk material E = 100 GPa at error level > 0.05 pixel shown in Figure 4.39. In practice, this can be done by taking several DIC measurements at the same loading and using the average of the computed CZM from each measurement. Another way, which may be more preferable and may give more confidence, is to use the DIC measurement at several loadings. As a demonstration, we use the displacement field taken at 40%, 60% and 80%

of the peak load at post-peak regime. All five cases (Table 4.1) are applied an error level = 0.1 pixel. Figure 4.42 shows the result.

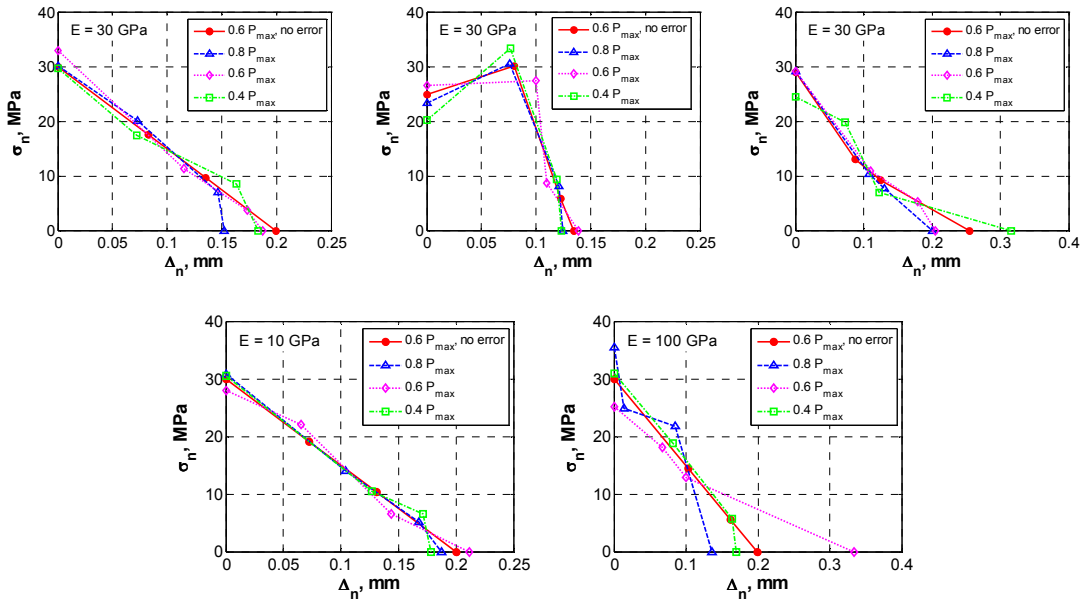

Figure 4.42: CZMs computed using displacement field taken at different post-peak loadings. An error level = 0.1 pixel is applied to all cases

As shown in Figure 4.42, the exact CZM is close to the average of the computed CZMs from displacement data with errors, even for the case of bulk material E = 100 GPa.

4.5.5.2 Other numerical aspects

Some other features of the proposed optimization scheme are: (1) the initial guess of CZM for the optimization; (2) the number of control points defining the CZM; (3) the interpolation used for constructing the CZM; (4) the aid to optimization. In previous sections, the presented results are all determined by using four control points and linear splines as interpolant, the initial guesses of the CZM are all estimated by using P versus δ curve, which is not far from the exact solution. For a further demonstration of the effectiveness of the proposed inverse procedure, four cases are presented (corresponding to different initial guesses) as outlined in Table 4.4. For these four cases, we use six

control points to illustrate the more flexible shape representation, although this is more than enough for the current need. There are only three relative relations of CZM curves between the initial guess and the exact solution: (1) intersecting, which is the case for all previously presented cases; (2) below (Figure 4.44 left); and (3) above (Figure 4.44 right). The initial guesses and the computed converged CZMs for these four cases are shown in Figure 4.44.

Table 4.4: Effect of the initial guess (six control points), and use of different interpolants.

Cases	Target CZM	Bulk material E	Number of control points	Initial guess	Interpolant
I	Hardening (HD)	30 GPa	6	Below	LS
II	Hardening (HD)	30 GPa	6	Below	PCH
III	Power-law (PL)	30 GPa	6	Above	LS
IV	Power-law (PL)	30 GPa	6	Above	PCH

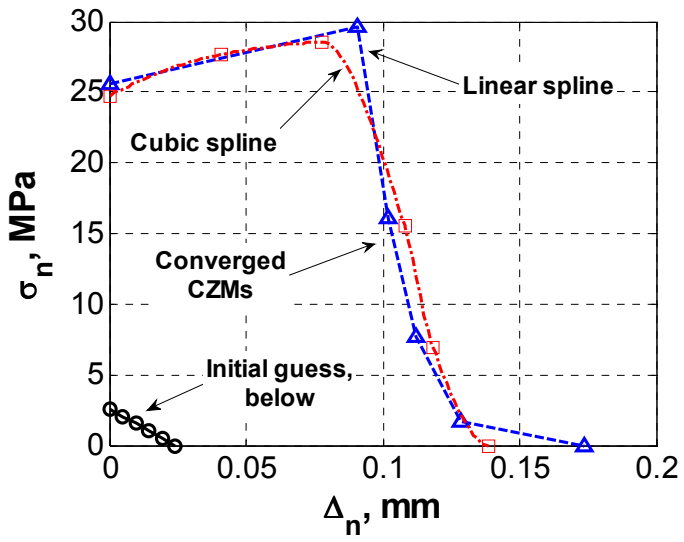

Figure 4.43: Optimization result with initial guess *below* the solution using *six* control points linear and cubic spline interpolations for the hardening CZM

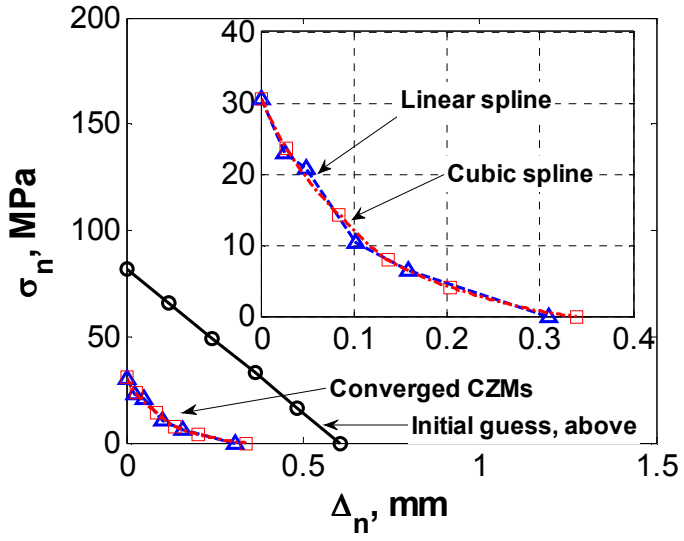

Figure 4.44: Optimization result with initial guess *above* the solution using *six* control points linear and cubic spline interpolations for the power-law CZM

Notice that in Figure 4.43, the computed hardening CZM using linear spline interpolations is not exact due to a small "tail" present in the solution, which is not removed during optimization. However, as can be seen, the computed hardening CZMs using both interpolants are accurate. For the power-law CZM, both interpolants yield accurate CZMs. A close examination of the curve confirms the expectation that the cubic spline interpolations provide smoother and more accurate results. The evolution of the objective function value for these four cases is presented in Figure 4.45 and Figure 4.46. In each plot shown in the figures, the locations where clustering or "tail" forms, as described in section 4.3.6.2, are marked in one of the two curves. The initial objective function values for these four cases are much larger than those shown in Table 4.3. In addition, the number of iterations to convergence is much larger. The objective function values steadily decrease except at "tail" points when the CZM parameters are recalculated. Although the cohesive stress contributed by the "tail" is small, it is located away from the beam neutral axis. With a long moment arm, the influence of the "tail" to the deformation of the specimen is apparent. The treatment of the clustered points may only influence the objective function negligibly, as seen closely at point "C" on the right plot of Figure 4.46.

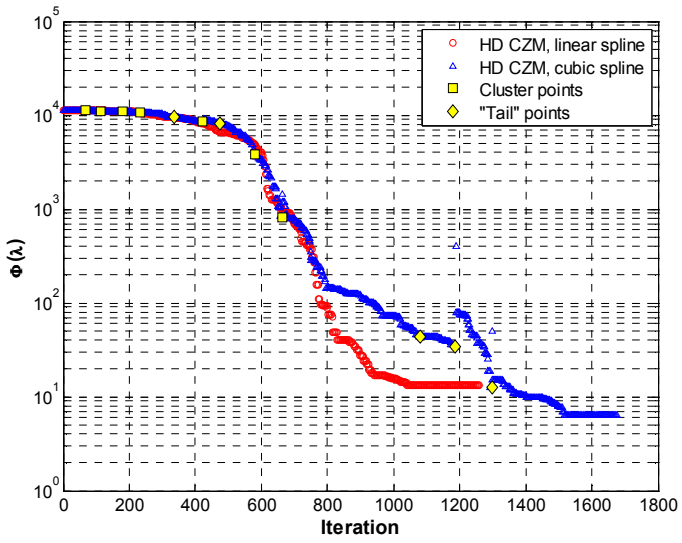

Figure 4.45: Evolution of the objective function value for the two cases (Figure 4.43)

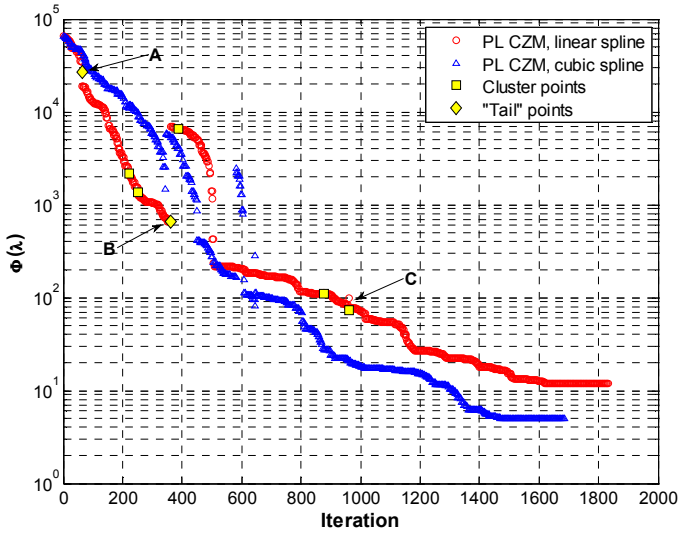

Figure 4.46: Evolution of the objective function value for the two cases (Figure 4.44)

Figure 4.47 shows the adjustment of control points for the two “tails” found at point “A” and “B” and for the clustering found at point “C” in Figure 4.46. The removal of the “tail” at point “A” does not affect the objective function value as the “tail” corresponds to crack opening larger than the actual case. At point “B” the cohesive stress within the tail acts on the specimen thus affect the deformation and the value of the objective function.

The treatment of the clustering, as illustrated, does not change the CZM curve significantly, therefore does not influence the objective function value much. A comparison between cases with and without cluster removal shows that the cluster treatment reduces the number of iterations significantly.

Point "A":

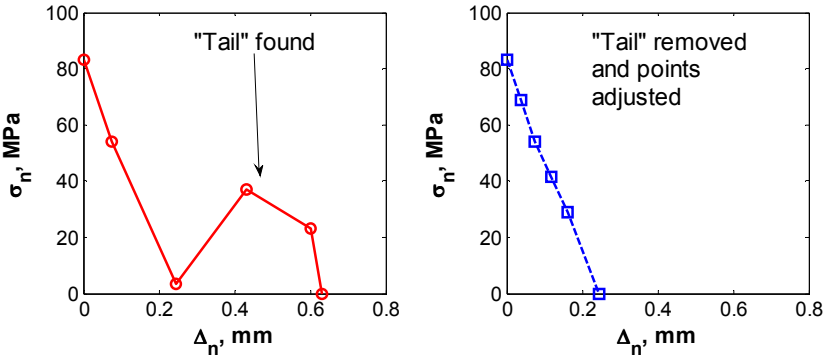

Point "B":

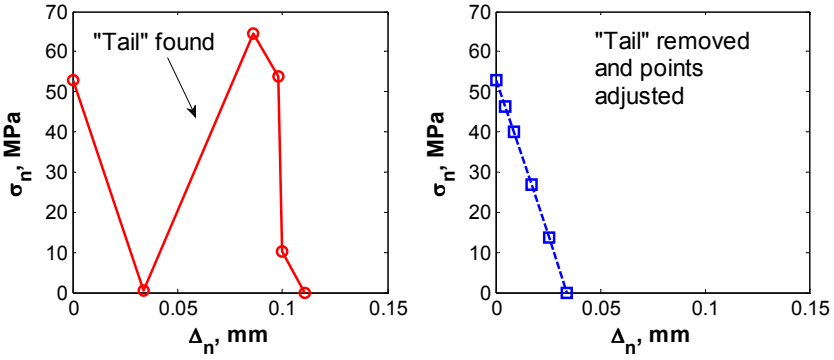

Point "C":

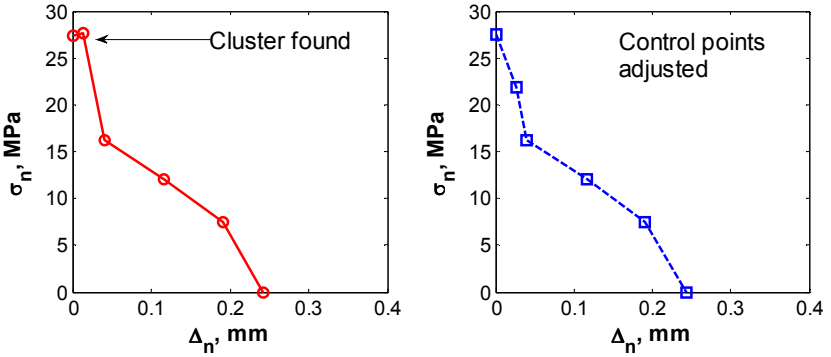

Figure 4.47: Demonstration of the removal of "tail" or cluster formed in the CZM representation. Points "A", "B" and "C" correspond to the points shown in Figure 4.46

4.5.6 Remarks on the Uniqueness of the Inverse Solutions

In general, inverse problems do not have unique solutions in a feasible domain. In optimization description, this means there may be a finite or infinite number of local minimums in the feasible domain. The solution is usually one of these local minimums and may not be the global minimum. Therefore, it is important to identify the local minimum that is physically representative. In the current application, it seems that the unwanted local minimums are mostly induced by the CZM "tail". Point "B" in Figure 4.47 in fact leads to a local minimum if the tail is not removed, as removal of the "tail" cause an increase of the objective function value (Figure 4.46). As one can imagine, if the "tail" is totally to the right of the actual maximum COD, the cohesive stress due to the "tail" will not contribute to the deformation of the specimen, i.e., the existence of the will not affect the objective function value. Apparently, one does not expect a CZM to have a "tail" like the ones shown in Figure 4.47. In practice, this probably is not an issue as the CZM will be computed from different sets of experimental data, e.g., at different load levels (Figure 4.42), or from specimens with different geometries (either numerical or actual experimental specimens).

CHAPTER 5 – EXTRACTION OF COHESIVE PROPERTIES OF PLASTICS USING A HYBRID INVERSE TECHNIQUE

The primary purpose of this chapter is to verify the proposed inverse technique through "well-behaved" materials. The first requirement for the materials is that they have quasi-brittle fracture behavior, and during fracture process, the bulk material remains linear elastic. For the current investigation, it is also desired that the materials be homogeneous and isotropic at the scale of observation. Another important requirement relating to the ease of success and accuracy of results of the procedure is the ratio of cohesive strength to bulk material elastic modulus. The higher the ratio, the smaller the relative errors in DIC measurement are and the more consistent the computed CZM is. The cohesive properties are extracted by means of a hybrid inverse technique using both experimental and numerical approaches. The fracture experiments are based on digital image correlation (DIC). An inverse numerical procedure is used to determine the cohesive properties by minimizing the difference between experimental and computed displacements in a least squares sense.

5.1 INTRODUCTION

Based on the above requirements, two plastics, Devcon® Plastic Welder™ II and Garolite G-10/FR4 are selected. Devcon® Plastic Welder™ II is a toughened structural acrylic adhesive formulated for bonding difficult-to-bond substrates, e.g., the PMMA used in this study. It has high shear strength and high resistance to peeling. Its tensile peeling stress is higher than 24 MPa. The effectiveness of this adhesive in bonding PMMA and its ductility resulted in the desired cohesive failure of the adhesive. PMMA is an amorphous glassy polymer. The reason to select PMMA as substrate is that it behaves elastically up to a substantial percentage of its ultimate strength under room temperature and it has a low modulus of elasticity. Garolite is a high performance type of fiberglass, composed of woven glass cloth in an epoxy resin media. The Garolite has high strength and high toughness.

In the numerical examples presented in Chapter 4, the elastic properties of the bulk materials are assumed known. In reality, these properties may be known, usually from the manufacturer, or be measured through experiments. It is well known that plastics have a wider variability of mechanical properties. Therefore, the elastic properties of PMMA and Garolite G-10/FR4 used in this study must be measured. In current study, as both PMMA and Garolite are considered homogeneous, linear elastic materials, only elastic modulus and Poisson's ratio need to be measured. Uniaxial tension or compression test can be used to measure these two properties. However, to demonstrate the usefulness of DIC technique, the elastic properties are also measured through DIC.

Section 5.2 presents the procedure to measure the elastic properties of PMMA and Garolite G-10/FR4. The average value of the elastic properties will be used directly in the inverse procedure presented in Section 5.3, which presents the detailed fracture tests result measured by DIC. Section 5.4 provides verification of the computed cohesive properties.

5.2 MEASUREMENT OF ELASTIC PROPERTIES

Compression tests and four-point bending tests are carried out to measure the elastic properties of PMMA, while only four-point bending tests are used for the measurement of Garolite G-10/FR4. Inverse procedures can also be used for the measurement of bulk elastic properties [84,104,122]. However, for isotropic case, such advanced computational technique is not necessary. Instead, the DIC measured displacement field will be used directly to compute the modulus of elasticity and Poisson's ratio. This simple, direct method, as will be demonstrated, yields accurate measurements.

The mechanical properties of these two plastics vary and the available ranges of their common mechanical properties are listed in Table 5.1. Notice that the Poisson's ratio for Garolite G-10/FR4 is not available in literatures or from the manufacturer's material datasheet.

Table 5.1: Mechanical properties of PMMA and Garolite G-10/FR4

Material	Tensile strength, MPa	Young's modulus, GPa	Poisson's ratio
PMMA	48.3 – 72.4	2.24 – 3.24	0.4
Garolite G-10/FR4	262 - 345	15.2 – 22.8	N/A

5.2.1 Experimental Setup

Two compressive prisms of PMMA with a nominal dimension 11.5mm × 23mm × 75 mm, two 4-point bend PMMA specimens of 11.5mm × 24mm × 120mm, and two 4-point bend GL specimens of 10mm × 25.5mm × 160mm are prepared. The test set-up is shown in Figure 5.1.

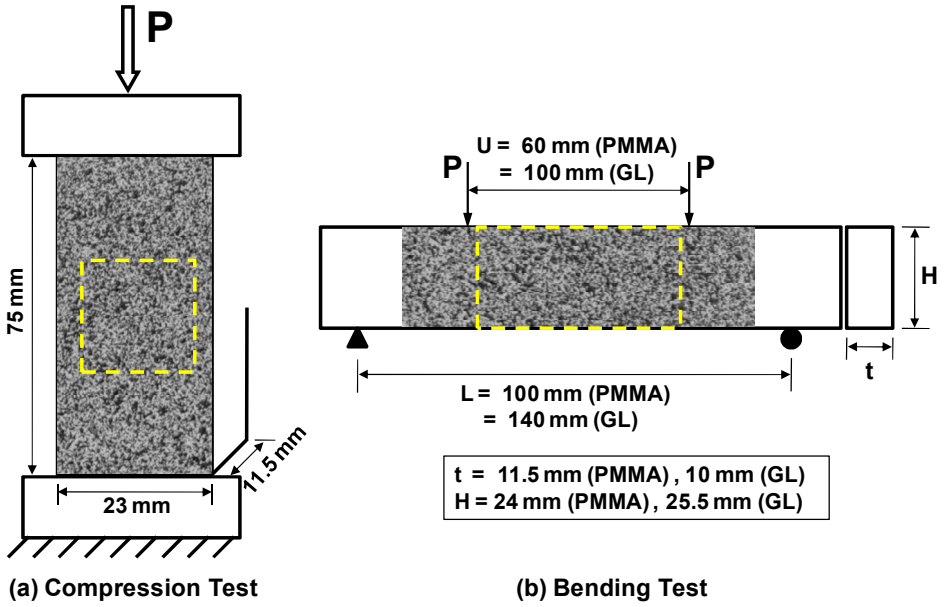

Figure 5.1: Compression and bending test set-up, the rectangles are the ROI analyzed by DIC

Black and white enamel-based paints are used to prepare the speckle pattern. A Paasche® Single Action – External Mix – Siphon Feed Airbrushes is used to first spray the white paint on the specimen as background. The amount of white paint sprayed is just enough to uniformly and fully cover the specimen. Then black paint is sprayed to generate the random speckle pattern. Figure 5.1 also shows the ROIs that are analyzed

using DIC. For the PMMA compression prisms, a ROI away from both ends is used to avoid end effects. For the bending specimens, the ROI is selected in the pure bending region away from the loading points. The digital image resolutions for the test specimens are listed in Table 5.2.

Table 5.2: Digital image resolutions for the test specimens

Specimen	PMMA compression specimens	PMMA bend specimens	GL bend specimens
Image resolution, μm/pixel	11.05	16.67	11.53

5.2.2 Uniaxial Compression

The PMMA prisms are loaded within elastic range. Figure 5.2 shows the load versus crosshead displacement for the compression test for both specimens. The surface speckle images are taken for each loading point. The reference image for DIC is the image taken at zero loading. The correlated displacement fields, u_x and u_y, for load P = 1900 N are shown in Figure 5.3. Notice that displacement is measured in pixels. The corresponding strain fields ε_x and ε_y are shown in Figure 5.4. The displacement u_y is due to the compressive loading, while the displacement u_x is due to the Poisson's effect. Notice the origin of *y*-axis in the field plots is at the top and the *y*-axis direction is reversed. This is to conform to the image processing convention that the origin of an image is usually designated at the upper-left corner.

The strain fields ε_x and ε_y shown in Figure 5.3 are uniform. The compressive stress, justified as uniformly distributed in accordance to the strain, can be calculated through the measured load. Average value of ε_x and ε_y are used to compute the Poisson's ratio directly. The measured Young's modulus and Poisson's ratio are summarized in Table 5.3, which shows consistently measured properties.

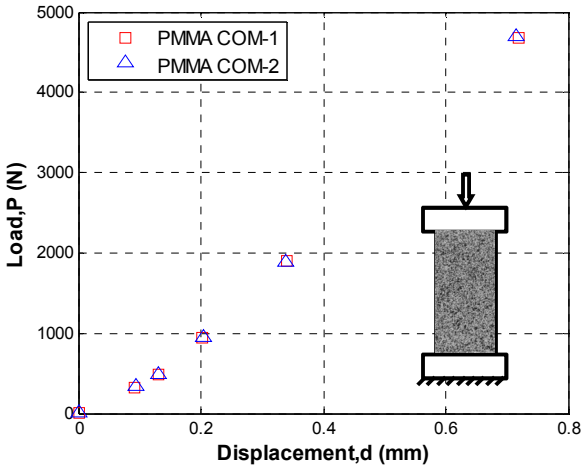

Figure 5.2: Load versus crosshead displacement for the PMMA under compression

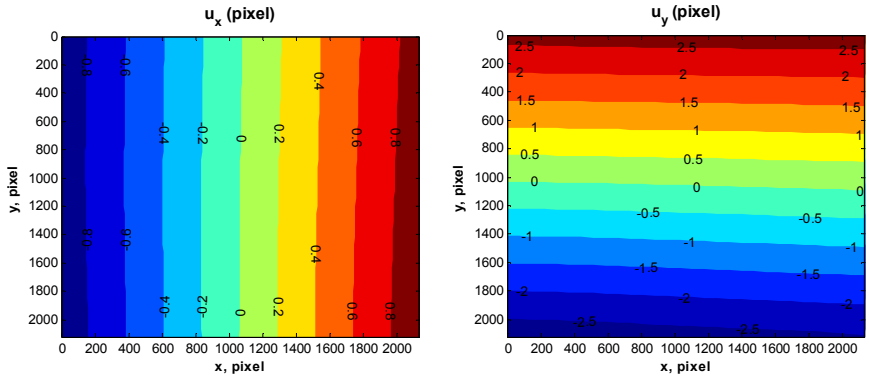

Figure 5.3: Displacement field u_x and u_y by DIC for PMMA compression specimens at P = 1900 N

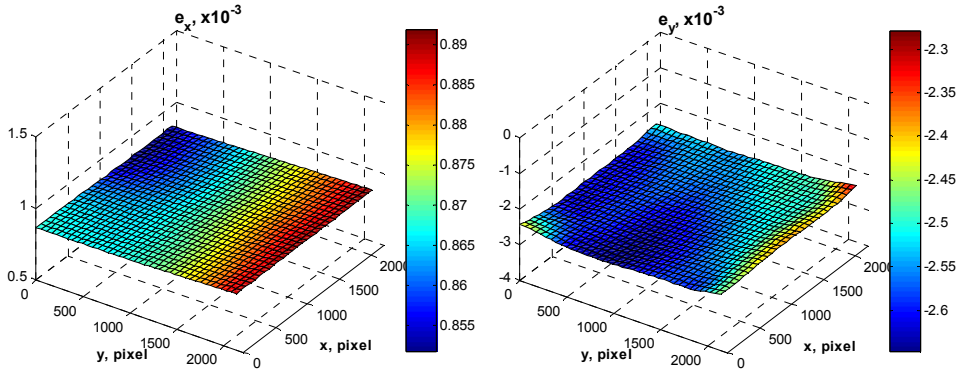

Figure 5.4: Strain field ε_x and ε_y by DIC for PMMA compression specimens at P = 1900 N

Table 5.3: The measured Young's modulus and Poisson's ratio for PMMA and GL from DIC

	Young's Modulus, GPa	Poisson's ratio
PMMA Com-1	3.12 ± 0.17	0.372 ± 0.02
PMMA Com-2	3.36 ± 0.15	0.401 ± 0.01
PMMA Bend-1	3.57 ± 0.20	0.381 ± 0.03
PMMA Bend-2	3.49 ± 0.23	0.389 ± 0.03
GL Bend-1	17.4 ± 0.09	0.209 ± 0.01
GL Bend-2	16.8 ± 0.11	0.198 ± 0.01

5.2.3 Four-Point Bending

Figure 5.5 shows the loading points when the DIC images are recorded. Apparently, the loading is within the elastic range. A typical displacement plots, u_x and u_y, at P = 1500 N is shown in Figure 5.6 (2D contour plot) and Figure 5.7 (3D surface plot). It can be seen that the displacement field conforms to beam theory result. The mean displacements in both the *x*- and *y*-directions have been subtracted to eliminate the rigid-body motion recorded and to have better visualization of the fields. The rigid body motion is unavoidable during actual experiments. However, it does not affect the as the relative displacements are the only ones of interest to obtain E and ν. The zero u_x isoline in the plots shows the symmetry plan (vertical) and the beam neutral axis (horizontal). The compression above and the tension below the neutral axis can be readily inferred from the relative movement of pixels. The vertical displacement field for the beam under pure bending can be rarely seen in literatures, because usually it is of little or no interest. However, DIC does reveal such significant difference between the vertical and horizontal displacement pattern of a beam.

Figure 5.8 shows the strain field ε_x and ε_y corresponding to the displacements presented in Figure 5.6. Notice the symmetry of the compression (negative ε_x) and tension (positive ε_y) regions about the neutral axis indicated by the zero-strain isoline. As presumably no vertical stress exists in pure bending, ε_y is due to Poisson's effect only. This is confirmed with the following observations: (1) ε_y has the opposite sign of ε_x; (2) ε_y is proportional to ε_x; (3) ε_y plots reveal the same location of neutral axis.

Again, with the presumption that the bending stress distribution through the beam depth is linear, the correlation between stress and DIC measured strain can be obtained to estimate the Young's modulus. The Poisson's ratio is better estimated by comparing the average gradient of ε_y to the average gradient of ε_x both in y-direction. The estimated Young's modulus and Poisson's ratio for PMMA from the two bending specimens are listed in Table 5.3. They are consistent with the measurements from compression tests.

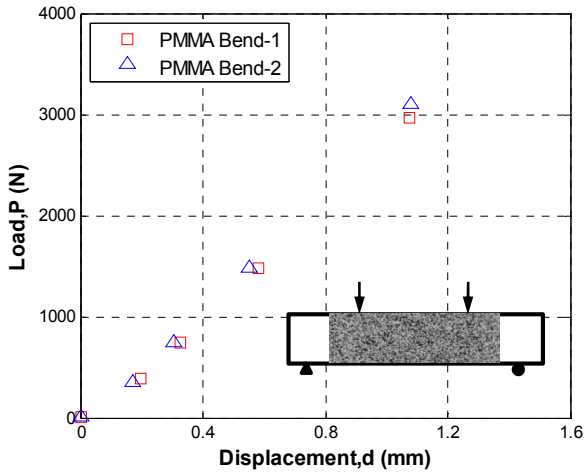

Figure 5.5: Load versus cross-head displacement for the PMMA under bending

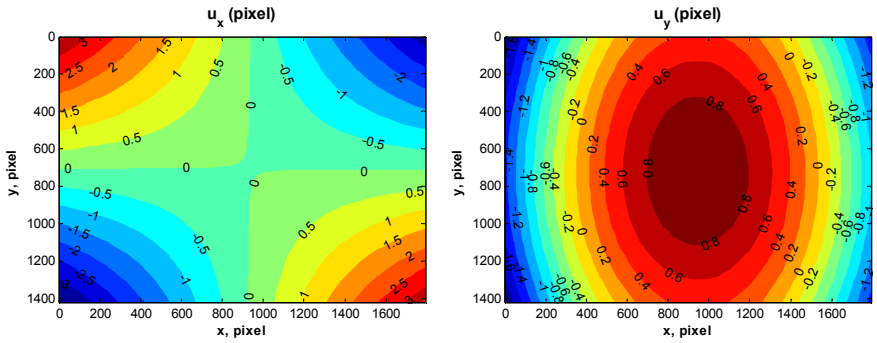

Figure 5.6: Contour plot of displacement field u_x and u_y by DIC for PMMA bending specimen at P = 1500 N

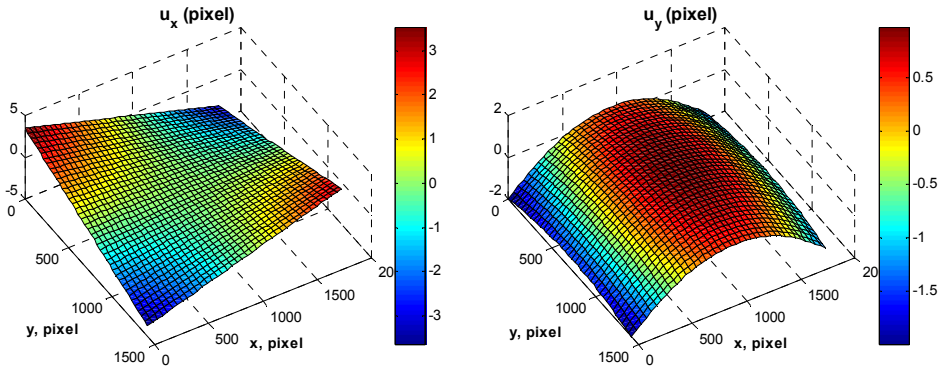

Figure 5.7: Surface plot of displacement field u_x and u_y by DIC for PMMA bending specimens at P = 1500 N

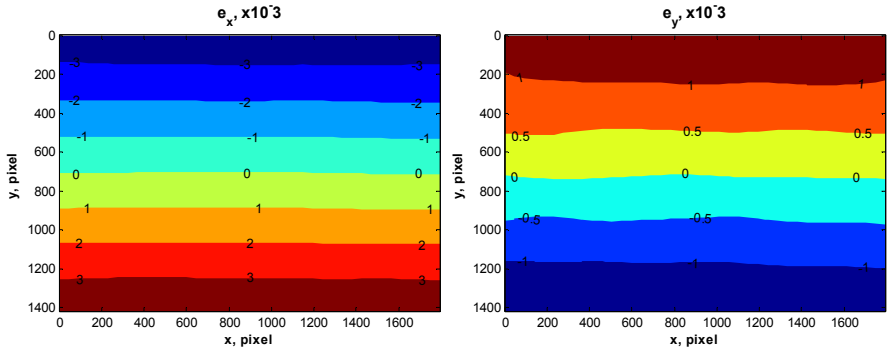

Figure 5.8: Contour plot of strain field ε_x and ε_y by DIC for PMMA bending specimen at P = 1500 N

The same procedures to measure the Young's modulus and Poisson's ratio using four-point bent specimens are applied to GL and will not be presented here. GL's Young's modulus and Poisson's ratio are also listed in Table 5.3.

5.3 FRACTURE TESTS

The Garolite G-10/FR4 has a particularly high tensile strength to Young's modulus ratio, which is about 0.01~0.015. The ratio of the tensile peeling strength of the Devcon® Plastic Welder™ II to the Young's modulus of PMMA is about 0.01. As demonstrated in Chapter 4, the synthetic material that has the highest cohesive strength (30MPa) to Young's modulus (10GPa) ratio, 0.003, is the most tolerable to errors. This ratio, 0.003, is

less than one-third of the two materials tested. Therefore, it is first expected that the inverse procedure would yield accurate estimation of the cohesive properties.

SENB specimens of PMMA bonded by adhesive and G10/FR4 Garolite are prepared for fracture testing. The specimen geometry is shown in Figure 5.9. The actual dimensions of the test specimens are listed in Table 5.4.

Table 5.4: Dimension of PMMA and G10/FR4 Garolite SENB specimens

	Specimen ID	Height, H (mm)	Width, t (mm)	Notch length, a_0 (mm)
PMMA	PWII-1	25.5	11.7	6.83
	PWII-3	30.5	9.13	6.13
G10/FR4 Garolite	GL-2	25.5	10.1	5.51
	GL-3	25.5	10.1	5.87

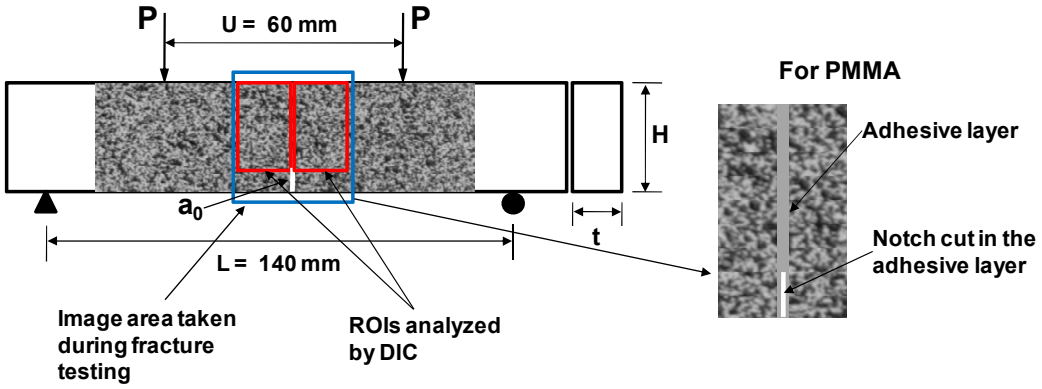

Figure 5.9: PMMA and G10/FR4 Garolite SENB specimen geometry and fracture test set-up

The procedure of bonding PMMA is as follows. The surfaces to be bonded are first roughened by a coarse sand paper, followed by cleaning using acetone, then a very thin layer of PW-II is applied on both surfaces to ensure full coverage, afterwards an even and thick layer is applied on one of the surface, and then the two PMMA prisms are assembled, firm pressure is applied to the adhesive layer before setting to eliminate gaps and enhance contact. The final widths of the PW-II layer for both specimens are 0.6 ± 0.05 mm, which is between the products recommended thickness ranges, 0.38mm – 0.76mm, for optimum adhesion.

The notches of both the PMMA and the G10/FR4 Garolite SENB specimens are first cut before the desired length by an ordinary band saw, and then a teeth-sharpened thin band saw is used to produce the final sharp notch tip (Figure 5.10). The notch tip radius is estimated to be less than 50 μm by using an optical microscope.

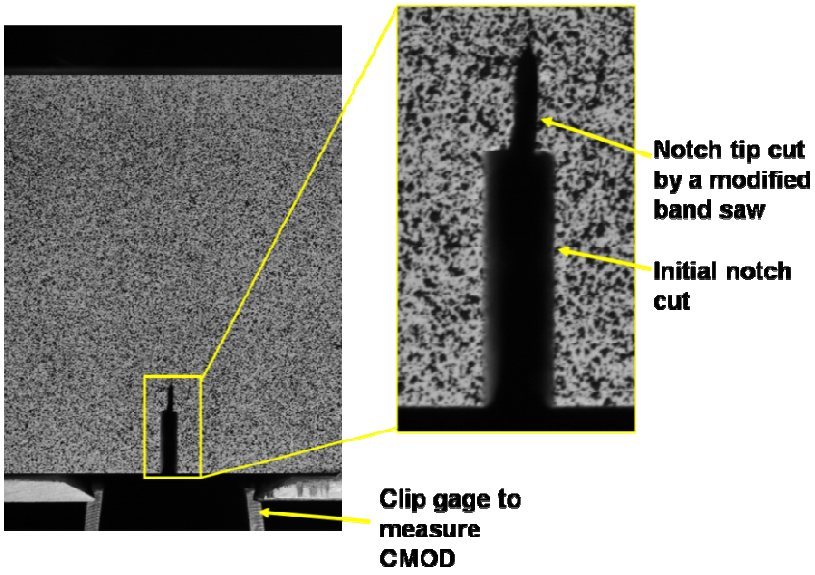

Figure 5.10: Image area taken during fracture testing and a room-in image of the initial notch

The fracture testing is conducted on a servo-hydraulic Instron testing frame. A clip gage is installed on the bottom of the SENB specimen to measure the crack mouth opening displacement (CMOD) (Figure 5.10). The loading rate is CMOD controlled and is set to 0.1 mm/min before peak load and increased to 0.2 to 0.5 mm/min during the softening part. Figure 5.11 shows the load versus CMOD curves for both PMMA and G10/FR4 Garolite SENB specimens. The locations where images are taken for DIC analysis are also shown. The testing is paused and held when the DIC images are to be taken. The period of the test holding is around 10 seconds. No load changes are observed during that period, even for PWII adhesive, which is expected to show a creep behavior under sustained loading. This observation indicates that the fracture process under the current rate of loading may not be affected by possible rate-dependent effect. Therefore, the CZM to be computed can be regarded as rate-independent for the testing rate used.

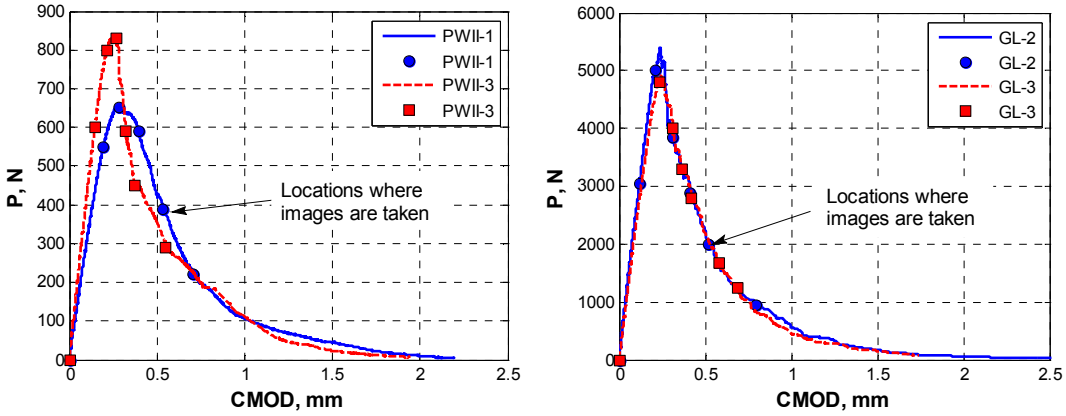

(a) (b)

Figure 5.11: Load P versus CMOD curves for (a) PWII bonded PMMA, and (b) G10/FR4 Garolite SENB specimens

Figure 5.12 shows the fracture surfaces. The cohesive failure through the PW-II adhesive can be clearly seen. The rough fracture surface of G10/FR4 Garolite shows rupture of the fine fibers.

5.3.1 Deformation Field

Using the image at P = 0N as reference, two ROIs right above the initial notch tip on either side of the crack path are selected as the reference images (Figure 5.9). After the image correlation, the displacement fields on the two ROIs are combined for each recorded image. Figure 5.13 and Figure 5.14 show the u_x deformation at different loads for one PW-II bonded PMMA and one G10/FR4 Garolite SENB specimen, respectively. The pixel resolution for PWII-3 is 9.93 μm/pixel and for GL-3 is 8.32 μm/pixel. On both figures, the left side is the surface plots showing crack profiles, the right side is the corresponding contour plots showing the u_x values. This full displacement field enables the calculation of the crack opening displacement.

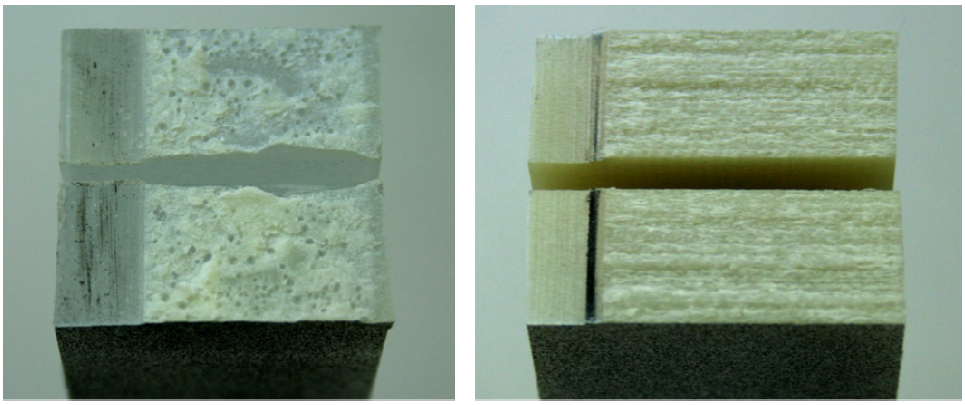

(a) (b)

Figure 5.12: Fracture surfaces of (a) PWII bonded PMMA, and (b) G10/FR4 Garolite SENB specimens

The crack length and the crack tip location can be easily seen on either the surface plot or the contour plot in Figure 5.13 and Figure 5.14. The accuracy of the crack tip location depends on the combined resolving power of the image system and the DIC algorithm. For our system, the estimated error is in an order of 10 μm/pixel × 0.015pixel = 0.15 μm.

5.3.2 Inverse Analysis

A 2D FE model represents the left half of the beam is used for the inverse analysis. The Q4 element is used to model the bulk material. The elastic properties used in the model are based on Table 5.3: for PMMA, E = 3.4 GPa, ν = 0.38 and for Garolite G-10/FR4, E = 18 GPa, ν = 0.20. The number of Q4 elements along the crack line is 600, equivalent to a cohesive element size of 42.5 μm. The displacements at the nodal locations are the average of the DIC measured displacements on the left and right sides of the crack. Figure 5.15 shows the Q4 mesh with zoom-in detail.

Based on the investigations from the numerical examples [108], an initial guess of the curve of the CZM that is below the exact CZM curve will converge faster (less optimization iterations) to the exact CZM. Based on the measured DIC COD profile and the estimated tensile strength, the initial guesses of the CZM curves for both materials are used (Figure 5.16) for the inverse analysis. Five control points and cubic Hermite

interpolation are used to construct the CZM. For both materials, the inverse analyses are carried out for all displacement data measured at the different post-peak loadings (Figure 5.11). This is because the complete formation of the cohesive fracture process zone can only happen after peak load has reached (section 4.5.3.2). Furthermore, an example of the evolution of the objective function value is shown in Figure 5.17. The three curves are for images of the PWII-3 taken after peak loading.

The computed CZMs (three inverse analysis results for each material) for PW-II and Garolite G-10/FR4 are shown in Figure 5.18. The computed CZMs of both PWII and Garolite G-10/FR4 show a softening behavior. More variations are seen on the computed CZMs of PWII while for Garolite, the computed CZMs are more consistent. This may be due to the fact that PMMA SENB specimens are bonded manually using PWII in our in which case variations of bond strength may be significant. While the Garolite is a continuous manufactured piece, the cohesive properties along the crack are expected to be more uniform. The computed PWII CZMs have a critical cohesive strength about 15 MPa, in comparison to the manufacturer provided peel strength of 24 MPa. The maximum computed critical cohesive stress for Garolite G-10/FR4 is 250 MPa, which is close to the lower bound of its tensile stress, 262 MPa. Surprisingly, the critical separations of the CZMs do not vary as seen in [86]. This may be due to the enhanced smoothness of DIC measurement using the full-field correlation algorithm.

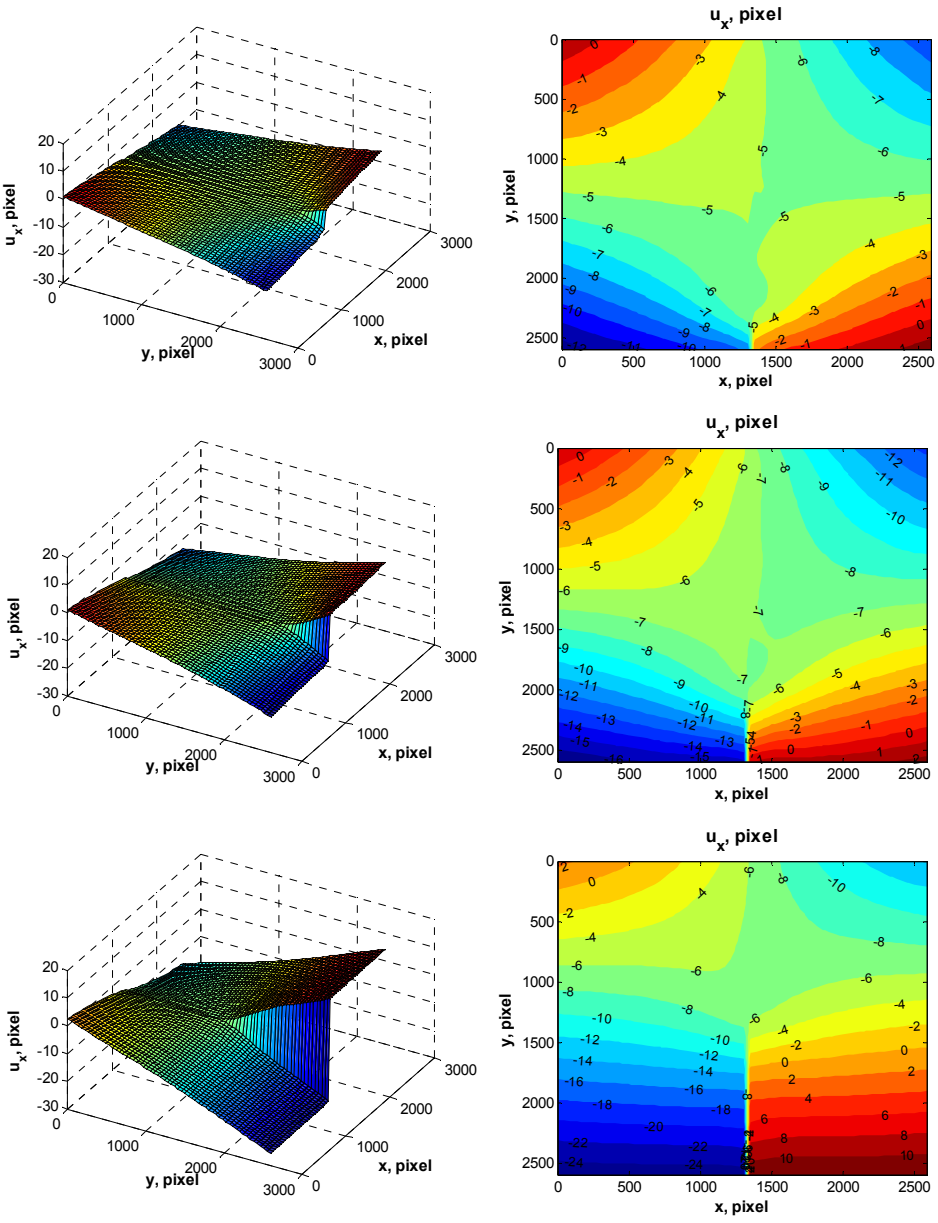

Figure 5.13: Displacement u_x fields for PWII-3 at different loads (from top to bottom): 800 N, post-peak 450 N, and post-peak 290 N.

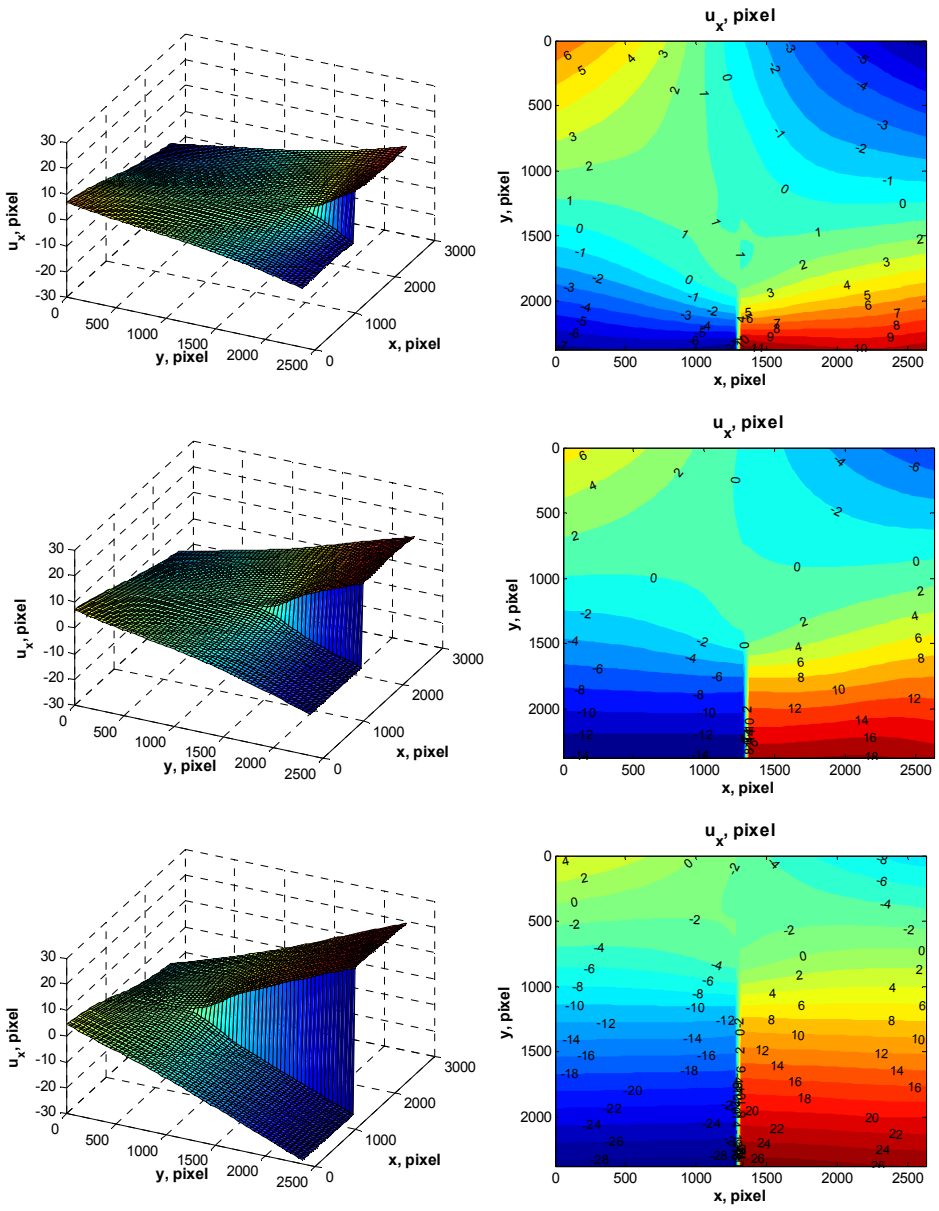

Figure 5.14: Displacement u_x fields for GL-3 at different post-peak loads (from top to bottom): 4000 N, 2800 N and 1250 N.

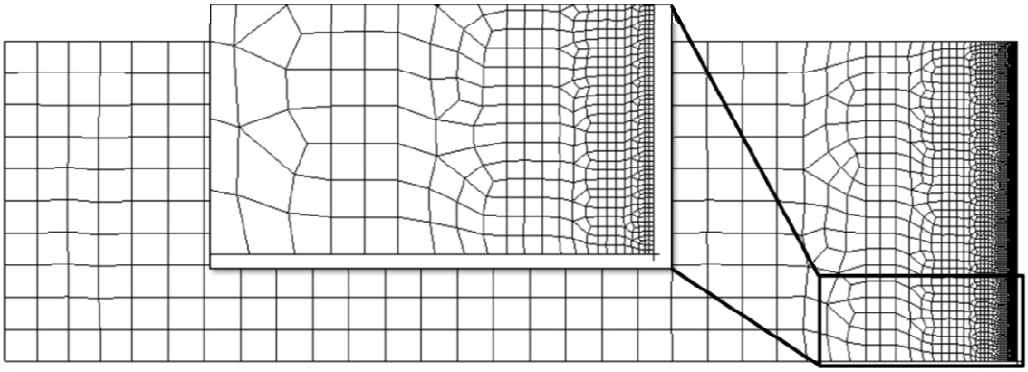

Figure 5.15: FEM mesh for inverse analysis to compute the CZM

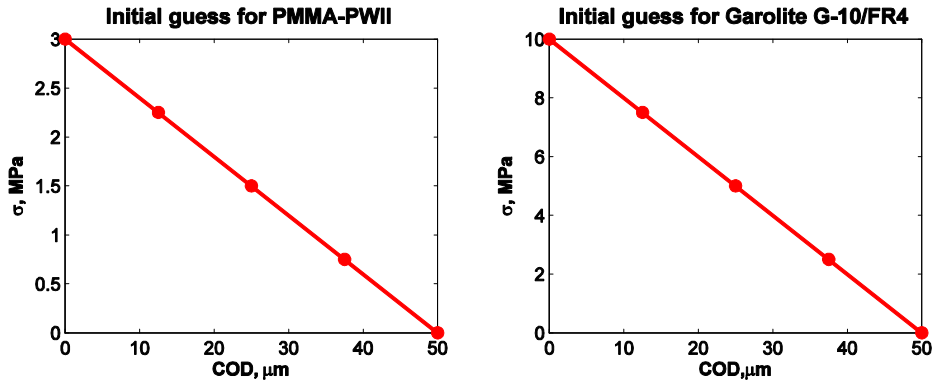

Figure 5.16: Initial guesses used for PMMA-PWII and Garolite G-10/FR4

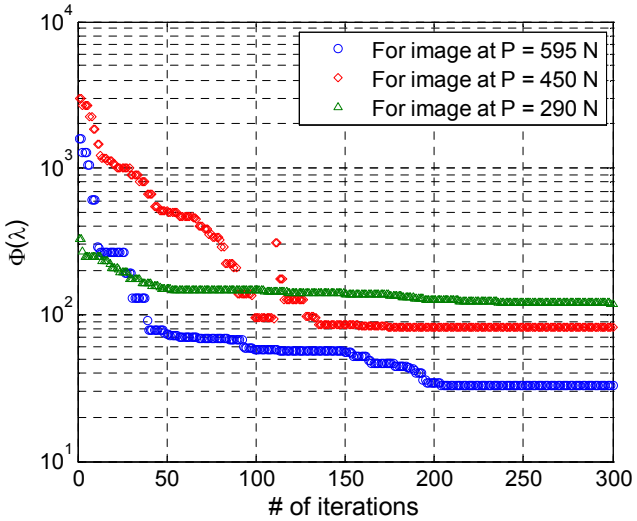

Figure 5.17: Evolution of the objective function during optimization for PWII-3 for the three post-peak images shown in Figure 5.11

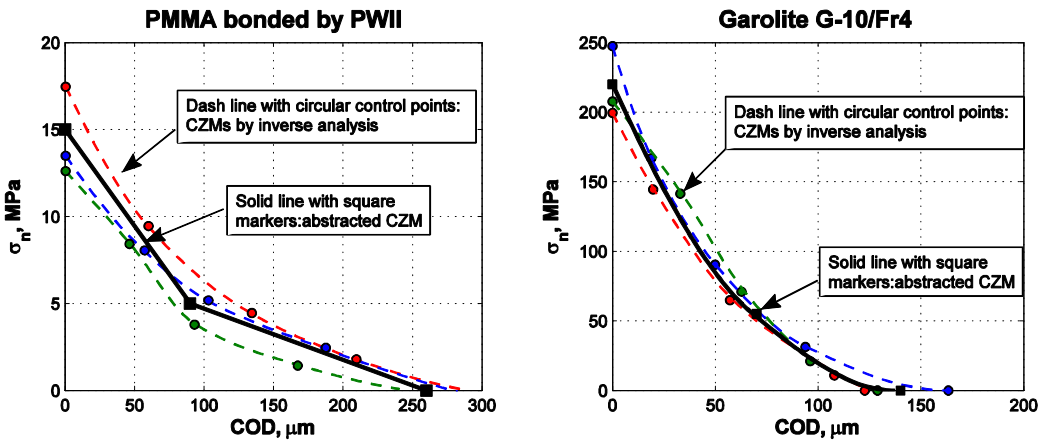

Figure 5.18: The computed CZMs for PW-II and G-10/FR4 Garolite

5.4 VERIFICATION OF THE EXTRACTED CZMS

We verify the computed CZMs by examining the fracture energies and by comparing the FEM simulation using the computed CZMs to the experiments. Taking the average of the CZMs, we abstract the computed CZMs with a simple curve for convenience. For PWII, the computed CZMs are banded and vaguely show a "kink" point, therefore we use a bilinear softening curve to abstract the computed curves (Figure 5.18). While for the Garolite G-10/FR4, we found a power-law curve with power index = 1.92 that fits well the computed CZMs. The fracture energy can then be directly computed from these abstracted CZMs by

$$G_f = \int_0^{\Delta_{nc}} \sigma(\Delta_n) d\Delta_n \ , \qquad (5.1)$$

where G_f is the fracture energy. The fracture energy can also be estimated from the area under the curve of load versus load-line displacement. The fracture energies computed from equation (5.1) using the exacted CZMs and from the experimental load versus load-line displacement curves are compared in Table 5.5, and demonstrate good agreement.

Table 5.5: Comparison of fracture energies (N/mm) between experiments and inverse computation

	PWII-1	PWII-3	GL-2	GL-3
Experiments	1.36	1.41	10.31	10.57
DIC-FEM inverse analysis	1.33 ± 0.12		10.27 ± 0.35	

The extracted CZMs for both materials are then used as the input to the FEM model to compute the global response, i.e. P versus CMOD curve. The FEM simulated P versus CMOD curves are compared with experimental results and are shown in Figure 5.19.

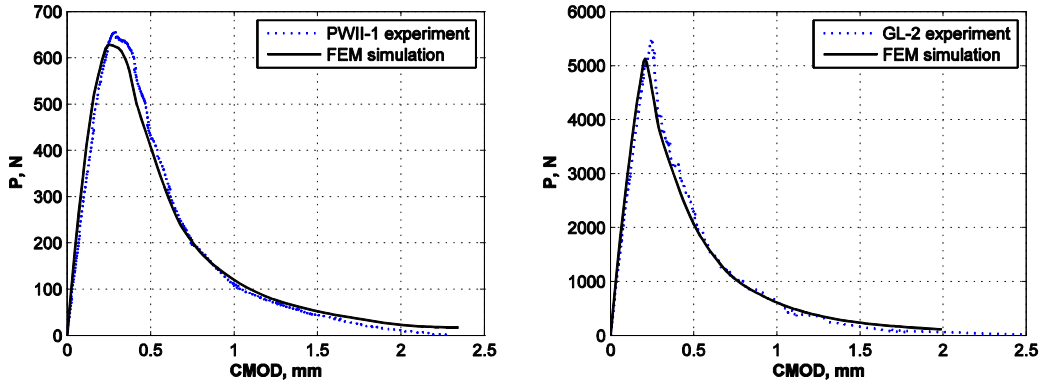

Figure 5.19: Comparison of the P versus CMOD curves between experiments and FEM simulation

Notice that globally the simulated results have good agreement with experiments both in elastic range and the softening. The agreement in the initial slope of the P versus CMOD curves illustrates the accurate measurement of the Young's modulus. Moreover, the good fit around the peak load and for the softening part of P versus CMOD may imply that the shapes of the computed CZMs are accurately estimated.

CHAPTER 6 – FRACTURE BEHAVIOR OF FUNCTIONALLY GRADED FIBER-REINFORCED CEMENTITIOUS COMPOSITES (FGFRCC)

This chapter investigates mode I cohesive properties of FRCCs and both mode I and mixed-mode fracture behavior of FGFRCCs. Both FRCCs and FGFRCCs were manufactured by means of the extrusion technique described in Chapter 2. The procedure described in Chapter 5 is used to prepare FRCC specimens for bending and fracture tests, as well as for DIC measurements. The cohesive properties of FRCCs are obtained by means of the hybrid (experimental/numerical) technique developed in this work (see Chapter 5).

The fracture experiments of FGFRCC specimens concentrate on mixed-mode fracture behavior. It addresses crack initiation and propagation as the crack is offset from the middle of the SENB specimen. It also addresses the so-called crack competition phenomenon, i.e., what is crack-offset that nucleates a crack in the middle of the specimen. In this case, the offset crack does not propagate, damage is generated in the middle of the specimen, which leads to microcracking and finally a macrocrack that propagates.

6.1 EXPERIMENTS

The nominal specimen dimensions for both the bending and fracture test specimens are 26 × 13 × 140 mm (height × width × length). For the single edge-notched beam (SENB) specimen for fracture testing, the nominal notch size is 6 mm. Four different fiber volume fractions are used: 0.5%, 1%, 2% and 3%. The matrix mix proportion is kept the same, except water amount is slightly adjusted for ease of extrusion for different fiber amount.

Table 6.1: Mix proportions of FRCCs with different fiber volume fraction

Cement (wt.)	Fly ash Class F (wt.)	Water (wt.)	Fiber (vol.)	Superplasticizer* (wt.)	HPMC/water (wt.)
0.573	0.427	0.210	0.5%	0.002	0.04
		0.215	1%		
		0.220	2%		
		0.225	3%		

The speckle preparation procedure is the same as for the plastics, except that a little thicker back paint is needed due to the dark color of the FRCC. Similar to the DIC bend test for the plastics, the specimen setup is shown in Figure 6.1.

Unlike the Garolite and bonded PMMA SENB specimens, the FRCC SENB specimens do not show straight crack paths. A shallow straight groove on both sides of the specimens is introduced to confine the crack path within the groove (Figure 6.2). The grooves are made by a specially tailored thin band saw. It is hard to produce the grooves and even harder to control the desired cut depth. It is estimated that all grooves are between 1 to 1.5 mm.

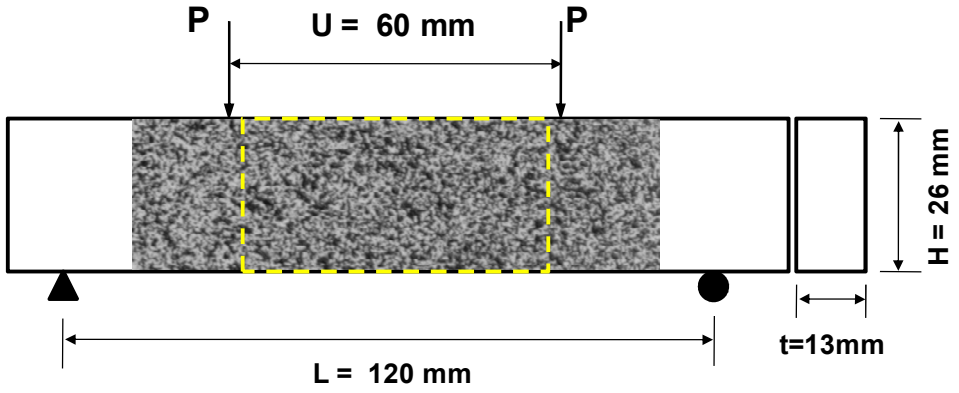

Figure 6.1: Bending test set-up, the rectangle is the region of interest that DIC displacement is computed

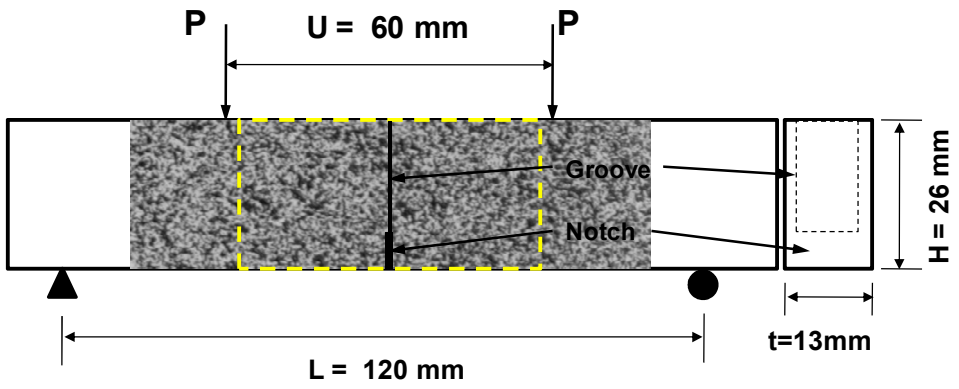

Figure 6.2: Fracture test set-up, the rectangle is the region of interest that DIC displacement is computed, notice the profile of the groove and notch

6.2 MEASUREMENT OF BULK ELASTIC PROPERTIES

Compared to the PMMA and Garolite described in Chapter 5, the FRCC has a much lower elastic tensile strength to modulus of elasticity ratio. This means that only very small tensile elastic strain can be generated before the specimens crack. Therefore, direct computation of the strain field using the measured displacement field from DIC will be inaccurate, as the noise to signal ratio now for the FRCC is expected to be high. Instead, an inverse procedure similar to the one presented in Chapter 4 for computing the cohesive properties is used for the identification of the elastic properties of FRCCs. In the following, the numerical procedure is first described, and then the experimental results and inverse analyses are presented.

6.2.1 Linearization of Stress-Strain Constitutive Matrix

In elasticity, identification of material constants is done through inverse determination of the Hooke's tensor, $\mathbf{H}$. Denote the N constitutive parameters as a vector $\boldsymbol{\theta} = \{\theta_1,...,\theta_N\}$, thus $\mathbf{H} = \mathbf{H}(\boldsymbol{\theta})$. Usually the Hooke's tensor is decomposed as a linear combination of all the independent scalar moduli

$$\mathbf{H} = \sum_{i=1}^{N} \theta_i \mathbf{H}_i \qquad (6.1)$$

.

For homogeneous, isotropic materials, the elastic properties can be described in terms of the Lamé constants λ and μ, which are two independent scalar moduli. The stress-strain constitutive relations, or Hooke's Law, can be written as

$$\sigma_{ij} = 2\mu\varepsilon_{ij} + \lambda\delta_{ij}\varepsilon_{kk}, \tag{6.2}$$

where $i, j = 1, 2, 3$ satisfying 3D relations. The Lamé's first parameter, λ, has no physical meaning but to simplify the Hooke's stiffness matrix, and it can be converted by

$$\lambda = \frac{E\nu}{(1+\nu)(1-2\nu)}. \tag{6.3}$$

The Lamé's second parameter, μ, is the shear modulus. The linearized form of Hooke's law, Equation (6.2), can only be directly applied in 3D problems. For plane stress condition, the form is different, which is derived as the following.

For plane stress condition, there is $\sigma_{23} = \sigma_{31} = \sigma_{33} = 0$. From $\sigma_{33} = 0$ and equation (6.2), one obtains

$$\varepsilon_{33} = -\frac{\lambda(\varepsilon_{11} + \varepsilon_{22})}{\lambda + 2\mu}. \tag{6.4}$$

Substituting (6.4) into σ_{11} and σ_{22} in equations (6.2), one obtains

$$\begin{aligned} \sigma_{11} &= \frac{4\mu(\lambda+\mu)}{\lambda+2\mu}\varepsilon_{11} + \frac{2\mu\lambda}{\lambda+2\mu}\varepsilon_{22} \\ \sigma_{22} &= \frac{4\mu(\lambda+\mu)}{\lambda+2\mu}\varepsilon_{11} + \frac{2\mu\lambda}{\lambda+2\mu}\varepsilon_{22} \end{aligned}. \tag{6.5}$$

Rearranging (6.5) leads to

$$\begin{aligned} \sigma_{11} &= 4\mu\varepsilon_{11} - \frac{4\mu^2}{\lambda+2\mu}\varepsilon_{11} + 2\mu\varepsilon_{22} - \frac{4\mu^2}{\lambda+2\mu}\varepsilon_{22} \\ \sigma_{22} &= 2\mu\varepsilon_{11} - \frac{4\mu^2}{\lambda+2\mu}\varepsilon_{11} + 4\mu\varepsilon_{22} - \frac{4\mu^2}{\lambda+2\mu}\varepsilon_{22} \end{aligned}. \tag{6.6}$$

Together with $\sigma_{12}=\sigma_{21}=2\mu\varepsilon_{12}$, the Hooke's law for isotropic material in plane stress condition can be written explicitly as

$$\begin{Bmatrix}\sigma_{11}\\ \sigma_{22}\\ \sigma_{12}\end{Bmatrix}=\left(2\mu\begin{bmatrix}2&1&0\\1&2&0\\0&0&1\end{bmatrix}-\frac{4\mu^2}{\lambda+2\mu}\begin{bmatrix}1&1&0\\1&1&0\\0&0&0\end{bmatrix}\right)\begin{Bmatrix}\varepsilon_{11}\\ \varepsilon_{22}\\ \varepsilon_{12}\end{Bmatrix}. \tag{6.7}$$

According to equation (6.1), one can define $\theta_1=2\mu$, $\theta_2=-4\mu^2/(\lambda+2\mu)$, and

$$\mathbf{H}_1=\begin{bmatrix}2&1&0\\1&2&0\\0&0&1\end{bmatrix},\ \mathbf{H}_2=\begin{bmatrix}1&1&0\\1&1&0\\0&0&0\end{bmatrix}.$$

For orthotropic materials under plane stress condition, the Hooke's Law is written as

$$\begin{Bmatrix}\sigma_{11}\\ \sigma_{22}\\ \sigma_{12}\end{Bmatrix}=\begin{bmatrix}Q_{11}&Q_{12}&0\\Q_{12}&Q_{22}&0\\0&0&2Q_{66}\end{bmatrix}\begin{Bmatrix}\varepsilon_{11}\\ \varepsilon_{22}\\ \varepsilon_{12}\end{Bmatrix}, \tag{6.8}$$

where $Q_{11}=E_1/(1-\nu_{12}\nu_{21})$, $Q_{12}=\nu_{12}E_2/(1-\nu_{12}\nu_{21})$, $Q_{22}=E_2/(1-\nu_{12}\nu_{21})$, and $Q_{66}=G_{12}$.

Similarly, one can define $\theta_1=Q_{11}$, $\theta_2=Q_{12}$, $\theta_3=Q_{22}$, $\theta_4=2Q_{66}$, and

$$\mathbf{H}_1=\begin{bmatrix}1&0&0\\0&0&0\\0&0&0\end{bmatrix},\ \mathbf{H}_2=\begin{bmatrix}0&1&0\\1&0&0\\0&0&0\end{bmatrix},\ \mathbf{H}_3=\begin{bmatrix}0&0&0\\0&1&0\\0&0&0\end{bmatrix},\ \mathbf{H}_4=\begin{bmatrix}0&0&0\\0&0&0\\0&0&1\end{bmatrix}.$$

The standard FEM system of equations for elastic problems can be expressed as

$$\mathbf{K}\left(\mathbf{H}\left(\boldsymbol{\theta}\right)\right)\mathbf{u}=\mathbf{F}^{ext}. \tag{6.9}$$

With the decomposed Hooke's tensor, the global stiffness matrix can be set in the form

$$\mathbf{K}\left(\mathbf{H}\left(\boldsymbol{\theta}\right)\right)=\mathbf{K}\left(\sum\theta_i\mathbf{H}_i\right)=\theta_i\tilde{\mathbf{K}}\left(\mathbf{H}_i\right). \tag{6.10}$$

Apparently,

$$\tilde{\mathbf{K}}\left(\mathbf{H}_i\right)=\frac{\partial \mathbf{K}}{\partial \theta_i}, \tag{6.11}$$

which is the sensitivity of $\mathbf{K}$ with regard to θ_i. The convenient form of (6.10) will facilitate the inverse identification procedure.

6.2.2 Solution Procedure

Using the displacement-based optimization approach introduced in Chapter 4, an objective function is defined as

$$\Phi(\boldsymbol{\theta})=\frac{1}{2}\left(\mathbf{u}^*-\bar{\mathbf{u}}\right)^T\left(\mathbf{u}^*-\bar{\mathbf{u}}\right). \tag{6.12}$$

where $\mathbf{u}^*$ is the displacement vector computed from equation (6.9), and $\bar{\mathbf{u}}$ is the displacement measured from DIC. With the linearized form (6.10), the gradient and Hessian of $\Phi(\boldsymbol{\theta})$ can be derived analytically:

$$\nabla\Phi=\nabla\mathbf{u}^*\left(\mathbf{u}^*-\bar{\mathbf{u}}\right), \tag{6.13}$$

$$\nabla^2\Phi=\left(\nabla^2\mathbf{u}^*\right)\left(\mathbf{u}^*-\bar{\mathbf{u}}\right)+\left(\nabla\mathbf{u}^*\right)\left(\nabla\mathbf{u}^*\right)^T. \tag{6.14}$$

where each component of $\nabla\mathbf{u}^*$, $\frac{\partial \mathbf{u}^*}{\partial \theta_i}$, can be derived using (6.9) and (6.10):

$$\begin{aligned}\frac{\partial \mathbf{u}^*}{\partial \theta_i}&=\frac{\partial \mathbf{K}^{-1}\mathbf{F}^{ext}}{\partial \theta_i}\\&=-\mathbf{K}^{-1}\mathbf{K}_i\mathbf{K}^{-1}\mathbf{F}^{ext}\\&=-\mathbf{K}^{-1}\mathbf{K}_i\mathbf{u}^*\end{aligned}. \tag{6.15}$$

Furthermore, each component of $\nabla^2\mathbf{u}^*$, explicitly as $\frac{\partial^2 \mathbf{u}^*}{\partial \theta_i \partial \theta_j}$, can also be derived

$$\frac{\partial^2 \mathbf{u}^*}{\partial \theta_i \partial \theta_j}=\mathbf{K}^{-1}\mathbf{K}_j\mathbf{K}^{-1}\mathbf{K}_i\mathbf{u}^*+\mathbf{K}^{-1}\mathbf{K}_i\mathbf{K}^{-1}\mathbf{K}_j\mathbf{u}^*. \tag{6.16}$$

Efficient Newton-Raphson algorithm can be applied with the availability of $\nabla\Phi$ and $\nabla^2\Phi$:

$$\nabla^2\Phi\left(\boldsymbol{\theta}^{(m)}\right)\left(\boldsymbol{\theta}^{(m+1)}-\boldsymbol{\theta}^{(m)}\right)=-\nabla\Phi\left(\boldsymbol{\theta}^{(m)}\right), \tag{6.17}$$

where m denotes the m^{th} iteration. In fact, the Newton-Raphson algorithm is preferred over the Nelder-Mead method. This is because although for both methods, the global stiffness matrix, $\mathbf{K}(\boldsymbol{\theta})$, needs to be recalculated using the updated $\boldsymbol{\theta}$ and then be inverted to compute $\mathbf{u}^*$, however, convergence rate of the Newton-Raphson method is much faster than the Nelder-Mead method.

6.2.3 Displacement Field by DIC

The loading of the FRCC 4-point bending test is displacement (crosshead) controlled at a rate of 0.2 mm/min. The load versus crosshead displacement curves for the four FRCCs are shown in Figure 6.3. Notice for 2% and 3% FRCCs, the ratios of the limit of proportion to the ultimate strength are relatively small. Multiple images are taken for each specimen for DIC measurement. However, only those images taken at not too low a load level, but before the specimens start to crack are suitable for inverse analysis to exact the elastic properties. In addition to the reference image taken at zero loading, two deformed images are used for each specimen.

Table 6.2: Loadings when specimen images are taken for DIC, in N (note: FRCC-0.5 means the FRCC has 0.5% fiber volume fraction, same for the rest specimen IDs)

	Reference point	Deform 1	Deform 2
FRCC-0.5	0	440	585
FRCC-1	0	480	723
FRCC-2	0	597	866
FRCC-3	0	596	992

The full-field DIC is used to measure the displacement field within the region of interest (Figure 6.1). A typical displacement field is shown in Figure 6.4, with DIC resolution equals 17.6 μm/pixel. Notice the very small displacement variation over the

region of interest: 1.9 pixels over a width of 3414 pixels for u_x and 1.3 over a height of 1480 pixels. The corresponding maximum compression or tension strain at top or bottom fibers is 0.56×10^{-3}. Comparing to the typical strain measured for DIC (Figure 5.8), which is close to 4×10^{-3}. This is expected, as the Young's modulus of FRCC is about an order of magnitude larger than that of PMMAs. Although for such small displacement level the measurement is prone to noise, the smooth field shown in Figure 6.4 indicate that the full-field DIC can is not very sensitive to local noise but maintain the global feature of the displacement field. As said, however, the relative accuracy is still controlled by the displacement level due to the finite resolution of DIC. Using the conservative resolution of the full-field DIC, 0.05 pixel, which is three times of the resolution evaluated in Chapter 3 and summarized in Table 3.1, the estimated relative error for the strain measurement will be $\pm 0.05/1.9 = \pm 2.6\%$ for ε_x, and $\pm 0.05/1.3 = \pm 3.8\%$ for ε_y. This bound of relative error estimates will be translated to the final error of the computed elastic properties.

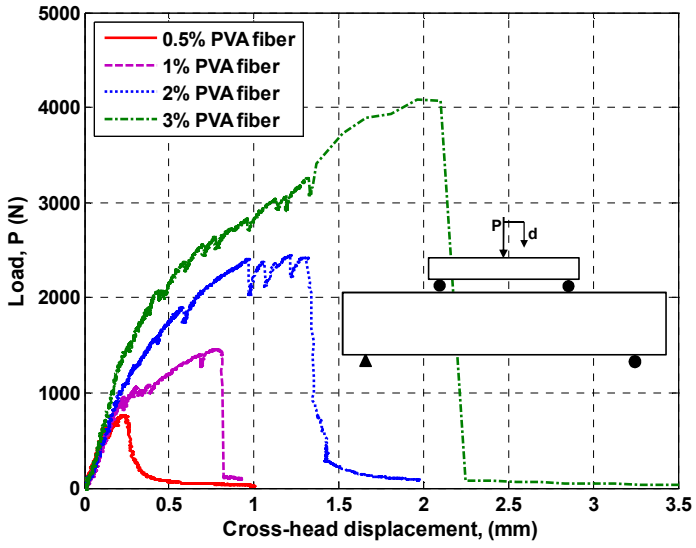

Figure 6.3: Load versus displacement curves for FRCCs with different fiber volume fractions

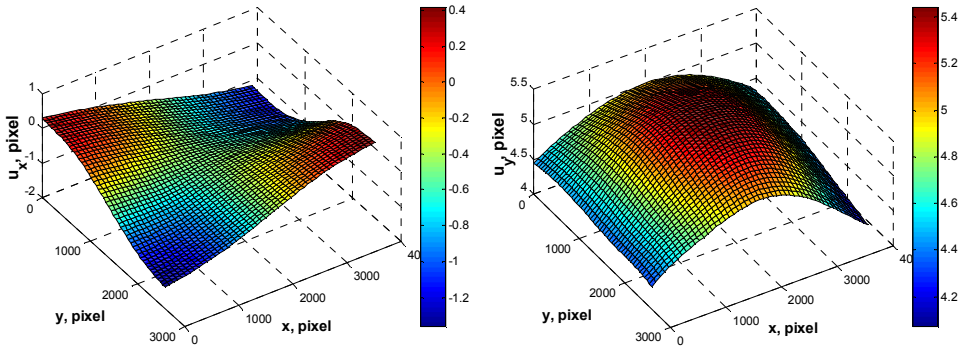

Figure 6.4: Surface plot of displacement field u_x and u_y by DIC for FRCC-3 bending specimens at P = 992 N

6.2.4 Computed Bulk Elastic Properties

Assuming the FRCC is isotropic and homogeneous, starting with an initial guess of E = 10 GPa and v = 0.2 for the Newton-Raphson procedure described previously, the inversely computed properties can be obtained in few iterations. The computed as well as the initial and final values of the cost function, and the number of iterations reaching convergence are summarized in Table 6.3. The computed Young's moduli and Poisson's ratios are also shown in Figure 6.5. For each specimen, the computed E and v are accurate: the difference computed at the two different loads for the same specimen is less than 7% for E and 6% for v. The Poisson's ratios computed from higher load data are consistently lower than those computed from lower load data. The lower Poisson's ratio may be more accurate due to higher deformation at higher loads reduce the relative DIC measurement errors. The presence of PVA fibers does not affect the bulk elastic properties, which is expected. The PVA fiber has a Young's modulus of 37 GPa, which is not significant higher than that of ordinary cement paste, which is in the range of 10-20 GPa. In addition, rule of mixture for composite also indicates that for small volume fraction of one component, less than 3% PVA fiber for current FRCC, the bulk elastic properties are determined by the prevalent component.

Reference [66] has reported a 2% PVA FRCC with a 20.3 GPa Young's modulus and reference [123] has reported 18.7 GPa for a 2.8% PVA ECC. However, both references do not provide the measurement for Poisson's ratio. It has been generally accepted that

concrete has a Poisson's ratio between 0.15 and 0.2 [1,124], depending on the mix proportion. The FRCC is primarily composed of cementitious matrix, thus the lower-end Poisson's ratio, 0.15, shall be expected for FRCC. This correlates very well with the computed Poisson's ratios.

Table 6.3: The inverse computed isotropic elastic properties

	Initial guess		Load level	Converged results		$\Phi\left(\boldsymbol{\theta}^{(0)}\right)$	$\Phi\left(\boldsymbol{\theta}^{(n)}\right)$	# of iterations
	E, GPa	ν		*E*, GPa	ν			
FRCC-0.5	10.0	0.2	440 N	17.9	0.150	0.0015	0.000212	11
			585 N	18.1	0.141	0.0033	0.000376	16
FRCC-1			480 N	17.6	0.148	0.0019	0.000293	10
			723 N	17.7	0.142	0.0043	0.000540	15
FRCC-2			597 N	18.5	0.149	0.0029	0.000411	9
			866 N	18.3	0.144	0.0068	0.000798	14
FRCC-3			596 N	19.0	0.147	0.0032	0.000446	8
			992 N	20.4	0.141	0.0106	0.000825	12

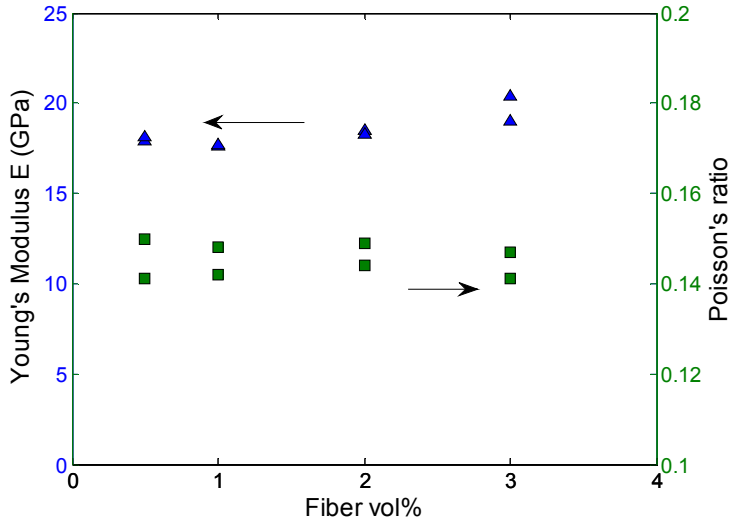

Figure 6.5: The computed Young's modulus and Poisson's ratio versus fiber volume fraction

The convergence rate of Newton-Raphson algorithm is much faster in comparison to the Nelder-Mead optimization method. An illustration of a typical evolution of the *E* and *v* during optimization is shown in Figure 6.6, for the FRCC-3 specimen at the higher load. As can be seen, the convergence of *v* is faster than the convergence of *E*. The

horizontal displacement is almost solely sensitive to E while the variation of vertical displacement is sensitive only to v. For the particular experimental setup, it may be easier for v to converge.

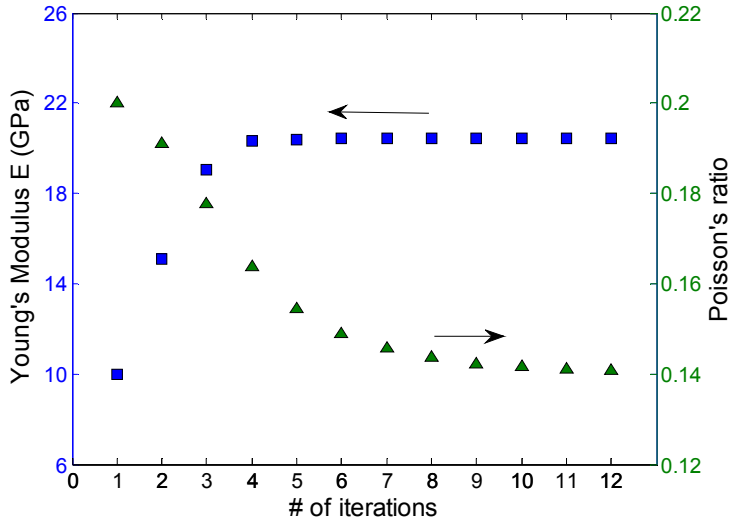

Figure 6.6: Evolution of the computation of Young's modulus and Poisson's ratio for FRCC-3 with DIC taken at load = 992 N

In the subsequent computation of the FRCC cohesive properties, the average of E and v computed at higher and lower loads for each FRCC are used. As will be shown, the dominant deformation of an FRCC SENB specimen under fracture is the rigid body rotation; the computation of CZM may be sensitive to the accuracy of the bulk E and v. However, this is beyond current interest of exploration.

6.3 EXTRACTION OF CZM THROUGH DIC AND INVERSE ANALYSIS

The global response of the fracture test on the FRCC SENB specimens, load P versus CMOD and load P versus displacement, are shown in Figure 6.7 and Figure 6.8, respectively. In both figures, all the curves show multiple vertical short drops. Those are the points when the testing is held for taking the DIC images. Since the loading is CMOD

rate controlled, the *P* versus CMOD curves are smoother than the *P* versus d curves. The short load drops are due to the readjustment of the fractured specimens. The DIC images are taken when the load reading is stable, which corresponds to the lower point of the drops. The corresponding load level when the images are taken are recorded and used in the FEM-DIC inverse analysis as the key force boundary conditions.

As have been discussed in Chapter 4, only the deformation fields measured at post-peak range are appropriate for the inverse analysis. Therefore, three points are used at different load levels for each specimen, as indicated by the black circles in Figure 6.7.

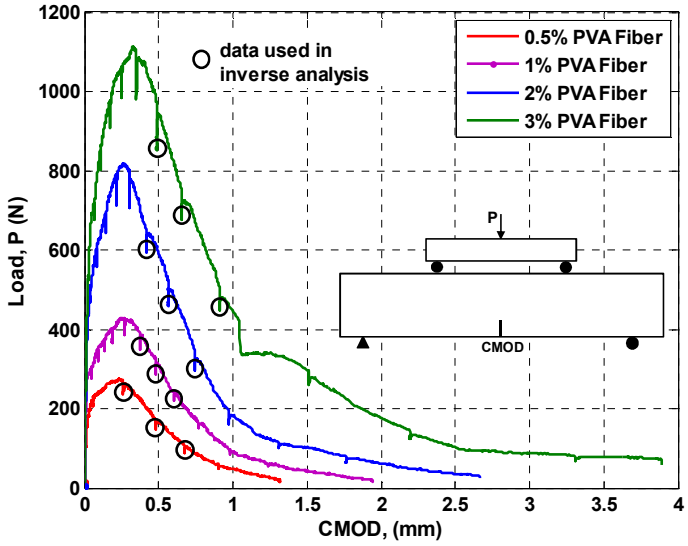

Figure 6.7: Load versus CMOD for FRCC with different fiber volume fractions

The fracture energy can be well estimated from area under the load versus load-line displacement curves (Figure 6.8). The testing fractured the specimen completely, however, the area under the unrecorded part of the *P* versus *d* curve shall be negligible. In addition, due to the missing part of the curve, the fracture energy estimated will be the lower bound of the actual fracture energy. The computed fracture energies for all specimens are listed in Table 6.4. This fracture will be used to construct the initial CZM guess for the inverse computation. In addition, it can also be a reference of comparison for the computed CZM, which shall have slightly higher fracture energy.

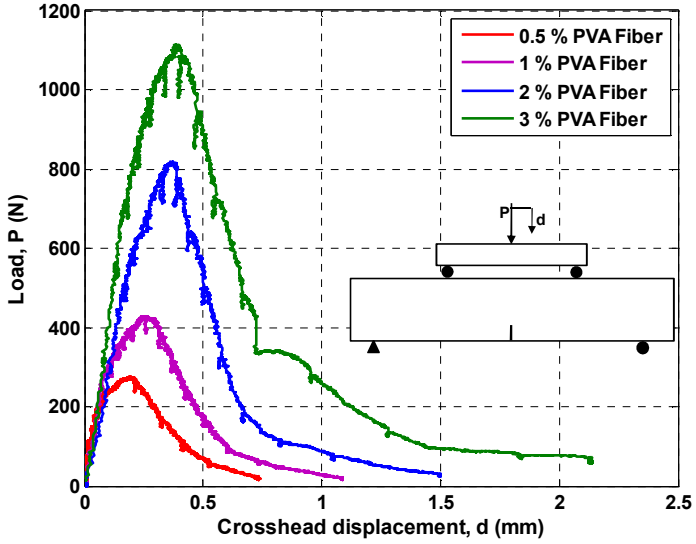

Figure 6.8: Load versus load-line displacement for FRCC with different fiber volume fractions

Table 6.4: FRCC fracture energies estimated from load versus load-line curves

	FRCC-0.5	FRCC-1	FRCC-2	FRCC-3
G_f, N/mm	0.44	0.87	1.90	3.58

6.3.1 Displacement Fields

The procedure outlined in Chapter 5 is used for the measurement of the displacement field of the FRCC SENB specimens. A typical post-peak DIC image is shown in Figure 6.9. The distance between the two loading point is 60 mm, or 3400 pixels. This corresponds to a camera resolution of 17.7 μm/pixel. Notice that it is hard to see any elastic deformation of the specimen visually due to the very low cohesive strength to elastic modulus ratio of the FRCC specimen. One can see the effectiveness of the groove in constraining the crack path.

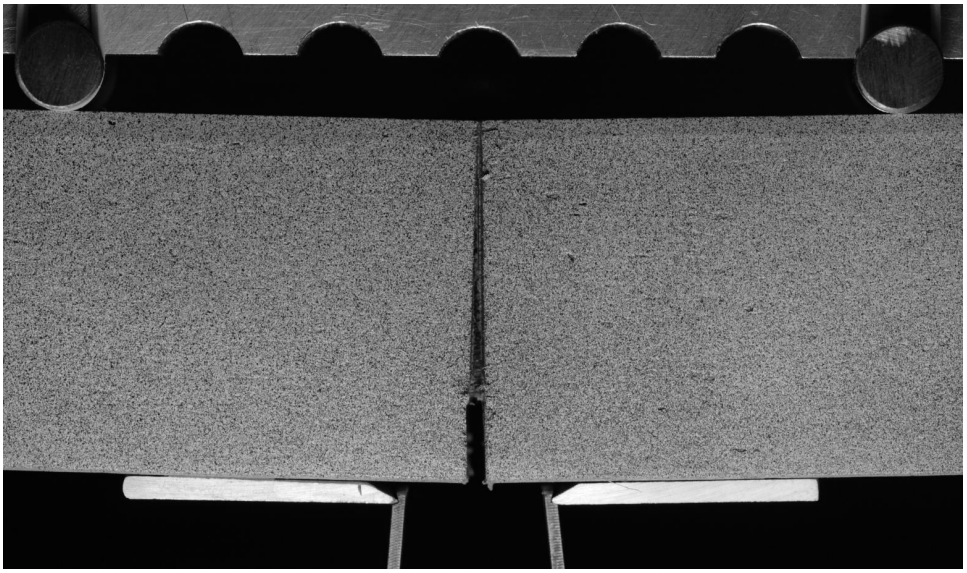

Figure 6.9: Typical DIC image of the FRCC SENB taken at a post-peak point

An illustration of the displacement fields measured by DIC for the FRCC-1 specimen at the three load levels indicated in Figure 6.7 is shown in Figure 6.10. As seen, the parallelism of the field isolines to the direction of the displacement to be measured shows that displacement field is dominated by the rigid-body components of the displacement field. As FRCC matrix is very brittle, the post-peak crack tip location does not change significantly, at least not indicated from the measurement.

6.3.2 Inverse Computation of the CZM

The initial guess of the CZM for the inverse computation is constructed using the same procedure as presented in Chapter 4. The displacement field measured at each load level is used as an individual set to compute the CZM, thus there are three sets of computed CZMs corresponding to the three displacement field measurements. The computed CZMs are shown in Figure 6.11 to Figure 6.14 for the FRCC with 0.5%, 1%, 2% and 3% PVA fibers, respectively.

From the computed CZM curves, first, the CZMs corresponding to the two higher loads are more consistent in the computed shape while the one corresponding the lowest load deviates from the former two. The computed critical stress (at $\Delta_n = 0$) decreases with decreasing load level. All computed FRCC CZMs show bi-linear characteristic, with an

initial hardening curve, followed by a linear softening cohesive stress. The kink points are all around one-sixth of the critical separation. The critical stress and critical separation of the CZMs increase with increasing fiber volume fractions.

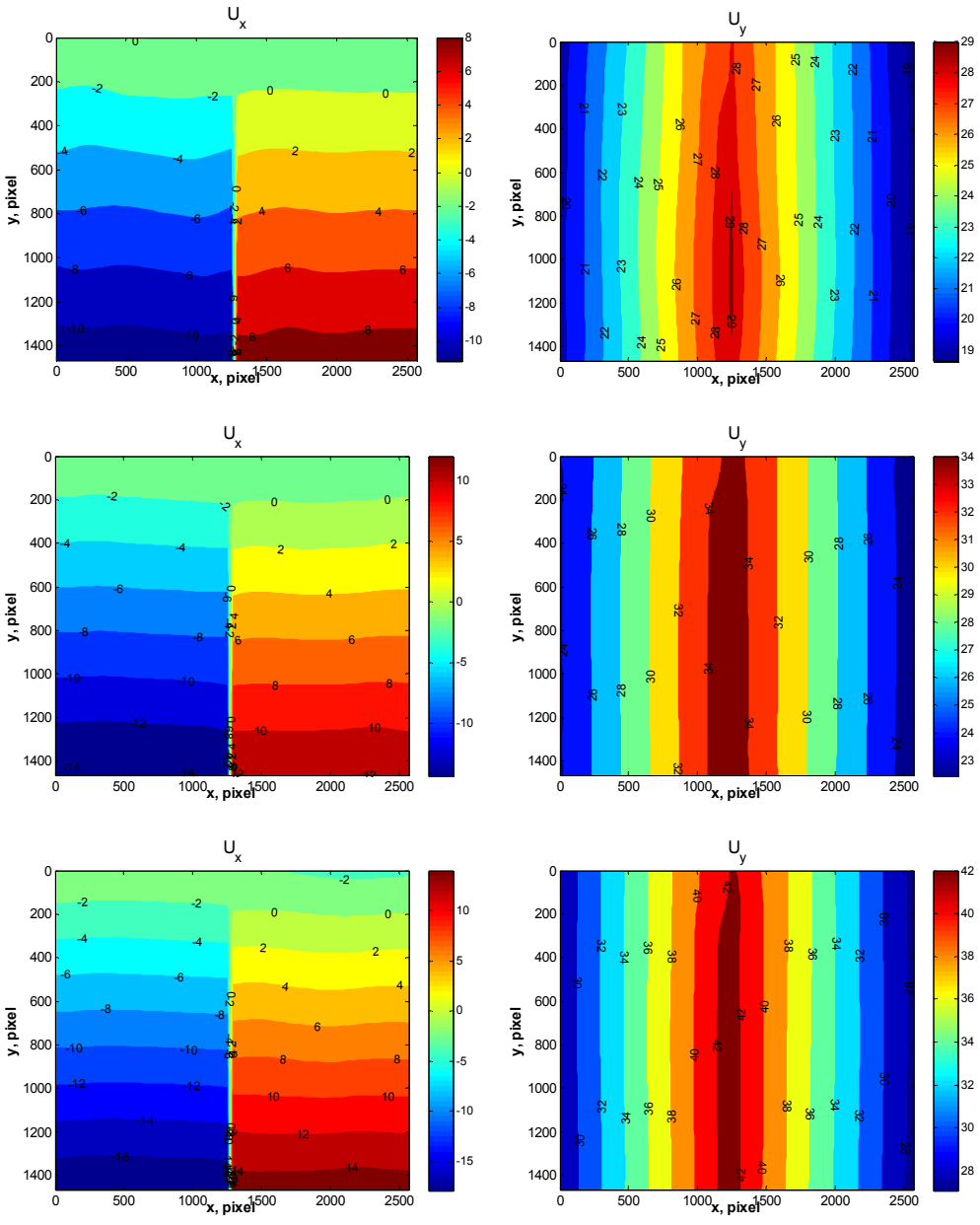

Figure 6.10: Displacement field measured by DIC for the FRCC-1 specimen at three post-peak load levels; left: horizontal displacement, right: vertical displacement; measurement unit: pixel

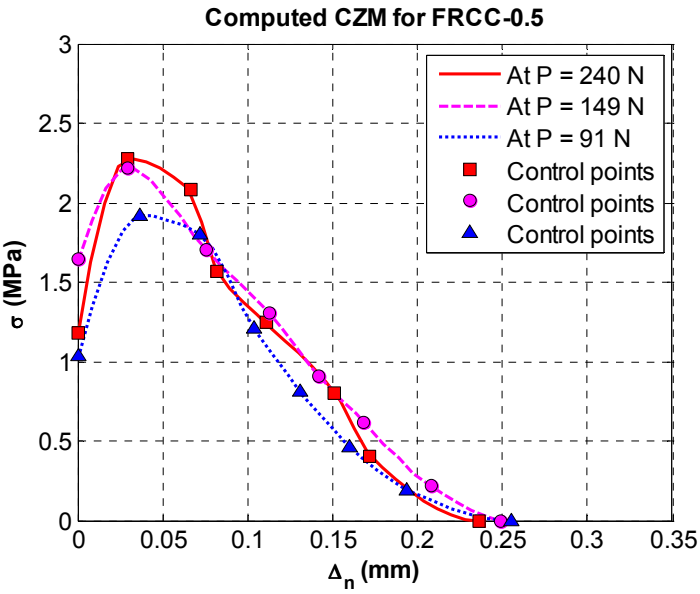

Figure 6.11: Inverse computed CZMs for FRCC with 0.5% PVA fiber

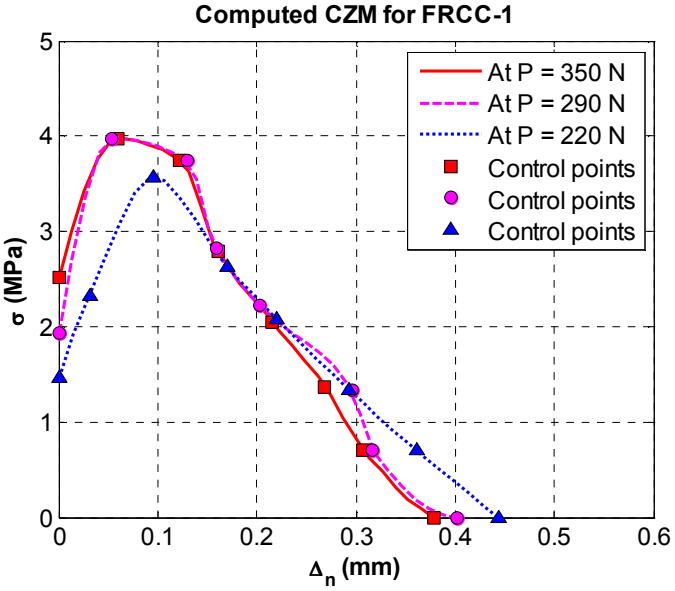

Figure 6.12: Inverse computed CZMs for FRCC with 1% PVA fiber

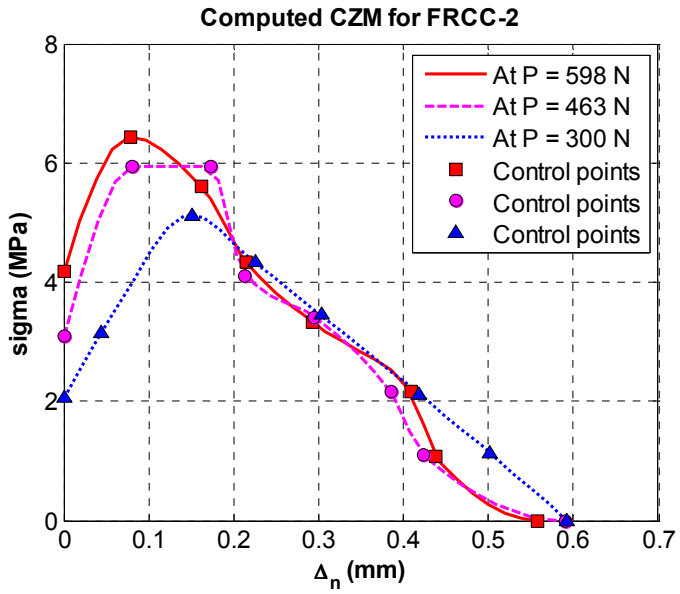

Figure 6.13: Inverse computed CZMs for FRCC with 2% PVA fiber

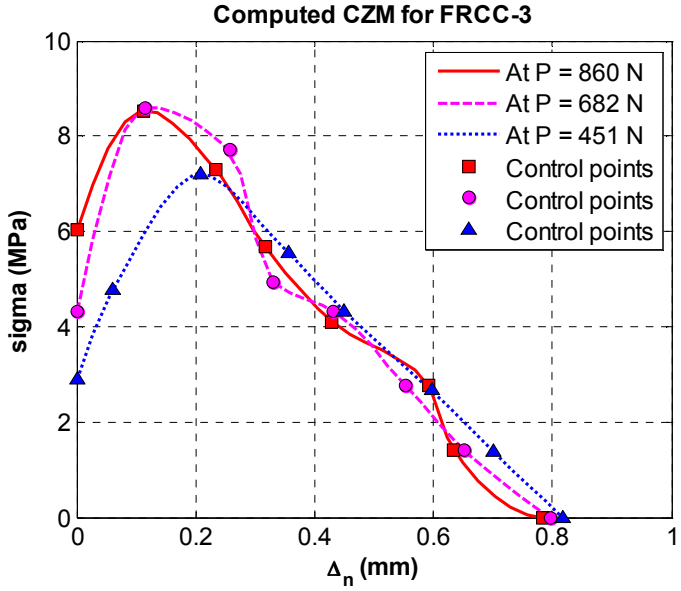

Figure 6.14: Inverse computed CZMs for FRCC with 3% PVA fiber

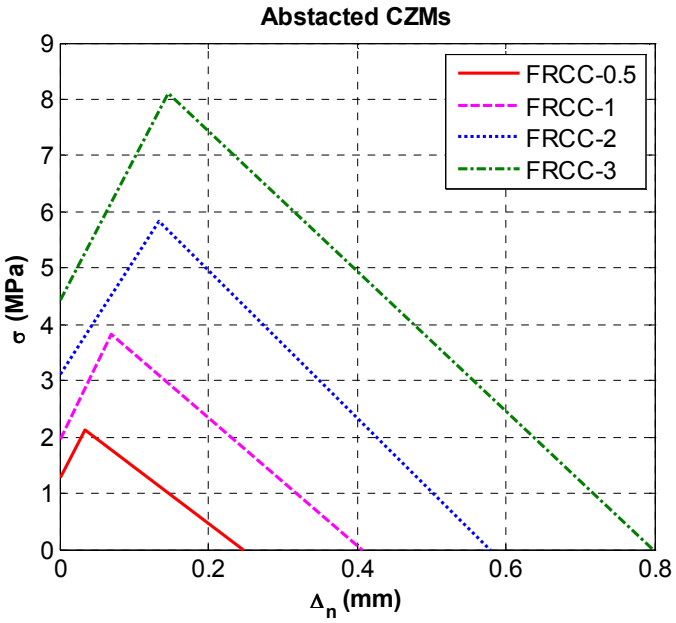

Figure 6.15: Comparison of the computed CZMs of FRCC with different fiber volume fractions

Averaging all three computed CZMs for each specimen and applying a bilinear least square fit, the computed CZM can be abstracted. A comparison between the abstracted CZMs is made as shown in Figure 6.15. All the CZMs show similar slope for the initial stress drop. The COD at the kink point increases with increasing fiber volume fractions. The characteristic of shapes of the computed CZMs conform to the experimental observation reported from [54,120].

Taking the average results of CZMs at higher loads, the critical stress σ_{cr}, critical separation Δ_{nc}, maximum stress σ_{max} and corresponding COD Δ_{np}, and the fracture energy can be computed, which is shown in Table 6.5. The critical stress of the FRCC has a linear relation with respect to fiber volume fraction (Figure 6.16). This is expected as the tensile strength of FRCC is controlled by the volume fraction of the fibers. On the other hand, the fracture resistance also increases with increasing fiber volume fraction. Such effect reflects in the averaged CZM model as the increased critical stress. The increase of critical separation with fiber volume fraction conforms to the increased ultimate CMOD measured (Figure 6.7). Table 6.5 also shows the fracture energy

computed from global response curve, *P* versus *d*. The fracture energies computed from two very different methods are close (Figure 6.17), except for FRCC-0.5. It has been explained that the fracture energy from computed CZM shall be higher than the one computed from *P* versus d curve. If only the CZM computed from the highest load is used to compute the fracture energy, the value will be slightly higher and may be more reasonable. At the current stage, this is not of the major interest and there is no sufficient amount of experiments to quantify the exact difference. The fracture energy is also proportional to the fiber volume fraction, which is expected as the cement matrix has negligible fracture energy in comparison to the fracture of PVA fibers.

Table 6.5: Critical cohesive stress, critical separation and fracture energy computed CZM, also listed is the fracture energy computed from global curve

	FRCC-0.5	FRCC-1	FRCC-2	FRCC-3
σ_{cr}, MPa	1.277	1.970	3.102	4.421
σ_{max}, MPa	2.137	3.840	5.834	8.117
Δ_{np}, mm	0.033	0.069	0.134	0.146
Δ_{nc}, mm	0.247	0.408	0.580	0.800
G_f, N/mm (from CZM)	0.261	0.860	1.834	3.563
G_f, N/mm (from P-d curves)	0.274	0.87	1.90	3.58

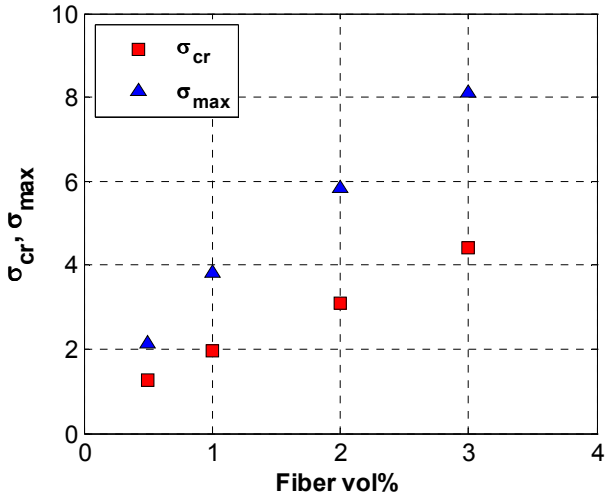

Figure 6.16: FRCC critical stress versus fiber volume fraction

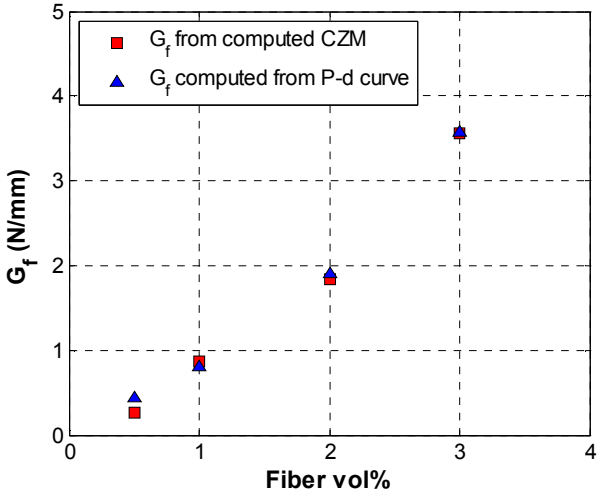

Figure 6.17: Fracture energy versus fiber volume fraction

6.4 VERIFICATION OF THE COMPUTED CZM

The approach for the verification of the computed CZMs is to use it in the direct simulation to obtain the global response and compare with the experimental Since only a few snapshots of the experimental points are used, but not the global response, e.g., P versus CMOD, in the computation of the CZMs, thus verification by comparing to the global response is somewhat justified. The FEM simulated *P* versus CMOD curves are plotted together and shown in Figure 6.18.

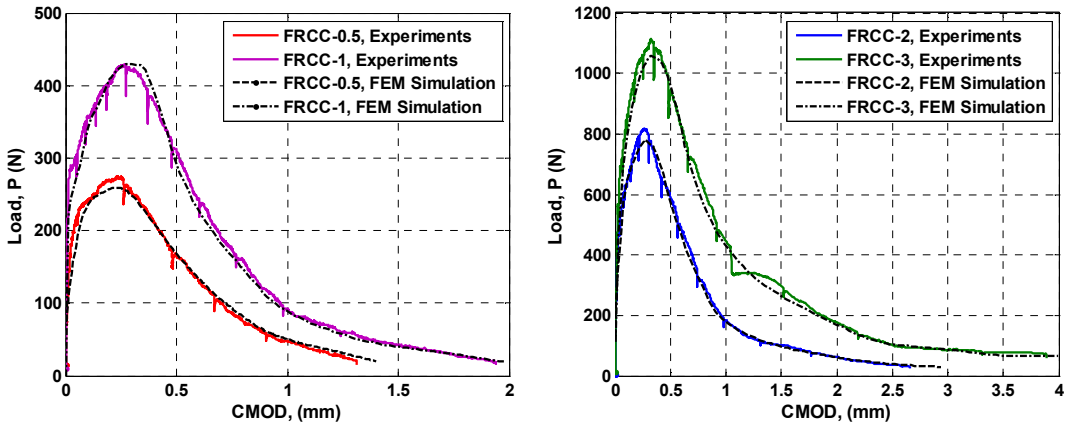

Figure 6.18: Comparison experiment and FEM simulation of the P versus CMOD curves (FEM simulation use the inverse computed CZMs)

It can be seen from Figure 6.18 that the computed results match very well to the experimental results. This is consistent with the study carried out for plastics, which is presented in Chapter 5. Notice the particular good match of the curves for the softening part of the curves. The initial portion of the curves is only elastic, and the FEM simulations match well with the experiments, which indicate that the measured Young's modulus and Poisson's ratio are accurate. However, the FEM simulation of the onset of cracking is lower than the experiments. This is expected, because the CZM is not able to capture the very high stress concentration presents at the sharp crack tip.

6.5 MIXED-MODE FRACTURE OF FGFRCC: EXPLORATORY INVESTIGATION

In this section, preliminary investigation on the fracture behavior of FGFRCC under mode I and mixed-mode loadings is presented using SENB fracture specimens. The specimens are made from uniform FRCCs with four different fiber volume fractions: 0.5%, 1%, 2% and 3%. The configuration of the FGFRCC is that the fiber volume fraction is graded monotonically through the beam depth (see Figure 6.19). The nominal dimensions of the FGFRCC specimen are the same as the fracture specimen shown in Figure 6.2. Three-point bending is used for fracture testing. A notch size of about 3mm, which is about half of the thickness of a single FRCC layer, is introduced at different configurations, as shown in Figure 6.19. The FGFRCC SENB specimens are loaded in both normal and reverse loading directions. For mode I fracture, $x = 0$; while for mixed-mode fracture, notches at $x = 0.5L$ and $x = 0.7L$ are introduced. A similar investigation considering pavement materials was conducted by Song [125].

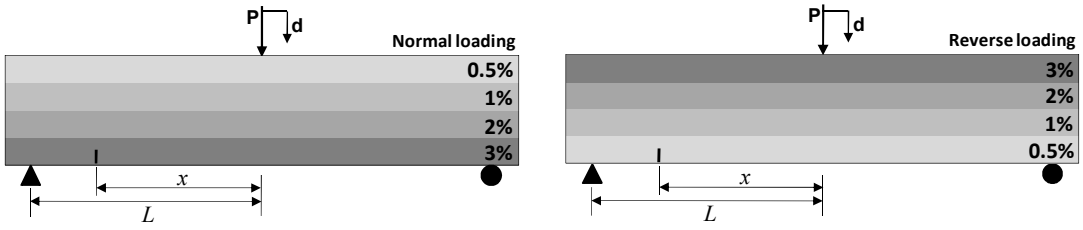

Figure 6.19: Normally and reverse loaded SENB specimens for mode I ($x = 0$) and mixed-mode, ($x > 0$)

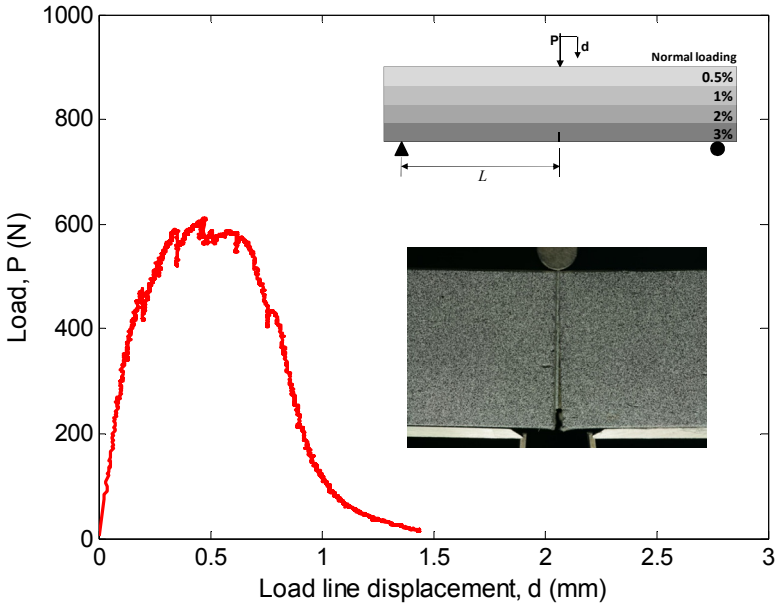

Figure 6.20: Load versus load line displacement for mode I fracture of FGFRCC under normal loading condition

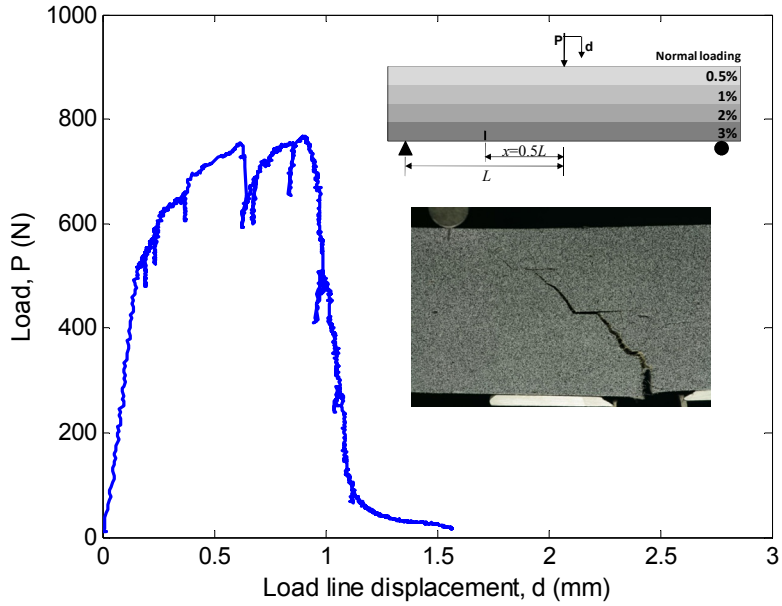

Figure 6.21: Load versus load line displacement for mixed-mode fracture ($x = 0.5L$) of FGFRCC under normal loading condition

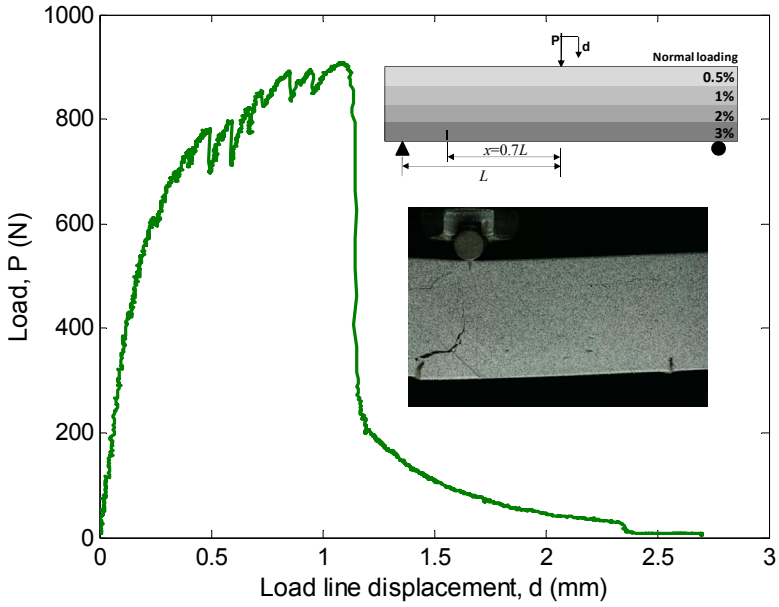

Figure 6.22: Load versus load line displacement for mixed-mode fracture ($x = 0.7L$) of FGFRCC under normal loading condition

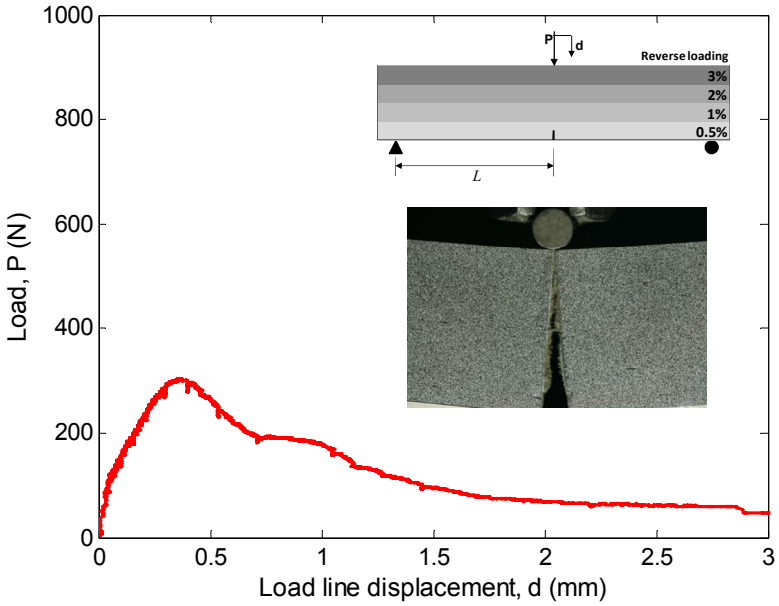

Figure 6.23: Load versus load line displacement for mode I fracture of FGFRCC under reverse loading condition

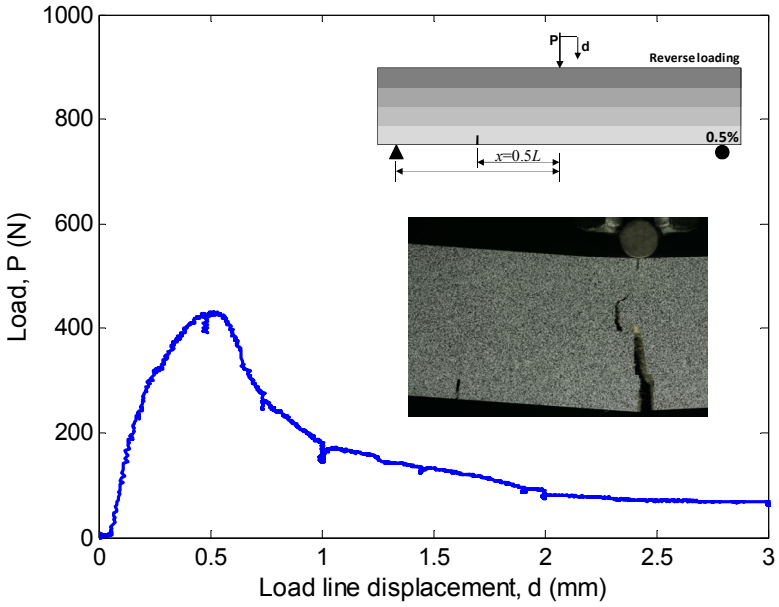

Figure 6.24: Load versus load line displacement for mixed-mode fracture ($x = 0.5L$) of FGFRCC under reverse loading condition

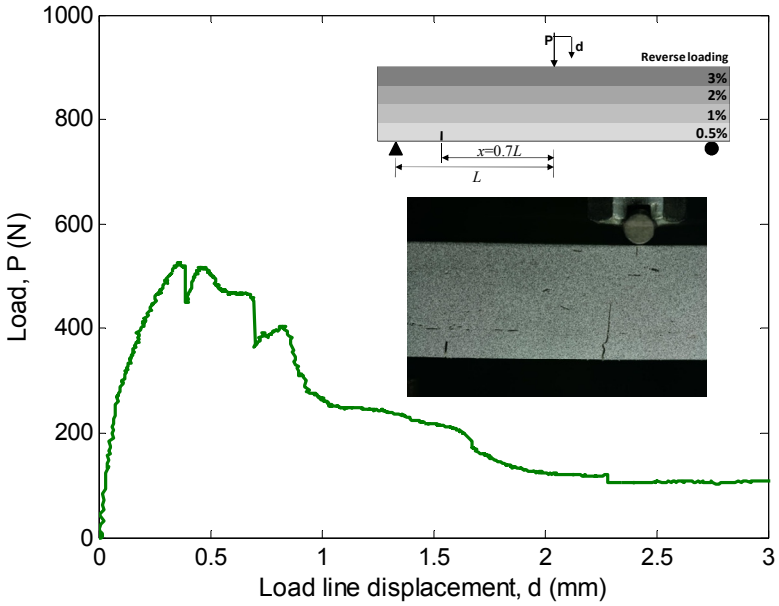

Figure 6.25: Load versus load line displacement for mixed-mode fracture ($x = 0.7L$) of FGFRCC under reverse loading condition

Figure 6.20 to Figure 6.22 show the load, P, versus load line displacement, d, curves for normally loaded FGFRCC at notch offset $x = 0$ (i.e., no offset), $x = 0.5L$ and $x = 0.7L$, respectively. The peak load increases from 601N to 763N to 908N with the increase of the offset of the notch location, x, from 0 to 0.5L to 0.7L, respectively. All curves (P versus d) feature relatively high load carrying capacity with a deflection-hardening plateau followed by sharp drop of the load right after the peak load has been reached.

Figure 6.23 to Figure 6.25 show P versus d curves for reverse loaded FGFRCC at notch offset $x = 0$, $x = 0.5L$ and $x = 0.7L$, respectively. The peak load increases from 301N to 428N to 526N with the increase of the offset of the notch location, x, from 0 to 0.5L to 0.7L, respectively. All responses for reverse loading cases feature low peak loads in comparison to normal loading cases. No apparent deflection-hardening plateau but long post-peak softening is observed. The observed characteristics of the global response, P versus d, due to direction of loading are similar to those of FGFRCC beams presented in section 2.4.3.

As for the fracture initiation location, for normal loading FGFRCC cases, crack initiates at mid-span for mode-I configuration and for notch offset $x = 0.7L$. For notch offset $x = 0.5L$, the crack initiates from the crack tip, resulting in mixed-mode fracture. For reverse loading FGFRCC cases, the crack initiates at mid-span location, which is probably due to the low tensile strength of the 0.5% FRCC layer.

The above discussion is essentially qualitative and is based on phenomenological observation. Replication of the tests is needed in order to obtain quantitative and definite conclusions.

6.6 REMARKS

It has been shown that inverse analysis is particularly useful for measuring the elastic properties simultaneous (Young's modulus and Poisson's ratio in current study). The computed results are quite accurate. Although the DIC resolution is still two to three orders lower than precision laboratory length or strain gages, it uses the whole field data to compute the properties, which counterbalance its relatively low resolution. However,

the advantage is apparent. Tensile testing for brittle composite like FRCC is extremely difficult and can be costly. The use of DIC and FEM inverse technique allows simple bending test setup. No gages are necessary, and a reasonably good camera is sufficient for the precision desired. Furthermore, for orthotropic materials, or even inhomogeneous materials, the DIC and FEM inverse technique shows even greater advantage over traditional methods for the measurement of the multiple elastic properties [122].

The power of this hybrid technique is further illustrated through the extraction of the nonlinear CZMs from FRCCs. The FRCC is a "difficult" material for DIC in that DIC measurement has a low signal-to-noise ratio. However, with proper inverse scheme, it has been shown that good results are still possible. Lastly, the computed CZMs are verified through the same set of experimental test results. It would be more convincing if different experimental tests could be used for the DIC measurements and the computations of CZMs. For example, Figure 6.26 shows the two configurations for mode I fracture tests, where (a) is SENB specimen, and (b) is double edge-notched tension (DENT) specimen. If the CZM is computed from SENB configuration with the DIC-FEM technique, the computed CZM can then be used in the FE simulation for the DENT configuration to obtain the computed global response for DENT configuration. If the computed global response of DENT configuration agrees well with the experimentally measured global response, more confidence is achieved for the computed CZM. The reverse procedure can be used as well, i.e. DENT configuration can be used for the computation of CZM and SENB configuration can be used for the verification.

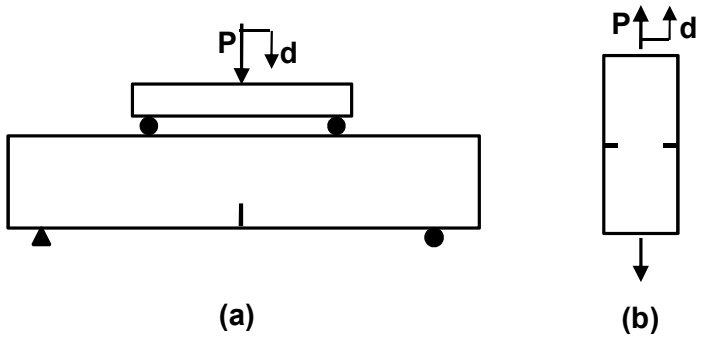

Figure 6.26: Configuration for mode I fracture test, (a) SENB specimen, (b) double edge notched tension specimen

In Figure 6.7, when tests are paused for taking DIC images, specimen self-unloading was observed. This behavior may be due to rate-dependence of the actual cohesive behavior. However, as the self-unloading seem to have little effect on the load level, it may be justifiable to use the rate-independent assumption for the CZMs of the FRCCs. An investigation of rate dependant behavior associated to the CZM can be found in the thesis by Zhang [52].

CHAPTER 7 - CONCLUSIONS AND FUTURE WORK

Three major tasks have carried out in this study: (1) fabrication of a novel functionally graded fiber-reinforced cementitious composites; (2) development of a hybrid DIC-FEM inverse technique for extracting the mode I cohesive fracture properties; and (3) application of the hybrid technique to plastics and FRCCs. In addition, an exploratory investigation of mixed-mode fracture of FGFRCCs has also been conducted. The primary goals are to explore the functionally graded material concept for potential application in FRCC, and to develop a state-of-the-art hybrid experimental-numerical framework for the extraction of the constitutive material properties associated with the nonlinear material behavior. In the concluding chapter, some major conclusions and contributions are presented, followed by a few suggestions for the future work.

7.1 CONCLUSIONS

7.1.1 Fabrication of the FGFRCC

A novel four-layer FGFRCC has been successfully fabricated. A small laboratory-scale extruder was fabricated for the manufacturing of the homogeneous FRCCs with aligned fibers and low water-to-binder ratio. FRCCs with different fiber volume fractions are stacked and pressed to produce an integrated FGFRCC beam with fiber gradation of 0%, 0.67%, 1.33% and 2% through the beam depth. The FGFRCC with 1% overall fiber volume fraction shows higher flexural strength and work of fracture compared to the homogeneous FRCC with similar fiber content. The enhancement is anticipated, yet the significance is in the successful distribution of fibers. The FGM system avoids the potential interface problem commonly seen in binary material systems. No interface delamination and cracking has been observed for the FGFRCC during bending tests.

Microstructure verification of this new FGFRCC needs proper facilities such as the SEM used in current study. The SEM images show seamless transition between adjacent FRCC layers. In addition, image processing is important in the quantification of the microstructure of FGFRCC.

The successful fabrication of FGFRCC lies in the proper matching of plasticity between layers. This is particularly difficult due to the many material ingredients in the FRCC layers, and the significant change of plasticity when fiber content varies. It has been shown that incompatible layers result in an FGFRCC with wavy inter-layer boundaries and uneven layer thickness. For pressing of extruded FRCCs, it was found that extrusion pressure is a good index to find plasticity-matched FRCC layers.

7.1.2 Adoption of a Full-Field DIC

A new full-field DIC program, which is available in the area of biological research, is adopted for the current study. It assumes a continuous, smooth elastic displacement field for the whole region, which is correlated simultaneously. This is in contrast to the traditional DIC algorithm, which is subset based with the assumption of a uniform Taylor's approximation of the kinematic field for each sub-region that is correlated independently.

A MATLAB program has been implemented to post-process the output from the full-field DIC program. An in-house subset DIC was also implemented for the purpose of verification of the full-field DIC and benchmark comparison with the full-field algorithm. For the latter purpose, an image transformation algorithm was implemented to generate an arbitrary displacement field.

The benchmark is carried out through a heterogeneous displacement field. The measurement errors of full-field DIC is about half of those by subset DIC. Near the image boundaries, the full-field DIC has much higher accuracy than the subset DIC. A relevant conclusion of the study is that the DIC accuracy depends not just on the algorithm, but also on the actual deformation investigated.

7.1.3 Hybrid Inverse Technique

The DIC-FEM inverse procedure has been implemented in MATLAB based on both displacement-based and residual-based formulations. The key contribution in this inverse procedure is that no "*a priori*" assumption is made on the shape of the CZM. Flexible splines are used to construct the CZM, and the ordinates of the control points become the unknown to be optimized in the inverse problem. The Nelder-Mead (N-M) method is

employed for the optimization procedure. The derivative-free feature of the N-M method enables the implementation of: (1) the parametric mapping used in the residual-based formulation; (2) barrier and regularization functions used in the displacement-based formulation.

In the numerical examples, SENB specimens are used and the synthetic displacement fields are obtained from the direct problem. The residual-based procedure demonstrates the verification of the solution within the valid parametric space. The displacement-based procedure focuses on the evaluation of the error tolerance. The results demonstrate that the error tolerance heavily depends on the ratio between the cohesive strength to the bulk modulus of elasticity. The higher this ratio, the more tolerant the inverse procedure is for the satisfactory estimation of the CZMs.

7.1.4 Extraction of CZMs of Plastics and FRCCs

The DIC-FEM inverse procedure is applied to two plastics, an adhesive: Devcon® Plastic Welder™ II (PW-II) and a high-strength and high-toughness composite: Garolite G-10/FR4. The substrate, or bulk, material for the adhesive is PMMA. The displacement-based approach is used for both the plastics and the FRCCs.

For the plastics, the DIC measured displacement field can be used directly for accurate estimation of the Young's modulus and Poisson's ratio. Both plastics show high ratios of cohesive strength to bulk modulus of elasticity, which result in the particularly consistent measurement between different data sets. The computed CZM of the PW-II shows a bilinear softening curve, while for Garolite the computed CZM shows a power-law softening behavior.

For the FRCCs, the ratio of cohesive strength to bulk modulus of elasticity is much lower than that of the plastics. Direct estimation of the Young's modulus and Poisson's ratio from the DIC measured displacement field is inaccurate. Instead, an inverse procedure is applied using pure bending tests to extract the Young's modulus and Poisson's ratio of the FRCCs. The results are consistent between FRCCs with different fiber content. The Young's modulus increases slightly with increasing volume fraction of PVA fibers, while the Poisson's ratio remains constant. The computed CZMs for FRCCs

all show an initially hardening curve followed by an almost linear softening curve. Four parameters can be used to describe the CZMs of FRCC, namely, the critical stress, the peak cohesive stress and associated crack opening displacement, and the critical separation. All four parameters increase with increasing fiber volume fraction. The characteristic CZM curves of FRCCs conform to recent experimental observations.

The computed CZMs are used in the direct problems. The computed global responses are compared with experimental ones, which show very good agreement.

7.1.5 Contributions

In a summary, the primary contributions are listed as follows:

- Successful fabrication of a novel FGFRCC, including development of a novel tailored extrusion and pressing system;
- Utilization of a full-field DIC program in the mechanics of elasticity with enhanced accuracy of measurement;
- Implementation of a universal image transformation algorithm for the benchmark test of DIC;
- Development and implementation of a hybrid DIC-FEM inverse procedure using Newton-Raphson solver for the extraction of material elastic properties;
- Development and implementation of a hybrid DIC-FEM inverse procedure for the extraction of the local mode I cohesive properties;
- Demonstration of the practical effectiveness of the inverse procedure for two plastics and FRCCs.

7.2 FUTURE WORK

This work offers room for further investigation. A few potential research areas are highlighted below. Two suggestions are related to the FGFRCC, while the remaining ones are related to the DIC and FEM.

7.2.1 New Fabrication Method of FGFRCC

There is no limit in the processing method of FGFRCC. In fact, exploration of effective, efficient and stable techniques is the most important topic in the list of future works because only realization of a useful product would make the associated research meaningful. Besides the extrusion and pressing techniques, two other relatively simple techniques, precast of self-consolidating FRCC and shotcrete, have the potential, as described below.

Self-consolidating concrete, or SCC, has been widely used in construction industry. The self-consolidating FRCC has been an active research area. The ease of forming of the self-consolidating FRCC will enable the manufacturing of directionally graded FGFRCC with arbitrary configuration. The biggest challenge, however, is to obtain the desired rheological property of each layer. Thus, this research work is material science oriented.

Shotcrete has been an effective method to produce medium size cement-based components. If the feeding rates of the paste and fibers can be controlled dynamically and precisely, an FGFRCC with almost smooth gradation of fibers can be manufactured. The practical challenge, however, is that expensive facilities are needed.

7.2.2 Optimal Design of FGFRCC

For a fixed fiber volume fraction, the mechanical performance of an FGFRCC depends on the profile of the fiber gradation. In addition, different applications may have different optimal gradation profile. For example: monotonic gradation of fibers is appropriate for an FGFRCC beam that carries only positive moment, while a gradation with decreasing fiber content towards the beam neutral axis is more suitable for FGFRCC beam that carries both negative and positive moments. Therefore, the design of FGFRCC cannot be solely based on experimental trial and error. Appropriate model, either analytical or numerical must be adopted to compute the optimal configuration that satisfies a certain requirements. For the integrated design of FGFRCC that also involves the determination of component dimension, materials usage, material costs, etc., numerical optimization technique might be the most versatile tool.

7.2.3 Development of DIC for Multiple Cracks

So far, the DIC techniques used in kinematic field measurement are primarily for the continuous field. While the subset DIC can be used to find the crack location approximately, it lacks the ability to correlate the subset accurately (that covers part of a crack) representing a disruption of the kinematic field. When the crack path is known, as is the case in current study, the full-field DIC can still be used on each side of the crack. There are many situations where accurate information of multiple cracks needs to be extracted. The complete information about the cracks includes the crack path and crack opening displacement. At the same time, when there are tractions on the crack surface, the deformation field of the base material near the crack may also need to be accurately measured. Traditional DIC is incapable of these requirements. A new algorithm of DIC may need to be developed with the capability to measure such non-continuous fields capturing crack interaction phenomenon.

One immediate application of the anticipated new DIC algorithm is related to the future work mentioned in the next section. For mixed-mode cracking, there may be only one crack, but the crack path is not smooth and fully known. The new DIC algorithm shall be able to measure accurately the crack tip location, the complete crack path, and COD profile for the non-straight crack path.

7.2.4 Mixed-mode Cracking: cohesive and non-cohesive

The natural extension of the inverse computation of mode I CZM is the computation of mode II CZM, and furthermore, the mixed-mode CZM. The mode I and mode II CZMs may be computed separately using two different test configurations. However, when the two modes are coupled, the mixed-mode cracking becomes complicated because the parameters related to both modes must be simultaneously computed. This case becomes very challenging in that, first, it is unclear how in reality the two modes are coupled, and secondly, one does not know whether a test that shows mix-mode crack contains sufficient information for the inverse computation. In such case, the more advanced potential-based CZMs, which is mentioned in section 7.2.6, may be used as the basis for the inverse problem.

7.2.5 Improvement of Efficiency of the Inverse Procedure

The current optimization solver is the Nelder-Mead method. Although it is robust for practical usage, it is not an efficient solver. A good candidate is the Levenberg–Marquardt algorithm, which is a nonlinear optimization method that has reasonably good combination of robustness and efficiency. The challenge in employing this algorithm is to implement the constraints and to derive the gradient of the objective function. Another improvement can be achieved by using higher-order elements in the FE model, e.g. T6 and Q8/Q9 elements. Thus the total number of degrees of freedom of the system can be reduced significantly and computation cost can be reduced.

7.2.6 Potential-Based CZM

In the potential-based CZM, the constitutive parameters are derived from a unified potential [126]. With only a few parameters, such potential function provides full description of the coupled properties of the mode I and mode II CZMs. This is the primary advantage of employing the potential-based CZMs in the inverse procedure. The challenges of using the potential-based CZM in the inverse analysis are: (1) the sensitivity analysis of the fracture to the model parameters; (2) the design of feasible test configurations of both specimen geometry and loading condition. The use of a potential theory based CZM, in conjunction with a hybrid inverse technique (see Chapter 4 and 5), offers a solid basis for further development and integration of the underlying experimental theoretical, and computational approaches.

REFERENCES

[1] Mehta PK and Monteiro PJM (2006) Concrete: Microstructure, Properties, and Materials. 3rd Edn. McGraw-Hill, New York

[2] Balaguru PN and Shah SP (1992) Fiber-Reinforced Cement Composites. McGraw-Hill, New York

[3] Bentur A and Mindess S (1990) Fibre Reinforced Cementitious Composites. Elsevier Applied Science, London; New York

[4] Naaman AE and Reinhardt HW (1992) High Performance Fiber Reinforced Cement Composites. Mainz, Germany, June 23-26, 1991. E & FN Spon, London; New York

[5] Naaman AE and Reinhardt HW (2003) High Performance Fiber Reinforced Cement Composites (HPFRCC4), Ann Arbor, USA, June 15-18, 2003. RILEM Publications, Bagneux, France

[6] Reinhardt HW and Naaman AE (1996) High Performance Fiber Reinforced Cement Composites 2 (HPFRCC2), Ann Arbor, USA, June 11-14, 1995. E & FN Spon, London, New York

[7] Reinhardt HW and Naaman AE (1999) High Performance Fiber Reinforced Cement Composites (HPFRCC3), Mainz, Germany, May 16-19, 1999. Rilem, Cachan, France

[8] Li VC (2002) Large volume, high-performance applications of fibers in civil engineering. *Journal of Applied Polymer Science* 83: 660-686

[9] Suresh S and Mortensen A (1998) Fundamentals of Functionally Graded Materials: Processing and Thermomechanical Behaviour of Graded Metals and Metal-Ceramic Composites. IOM Communications Ltd, London

[10] Bolander JE and Lim YM (2008) Simulation of fiber distribution effects in fiber-reinforced cement composites In: Paulino GH, Pindera MJ, Dodds RH, Jr*., et al.* (eds) Multiscale and Functionally Graded Material 2006 (M&FGM 2006), AIP Conference Proceedings 973 American Institute of Physics, Oahu Island, Hawaii, pp 507-512

[11] Dias CMR, Savastano H, Jr. and John VM (2008) The FGM concept in the development of fiber cement components In: Paulino GH, Pindera MJ, Dodds RH, Jr*., et al.* (eds) Multiscale and Functionally Graded Material 2006 (M&FGM 2006), AIP Conference Proceedings 973 American Institute of Physics, Oahu Island, Hawaii, pp 525-531

[12] Roesler J, Bordelon C, Gaedicke C, Park K and Paulino GH (2008) Fracture behavior and properties of functionally graded fiber-reinforced concrete In: Paulino GH,

Pindera MJ, Dodds RH, Jr*., et al.* (eds) Multiscale and Functionally Graded Material 2006 (M&FGM 2006), AIP Conference Proceedings 973 American Institute of Physics, Oahu Island, Hawaii, pp 513-518

[13] Shen B, Hubler M, Paulino GH and Struble LJ (2008) Manufacturing and mechanical testing of a new functionally graded fiber reinforced cement composite In: Paulino GH, Pindera MJ, Dodds RH, Jr*., et al.* (eds) Multiscale and Functionally Graded Material 2006 (M&FGM 2006), AIP Conference Proceedings 973 American Institute of Physics, Oahu Island, Hawaii, pp 519-524

[14] Paulino GH, Jin Z-H and Dodds RHJ (2003) Failure of functionally graded materials. In: Karihaloo B and Knauss WG (Eds) Encyclopedia of Comprehensive Structural Integrity, Vol. 2, Chapter 13, Elsevier, Amsterdam

[15] Sun JH, Chang E, Chao CH and Cheng MJ (1993) The spalling modes and degradation mechanism of ZrO2-8wt.%Y2O3/CVD-Al2O3/Ni-22Cr-10Al-1Y thermal-barrier coatings. *Oxidation of Metals* 40: 465-81

[16] Ho S, Hillman C, Lange FF and Suo Z (1995) Surface cracking in layers under biaxial, residual compressive stress. *Journal of the American Ceramic Society* 78: 2353-9

[17] Tzimas E, Mullejans H, Peteves SD, Bressers J and Stamm W (2000) Failure of thermal barrier coating systems under cyclic thermomechanical loading. *Acta Materialia* 48: 4699-4707

[18] Zhou YC and Hashida T (2002) Thermal fatigue failure induced by delamination in thermal barrier coating. *International Journal of Fatigue* 24: 407-417

[19] Niino M and Maeda S (1990) Recent development status of functionally gradient materials. *ISIJ International* 30: 699-703

[20] Gooch WA, Chen BHC, Burkins MS, Palicka R, Rubin J and Rayichandran R (1999) Development and ballistic testing of a functionally gradient ceramic/metal applique (Mater. Sci. Forum (Switzerland)) Trans Tech Publications, Dresden, Germany, pp 614-21

[21] Chin ESC (1999) Army focused research team on functionally graded armor composites (Mater. Sci. Eng. A, Struct. Mater., Prop. Microstruct. Process. (Switzerland)) Elsevier, San Antonio, TX, USA, pp 155-61

[22] Yamada K, Sakamura J and Nakamura K (1999) Broadband ultrasound transducers using piezoelectrically graded materials (Mater. Sci. Forum (Switzerland)) Trans Tech Publications, Dresden, Germany, pp 527-32

[23] Zhao J, Ai X and Huang XP (2002) Relationship between the thermal shock behavior and the cutting performance of a functionally gradient ceramic tool. *Journal of Materials Processing Technology* 129: 161-166

[24] Gasik MM and Ueda S (1999) Micromechanical modelling of functionally graded W-Cu materials for divertor plate components in a fusion reactor (Mater. Sci. Forum (Switzerland)) Trans Tech Publications, Dresden, Germany, pp 603-7

[25] Watari F, Yokoyama A, Matsuno H, Saso F, Uo M and Kawasaki T (1999) Biocompatibility of titanium/hydroxyapatite and titanium/cobalt functionally graded implants. *Materials Science Forum* 308-311: 356-361

[26] Borovinskaya IP, Merzhanov AG and Uvarov VI (1999) SHS materials of graded porosity. *Materials Science Forum* 308-311: 151-156

[27] Watanabe R (1995) Powder processing of functionally gradient materials. *MRS Bulletin* 20: 32-34

[28] Pei YT, Ocelik V and De Hosson JTM (2002) SiCp/Ti6Al4V functionally graded materials produced by laser melt injection. *Acta Materialia* 50: 2035-2051

[29] Sampath S, Herman H, Shimoda N and Saito T (1995) Thermal spray processing of FGMs. *MRS Bulletin* 20: 27-31

[30] Prchlik L, Sampath S, Gutleber J, Bancke G and Ruff AW (2001) Friction and wear properties of WC-Co and Mo-Mo2C based functionally graded materials. *Wear* 249: 1103-15

[31] Hirai T (1995) CVD processing. *MRS Bulletin* 20: 45-47

[32] Cirakoglu M, Bhaduri S and Bhaduri SB (2002) Combustion synthesis processing of functionally graded materials in the Ti-B binary system. *Journal of Alloys and Compounds* 347: 259-265

[33] Abanto-Bueno J and Lambros J (2005) Experimental determination of cohesive failure properties of a photodegradable copolymer. *Experimental Mechanics* 45: 144-52

[34] Abanto-Bueno J and Lambros J (2006) An experimental study of mixed mode crack initiation and growth in functionally graded materials. *Experimental Mechanics* 46: 179-196

[35] Barenblatt GI (1959) The formation of equilibrium cracks during brittle fracture. General ideas and hypotheses. Axially-symmetric cracks. *Journal of Applied Mathematics and Mechanics* 23: 622-636

[36] Dugdale DS (1960) Yielding of steel sheets containing slits. *Journal of the Mechanics and Physics of Solids* 8: 100-104

[37] Hillerborg A, Modéer M and Petersson PE (1976) Analysis of crack formation and crack growth in concrete by means of fracture mechanics and finite elements. *Cement and Concrete Research* 6: 773-781

[38] Xu XP and Needleman A (1994) Numerical simulations of fast crack growth in brittle solids. *Journal of the Mechanics and Physics of Solids* 42: 1397

[39] Zhang Z and Paulino GH (2005) Cohesive zone modeling of dynamic failure in homogeneous and functionally graded materials. *International Journal of Plasticity* 21: 1195-254

[40] Camacho GT and Ortiz M (1996) Computational modeling of impact damage in brittle materials. *International Journal of Solids and Structures* 33: 2899-938

[41] Ortiz M and Pandolfi A (1999) Finite-deformation irreversible cohesive elements for three-dimensional crack-propagation analysis. *International Journal for Numerical Methods in Engineering* 44: 1267-1282

[42] Zhang Z and Paulino GH (2007) Wave propagation and dynamic analysis of smoothly graded heterogeneous continua using graded finite elements. *International Journal of Solids and Structures* 44: 3601-3626

[43] Moes N and Belytschko T (2002) Extended finite element method for cohesive crack growth. *Engineering Fracture Mechanics* 69: 813-33

[44] Wells GN and Sluys LJ (2001) A new method for modeling cohesive cracks using finite elements. *International Journal for Numerical Methods in Engineering* 50: 2667-2682

[45] Rahulkumar P (2000) Cohesive element modeling of viscoelastic fracture: application to peel testing of polymers. *International Journal of Solids and Structures* 37: 1873-1897

[46] Zhang Z, Paulino GH and Celes W (2007) Extrinsic cohesive modeling of dynamic fracture and microbranching instability in brittle materials. *International Journal for Numerical Methods in Engineering* 72: 893-923

[47] Roesler J, Paulino GH, Park K and Gaedicke C (2007) Concrete fracture prediction using bilinear softening. *Cement and Concrete Composites* 29: 300-12

[48] Shim D-J, Paulino GH and Dodds RH, Jr. (2006) J resistance behavior in functionally graded materials using cohesive zone and modified boundary layer models. *International Journal of Fracture* 139: 91-117

[49] Song SH, Paulino GH and Buttlar WG (2006) Simulation of crack propagation in asphalt concrete using an intrinsic cohesive zone model. *ASCE Journal of Engineering Mechanics* 132: 1215-1223

[50] Song SH, Paulino GH and Buttlar WG (2007) Influence of the cohesive zone model shape parameter on asphalt concrete fracture behavior. In: Paulino GH, Pindera M-J, Dodds RH, Jr*., et al.* (Eds) Multiscale and Functionally Graded Materials, AIP, Oahu Island, Hawaii

[51] Bazant ZP and Li YN (1997) Cohesive crack with rate-dependent opening and viscoelasticity: I. mathematical model and scaling. *International Journal of Fracture* 86: 247-265

[52] Zhengyu Z (2007) Extrinsic Cohesive Modeling of Dynamic Fracture and Microbranching Instability Using a Topological Data Structure, PhD thesis. University of Illinois at Urbana-Champaign, Urbana, Illinois

[53] van Mier JGM and van Vliet MRA (2002) Uniaxial tension test for the determination of fracture parameters of concrete: state of the art. *Fracture of Concrete and Rock* 69: 235-247

[54] Yang J and Fischer G (2006) Simulation of the tensile stress-strain behavior of strain hardening cementitious composites. In: Konsta-Gdoutos MS (Ed) Measuring, Monitoring and Modeling Concrete Properties, Springer, Dordrecht, pp 25-31

[55] Shah SP, Ouyang C and Swartz SE (1995) Fracture Mechanics of Concrete: Applications of Fracture Mechanics to Concrete, Rock and other Quasi-brittle Materials. Wiley, New York

[56] Volokh KY (2004) Comparison between cohesive zone models. *Communications in Numerical Methods in Engineering* 20: 845-856

[57] van Mier JGM (1997) Fracture Processes of Concrete: Assessment of Material Parameters for Fracture Models. CRC Press, Boca Raton

[58] Elices M (2002) The cohesive zone model: advantages, limitations and challenges. *Engineering Fracture Mechanics* 69: 137-163

[59] Seong Hyeok S, Paulino GH and Buttlar WG (2006) A bilinear cohesive zone model tailored for fracture of asphalt concrete considering viscoelastic bulk material. *Engineering Fracture Mechanics* 73: 2829-48

[60] Song SH, Paulino GH and Buttlar WG (2005) Cohesive zone simulation of mode I and mixed-mode crack propagation in asphalt concrete. Geo-Frontiers 2005 ASCE, Reston, VA, Austin, TX, U.S.A, pp 189-198

[61] Cheng P, Sutton MA, Schreier HW and McNeill SR (2002) Full-field speckle pattern image correlation with B-spline deformation function. *Experimental Mechanics* 42: 344-352

[62] Carrillo-Heian EM, Carpenter RD, Paulino GH, Gibeling JC and Munir ZA (2001) Dense layered molybdenum disilicide-silicon carbide functionally graded composites formed by field-activated synthesis. *Journal of the American Ceramic Society* 84: 962-968

[63] Jin G, Nishikawa T, Honda S and Awaji H (2003) Stress analysis in multilayered FGM plates under thermal shock. *Materials Science Forum* 423-425: 693-7

[64] Zhou X and Li Z (2005) Characterization of rheology of fresh fiber reinforced cementitious composites through ram extrusion. *Materials and Structures/Materiaux et Constructions* 38: 17-24

[65] Shah SP and Shao Y (1994) Extrusion processing of fiber-reinforced cement-matrix composites (American Society of Mechanical Engineers, Materials Division (Publication) MD) ASME, New York, NY, USA, Chicago, IL, USA, pp 205-210

[66] Shao Y and Shah SP (1997) Mechanical properties of PVA fiber reinforced cement composites fabricated by extrusion processing. *ACI Materials Journal* 94: 555-564

[67] Takashima H, Miyagai K, Hashida T and Li VC (2003) A design approach for the mechanical properties of polypropylene discontinuous fiber reinforced cementitious composites by extrusion molding. *Engineering Fracture Mechanics* 70: 853-870

[68] Akkaya Y, Peled A and Shah SP (2000) Parameters related to fiber length and processing in cementitious composites. *Materials and Structures/Materiaux et Constructions* 33: 515-524

[69] Peled A and Shah SP (2003) Processing effects in cementitious composites: Extrusion and casting. *Journal of Materials in Civil Engineering* 15: 192-199

[70] Li VC, Wu C, Wang S, Ogawa A and Saito T (2002) Interface tailoring for strain-hardening polyvinyl alcohol-engineered cementitious composite (PVA-ECC). *ACI Materials Journal* 99: 463-472

[71] Peled A, Cyr MF and Shah SP (2000) High content of fly ash (Class F) in extruded cementitious composites. *ACI Materials Journal* 97: 509-517

[72] Mindess S, Young JF and Darwin D (2003) Concrete. 2nd Edn. Prentice Hall, Upper Saddle River, N.J.

[73] Kanda T and Li VC (1999) Effect of fiber strength and fiber-matrix interface on crack bridging in cement composites. *ASCE Journal of Engineering Mechanics* 125: 290-299

[74] Shen B (2003) Experimental approaches for determining rheological properties of cement-based extrudates. Hong Kong University of Science and Technology, Hong Kong

[75] Naaman AE (2003) Strain Hardening and Deflection Hardening Fiber Reinforced Cement Composites In: Naaman AE and Reinhardt HW (eds) High Performance Fiber Reinforced Cement Composites (HPFRCC4) RILEM Publications, Ann Arbor, USA, pp 95-113

[76] Shin SK, Kim JJH and Lim YM (2007) Investigation of the strengthening effect of DFRCC applied to plain concrete beams. *Cement and Concrete Composites* 29: 465-473

[77] Shao Y, Qiu J and Shah SP (2001) Microstructure of extruded cement-bonded fiberboard. *Cement and Concrete Research* 31: 1153-1161

[78] Dally JW and Riley WF (2005) Experimental Stress Analysis. College House Enterprises, Knoxville, Tenn.

[79] Peters WH and Ranson WF (1982) Digital imaging techniques in experimental stress analysis. *Optical Engineering* 21: 427-31

[80] Sutton MA, Wolters WJ, Peters WH, Ranson WF and McNeill SR (1983) Determination of displacements using an improved digital correlation method. *Image and Vision Computing* 1: 133-139

[81] Chu TC, Ranson WF, Sutton MA and Peters WH (1985) Applications of digital-image-correlation techniques to experimental mechanics. *Experimental Mechanics* 25: 232-44

[82] Bruck HA, McNeill SR, Sutton MA and Peters WH, III (1989) Digital image correlation using Newton-Raphson method of partial differential correction. *Experimental Mechanics* 29: 261-267

[83] Bonnet M and Constantinescu A (2005) Inverse problems in elasticity. *Inverse Problems* 21: 1-50

[84] Avril S, Bonnet M, Bretelle A-S, Grediac M, Hild F, Ienny P, Latourte F, Lemosse D, Pagano S, Pagnacco E and Pierron F (2008) Overview of identification methods of mechanical parameters based on full-field measurements. *Experimental Mechanics* 48: 381-402

[85] Abanto-Bueno J and Lambros J (2002) Investigation of crack growth in functionally graded materials using digital image correlation. *Engineering Fracture Mechanics* 69: 1695-1711

[86] Tan H, Liu C, Huang Y and Geubelle PH (2005) The cohesive law for the particle/matrix interfaces in high explosives. *Journal of the Mechanics and Physics of Solids* 53: 1892-917

[87] Choi S and Shah SP (1997) Measurement of deformations on concrete subjected to compression using image correlation. *Experimental Mechanics* 37: 307-313

[88] Sokhwan C and Shah SP (1998) Fracture mechanism in cement-based materials subjected to compression. *Journal of Engineering Mechanics - ASCE* 124: 94-102

[89] Corr D, Accardi M, Graham-Brady L and Shah SP (2007) Digital image correlation analysis of interfacial debonding properties and fracture behavior in concrete. *Engineering Fracture Mechanics* 74: 109-21

[90] Zitova B and Flusser J (2003) Image registration methods: A survey. *Image and Vision Computing* 21: 977-1000

[91] Vendroux G and Knauss WG (1998) Submicron deformation field measurements: Part 2. Improved digital image correlation. *Experimental Mechanics* 38: 85-92

[92] Lu H and Cary PD (2000) Deformation measurements by digital image correlation: implementation of a second-order displacement gradient. *Experimental Mechanics* 40: 393-400

[93] Lecompte D, Smits A, Bossuyt S, Sol H, Vantomme J, Van Hemelrijck D and Habraken AM (2006) Quality assessment of speckle patterns for digital image correlation. *Optics and Lasers in Engineering* 44: 1132-1145

[94] Lecompte D, Sol H, Vantomme J and Habraken A (2006) Analysis of speckle patterns for deformation measurements by digital image correlation In: Proceedings of SPIE Vol 6341 International Society for Optical Engineering, Bellingham, WA, United States, Nimes, France, pp 63410E1-6

[95] Sorzano COS, Thevenaz P and Unser M (2005) Elastic registration of biological images using vector-spline regularization. *IEEE Transactions on Biomedical Engineering* 52: 652-663

[96] Abanto-Bueno JL (2004) Fracture of a Model Functionally Graded Material Manufactured from a Photo-Sensitive Polyethylene, PhD thesis. University of Illinois at Urbana-Champaign, United States -- Illinois

[97] Schweizerhof KH and Wriggers P (1986) Consistent linearization for path following methods in nonlinear FE analysis. *Computer Methods in Applied Mechanics and Engineering* 59: 261-79

[98] Crisfield MA (1981) A fast incremental/iterative solution procedure that handles `snap-through'. *Computers and Structures* 13: 55-62

[99] De Boor C (2001) A Practical Guide to Splines. Springer, New York

[100] Deuflhard P and Hohmann A (2003) Numerical Analysis in Modern Scientific Somputing: An Introduction. Springer, New York

[101] Fletcher R (1987) Practical Methods of Optimization. Wiley, Chichester ; New York

[102] Nelder JA and Mead R (1965) Simplex method for function minimization. *Computer Journal* 7: 308-313

[103] Nocedal J and Wright SJ (2006) Numerical Optimization. Springer, New York

[104] Avril S and Pierron F (2007) General framework for the identification of constitutive parameters from full-field measurements in linear elasticity. *International Journal of Solids and Structures* 44: 4978-5002

[105] Bezerra LM and Saigal S (1993) A boundary element formulation for the inverse elastostatics problem (IESP) of flaw detection. *International Journal for Numerical Methods in Engineering* 36: 2189-202

[106] Tarantola A (2005) Inverse Problem Theory and Methods for Model Parameter Estimation. Society for Industrial and Applied Mathematics, Philadelphia, PA

[107] Schnur DS and Zabaras N (1990) Finite element solution of two-dimensional inverse elastic problems using spatial smoothing. *International Journal for Numerical Methods in Engineering* 30: 57-75

[108] Shen B, Stanciulescu I and Paulino GH (2008) Inverse computation of cohesive fracture properties from displacement fields. *Submitted for journal publication*

[109] Maniatty AM and Zabaras NJ (1994) Investigation of regularization parameters and error estimating in inverse elasticity problems. *International Journal for Numerical Methods in Engineering* 37: 1039-1052

[110] Marin L, Elliott L, Heggs PJ, Ingham DB, Lesnic D and Wen X (2004) Comparison of regularization methods for solving the Cauchy problem associated with the Helmholtz equation. *International Journal for Numerical Methods in Engineering* 60: 1933-1947

[111] Marin L and Lesnic D (2002) Regularized boundary element solution for an inverse boundary value problem in linear elasticity. *Communications in Numerical Methods in Engineering* 18: 817-825

[112] Tikhonov AN (1995) Numerical Methods for the Solution of Ill-posed Problems. Kluwer Academic Publishers, Dordrecht; Boston

[113] Marin L and Lesnic D (2003) BEM first-order regularisation method in linear elasticity for boundary identification. *Computer Methods in Applied Mechanics and Engineering* 192: 2059-2071

[114] Colton DL and Kress R (1992) Inverse Acoustic and Electromagnetic Scattering Theory. Springer-Verlag, Berlin ; New York

[115] Barraud S, Dubard JL and Pompei D (1998) 3D-TLM pattern recognitions in free space. *IEE Proceedings-Microwaves, Antennas and Propagation* 145: 387-91

[116] Buchanan J, Gilbert R, Wirgin A and Xu Y (2002) Depth sounding: An illustration of some of the pitfalls of inverse scattering problems. *Mathematical and computer modelling* 35: 1315-1354

[117] Graham BM and Adler A (2006) Objective selection of hyperparameter for EIT. *Physiological Measurement* 27: 65-79

[118] Jiang M, Zhou T, Cheng J, Cong W and Wang G (2007) Image reconstruction for bioluminescence tomography from partial measurement. *Opt Express* 15: 11095-11116

[119] Song SH, Paulino GH and Buttlar WG (2006) Simulation of crack propagation in asphalt concrete using an intrinsic cohesive zone model. *Journal of Engineering Mechanics* 132: 1215-1223

[120] Dick-Nielsen L, Stang H and Poulsen PN (2006) Condition for strain-hardening in ECC uniaxial test specimen. In: Konsta-Gdoutos MS (Ed) Measuring, Monitoring and Modeling Concrete Properties, Springer, Dordrecht, pp 41-47

[121] Kyoungsoo P, Paulino GH and Roesler JR (2008) Determination of the kink point in the bilinear softening model for concrete. *Engineering Fracture Mechanics* 75: 3806-18

[122] Molimard J, Le Riche R, Vautrin A and Lee JR (2005) Identification of the four orthotropic plate stiffnesses using a single open-hole tensile test. *Experimental Mechanics* 45: 404-11

[123] Li VC, Wang S and Wu C (2001) Tensile strain-hardening behavior or polyvinyl alcohol engineered cementitious composite (PVA-ECC). *ACI Materials Journal* 98: 483-492

[124] Mindess S, Young JF and Darwin D (2003) Concrete. 2nd Edn. Prentice Hall, Upper Saddle River, NJ

[125] Song SH (2006) Fracture and Size Effect of Asphalt Concrete: A Cohesive Zone Modeling Approach Considering Rate Effects, PhD thesis. University of Illinois at Urbana-Champaign, Urbana, Illinois

[126] Park K, Paulino GH and Roesler JR (2009) A unified potential-based cohesive model of mixed-mode fracture. *Journal of the Mechanics and Physics of Solids* In Press, Accepted Manuscript

APPENDIX A - BICUBIC INTERPOLATION

The bicubic interpolation of a unit cell (Figure A.1)

$$f(h,t) = \sum_{m=0}^{3}\sum_{n=0}^{3} \alpha_{mn} h^m t^n , \tag{A.1}$$

consists of determining its 16 coefficients, α_{mn}.

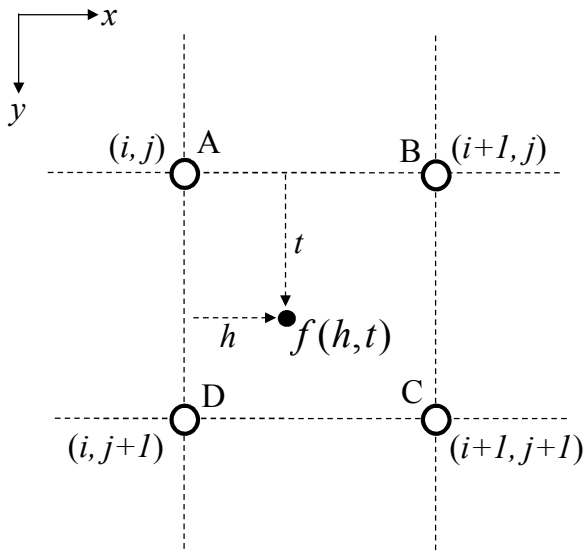

Figure A.1: Unit cell to be interpolated by a bicubic function, $f(h,t)$

The values of $f(h,t)$, together with its first derivatives with respect to t and u,

$$\begin{aligned} f_x &= f_h(h,t) = \sum_{m=1}^{3}\sum_{n=0}^{3} m\alpha_{mn} h^{m-1} t^n \\ f_y &= f_t(h,t) = \sum_{m=0}^{3}\sum_{n=1}^{3} n\alpha_{mn} h^m t^{n-1} , \end{aligned} \tag{A.2}$$

and cross-derivative,

$$f_{xy} = f_{ht} = \sum_{m=1}^{3}\sum_{n=1}^{3} mn\alpha_{mn} h^{m-1} t^{n-1} , \tag{A.3}$$

at the four cell nodes provides a system of 16 equations

$$\begin{bmatrix}
1 & 0 & 0 & 0 & 0 & 0 & 0 & 0 & 0 & 0 & 0 & 0 & 0 & 0 & 0 & 0 \\
1 & 0 & 0 & 0 & 1 & 0 & 0 & 0 & 1 & 0 & 0 & 0 & 1 & 0 & 0 & 0 \\
1 & 1 & 1 & 1 & 1 & 1 & 1 & 1 & 1 & 1 & 1 & 1 & 1 & 1 & 1 & 1 \\
1 & 1 & 1 & 1 & 0 & 0 & 0 & 0 & 0 & 0 & 0 & 0 & 0 & 0 & 0 & 0 \\
0 & 0 & 0 & 0 & 1 & 0 & 0 & 0 & 0 & 0 & 0 & 0 & 0 & 0 & 0 & 0 \\
0 & 0 & 0 & 0 & 1 & 0 & 0 & 0 & 2 & 0 & 0 & 0 & 3 & 0 & 0 & 0 \\
0 & 0 & 0 & 0 & 1 & 1 & 1 & 1 & 2 & 2 & 2 & 2 & 3 & 3 & 3 & 3 \\
0 & 0 & 0 & 0 & 1 & 1 & 1 & 1 & 0 & 0 & 0 & 0 & 0 & 0 & 0 & 0 \\
0 & 1 & 0 & 0 & 0 & 0 & 0 & 0 & 0 & 0 & 0 & 0 & 0 & 0 & 0 & 0 \\
0 & 1 & 0 & 0 & 0 & 1 & 0 & 0 & 0 & 1 & 0 & 0 & 0 & 1 & 0 & 0 \\
0 & 1 & 2 & 3 & 0 & 1 & 2 & 3 & 0 & 1 & 2 & 3 & 0 & 1 & 2 & 3 \\
0 & 1 & 2 & 3 & 0 & 0 & 0 & 0 & 0 & 0 & 0 & 0 & 0 & 0 & 0 & 0 \\
0 & 0 & 0 & 0 & 0 & 1 & 0 & 0 & 0 & 0 & 0 & 0 & 0 & 0 & 0 & 0 \\
0 & 0 & 0 & 0 & 0 & 1 & 0 & 0 & 0 & 2 & 0 & 0 & 0 & 3 & 0 & 0 \\
0 & 0 & 0 & 0 & 0 & 1 & 2 & 3 & 0 & 2 & 4 & 6 & 0 & 3 & 6 & 9 \\
0 & 0 & 0 & 0 & 0 & 1 & 2 & 3 & 0 & 0 & 0 & 0 & 0 & 0 & 0 & 0
\end{bmatrix}
\begin{bmatrix} \alpha_{11} \\ \alpha_{12} \\ \alpha_{13} \\ \alpha_{14} \\ \alpha_{21} \\ \alpha_{22} \\ \alpha_{23} \\ \alpha_{24} \\ \alpha_{31} \\ \alpha_{32} \\ \alpha_{33} \\ \alpha_{34} \\ \alpha_{41} \\ \alpha_{42} \\ \alpha_{43} \\ \alpha_{44} \end{bmatrix}
=
\begin{bmatrix} f^A \\ f^B \\ f^C \\ f^D \\ f_x^A \\ f_x^B \\ f_x^C \\ f_x^D \\ f_y^A \\ f_y^B \\ f_y^C \\ f_y^D \\ f_{xy}^A \\ f_{xy}^B \\ f_{xy}^C \\ f_{xy}^D \end{bmatrix} . \tag{A.4}$$

The sixteen coefficients can now be easily solved.

From equation (A.4), one notes that the bicubic coefficients depends on the value of $f(h,t)$ and its first and cross-derivatives at the cell nodes. For a discrete image intensity data, the derivatives at each grid point have to be computed numerically, and their approximation depends on whether the grid point are on the boundary, adjacent to the boundary, or inside the image. Suppose the image size is $N \times M$, any pixel location (i, j) satisfies:

$$\begin{aligned} 1 \le i \le M \\ 1 \le j \le N \end{aligned} .$$

The derivatives can be computed, for f_x,

$$
\begin{aligned}
&f_x(j,1) = f(j,2) - f(j,1) \\
&f_x(j,M) = f(j,M) - f(j,M-1) \\
&f_x(j,2) = \big(f(j,3) - f(j,1)\big)/2 \\
&f_x(j,M-1) = \big(f(j,M) - f(j,M-2)\big)/2 \\
&f_x(j,i) = \big(f(j,i-2) - 8f(j,i-1) + 8f(j,i+1) + f(j,i+2)\big)/12 \ ,
\end{aligned}
\tag{A.5}
$$

for f_y,

$$
\begin{aligned}
&f_y(1,i) = f(2,i) - f(1,i) \\
&f_y(N,i) = f(N,i) - f(N-1,i) \\
&f_y(2,i) = \big(f(3,i) - f(1,i)\big)/2 \\
&f_y(N-1,i) = \big(f(N,i) - f(N-1,i)\big)/2 \\
&f_y(j,i) = \big(f(j-2,i) - 8f(j-1,i) + 8f(j+1,i) + f(j+2,i)\big)/12 \ ,
\end{aligned}
\tag{A.6}
$$

and for f_{xy},

$$
\begin{aligned}
&f_{xy}(1,i) = f_x(2,i) - f_x(1,i) \\
&f_{xy}(N,i) = f_x(N,i) - f_x(N-1,i) \\
&f_{xy}(j,1) = f_y(j,2) - f_y(j,1) \\
&f_{xy}(j,M) = f_y(j,M) - f_y(j,M-1) \\
&f_{xy}(2,i) = \big(f_x(3,i) - f_x(1,i)\big)/2 \\
&f_{xy}(N-1,i) = \big(f_x(N,i) - f_x(N-2,i)\big)/2 \\
&f_{xy}(j,2) = \big(f_y(j,3) - f_y(j,1)\big)/2 \\
&f_{xy}(j,M-1) = \big(f_y(j,M) - f_y(j,M-2)\big)/2 \\
&f_{xy}(i,j) = \sum_{r=i-2}^{i+2} \sum_{s=j-2}^{j+2} c_{r,s} f(r,s)
\end{aligned}
\ ,
\tag{A.7}
$$

where coefficient matrix $\left[c_{r,s}\right]$ is

$$
\left[c_{r,s}\right] = \frac{1}{24}
\begin{bmatrix}
0 & 1 & 0 & -1 & 0 \\
1 & -10 & 0 & 10 & -1 \\
0 & 0 & 0 & 0 & 0 \\
-1 & 10 & 0 & -10 & 1 \\
0 & -1 & 0 & 1 & 0
\end{bmatrix}.
\tag{A.8}
$$

APPENDIX B - COMPUTATION OF CUBIC B-SPLINE INTERPOLATION

Define the B-spline sequence of knots as

$$\boldsymbol{\tau} = \{\tau_1,\ \tau_2,\ \ldots\ ,\ \tau_{l+8}\}, \tag{B.1}$$

where

$$\begin{array}{c} \tau_1 = \cdots = \tau_4 < \tau_5 < \cdots < \tau_{l+4} < \tau_{l+5} = \cdots = \tau_{l+8} \\ \updownarrow \quad \updownarrow \qquad\qquad \updownarrow \quad \updownarrow \\ 0 < \Delta_{\mathrm{n}1} < \cdots < \Delta_{\mathrm{n}l} < \Delta_{\mathrm{nc}} \end{array} .$$

Now the spline can be constructed

$$\sigma(\tau) = \sum_{i=1}^{l+4} d_{i-2} B_{i,4}(\tau), \tag{B.2}$$

where d_i is the de Boor point and $B_{i,4}$ is the 4th order B-spline associated with knots $\tau_i,\ \tau_{i+1},\ \ldots\ ,\ \tau_{i+4}$, and $\boldsymbol{\lambda} = \{\Delta_{\mathrm{nc}},\ d_{-1},\ d_0,\ \ldots\ ,\ d_{l+2}\}$. The explicit expression of $B_{i,4}$ for non-uniformly spaced $\boldsymbol{\tau}$ is

$$B_{i,4}(\tau) = \begin{cases} \dfrac{\tau-\tau_i}{\tau_{i+3}-\tau_i}\dfrac{\tau-\tau_i}{\tau_{i+2}-\tau_i}\dfrac{\tau-\tau_i}{\tau_{i+1}-\tau_i}, & \tau_i \le \tau \le \tau_{i+1} \\ \dfrac{\tau-\tau_i}{\tau_{i+3}-\tau_i}\dfrac{\tau-\tau_i}{\tau_{i+2}-\tau_i}\dfrac{\tau_{i+2}-\tau}{\tau_{i+2}-\tau_{i+1}} + \dfrac{\tau-\tau_i}{\tau_{i+3}-\tau_i}\dfrac{\tau_{i+3}-\tau}{\tau_{i+3}-\tau_{i+1}}\dfrac{\tau-\tau_{i+1}}{\tau_{i+2}-\tau_{i+1}} + \dfrac{\tau_{i+4}-\tau}{\tau_{i+4}-\tau_{i+1}}\dfrac{\tau-\tau_{i+1}}{\tau_{i+3}-\tau_{i+1}}\dfrac{\tau-\tau_{i+1}}{\tau_{i+2}-\tau_{i+1}}, & \tau_{i+1} \le \tau \le \tau_{i+2} \\ \dfrac{\tau-\tau_i}{\tau_{i+3}-\tau_i}\dfrac{\tau_{i+3}-\tau}{\tau_{i+3}-\tau_{i+1}}\dfrac{\tau_{i+3}-\tau}{\tau_{i+3}-\tau_{i+2}} + \dfrac{\tau_{i+4}-\tau}{\tau_{i+4}-\tau_{i+1}}\dfrac{\tau-\tau_{i+1}}{\tau_{i+3}-\tau_{i+1}}\dfrac{\tau_{i+3}-\tau}{\tau_{i+3}-\tau_{i+2}} + \dfrac{\tau_{i+4}-\tau}{\tau_{i+4}-\tau_{i+1}}\dfrac{\tau_{i+4}-\tau}{\tau_{i+4}-\tau_{i+2}}\dfrac{\tau-\tau_{i+2}}{\tau_{i+3}-\tau_{i+2}}, & \tau_{i+2} \le \tau \le \tau_{i+3} \\ \dfrac{\tau_{i+4}-\tau}{\tau_{i+4}-\tau_{i+1}}\dfrac{\tau_{i+4}-\tau}{\tau_{i+4}-\tau_{i+2}}\dfrac{\tau_{i+4}-\tau}{\tau_{i+4}-\tau_{i+3}}, & \tau_{i+3} \le \tau \le \tau_{i+4} \end{cases} \tag{B.3}$$

where τ is the same as Δ_{n}.

To solve for d_i in Equation (B.2), $l+4$ number of equations are needed. With $\sigma(\Delta_{\mathrm{n}i}) = \sigma_i$, there are $l+2$ number of equations. Applying a natural boundary condition for $\sigma(\tau)$

$$\left.\frac{\partial^2\sigma(\Delta_n)}{\partial\Delta_n^2}\right|_{\Delta_n=0} = \left.\frac{\partial^2\sigma(\Delta_n)}{\partial\Delta_n^2}\right|_{\Delta_n=\Delta_{nc}} = 0 \tag{B.4}$$

adds two more equations so that d_i can be solved to obtain the explicit expression of CZM in B-spline form.

APPENDIX C – NOMENCLATURE

$c_{x,i,j}, c_{y,i,j}$	Coefficients of a bicubic B-spline surface
C	Correlation coefficient
C_{img}	Objective function for full-field DIC
$d_{\max}$	Displacement corresponding to $f_{\max}$
E	Young's modulus
f_{fc}	First cracking stress
$f_{\max}$	Maximum flexural stress
$\mathbf{E}$	Green Strain tensor
$\mathbf{F}^{\text{ext}}, \hat{\mathbf{F}}^{\text{ext}}$	Global external force
G_f	Fracture energy
G_{img}	Regularization term for full-field DIC
h,t	Local ordinates within a bilinear computational cell
H	Height of an image in pixel
$\mathbf{H}$	Hooke's tensor
I_r	Intensity of the reference image
I_d	Intensity of the source (i.e., deformed) image
k_{c}	Defined as σ/Δ_{n}
$\mathbf{K}_{\text{b}}^{e}$	Bulk element stiffness matrix
$\mathbf{K}_{\text{c}}^{e}$	Element cohesive stiffness matrix
$\mathbf{K}_{\text{b}}$	Global stiffness matrix of the bulk material
$\mathbf{K}_{\text{c}}$	Global cohesive stiffness matrix
l	Size of Q4 element along crack surface
$\mathbf{L}^{(i)}$	*i*th order linear differential operator
M	Number of unknown parameters of the CZM
$\mathbf{N}_{\text{s}}$	Shape function in natural coordinate system
$\mathbf{N}$	Shape function in isoparametric coordinate system
s	Local natural coordinate along a Q4
u_0, v_0	Components of rigid body translation
u_x, u_y, v_x, v_y	First-order displacement gradients

$u_{xx}, u_{xy}, u_{yy}, v_{xx}, v_{xy}, v_{yy}$	Second-order displacement gradients
$\mathbf{r}$	Element nodal force
$\mathbf{R}$	Residual of the FE system of equations
R_p	Single pixel point in subset domain Ω_P
$\mathbf{T}_{ext}$	Surface traction
$\mathbf{T}_{coh}$	Cohesive traction
$\mathbf{u}^e$	Element nodal displacement
$\mathbf{u}$	Displacement field, also global displacement vector
$\bar{\mathbf{u}}$	Known displacement field from direct problem or from experimental measurement
$\mathbf{u}^*$	Computed displacement field during inverse procedure
$\mathbf{u}_x$	Element nodal displacement vector in x direction
w_{β_1}, w_{β_2}	Weighting factors for the barrier functions
w_c	Weighting factor for C_{img}
w_g	Weighting factor for G_{img}
$\mathbf{w}_u$	Vector of weighting factors for displacement-based formulation
$\mathbf{w}_R$	Vector of weighting factors for residual-based formulation
W	Width of an image in pixel
(x, y)	Coordinates of point before deformation
$(\tilde{x}, \tilde{y})$	Coordinates of point after deformation
(x_0, y_0)	Nodal coordinates
$\mathbf{X}, \mathbf{Y}$	Mapped CZM parameters
α_{mn}	Fitting coefficients for bilinear or bicubic interpolation
β_1, β_2	Barrier functions
$\beta^3(x)$	Fourth-order B-spline basis function
γ	Power-law softening index, also Tikhonov parameter
Γ_{ext}	Specimen boundary
Γ_{coh}	Cohesive surface
Δ_{n}	Crack opening displacement
Δ_{nc}	Critical crack opening displacement
$\mathbf{\Delta}_{\text{n}}$	Coordinates of the control points

ε	Error defined for optimization
ε_T	Convergence measure
θ_b , N_b	Parameters that define the barrier functions
$\boldsymbol{\theta}$	Hooke's parameters
λ	Lame's first parameter
$\boldsymbol{\lambda}$	CZM parameters
μ	Lame's second parameter
μ	Number of internal control points
ν	Poisson's ratio
ξ_i	Normalized horizontal distance measure between control points
σ	Cohesive stress/traction
σ_{c}	Critical cohesive stress
$\boldsymbol{\sigma}$	Cauchy stress tensor
$\Phi(\boldsymbol{\lambda})$	Objective function
χ	Differences of the intensity between reference and deformed images
ψ	Regularization terms
Ψ	Objective function for full-field DIC including regularization term
Ω_P	Subset domain
Ω_{img}	Domain of the region of interest
Ω	Specimen domain

AUTHOR'S BIOGRAPHY

Bin Shen was born in Guizhou, China, on December 5, 1976. He graduated from Zhejiang University, China, in 1999 with a Bachelor's degree in Structural Engineering. In 2003, he obtained a Master of Philosophy degree in Civil Engineering with Dr. Zongjin Li from Hong Kong University of Science and Technology (HKUST). He then worked as a construction laboratory supervisor and later as a research assistant in the Civil Engineering Department, HKUST, before coming to Urbana, Illinois to pursue his doctoral degree in Civil Engineering. During his study at the University of Illinois at Urbana-Champaign (UIUC), he has been a research assistant for an NSF project and a teaching assistant for two undergraduate courses. He has four published journal papers and two conference papers, and he has given two conference presentations. Upon completion of his Ph.D, he will work at California Department of Transportation (CalTrans).